HAPTIC CONTROL OF HYDRAULIC MACHINERY USING PROPORTIONAL VALVES

A Dissertation
Presented to
The Academic Faculty

by

Matthew E. Kontz

In Partial Fulfillment
of the Requirements for the Degree
Doctor of Philosophy in the
G.W. Woodruff School of Mechanical Engineering

Georgia Institute of Technology
December 2007

HAPTIC CONTROL OF HYDRAULIC MACHINERY USING PROPORTIONAL VALVES

Approved by:

Professor Wayne Book, Advisor
G.W. Woodruff School of Mechanical Engineering
Georgia Institute of Technology

Professor Amy Pritchett
School of Aerospace / Industrial and Systems Engineering
Georgia Institute of Technology

Professor Nader Sadegh
G.W. Woodruff School of Mechanical Engineering
Georgia Institute of Technology

Dr. Mark Evans
Staff Engineer
John Deere Commercial Products

Professor Kok-Meng Lee
G.W. Woodruff School of Mechanical Engineering
Georgia Institute of Technology

Date Approved: July 25, 2007

To those who have encouraged me, believed in me and challenged me to do better.

ACKNOWLEDGEMENTS

My first acknowledge needs to go to my advisor, Wayne Book, whose guidance, support and encouragement has been invaluable. Working in your research group has been a joy and privilege. Thanks to Nader Sadegh, Kok-Meng Lee, Amy Pritchett and Mark Evans for serving on my thesis committee. Thank to James Huggins for help developing the backhoe test-bed. You have also been a valuable sounding board for numerous ideas.

Thanks to HUSCO International, John Deere and other supporting companies of the Fluid Power and Motion Control Center of Georgia Tech for supporting this work. A special thank to John Deere for donating the tractor, backhoe and numerous spare parts in additional to monetary support.

A thanks is due to technical advice given by Shraham Tafazoli, Derek Eagles, Mark Evans, Bob Koski, Randy Bobbitt, Maria Cristina Herrera and Simon DiMaio. Thanks to expert operators Ron Faber, Gert Ploeg and Michael Bryson for taking the time to talk about backhoe/excavator operation. Your perspective was extremely valuable. I would also like to acknowledge comments and suggestions from anonymous reviewers who have critiqued some of the work presented in this document.

I would like to acknowledge my mentors: Rod Heisler (Walla Walla College), Emmanuel Nwadiogbu (Honeywell) and Jeff Kuehn (Caterpillar).

Thanks to all of my undergraduate engineering professors at Walla Walla College (Walla Walla University as of September 1, 2007) for encouraging me to pursue graduate school and for preparing me to do so. Thanks to all my teachers at the Lincoln City SDA School who taught me from third grade to my senior year of high school.

Special thank to my parents who encouraged me to develop my strengths and

work hard on my weaknesses. A special thanks is also due to my fiancée, Maria Cristina, for encouragement and for supplying incentive to finish. Since she has already completed her Ph.D., I am one of the few Ph.D. students who can say that his(her) girlfriend/fiancée/wife (boyfriend/fiancé/husband) truly has empathy for the Ph.D. process.

Laurel Dovich (Walla Walla College (University as of Sep 1, 2007) Civil/Structural Engineering Professor), you guided me from Civil Engineering with a structural emphasis to Mechanical Engineering the first week of my junior year. Andrew Alleyne (UIUC Professor), you helped me to choose Dr. Book as my advisor and then less than two years later you helped me make the decision to stay for my Ph.D studies. Probably neither of you realizes the positive and important roles you played in these decisions.

Thanks to all of my lab mates in the Intelligent Machines Dynamics Laboratory. It has been a pleasure working with all of you. Special thanks is due to Davin Swanson, L.J. Tognetti and Young Joon Lee for helping to teach me the ropes when I first started graduate school. A special acknowledge is also due to Joe Frankel. The quality and quantity of the work you put into your master's thesis has been a real asset to my Ph.D. work. It was a pleasure working with you. In addition, I would like to acknowledge officemates Amir Shenouda and Scott Driscoll for allowing me to vent during the more frustrating periods of my Ph.D. journey.

Lastly, I would like to thank all of the friends during my years at Georgia Tech who supplied the ridiculous moments to compliment my otherwise sublime life as a graduate student.

TABLE OF CONTENTS

LIST OF TABLES

LIST OF FIGURES

SUMMARY

Supplying haptic or force feedback to operators using hydraulic machinery such as excavators has the potential to increase operator capabilities. Haptic, robotic, human-machine interfaces enable several enhancing features including coordinated motion control and programmable haptic feedback. Coordinated or resolved motion control supplies a more intuitive means of specifying the equipment's motion. Haptic feedback is used to relay meaningful information back to the user in the form of force signals about digging force acting on the bucket, programmable virtual constraints and system limitations imposed by the mechanism, maximum pressure or maximum flow. In order to make this technology economically viable, the benefits must offset the additional cost associated with implementation. One way to minimize this cost is to not use high-end hydraulic components. For smaller backhoes and mini-excavators this means that the hydraulic systems are comprised of a constant displacement pump and proportional direction control valves. Hydraulic and haptic control techniques suitable for backhoes/excavators are developed and tested on a small backhoe test-bed. A virtual backhoe simulator is created for controller design and human evaluation. Not only is the virtual simulator modeled after the test-bed, but the control algorithm used in the simulator is the same as the actual backhoe test-bed. Data from human subject tests are presented that evaluate the control strategies on both the real and virtual backhoe. The end goal of this project is to incorporate coordinated haptic control algorithms that work with low-cost systems and maximize the enhancement of operator capabilities.

CHAPTER I

INTRODUCTION

The word **haptics** means *of or relating to the sense of touch or tactile.* The addition of haptic feedback to human operated hydraulic machinery can improve productivity and dexterity by relaying information back to the user. Using a robotic human-machine interface allows the haptic feedback to be programmed to display meaningful forces to the operator. These signals could be used to reflect the limitations of the machinery or the forces acting on the end effector. Electronic joysticks and manual levers are the standard methods used to manipulate mobile hydraulic machinery such as excavators. Both of these incorporate haptic feedback; however, it is limited and is not programmable. Traditional manual levers reflect some forces from the line pressures due to their direct coupling to the hydraulic system. Both manual levers and electronic joysticks have some haptic feedback from a restoring spring force which is directly related to their displacement and the commanded velocity of the manipulator. In the case of electronic joysticks this haptic feedback is inherently decoupled from the system being controlled. This means that the human-machine interface is unilateral since information signals are only flowing from the human to the remote manipulator. This requires the operators to rely on other cues such as vibrations, manipulator slowdown/stall and audibles such as engine speed and lug. If a haptic display is used, the human machine interface becomes bilateral and information can also flow back to the operator from the end-effector via haptic feedback.

The goal of this research is to explore how haptic feedback can be applied to control cost effective hydraulic systems. For smaller backhoes and mini-excavators this means that the hydraulic systems are comprised of a constant displacement pump

and proportional direction control (PDC) valves. On larger excavators and backhoes, variable displacement pumps are typically used due to improved system efficiency outweighing the additional cost. The primary test-bed is a small tractor-mounted backhoe. In the original configuration a constant displacement pump supplies flow proportional to engine speed and open-center valves allow flow through the valve assembly with minimal pressure drop when flow does not need to be diverted to the actuators. In the modified system, electronically controlled closed-center valves are used for computer controlled manipulation. Since the electro-hydraulic (EH) valves are closed-center, there must be an additional pressure regulating valve that diverts flow to the closed center PDC valves. In other words, the pressure regulating valve throttles the main flow to create the pressure needed to operate the closed-center PDC valves.

The main pressure regulating valve would not be needed if the closed-center proportional valves were used with a variable displacement pump. Variable displacement pumps use a swash plate to adjust the flow to meet the needs of the system. In an industrial setting the pressure is normally held constant, but on many mobile applications the pressure(s) as well as the flow(s) of the pump(s) follow the demands of the task. A typical pressure control strategy for variable displacement pumps is called load-sensing. The highest load pressure is fed back to the pump hydro-mechanically and the pump pressure maintains a preset pressure margin above this pressure. By maintaining this pressure margin, the pump is also matching the required flow. Since both the flow and pressure can be adjusted, this results in less energy waste. While using these pumps are more energy efficient, they are also generally more expensive and physically bigger. Because of this trade off, variable displacement pumps are not found on smaller backhoes and excavators like the test-bed used in this project.

High end direction control valves are known as servo valves. These valves offer high bandwidth and use tight tolerances to prevent internal leakage while minimizing

dead-band. Servo valves also have their disadvantages for mobile applications. The first is cost and the second is that they require a clean oil system. Due to their small tolerance, even small particles can cause the spools to seize. This means that they are not well suited for mobile applications. As mentioned earlier, lower cost alternatives to servo valves are proportional directional control (PDC) valves. These valves have slower dynamics and more dead-band to prevent internal leakage and avoid high cost, high precision machining. Unfortunately, the combination of dead-band and slow valve dynamics limit the performance of these valves, since the main spool must move through the dead-band in order to change the direction of the flow. This performance is degraded even more because of the delay associated with the pressure building up in the main pressure regulator. This research addresses issues and limitations associated with applying haptic control to hydraulic systems controlled by proportional directional control valves. In addition, haptic control strategies deemed appropriate for mobile hydraulic applications are presented.

The following chapter presents background and literature topics that are relevant coordinated haptic control of hydraulic machinery. Chapter 3 summarizes the kinematics transformations required for coordinated backhoe control including methods to deal with kinematics constraints. Chapter 4 presents methods for controlling pump pressure and cylinder flow/velocity. Combined, these two chapters represent algorithms that can achieve coordinated motion of the backhoe bucket which is one of the central themes of this work. Chapters 5 and 6 briefly present the topics of pressure-based exogenous force estimation and the creation of a virtual backhoe simulator. Chapter 7 presents techniques for haptic control of backhoe/excavators and evaluation based on human factors testing. The dissertation concludes with Chapter 8's summary of the contributions of this work and proposal of future avenues of exploration related to haptic control of hydraulic machinery.

CHAPTER II

BACKGROUND

2.1 Haptics

The first modern teleoperators were created by Goertz at Argonne National Labs ([35] as cited by Sheridan [123]). This electrically operated teleoperator was designed to replace mechanical master-slave manipulators [34] being used to handle dangerous radioactive material. Due to the identical master and slave manipulators, the system was able to reflect the forces acting on the slave back to the human operator grasping the master. Due to the advantages associated with using hydraulically actuated slaves, the nuclear industry also experimented with totally hydraulic force reflecting master-slave manipulators [57]. Today, electro-hydraulic valves allow for electrically controlled, hydraulically actuated remote manipulators. How to best reflect and display force signals remains an active area of research.

For a survey of work on teleoperation between 1954 and 1989 see Sheridan [123]. With the emergence of robots and computing power in the 1980s came an increase in research on teleoperation as researchers began to realize that robots were not going to replace humans, but could be used to cooperate with humans [123]. A perfect example of human-robot collaboration is a force-reflecting human-machine interfaces or haptic interfaces. The word **haptics** means *of or relating to the sense of touch or tactile*. Haptic interfaces allow for sensory information from the remote environment or virtual environment to be relayed back to the human via force signals displayed to the user.

Two areas of robotics research that helped stimulate haptic teleoperation was virtual reality and robot motion/force control. It was soon discovered that controllers

that worked well for free motion did not work well when a robot was in contact with a remote environment. This is because during free motion the force is constrained to zero, but during hard contact the position of a robotic end effector's motion is constrained by the surface of the object. One solution to this problem was hybrid position/force control proposed by Raibert and Craig [113]. Hybrid control splits the motion of the robot's end effector into motion that is perpendicular and tangent to the surface of the object being manipulated. The perpendicular or constrained motion is controlled in force mode and the tangential or free motion to be controlled using a position control loop. This assures that the appropriate controller is always being used and facilitates stable interaction with stiff objects.

Like a lot of other haptic researchers, Hogan borrowed from concepts used in the analysis of electrical circuits [54, 55, 56]. He noted that, just as electrical networks can be broken into Thevenin and Norton equivalent circuits, remote environments as well as mechanical manipulators can be more or less treated the same way. The only difference is that mechanical flow variables such as fluid flow, velocity or angular velocity are used instead of current, and similarly, pressure, force or torque are used instead of voltage. These pairs are called energy variables because they each describe the flow of energy between the interacting systems. Borrowing words from circuit analysis, he proposed that mechanical manipulators can be looked at as either an admittance (measure force and control velocity) or impedance (measure velocity and control force). The basic idea behind this type of controller analysis is that neither of the two interacting systems (i.e., robot and remote environment) can independently control both variables. This type of control has provided a framework for robots to interact with objects without switching control modes as is required with hybrid control.

Another idea borrowed from circuit theory is two-port networks. Hannaford proposed that this could be used to analyze the behavior of teleoperators [42]. For

example, a two-port network can be used to describe the impedance of a system as seen by each side and the relationships between the corresponding force and velocity signals. One system attribute that can be specifically analyzed using two-port networks is system transparency. Transparency is a visual parallel used by haptic researchers to describe how well a system can relay the force and motions of the opposite side of the network. Just as transparent glass allows a human to see objects on the other side, a transparent teleoperator allows a human to experience the same motion and forces acting on the remote end effector.

A simple mathematical explanation for transparency can be given by looking at two-port network parameters that describe a system. A two-port network can describe the relationship between teleoperator's inputs and outputs. The subscripts h stands for hand or human and the subscript e stands for end-effector, environment or exogenous force. The variables V and F are velocity and force respectively. Z_{in} is the impedance of the input haptic interface and Z_{out} is the impedance of the remote manipulator.

$$\begin{bmatrix} F_h \\ -V_e \end{bmatrix} = \begin{bmatrix} h_{11} & h_{12} \\ h_{21} & h_{22} \end{bmatrix} \begin{bmatrix} V_h \\ F_e \end{bmatrix} \tag{2.1}$$

$$\begin{bmatrix} h_{11} & h_{12} \\ h_{21} & h_{22} \end{bmatrix} = \begin{bmatrix} Z_{in} & Force\ Scale \\ Velocity\ Scale & \frac{1}{Z_{out}} \end{bmatrix} \tag{2.2}$$

The system is "Perfectly Transparent" if and only if the following holds:

$$\begin{bmatrix} F_h \\ -V_e \end{bmatrix} = \begin{bmatrix} 0 & 1 \\ -1 & 0 \end{bmatrix} \begin{bmatrix} V_h \\ F_e \end{bmatrix} \tag{2.3}$$

It has also been shown that a perfectly transparent teleoperator is impossible to achieve without limitations on bandwidth because a perfectly transparent system by definition is marginally stable [79]. However, transparency is still an ideal for which

many haptic researchers strive to achieve with maximum bandwidth. A less strict definition of transparency also includes spatial and power scaling factors [20].

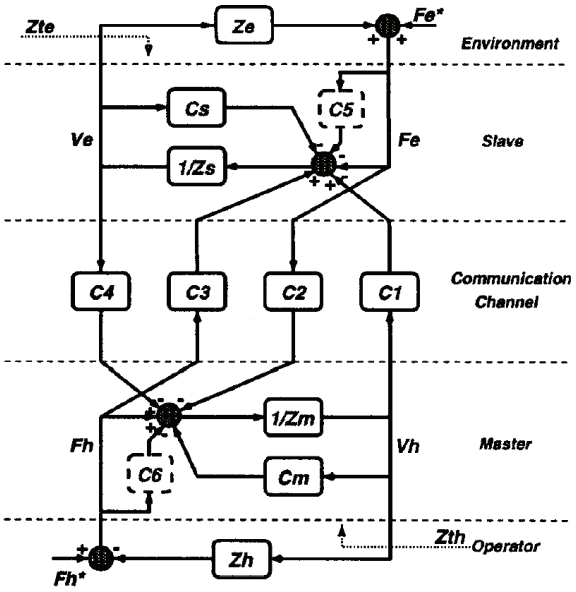

Figure 2.1: Hashtrudi-Zaad and Salcudean's [45] modified Lawrence [79] 4-channel architecture for transparent design.

A generic architecture that achieves transparency with limited bandwidth is shown in 2.1. Hashtrudi-Zaad and Salcudean [45] added local force feedback term C_5 and C_6 to this architecture originally presented by [79]. This results in the following conditions for transparency. A similar result was also found by [152].

$$\begin{aligned} C_1 &= Z_s + C_s \\ C_2 &= 1 + C_6 \\ C_3 &= 1 + C_5 \\ C_4 &= -(Z_m + C_m) \end{aligned} \tag{2.4}$$

These local feedback terms can be used to increase contact stability, improve robustness, or even to eliminate one of the force forward channel C_2 or C_3. This result can be extended to other admittance and impedance combinations [46]. Transparency and robustness can be optimized using linear robust theory [27, 25].

Transparency is most intuitive when position mode is used because the network is simply making the force and movement from each side correspond to one another. A rate control version of transparency has also been defined where slave velocity is the integral of the haptic interface's velocity and the force exerted on the operator's hand is the derivative of the force the environment exerts on the slave manipulator [45]. This means that a constant steady-state force will not be reflected since its derivative is zero.

The other aforementioned area of research that has contributed to haptic teleoperation is virtual reality. Virtual reality is a modeled environment that only exists inside a computer. As well as visual and audio feedback, haptic forces can also be used to portray these imaginary worlds [102]. Creating simple force models is relatively straight forward since they are usually built using Hook's Law for linear springs. Implementing multiple surfaces can be challenging [159] from a control point of view, as haptic interfaces have a limited impedance or range of stiffness that they can display in a stable manner [21]. A wide range of researchers have addressed the issue of displaying stiff virtual walls [1, 21, 33, 37, 118]. One solution to this problem is to create a virtual coupling between the virtual model and the haptic interface [1, 18, 19, 44]. This technique essentially limits the displayed stiffness regardless of the stiffness of the model. Again much of this work draws from concepts that originated in active network theory. In addition to two-port networks, much of this work considers either passivity [47, 77] or absolute stability using the Llewellyn Stability Criterion [90]. Passivity means that a system can only store, redirect or dissipate energy; if a system is passive it can not add energy into the system. The great thing about passivity is that passive systems linked to passive systems are inherently passive and almost all naturally occurring remote environments are passive. Note this is not necessarily true for virtual environments due to sampling delay [21]. Since stability is inferred by passivity, passivity has been widely used in haptics. Absolute stability can also

guarantee the stability of coupled network and is less conservative than passivity.

Many passive systems are characterized as sluggish. This sluggishness is caused by the coupling network being designed to be passive for contact with stiff environments. One explanation for the sluggishness is that the system has more damping than is necessary during normal operation [43]. Two conflicting goals of force reflecting teleoperation is low force during free, unconstrained motion and stable interaction with stiff environments. A system's damping affects both of these goals [43]. Low damping allows the force displayed to the human to be small during free motion. High damping is desirable during contact with stiff environments because it dampens oscillations and dissipates energy that could otherwise destabilize the system.

Hannaford [42] proposed adapting the impedance control law based on an estimation of environment impedance. Salcudean et al. [120] implemented Hannaford's bilateral matched impedance on a mini-excavator. It is called bilateral match impedance control because both the remote environment and the human's impedances are estimated on-line and used to adjust the impedance of the opposite device. Love and Book developed and implemented a different adaptive impedance control [92, 93] strategy. This controller used a learning routine to estimate the environmental impedance as the manipulator moved through the workspace. This allows the damping (i.e. stability margin) to be reduced after a lower, less conservative environmental stiffness estimation was found.

Another way to adapt a haptic network's impedance is to monitor a system's passivity or flow of energy. This method was first applied to time-delayed teleoperation. Time delay has a destabilizing effect on force feedback teleoperators. This was first observed and explored by Ferrell [24]. To over simplify the problem, time delay decreases the phase margin of a system pushing it toward instability. Many researchers have looked into this problem: Anderson and Spong [6], Niemeyer and Slotine [105], Yokokohji et al. [151], Munir and Book [103], Fite et al. [26] and Ching and Book

[17]. This required non-traditional methods to maintain stability. One of these methods which was first proposed by Yoshikawa et al. is to monitor the net flow of energy entering the system. A similar concept called Time-Domain Passivity was proposed by Ryu and Hannaford [44] to optimize the damping in haptic interfaces coupled to virtual environments. This method's name came from the fact that it is derived from the time-domain definition of passivity in Equation 2.5 [124].

$$\int_0^t (y_1(\tau)u_1(\tau) + \cdots + y_n(\tau)u_n(\tau))dt > \alpha,\ \exists\ \alpha > -\infty,\ \forall\ t \geq 0 \tag{2.5}$$

The inputs, $u_i(t)$, and outputs, $y_i(t)$s, are energy variable pairs so the sum of their products represent power flowing into the system. Integrating this sum represents the net flow of energy into the system. If the system is passive this value is bounded by the initial energy store in the system α.

When the system becomes non-passive, the damping of the master can be increased. Essentially, this acts to dissipate the energy being introduced into the system by the human operator. More importantly, the energy exerted by the slave onto the environment can also be limited. If force and velocity scaling is not an issue, this is often a more practical method to enforce the passivity of the overall system. One constraint on how much energy can be dissipated through the haptic interface is the physical damping of the system. This is because there are stability limits on the virtual damping and stiffness imposed by the physical damping [21]. One way to get around this is to incorporate variable physical damping as proposed and implemented by Gosline and Hayward [37]. Tognetti and Book studied the effect of physical damping on haptic performance and poised the question of when and how to vary the physical damping [136, 137]. This is important for systems like excavators, where the energy of the haptic interface is magnified by both velocity and force scaling. In addition, the haptic display would generally have better bandwidth and less delay than the excavator or backhoe. Using this method helps the transparency

of the teleoperator because it reduces force during free motion and the haptic display has higher bandwidth than the hydraulic system. It has been shown through human factors testing that higher damping during contact with stiff environments can not only improve stability, but also improve the perceived stiffness of the object [80].

Time-domain passivity was extended to teleoperators by Ryu et al. [116] and general control systems [115]. Kanaoka and Yoshikawa also proposed using a passivity monitor to guarantee global stability of an arbitrary robotic manipulator during free and constrained motion. This method requires that that robot be asymptotically stable during free motion and works using the same basic concept as time-domain passivity. A similar technique has also been developed by Lee and Li [83]. These methods are similar to Love and Book's adaptive impedance control in the sense that they limit the net energy flowing out of the system by adjusting damping. The difference is that adaptive impedance control is based on spatial learning and the other techniques are based on the flow in energy in and out of the system and the concept of passivity.

2.2 Robotics Excavators

Using a haptic robotic human-machine interface offers several possible enhancements. These devices enable coordinated motion control, reflection of forces on the end effector and the ability to program virtual fixtures [68, 114, 138] into the workspace. Usually, force reflection is defined and evaluated in terms of transparency. Transparency is a property that describes how accurately a haptic interface can display the forces from a virtual model or a remote environment. In the case of haptic control of hydraulic equipment a more practical, albeit more abstract, measure of force reflection is the enhancement to human performance. The only way to measure this is through human factors testing [66, 141, 142].

Some of the first researchers to propose the application of force feedback to hydraulic systems such as excavators were Starzewski and Skibniewski [107]. They predicted enhancements due to coordinated motion and "feel" or haptic feedback that could be provided by such an interface. This concept paper predicted the commercial use of such systems when it was technically and economically feasible. Patents related to haptic or force feedback devices to control hydraulic machines were received by Caterpillar Inc. [16] in the same year that his paper was published and by Kraft [75] two years later. Like many other robotic researchers with an interest in excavators, Skibniewski turned toward autonomous robotic excavators that could work independently of humans instead of with humans [38, 63, 84, 126, 134, 139]. Others in academia [9, 76, 121, 133] and the nuclear industry [8, 7, 15, 78, 59] have focused on coordinated teleoperation of excavators with various levels of haptic feedback. By the early 1990s, this topic was explored by the nuclear industry: HAZ-TRAK remotely operated excavator [8, 78] and a telerobotic small emplacement excavator [15]. Better documented work was conducted at the University of British Columbia on resolved mode teleoperation by Sepehri et al. [121] and force feedback of hydraulic machines by Parker et al. [109]. An impedance based teleoperation scheme designed for transparency was later implemented on a mini-excavator and presented by Salcudean et al. [120] and Tafazoli et al. [133]. Krishnaswamy and Li used a passive control based on bond graphs to control a backhoe. One advantage of the passivity approach that it is inherently safe.

Coordinated control is a subtle, but a profound improvement over conventional hand controllers that work in joint space. Using joysticks that individually control the joints of the manipulator puts a "high perceptual and psychomotor demand" on the operator [141, 142]. Using coordinated motion control and a single hand controller whose motion corresponds directly to the slave manipulator reduces this mental load by doing the inverse kinematics for the operator. Human-in-the-loop experiments

indicate improved accuracy, better or equal completion times and decreased training time for novice users [142]. Experiments done on a log loader were also conducted using 10 novice and 6 expert operators [141]. As expected, the novice operators perform better using the coordinated controller, while the expert operators perform better using the joint controller due to years of experience. However, the expert's performance on the two controllers was converging as the testing concluded after six days. This implies that the expert operators could be just as proficient on the new controllers in a relatively short period of time. Experienced operators also expressed positive comments on the new hand controllers.

The most relevant patents on coordination or resolved motion of backhoes and excavators are held by Caterpillar Inc. [4, 5, 13, 14, 39, 91, 108, 117, 127] and Lawrence et al. of the University of British Columbia [31, 82, 110, 122]. Other companies who manufacture backhoes, excavators and related components who hold patents related to some kind of coordinated motion control include Case [10, 11], John Deere [49, 50], Hitachi [53, 143, 144, 148], HUSCO [100], Komatsu [58] and Sundstrand-Sauer [48]. One example of coordinated control that has been implemented on a commercial product was presented by Haga et al. [41] of the Hitachi corporation. In this method, the z-axis (vertical direction) is controlled automatically using the boom once the bucket reaches a preset depth or, in more general, a plane. Since the boom is the bucket on a plane, the left joystick lever that controls the swing and arm (stick) become like an X-Y Cartesian control.

Traditionally most teleoperation has been conducted in one of two ways: unresolved rate control with joysticks/levers or resolved position to position master-slave control [145]. Rate control refers to the position of the master device controlling the rate or speed of the slave device. On the other hand, position control refers to mapping the position/motion of the master device to the position/motion of the slave device. Historically, most position control devices were similar kinematically. In this

configuration correspondence can be achieved through servo-loops around respective master and slave joints [35]. In general, this can not be done with rate control-device because the configuration of the slave will change with respect to the master. This explains why historically most rate control schemes are unresolved and instead directly control the rate or velocity of the actuators. Most mobile hydraulic equipment including backhoe and excavators fall into this category. They use levers or joysticks to directly control the rate of the actuators. With modern computing power having similar master-slaves is not required since accurate kinematics transformations can be used to map the motion between coordinate systems. Whitney [145] proposed a resolved motion rate control for human prostheses. One major advantage of this scheme is that a small master (input device) can control a larger slave (remote device) in an intuitive fashion.

Adding haptic feedback to a rate control scheme presents another challenge. How should forces be reflected? One such force reflecting architecture was proposed by Parker et al. [109]. The incoming force signal is differentiated and adjusts the stiffness of the hand controller's spring based on the forces acting on the manipulator. The equation for this spring is given in Equation 2.6.

$$K_c(f_e) = K_{nom} + K_r F_e \tag{2.6}$$

Another rate force reflection scheme was proposed by Zhu and Salcudean [158] that fits into the transparency framework. Since in rate mode, the velocity scale term is

$$h_{12} = \frac{1}{k_v s} \tag{2.7}$$

and the force scale term is set to

$$h_{21} = k_v s \tag{2.8}$$

so that $h_{12}h_{21} = -1$. With this scheme it is harder for the human to interpret forces from the remote manipulator since damping applied to the remote device is perceived as stiffness and inertia is perceived as damping[119]. Differentiating the force signal also means that constant forces are not reflected. Only the change in force can be felt.

To summarize, force signals feel more intuitive in position mode, but workspace size is a concern. Human factors testing by Kim et al. [62] confirm why position mode is preferred for tasks requiring dexterous motion if the system's bandwidth is above 3Hz. One method proposed by Salcudean et al. [119] is a hybrid position/rate scheme where small displacement of the master is interpreted as a position command to the slave, but larger position displace of the master also results in a velocity command. This is implemented by sending the master's position through a dead-band function, integrating this signal and adding it to the position command being sent to the slave. The scaling and limited workspace problem can also be solved using a series of "scrolling" and "zooming" operations [94]. A switching position/rate controller was also proposed by Kontz and Book [65, 68] where the controller actually switches between position and rate mode.

2.3 Non-Ideal Features of Hydraulic Systems

While hydraulic systems offer a practical application of haptic feedback, their characteristics are detrimental to the implementation. In the case of proportional directional control valves these characteristics include nonlinear valve orifice coefficients, delay, dead-band and slow dynamics. Research exploring autonomous control of excavators shares these challenges. One solution to the problem is to buy higher cost hydraulic components. This was the solution used by Ha et al. [104] where the excavator's manual valves were replaced with servo valves. Other researchers kept the original

main spool valves and modified the pilot stage which moves the main spool back and forth for electro-hydraulic proportional control using both open-center valves [59, 121] and closed-center valves [84, 129]. All of these researchers had to deal with the slower response and dead-band in these systems. Slow spool response and dead-band are an issue when the spool starts from its centered position or has to move through its dead-band to change the direction of the valve's flow. Other modifications to the systems have also been tried. Lawrence et al. experimented with a system that used multiple variable displacement pumps to control individual actuators [81]. Pump controlled systems have also been explored by Rahmfeld and Ivantysynova [112] and Heybroek et al. [51]. Tafazoli et al. created a custom differential PWM pilot stage that could move the spool faster in order to minimize the effect of the dead-band [129].

Significant dead-band is a characteristic of many lower quality proportional valves suitable for use in excavators. Servo valves have much smaller dead-band due to their tight tolerances. Using tight tolerances allows the valves to prevent leakage with only a small overlap. However, the precision machining required to achieve these tolerances increases the overall cost of the valve. Proportional valves prevent this leakage with an overlap that can account for as much as thirty percent of the spool's travel [84]. Dead-band can limit the system's performance because high gains will cause a limit cycle with closed-loop control. This can be shown by describing function analysis of this problem [88]. In the case of a servo valve with fast dynamics a dead-band inverse can be implemented with good performance [28]. In the case of a proportional valve the effectiveness of the dead-band inverse is limited by the dynamics of the valve [89, 135]. This is due to the dead-band nonlinearity being sandwiched between the spool dynamics and the dynamics of the rest of the hydraulic system [135]. The inverse dead-band is located at the input and essentially corrects the desired spool position; however, the limitation on how fast the spool can move determines how fast the desired spool position can be achieved. In turn, this limits how well the system

can track a desired trajectory. The valve modification by Tafazoli et al. essentially reduces the effect of their spool's dead-band by increasing the speed and bandwidth of the spool [129].

Another factor that can limit how fast a system can respond is the rate at which the main system pressure can build up [84]. This is especially true of load-compensated pressure regulators or pumps that react to the maximum line pressures of any of the opened valves. This type of design is good from an energy savings point of view, but is detrimental to closed-loop control which is necessary for haptic teleoperation or autonomous operation. The system has to wait for pressure to build up when starting from rest and the pressure can drop and may need to build up again when the valve orifices are temporarily closed as the valves change the direction of the flow. This problem could be minimized by using a pressure regulating valve with an electronically controlled set point. Having to wait for the system pressure to build up also compounds the sandwiched dead-band problem because it reduces the responsiveness of the spool by limiting the pilot pressure.

An alternative to the proportional directional valve is to use multiple poppet valves [89, 106, 157]. Poppet valves are responsive and the sandwiched dead-band problem is minimized. Due to the fact that four or more valves are used to control a single actuator, the system can be more energy efficient, but require more inputs to control the system. Alternatives to proportional directional valves such as multiple poppet valves will not be addressed by this research.

2.4 Hydraulic Control

Before it is possible to do any kind of force reflecting teleoperation, it is necessary to be able to control the remote manipulator's motion (force) and measure its force (motion). How well this can be done will limit the performance of the teleoperator. Since the hydraulic valves control fluid flow, a controller will be designed to control

cylinder motion. Sepehri et al. [121] proposed a controller for open-center valves that incorporates a nonlinear feedforward term and a PD control law. The line pressures are measured and the desired flow is calculated from the desired cylinder speed. These variables are used to calculate the desired orifice size which corresponds to a desired spool position. It is important that the line pressures are used in this calculation. This feedforward term is used to get the valve close to the desired spool position and the PD term forces the system to track the desired velocity and position. A similar form of this controller was later used by Tafazoli et al. [120, 133] on closed-center valves and Johnson et al. [59] on open-center valves.

Other excavators have incorporated sliding mode robust control: servo valves [104, 96] and proportional valves [84]. In all of these cases the input had to be modified in order to avoid chatter. Zhang et al. [154, 156] applied fixed structure MIMO robust control to the control of earthmoving vehicles (wheeled loader) using hardware-in-the-loop simulation [155]. Yao et al. applied adaptive robust motion to single-rod actuators using both proportional directional control valves [150] and programmable valves each comprised of five poppet valves [89]. Due to the complex nature of these systems, it is often possible to improve performance by using learning and adaptive control techniques [59, 106, 125]. The concept of passivity, a concept central to many haptic controllers, has been applied to hydraulic valves by Li [85]. Li showed that it is possible to have a hydraulic valve behave passively by either modifying the spool or by using passivity theory and an active control law that passifies the system using an energy storage function. This work has been extended and applied to an excavator like manipulator with guaranteed passive behavior [76].

2.5 Test-bed

The primary test-bed (Figure 2.2) in this project is referred to as HEnRE (Haptically ENhanced Robotic Excavator) [29]. HEnRE is based around a 4410 series John

Deere tractor with a Model 47 backhoe and a PHANToM [99] haptic display built commercially by SensAble Technologies. The Model 47 backhoe has been modified. Originally manual valves were the only means available to operate the device. It has been retrofitted with Sauer-Danfoss PVG-32/PVES electro-hydraulic (EH) valves and an array of sensors for feedback control and monitoring. A mechanical valve is used to switch between the original valves and the retro-fitted EH valves. A Sun hydraulics RPEC-8WN/RBAP-MAN-224 electro-proportional pressure relief valve has also been added for electronic pressure control. Instrumentation installed on HEnRE includes: position of all four degrees of freedom (swing, boom, stick and bucket), capside and rodside pressures, main supply pressure, load-sense pressure, main pump flow, inlet oil temperature and load-cell/load-pin on bucket. The control software for the backhoe is based on Mathwork's xPC target. In order to improve ease of programming and computation efficiency, C-sfunctions are used to implement several parts of the control structure including kinematic transformations, filters and dynamics compensators. This real-time control software interfaces with another computer controlling the PHANToM via Ethernet cable using UDP protocol. PHANToM control is done using SensAble's C++ software libraries[65].

Digging experiments using the backhoe are conducted in a container filled with soil. The soil chosen is a manufactured sand called granite dust which contains a high percentage of fine particles. When this sand is in a loose, uncemented and dry condition, it is unable to hold its shape when it is disturbed by the bucket. In order to correct this and provide shear strength at zero lateral stress it is necessary to increase soil shear strength by compaction and wetting. Compaction increases contact forces between the soil particles and wetting increases the capillary effects which create a bonding force between the particles. Compaction is performed using a hand tamp with layers of loose sand 2-to-3 inches deep. Since the sand drains well, homogenous water content is achieved by saturating the sand and allowing it to drain overnight.

Figure 2.2: HEnRE test-bed in MARC hi-bay with soil bin.

Compacting the sand also slows down evaporation in the dry air-conditioned lab where the tractor and soil bin are located. It is the fine sand and silt size particles contained in the tested material that contribute the most to capillary forces which allow the soil to possess some apparent cohesion strength. The capillary forces are stronger for the smaller particles because the specific surface area or the ratio of surface area to volume is higher.

CHAPTER III

KINEMATICS

Today almost all commercial backhoes/excavators are controlled by joystick commands from human operators that are mapped directly into the joint-space of the manipulator. Due to shortage of skilled operators, another alternative to traditional human-machine interfaces is to use coordinated or Cartesian control. The purpose of this chapter is to present the kinematic algorithms that are necessary to map variable between task-space, joint-space and cylinder space. This is important to the overall goal of this project, coordinated haptic control of hydraulic machinery, because it allows high-level coordinated commands to be mapped in to low-level cylinder commands. Section 3.1 introduces the nomenclature used in this chapter. Next, Section 3.2 presents the task-space to joint-space forward kinematics, Jacobian transforms and inverse kinematics. One issue that must be addressed is the effect of joint constraints imposed by the hydraulic cylinders. Two solutions are presented: a closed form graphically derived method based on the position of the bucket's wrist and a more general numerical optimization approach that also penalizes bucket angle error. Section 3.3 presents the transformations between joint-space variable and cylinder-space variables. Much of the kinematics analysis presented in this chapter parallels work presented by other work on backhoes/excavators [29, 64, 140, 130]. All the material related to cylinder constraints represents new work, published in Kontz and Book [70].

3.1 Nomenclature

In addition to being included in the main nomenclature section, most of the notation being used in this chapter will be presented again for easy reference.

Subscripts:

- t - task-space or Cartesian-space
- j - joint-space
- c - cylinder-space
- x - x component of vector in Cartesian coordinates
- y - y component of vector in Cartesian coordinates
- z - z component of vector in Cartesian or cylindrical coordinates
- r - r component of vector in cylindrical coordinates
- θ - θ component of vector in cylindrical coordinates
- d - distal (tip) bucket control
- p - proximal (wrist) bucket control

Variables:

- O_i - origin of i^{th} coordinate system attached to i^{th} link in the distal location
- p - position of bucket with respect to base coordinate system
- P_{ij} - position vector of the j^{th} origin with respect to i^{th} origin measured in base coordinated system.
- F_i - force vector acting on bucket with respect to the i^{th} origin's coordinated system.
- ϕ - bucket angle in task-space
- τ_ϕ - bucket torque

- y_{c_i} - ith cylinder length
- f_{c_i} - force acting on ith cylinder
- θ_i - i^{th} joint angle
- τ_i - i^{th} joint torque
- $\hat{e}$ - unit vector
- J - Jacobian transform
- X - vector of task-space coordinates=(x, y, z, ϕ)
- Θ - vector of joint-space coordinates = $(\theta_1, \theta_2, \theta_3, \theta_4)$
- Y - vector of cylinder-space coordinates = $(y_{c_1}, y_{c_2}, y_{c_3}, y_{c_4})$
- F - vector of task-space forces = $(F_x, F_y, F_z, \tau_\phi)$
- T - vector of joint-space torques = $(\tau_1, \tau_2, \tau_3, \tau_4)$

3.2 Joint-Space to Task-Space Kinematics

The first of the backhoe kinematics problem is to relate the Joint-Space variables to the Task-Space variables. This includes the forward and reverse kinematics mappings and the standard robotics Jacobians that relate forces and velocities in the two domains.

3.2.1 Forward-Kinematics

The traditional way to derive dynamic equations for backhoe/excavator or generic robots is to start with Denavit-Hartenberg parameters (Table 3.1) and transformation matrices [29, 64, 140]. In this chapter a less traditional approach will be used to take advantage of the fact that the boom, stick and bucket move in a plane that is rotated by the swing joint (see Figure 3.1)[130]. Taking advantage of this fact, the

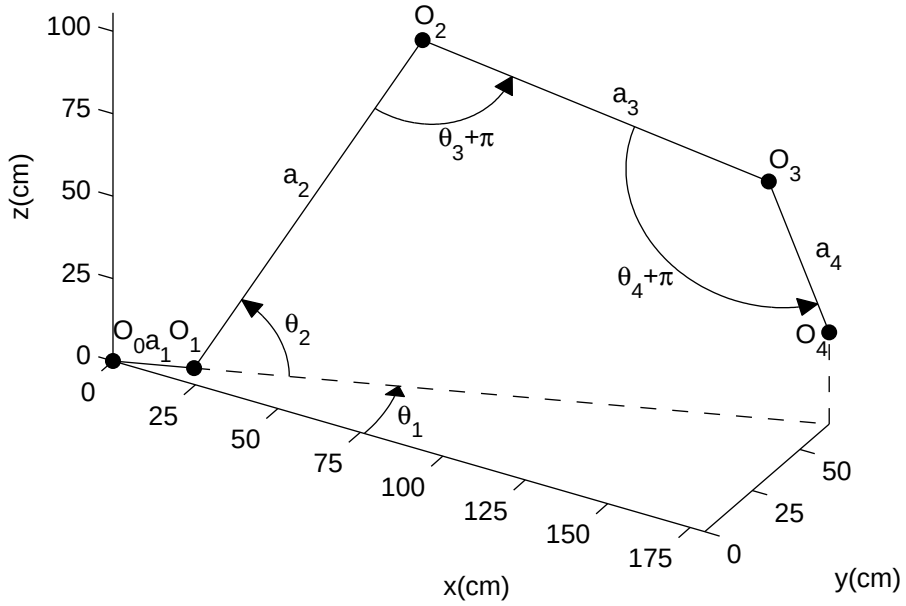

Figure 3.1: Joint angles in task-space. Notice that θ_1 rotates a plane common with all the other links and their motion. In this configuration $\theta_1 = 20^o$, $\theta_2 = 60^o$, $\theta_3 = -80^o$ and $\theta_4 = -50^o$.

position vectors can first be derived using cylindrical coordinates z, r, θ and then converted into Cartesian coordinates x, y, x (Equations 3.5 - 3.8) [130]. Both of these coordinates systems are located at the origin O_0. In the following equations $\hat{e}_i$ denotes unit vector in the direction i. The relationships between the two coordinates are as follows.

Table 3.1: Denavit-Hartenberg parameters.

i	a_i	α_i	z_i	θ_i
1	8.5”	90^o	0	θ_1
2	48”	0	0	θ_2
3	38.7”	0	0	θ_3
4	18.5”	0	0	θ_4

$$\begin{aligned} r &= \sqrt{x^2 + y^2} \\ \theta &= atan2(y, x) \end{aligned} \tag{3.1}$$

$$\begin{aligned} x &= rcos(\theta) \\ y &= rsin(\theta) \\ z &= z \end{aligned} \tag{3.2}$$

Before defining the position vector it is helpful to define the following notation.

$$\begin{aligned} c_1 &= \cos(\theta_1) \\ c_2 &= \cos(\theta_2) \\ c_{23} &= \cos(\theta_2 + \theta_3) \\ c_{24} &= \cos(\theta_2 + \theta_3 + \theta_4) \\ s_1 &= \sin(\theta_1) \\ s_2 &= \sin(\theta_2) \\ s_{23} &= \sin(\theta_2 + \theta_3) \\ s_{24} &= \sin(\theta_2 + \theta_3 + \theta_4) \end{aligned} \tag{3.3}$$

These trigonometric evaluations can then be multiplied to form the following variables.

$$\begin{aligned} a_{c_2} &= a_2 c_2 \\ a_{c_3} &= a_3 c_{23} \\ a_{c_4} &= a_4 c_{24} \\ a_{c_{23}} &= a_{c_2} + a_{c_3} \\ &\vdots \\ a_{c_{24}} &= a_{c_2} + a_{c_3} + a_{c4} \\ a_{c_{14}} &= a_1 + a_{c_2} + a_{c_3} + a_{c_4} \\ a_{s_2} &= a_2 s_2 \\ &\vdots \\ a_{s_{24}} &= a_{s_2} + a_{s_3} + a_{s_4} \end{aligned} \tag{3.4}$$

This notation can now be applied to the position vector which is shown in both

Cartesian and cylindrical coordinates.

$$P_{01} = \begin{bmatrix} a_1\hat{e}_r \\ 0 \\ 0 \end{bmatrix} = \begin{bmatrix} c_1 a_1 \hat{e}_x \\ s_1 a_1 \hat{e}_y \\ 0 \end{bmatrix} \tag{3.5}$$

$$P_{02} = P_{01} + P_{12} = \begin{bmatrix} a_{c_{12}}\hat{e}_r \\ 0 \\ a_{s_2}\hat{e}_z \end{bmatrix} = \begin{bmatrix} c_1 a_{c_{12}} \hat{e}_x \\ s_1 a_{c_{12}} \hat{e}_y \\ a_{s_2}\hat{e}_z \end{bmatrix} \tag{3.6}$$

$$P_{03} = P_{02} + P_{23} = \begin{bmatrix} a_{c_{13}}\hat{e}_r \\ 0 \\ a_{s_{23}}\hat{e}_z \end{bmatrix} = \begin{bmatrix} c_1 a_{c_{13}} \hat{e}_x \\ s_1 a_{c_{13}} \hat{e}_y \\ a_{s_{23}}\hat{e}_z \end{bmatrix} \tag{3.7}$$

$$P_{04} = \begin{bmatrix} a_{c_{14}}\hat{e}_r \\ 0 \\ a_{s_{24}}\hat{e}_z \end{bmatrix} = \begin{bmatrix} c_1 a_{c_{14}} \hat{e}_x \\ s_1 a_{c_{14}} \hat{e}_y \\ a_{s_{24}}\hat{e}_z \end{bmatrix} \tag{3.8}$$

For coordinated or resolved motion control there are two different logical mappings between the input and the bucket position. One is to map the Cartesian coordinates x, y and z to wrist of the bucket (P_{03}) and the alternative is to use the tip of the bucket (P_{04}). Mapping to the wrist will be referred to as proximal bucket control and mapping to the tip will be referred to as distal bucket control. Equation 3.9 holds for both cases (Figure 3.2).

$$\phi = \theta_2 + \theta_3 + \theta_4 - \pi \tag{3.9}$$

3.2.2 Jacobian Transforms

The Jacobian transformation is important for coordinated motion control because it maps velocity to joint velocities and equivalent forces and torques. For manipulator with only rotation joints

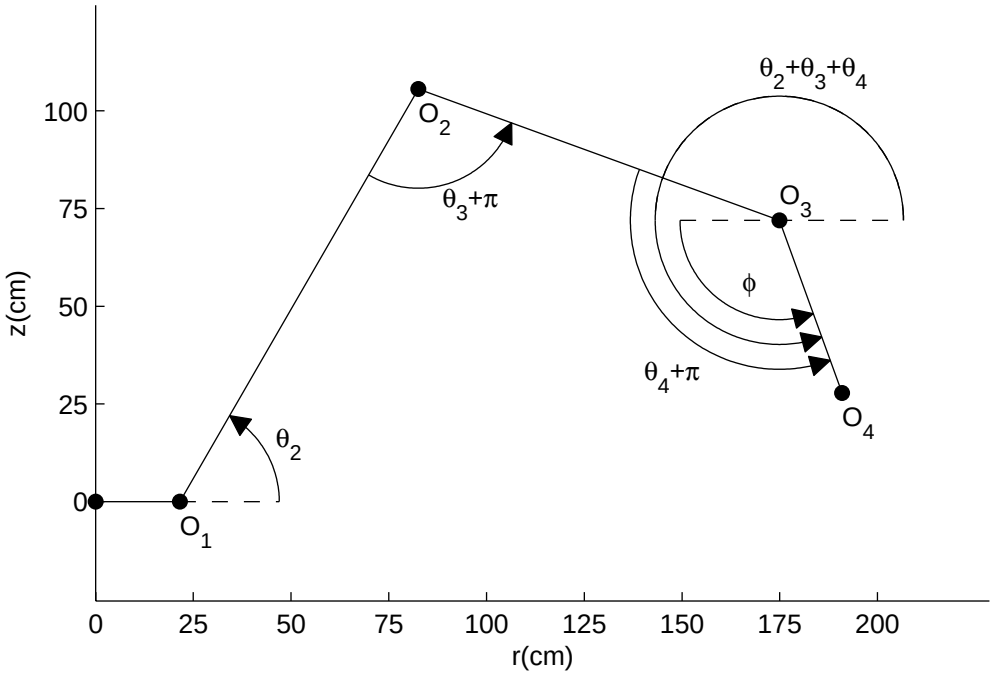

Figure 3.2: Bucket angle ϕ and its relationship to θ_2, θ_3, θ_4. This is also the $r-z$ planar view of the configuration shown in Figure 3.1.

$$\dot{X} = J\dot{\Theta} \tag{3.10}$$

$$T = J^T F \tag{3.11}$$

Where P and F are the vectors of position and force in the task-space and Θ and T are the vectors of joint angles and joint torques.

The Jacobian can be calculated from Equations 3.5 - 3.8 and 3.9

$$J_d = \begin{bmatrix} P_{40} \times \hat{e}_{z_1} & P_{41} \times \hat{e}_{z_2} & P_{42} \times \hat{e}_{z_3} & P_{43} \times \hat{e}_{z_4} \\ 0 & 1 & 1 & 1 \end{bmatrix} \tag{3.12}$$

P_{4i} can be found by subtracting P_{04} from P_{0i} (Equations 3.5-3.8).

$$P_{40} = \begin{bmatrix} -c_1 a_{c_{14}} \hat{e}_x \\ -s_1 a_{c_{14}} \hat{e}_y \\ -a_{s_{24}} \hat{e}_z \end{bmatrix} \tag{3.13}$$

$$P_{41} = P_{t0} + P_{02} = \begin{bmatrix} -c_1 a_{c_{24}} \hat{e}_x \\ -s_1 a_{c_{24}} \hat{e}_y \\ -a_{s_{24}} \hat{e}_z \end{bmatrix} \tag{3.14}$$

$$P_{42} = P_{t0} + P_{03} = \begin{bmatrix} -c_1 a_{c_{34}} \hat{e}_x \\ -s_1 a_{c_{34}} \hat{e}_y \\ -a_{s_{34}} \hat{e}_z \end{bmatrix} \tag{3.15}$$

$$P_{43} = P_{t0} + P_{04} = \begin{bmatrix} -c_1 a_{c_4} \hat{e}_x \\ -s_1 a_{c_4} \hat{e}_y \\ -a_{s_4} \hat{e}_z \end{bmatrix} \tag{3.16}$$

Taking the cross products.

$$\hat{e}_{z_1} = \begin{bmatrix} 0 \\ 0 \\ 1 \end{bmatrix} \hat{e}_{z_2} = \hat{e}_{z_3} = \hat{e}_{z_4} = \begin{bmatrix} s_1 \\ -c_1 \\ 1 \end{bmatrix} \tag{3.17}$$

$$P_{40} \times \hat{e}_{z_1} = \begin{bmatrix} -s_1 a_{c_{14}} \\ c_1 a_{c_{14}} \\ 0 \end{bmatrix} \tag{3.18}$$

$$P_{41} \times \hat{e}_{z_2} = \begin{bmatrix} -c_1 a_{s_{24}} \\ -s_1 a_{s_{24}} \\ a_{c_{24}} \end{bmatrix} \tag{3.19}$$

$$P_{42} \times \hat{e}_{z_3} = \begin{bmatrix} -c_1 a_{s_{34}} \\ -s_1 a_{34} \\ a_{c_{23}} + a_{c_{24}} \end{bmatrix} \tag{3.20}$$

$$P_{43} \times \hat{e}_{z_4} = \begin{bmatrix} -c_1 a_{s_4} \\ -s_1 a_{s_4} \\ a_{c_{24}} \end{bmatrix} \tag{3.21}$$

The distal Jacobian maps task-space coordinates related to the tip of the bucket to joint coordinates.

$$J_d = \begin{bmatrix} -s_1 a_{c_{14}} & -c_1 a_{s_{24}} & -c_1 a_{s_{34}} & -c_1 a_{s_4} \\ c_1 a_{c_{14}} & -s_1 a_{s_{24}} & -s_1 a_{s_{34}} & -s_1 a_{s_4} \\ 0 & a_{c_{24}} & a_{c_{34}} & a_{c_4} \\ 0 & 1 & 1 & 1 \end{bmatrix} \tag{3.22}$$

It can be shown that the inverse Jacobian for the distal case is as follows

$$J_d^{-1} = \frac{1}{d_d} \begin{bmatrix} -s_1 d_d / a_{c_{14}} & c_1 d_d / a_{c_{14}} & 0 & 0 \\ -c_1 a_{c_3} & -s_1 a_{c_3} & -a_{s_3} & a_{s_3} a_{c_4} - a_{s_4} a_{c_3} \\ c_1 a_{c_{23}} & s_1 a_{c_{23}} & a_{s_{23}} & a_{c_{23}} a_{s_4} - a_{s_{23}} a_{c_4} \\ -a_{c_2} c_1 & -a_{c_2} s_1 & -a_{s_2} & -a_{s_{34}} a_{c_2} + a_{s_2} a_{c_{34}} \end{bmatrix} \tag{3.23}$$

where

$$d_d = -a_{c_4} a_{s_2} + a_{c_{34}} a_{s_{23}} - a_{c_{24}} a_{s_3} \tag{3.24}$$

An equivalent Jacobian and inverse Jacobian can be found that maps between cylindrical variables and joint variables using a coordinate transform, T.

$$T = \begin{bmatrix} -s_1 & c_1 & 0 & 0 \\ c_1 & s_1 & 0 & 0 \\ 0 & 0 & 1 & 0 \\ 0 & 0 & 0 & 1 \end{bmatrix} \tag{3.25}$$

$$V_{cart} = T V_{cyl} = J_d \Theta \tag{3.26}$$

where,

$$V_{cart} = \begin{bmatrix} v_x \\ v_y \\ v_z \\ \dot{\phi} \end{bmatrix} \tag{3.27}$$

$$V_{cyl} = \begin{bmatrix} v_\theta \\ v_r \\ v_z \\ \dot{\phi} \end{bmatrix} \tag{3.28}$$

$$\Theta = \begin{bmatrix} \dot{\theta_1} \\ \dot{\theta_2} \\ \dot{\theta_3} \\ \dot{\theta_4} \end{bmatrix} \tag{3.29}$$

Note that T is symmetric, unitary and real, so $T = T^T = T^{-1}$, so

$$V_{cyl} = TJ_d\Theta = J_{d_{cyl}}\Theta \tag{3.30}$$

This means that the $J_{d_{cyl}} = TJ_d$, where $J_{d_{cyl}}$ is the equivalent Jacobian in cylindrical coordinates.

$$J_{d_{cyl}} = \begin{bmatrix} a_{c_{14}} & 0 & 0 & 0 \\ 0 & -a_{s_{24}} & -a_{s_{34}} & -a_{s_4} \\ 0 & a_{c_{24}} & a_{c_{34}} & a_{c_4} \\ 0 & 1 & 1 & 1 \end{bmatrix} \tag{3.31}$$

Similarly the closed form inverse Jacobian using cylindrical coordinates for the

distal case is

$$J_{d_{cyl}}^{-1} = \frac{1}{d_d}\begin{bmatrix} -d_d/a_{c_{14}} & 0 & 0 & 0 \\ 0 & -a_{c_3} & -a_{s_3} & a_{s_3}a_{c_4} - a_{s_4}a_{c_3} \\ 0 & a_{c_{23}} & a_{s_{23}} & a_{c_{23}}a_{s_4} - a_{s_{23}}a_{c_4} \\ 0 & -a_{c_2} & -a_{s_2} & -a_{s_{34}}a_2 + a_{s_2}a_{c_{34}} \end{bmatrix} \tag{3.32}$$

The Proximal Jacobian is simpler and is actually a special case of the distal Jacobians where $a_4 = 0$. The proximal Jaconian maps task-space coordinates related to position of the bucket's wrist and the joint coordinates. In Cartesian coordinates

$$J_p = \begin{bmatrix} -s_1 a_{c_{13}} & -c_1 a_{s_{23}} & -c_1 a_{s_3} & 0 \\ c_1 a_{c_{13}} & -s_1 a_{s_{23}} & -s_1 a_{s_3} & 0 \\ 0 & a_{c_{23}} & a_{c_3} & 0 \\ 0 & 1 & 1 & 1 \end{bmatrix} \tag{3.33}$$

$$J_p^{-1} = \begin{bmatrix} -s_1 d_d/a_{c_{13}} & c_1 d_d/a_{c_{13}} & 0 & 0 \\ -c_1 a_{c_3} & -s_1 a_{c_3} & -a_{s_3} & 0 \\ c_1 a_{c_{23}} & s_1 a_{c_{23}} & a_{s_{23}} & 0 \\ -a_{c_2} c_1 & -a_{c_2} s_1 & -a_{s_2} & -a_{s_3} a_{c_2} + a_{s_2} a_{c_3} \end{bmatrix} \tag{3.34}$$

where

$$d_p = a_{c_3} a_{s_{23}} - a_{c_{23}} a_{s_3} \tag{3.35}$$

In cylindrical coordinates,

$$J_{p_{cyl}} = \begin{bmatrix} a_{c_{13}} & 0 & 0 & 0 \\ 0 & -a_{s_{23}} & -a_{s_3} & 0 \\ 0 & a_{c_{23}} & a_{c_3} & 0 \\ 0 & 1 & 1 & 1 \end{bmatrix} \tag{3.36}$$

$$J_{p_{cyl}}^{-1} = \frac{1}{d_d} \begin{bmatrix} -d_d/a_{c_{13}} & 0 & 0 & 0 \\ 0 & -a_{c_3} & -a_{s_3} & 0 \\ 0 & a_{c_{23}} & a_{s_{23}} & 0 \\ 0 & -a_{c_2} & -a_{s_2} & -a_{s_3}a_2 + a_{s_2}a_{c_3} \end{bmatrix} \tag{3.37}$$

Note that given θ_1, θ_2, θ_3 and θ_4, the position vectors, Jacobian and Jacobian inverse can be evaluated with only eight trigonometric evaluations: c_1, c_2, c_{23}, c_{24}, s_1, s_2, s_{23}, s_{24} for either the cylindrical coordinate or Cartesian coordinate case. Another important fact that will later be exploited is that θ is decoupled from r, z and ϕ in the cylindrical coordinates Jacobians 3.31.

3.2.3 Inverse-Kinematics

The inverse kinematics can also be derived using cylindrical coordinates. It will be assumed that the radius will be constrained by a minimal value to assure that the point being used for coordinated motion control does not pass through the vertical z_0 axis. This is the only singularity that a backhoe can pass through due to joint angle limitations. This software constraint will be discussed later after the unconstrained inverse kinematic solution is derived. Given r, θ, z, ϕ, it is possible to calculate θ_{1-4}. First off $\theta_1 = \theta$.

For distal bucket control:

$$P_{03} = \begin{pmatrix} r - a_4 cos(\phi)\hat{e}_r \\ 0 \\ z - a_4 sin(\phi)\hat{e}_z \end{pmatrix} = \begin{pmatrix} r_3\hat{e}_r \\ 0 \\ z_3\hat{e}_z \end{pmatrix} \tag{3.38}$$

For proximal bucket control:

$$P_{03} = \begin{pmatrix} r\hat{e}_r \\ 0 \\ z\hat{e}_z \end{pmatrix} = \begin{pmatrix} r_3\hat{e}_r \\ 0 \\ z_3\hat{e}_z \end{pmatrix} \tag{3.39}$$

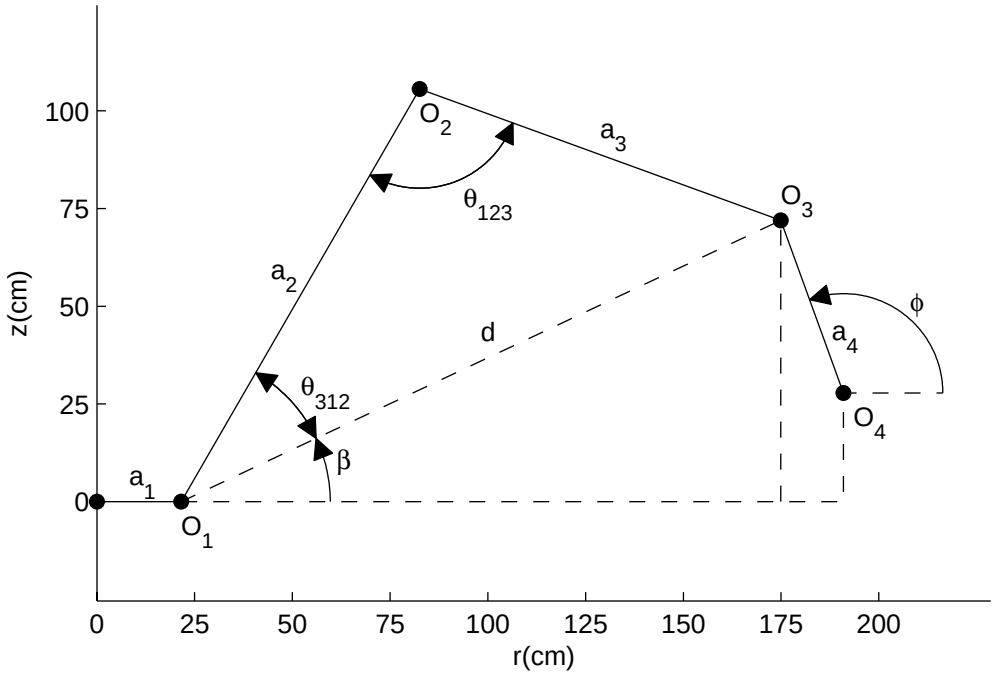

Figure 3.3: Variables used to calculate the inverse-kinematics.

The rest of the inverse-kinematics is based on P_{03} and therefore is the same for both proximal and distal inverse formulations(Figure 3.3).

$$\beta = atan2(z_3, (r_3 - a_1)) \tag{3.40}$$

$$d = \sqrt{(r_3 - a_1)^2 + z_3^2} \tag{3.41}$$

$$\theta_{312} = acos\left(\frac{a_2^2 + d^2 - a_3^2}{2a_2 d}\right) \tag{3.42}$$

$$\theta_{123} = acos\left(\frac{a_2^2 + a_3^2 - d^2}{2a_2 a_3}\right) \tag{3.43}$$

Equating the angles in Figure 3.2 & 3.3 results in the following joint angles.

$$\theta_2 = \theta_{312} + \beta \tag{3.44}$$

$$\theta_3 = \theta_{123} - \pi \tag{3.45}$$

$$\theta_4 = \pi + \phi - \theta_2 - \theta_3 \tag{3.46}$$

3.2.4 Constrained Inverse-Kinematics

Enforcing software joint constraints that are slightly less than the hard constraints inside the cylinder has several advantages. The advantage includes: better cylinder and component wear and in general less system pressure since the cylinders don't push on their stops. If pressure-based force estimation is being used, software cylinder constraints also ensure that cylinders do not hit their physical stops which would disrupt this estimation [132]. If these constraints are enforced at the cylinder level undesirable motion will be induced because the assumptions used to convert task-space coordinates to joint-space coordinates breakdown when the constraints are in place. This is because one or more of the joint angles is being held constant. This affects both the inverse kinematics calculations and makes the Jacobian become rank deficient since one or more of the joint velocities are set to zero. In general there is not a closed-form solution to the constrained inverse kinematics problem; however, numerical methods such as Newton-Raphson based techniques can be used to find a solution [36]. Projection methods have also been developed for this problem [2]. Essentially what needs to be found is a least-squares solution for both the desired joint angle and joint velocity.

Due to the kinematics of backhoes/excavators the swing can be dealt with separately since it creates motion that is perpendicular to the motion induced by the other three joints. This is evident in Equation 3.31. The boom, stick and bucket are coupled and all the motion can be described on the $r - z$ plane. What happens on the $r - z$ plane is illustrated in Figure 3.4. The commanded position of the wrist (P_{03}) of the bucket is constrained to be on or inside the workspace denoted by R_{00}. If the "desired" position coming from the master device lies outside the workspace it must be reassigned to the closest point on the workspace as demonstrated by the arrows. Since this is a planar problem it is possible to setup logic that will reassign the desired position to the closest point in the workspace. This will be referred to as

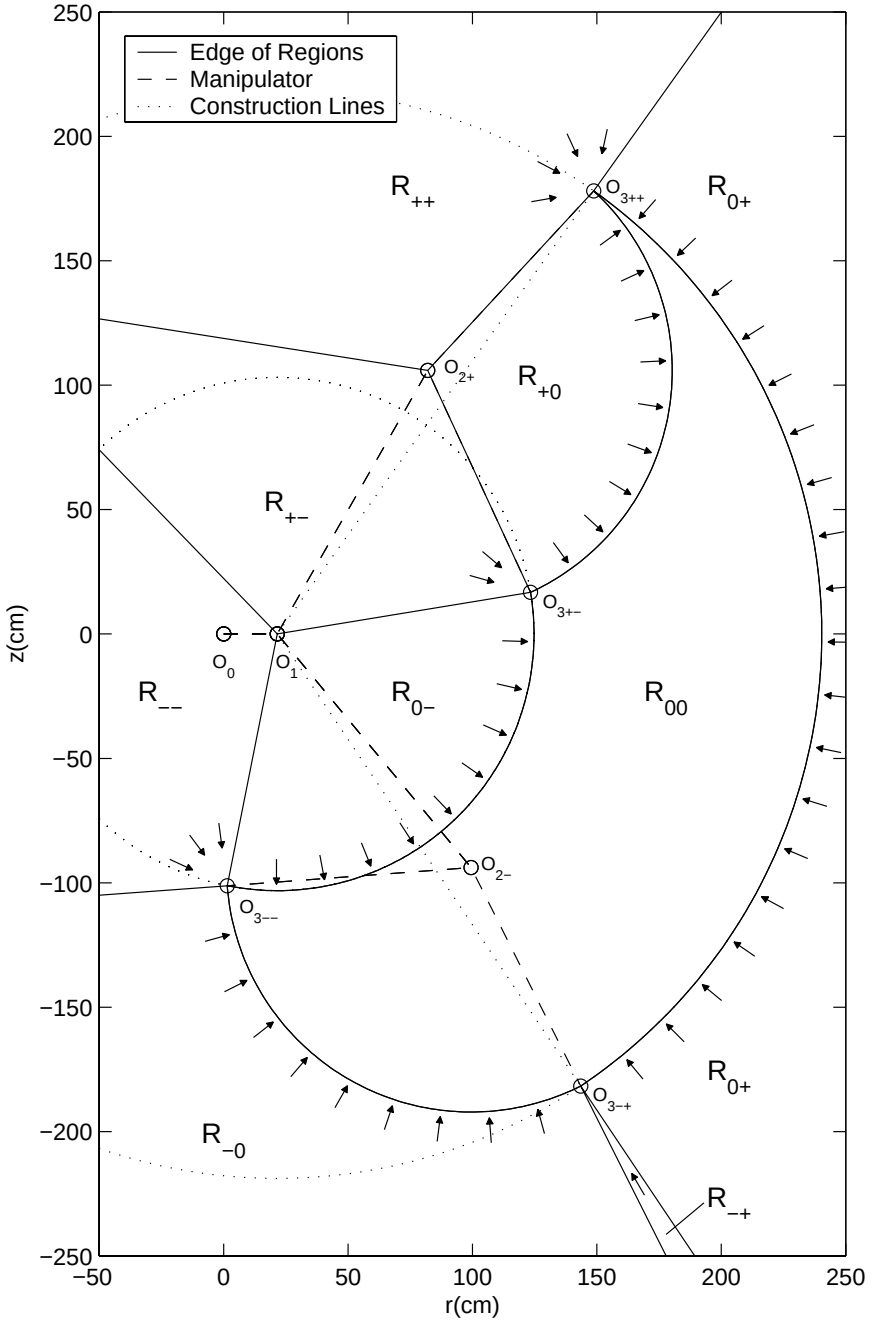

Figure 3.4: Graphical closed-form constrained inverse kinematic solution: The nine different regions where P_{03} can be commanded to go. The subscripts "i" and "j" represent the state of the second and third cylinders respectively: "+" = maximum angle constraint, "−" = minimum angle constraint and "0" = no constraint. For example, "R_{00}" means that both θ_2 and θ_3 are unconstrained and the P_{03} command does not need to be modified. The arrows show the point or curve on the edge of the workspace that the points in the constrained regions map.

the closed-form inverse kinematic solution. Geometrically different regions, denoted by R_{ij}, map to the workspace, or a point or curve on the edge of the workspace. Note that this can be done with out loss of generality for the case of both proximal and distal bucket control since both of these cases rely on calculating θ_2 and θ_3 based on P_{03} in the $r - z$ plane.

The downfall of this method is that it gives priority to the position of the bucket over its orientation. Another method would be to optimize a cost function, L, that includes a bucket angle error term (see equation 3.47).

$$L = \frac{1}{2}W_r\Delta r^2 + \frac{1}{2}W_z\Delta z^2 + \frac{1}{2}W_\phi\Delta\phi^2 \tag{3.47}$$

where $\Delta r = r_d - a_{c_1 4}$, $\Delta z = z_d - a_{s24}$ and $\Delta\phi = \phi_d + \pi - \theta_2 - \theta_3 - \theta_4$ represent the difference between the desired and commanded position. W_r, W_z and W_ϕ are weighting matrices. Since r and z are both measure distance, W_r is typically equal to W_z and W_ϕ is different. Minimizing this error can be done numerically using the steepest descent method to find the optimal vector of joint angles θ_{2-4} that minimize L.

$$\Xi_{k+1} = \Xi_k - \mu\nabla_\Xi L^T \tag{3.48}$$

where is the vector of joint angle that is being optimized to minimize L.

$$\Xi_k = \begin{bmatrix} \theta_2(k) \\ \theta_3(k) \\ \theta_4(k) \end{bmatrix} \tag{3.49}$$

and $\nabla_\Xi L^T$ is the transpose of the gradient of L with respect to Ξ.

$$\nabla_{\Xi} L^T = \begin{bmatrix} W_r(r_d - a_{c_14})a_{s24} - W_z(z_d - a_{s24})a_{c24} - W_\phi(\phi_d + \pi - \theta_2 - \theta_3 - \theta_4) \\ W_r(r_d - a_{c14})a_{s34} - W_z(z_d - a_{s24})a_{c34} - W_\phi(\phi_d + \pi - \theta_2 - \theta_3 - \theta_4) \\ W_r(r_d - a_{c14})a_{s4} - W_z(z_d - a_{s24})a_{c4} - W_\phi(\phi_d + \pi - \theta_2 - \theta_3 - \theta_4) \end{bmatrix} \tag{3.50}$$

Ξ_k would then be iterated a fixed number of times each clock cycle to converge on the optimum values for θ_{2-4}. Each cycle the initial guess, Ξ_0, is set to either the "closed-form" solution or the final value of Ξ_k from the last cycle based on respective cost, L, of each of these guesses.

Linear inequality constraints must be placed on this optimization in order to enforce the minimum and maximum joint angles. If $W_r = W_z >> W_\phi$ this will result in the same solution as the graphically derived closed form solution for proximal bucket control. With the addition of inequality constraints Equation 3.51 becomes

$$\Xi_{k+1} = \Xi_k - \mu \nabla_{\Xi} L^T + C\Lambda \tag{3.51}$$

where

$$\Lambda = [\lambda_1 \ \lambda_2 \ \lambda_3 \ \lambda_4 \ \lambda_5 \ \lambda_6]^T \tag{3.52}$$

$$C = [C_1 \ C_2 \ C_3 \ C_4 \ C_5 \ C_6] \tag{3.53}$$

For $i = 1, 2, 3$

$$\lambda_{2i-1} = \begin{cases} 1 & if \ (\theta_{i+1} \geq \theta_{i+1_{max}}) \\ 0 & else \end{cases} \tag{3.54}$$

$$\lambda_{2i} = \begin{cases} 1 & if(\theta_{i+1} \leq \theta_{i+1_{min}}) \\ 0 & else \end{cases} \tag{3.55}$$

$$C_1 = \begin{bmatrix} \theta_{2_{max}} - \theta_2 \\ 0 \\ 0 \end{bmatrix} \tag{3.56}$$

$$C_2 = \begin{bmatrix} \theta_{2_{min}} - \theta_2 \\ 0 \\ 0 \end{bmatrix} \tag{3.57}$$

$$C_1 = \begin{bmatrix} 0 \\ \theta_{3_{max}} - \theta_3 \\ 0 \end{bmatrix} \tag{3.58}$$

$$C_2 = \begin{bmatrix} 0 \\ \theta_{3_{min}} - \theta_3 \\ 0 \end{bmatrix} \tag{3.59}$$

$$C_5 = \begin{bmatrix} 0 \\ 0 \\ \theta_{4_{max}} - \theta_4 \end{bmatrix} \tag{3.60}$$

$$C_6 = \begin{bmatrix} 0 \\ 0 \\ \theta_{4_{min}} - \theta_4 \end{bmatrix} \tag{3.61}$$

Both of these methods have advantages. The closed-from solution is computationally more efficient and guarantees a solution. Using a numerical method to minimize a cost function allows weight to be placed on the bucket angle. However, the bucket kinematics is designed so that they should not need to hit the limits during normal operation. This can not be said for the θ_2 and θ_3 constraints. So it could be argued that optimizing a cost function that includes bucket angle is not necessary. This is especially true for the case of proximal bucket control since it would take relatively

large changes in r and z to allow ϕ to change even a small amount. On the other hand for distal bucket control, the position of the tip will be changed if the desired ϕ is not kinematically admissible. This is because the desired ϕ is used to calculated P_{03} which is used in the closed-form solution 3.38. However, using the closed-form solution is still a good initial guess for the gradient descent optimization even for distal bucket control.

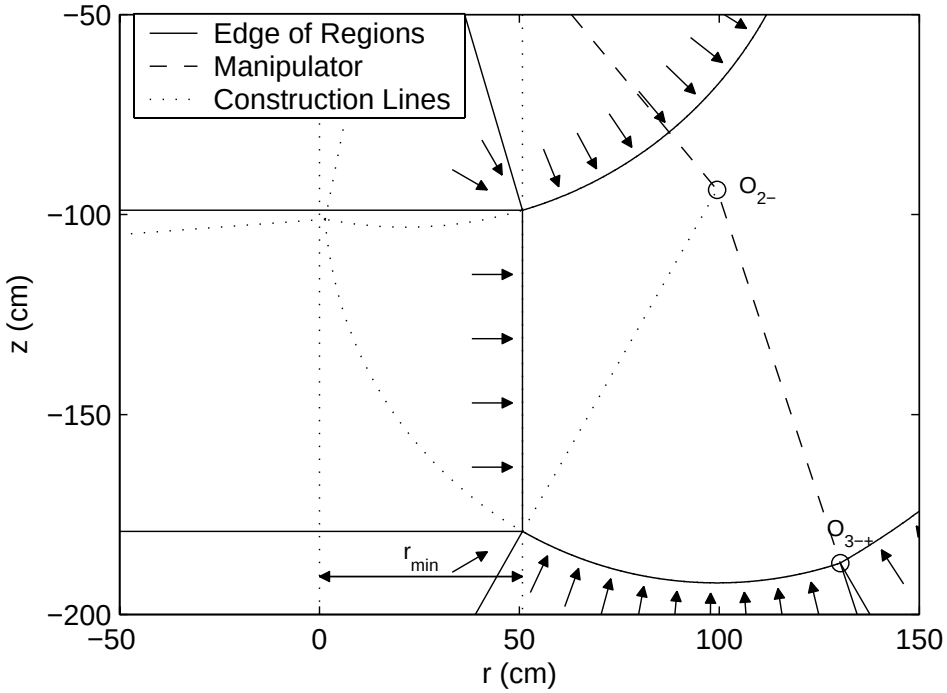

Figure 3.5: r_{min} constraint: In order to implement an r_{min} constraint it is necessary to modify Figure 3.4 as shown here.

Another constraint that is good to enforce is one that sets a minimum on r. This is because it is possible for the manipulator to pass through the aforementioned kinematic singularity when $r = 0$. This constraint can be added to either the closed-form or gradient descent constrained inverse kinematic solutions. Figure 3.5 demonstrates how Figure 3.4 is modified with the addition of an r_{min} constraint. For the gradient descent case an addition inequality constraint must be added to Equations 3.52 & 3.53 this inequality constraint can be linearized and is related to the second column

of the inverse Jacobian (Equation 3.52 & 3.53.

$$\lambda_7 = \begin{cases} 1 & if(r \leq r_{min}) \\ 0 & else \end{cases} \tag{3.62}$$

In order to enforce the constraint $\Delta r = r_{min} - r \leq 0$ this value must be linearized about 0 using the vector Θ. One way to do this is to start with the inverse Jacobian matrix (Equation 3.32) and assume that we only want to induce motion in the r direction.

$$\begin{bmatrix} \dot{\theta}_1 \\ \dot{\theta}_2 \\ \dot{\theta}_3 \\ \dot{\theta}_4 \end{bmatrix} = J^{-1}_{d_{cyl}} \begin{bmatrix} 0 \\ \dot{r} \\ 0 \\ 0 \end{bmatrix} = \frac{1}{d_d} \begin{bmatrix} 0 \\ -a_{c_3} \\ a_{c_{23}} \\ -a_{c_2} \end{bmatrix} \dot{r} \tag{3.63}$$

Just as in Equation 3.32 $d_d = -a_{c_4} a_{s_2} + a_{c_{34}} a_{s_{23}} - a_{c_{24}} a_{s_3}$. For small movements approximate $\dot{\alpha}$ with $\Delta\alpha/\Delta t$, divide by Δt. The first term, $\dot{\theta}_1$, can also be removed since swing is always decoupled from the other three joint angles.

$$\begin{bmatrix} \Delta\theta_2 \\ \Delta\theta_2 \\ \Delta\theta_2 \end{bmatrix} = \frac{1}{d_d} \begin{bmatrix} -a_{c_3} \\ a_{c_{23}} \\ -a_{c_2} \end{bmatrix} \Delta r \tag{3.64}$$

This means that the r_{min} constraint is equal to the vectors of the partial of the joint angles with respect to r multiplied by Δr.

$$C_7 = \begin{bmatrix} \partial\theta_2/\partial r \\ \partial\theta_3/\partial r \\ \partial\theta_4/\partial r \end{bmatrix} \Delta r = \frac{1}{d_d} \begin{bmatrix} -a_{c_3} \\ a_{c_{23}} \\ -a_{c_2} \end{bmatrix} \Delta r \tag{3.65}$$

In the case of position-based haptic control, a virtual spring force would typically be implemented that is proportional to the difference between actual position and

desired position (master position) of the slave manipulator. This means that in the cases of haptic feedback these constraints behave like virtual fixtures [114]. It has been shown that virtual fixtures are a way to enhance hydraulic equipment operator performance [66]. In this case they would be alerting the operator that the manipulator is at the edge of the workspace. Other virtual fixtures could also be added that alerted the operator to other information such as desired trench depth.

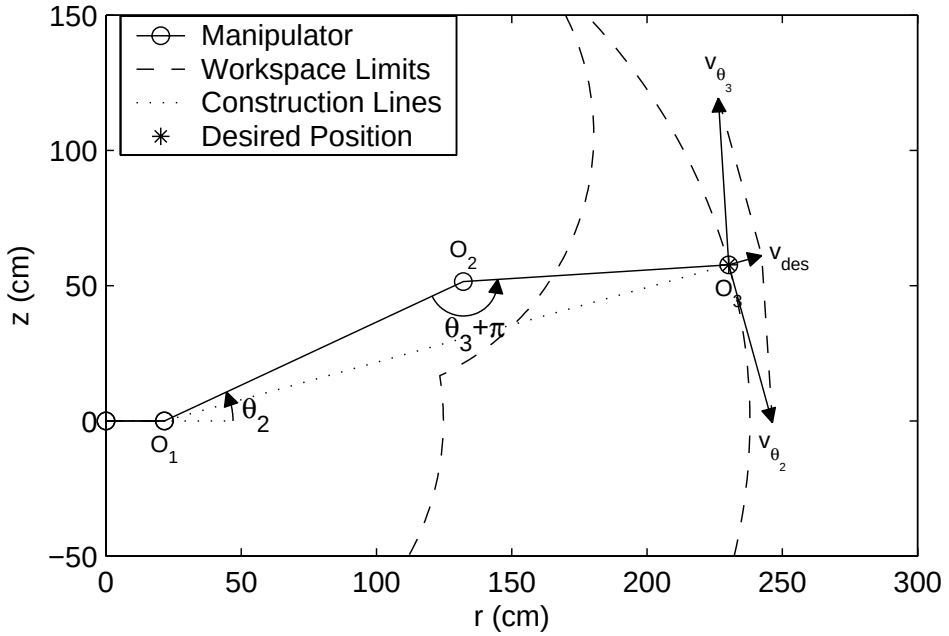

Figure 3.6: Constrained velocity: This shows a desired velocity, v_d, that is perpendicular to the edge of the workspace and the resulting velocity components that would need to be created by actuating θ_2 and θ_3. Note that if θ_3 is constrained the resulting movement would be v_{θ_2} which is perpendicular and much larger than v_d since θ_3 is close to a singularity.

Modifying the desired velocity is also necessary. The importance of this is demonstrated by Figure 3.6. The affect of this is magnified by the fact that when the stick is fully extended it is near a singularity. In this case, the stick or θ_3 constraint is active and a velocity command perpendicular to the edge of the workspace is given. Running this velocity through the full rank Jacobian results in the vectors v_{θ_2} and v_{θ_3} which represent the velocity components that need to be generated from the two

joints. But θ_3 is constrained so $\dot{\theta}_3 = 0$. This means that the actual command would result in velocity equal to v_{θ_2} which is perpendicular to the original velocity command. A similar phenomenon will occur if the unconstrained inverse kinematic equations are used to solve for θ_2 and θ_3 when θ_3 is constrained. A small movement in the direction of v_d will cause the bucket to move in the direction of v_{θ_2}.

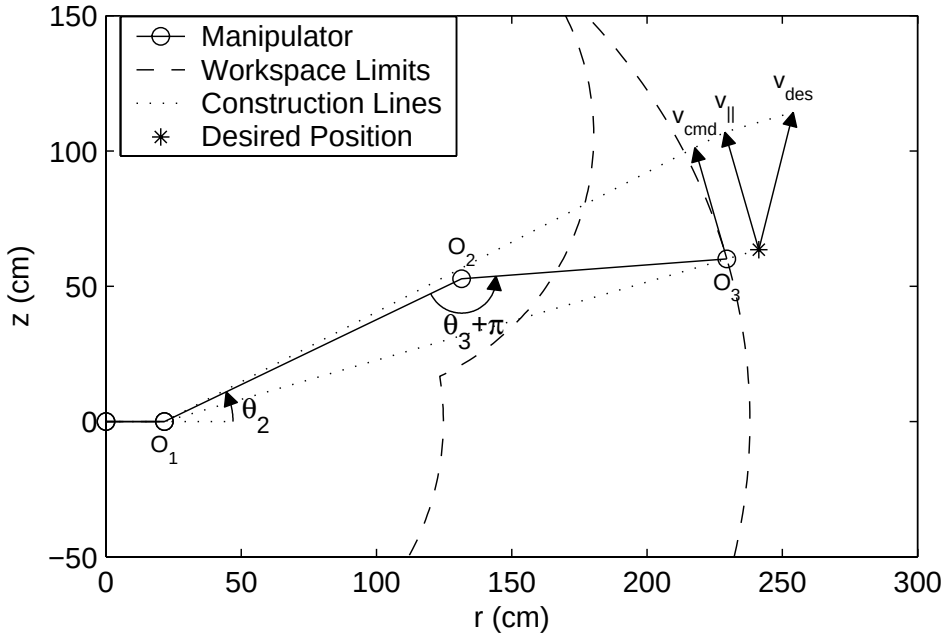

Figure 3.7: Corrected constrained velocity: This graphically demonstrates the correct way to calculate velocity when one of the joints is constrained. Remove the component of the desired velocity, v_d that is orthogonal to the edge of the workspace.

Since the Jacobian is rank deficient due to the active constraint, whether software or physical, this must be taken into account when task-space velocity is mapped into joint-space velocity. An alternative way of looking at this is to remove the component of velocity that is orthogonal to the surface of the constrained workspace. This is demonstrated by Figure 3.7. In this case $\dot{\omega}_2 = v_{||}/d = v_{cmd}/d_{max}$, where d is defined by Equation 3.41 and d_{max} is the maximum achievable value of d that occurs when $\theta_3 = \theta_{3_{max}}$. This is also evident in the two simulated paths of p_{03} when motion is induced around the $\theta_{3_{max}}$ constraint(Figure 3.8). Notice the large jumps caused in the

response when the constraint is enforced at the cylinder level. While there is some over shoot in the response when the constraints are considered in the task-space to joint-space mapping, the large motion along the edge of the constraint is not present.

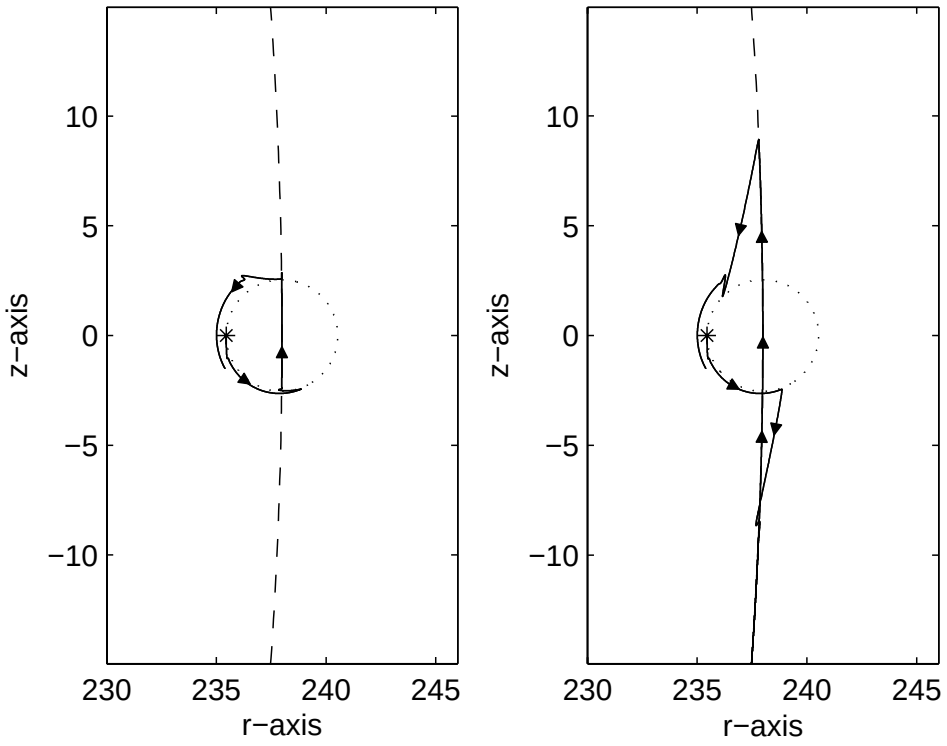

Figure 3.8: Simulations of constrained motion: The dashed circle represents the desired path P_{03}. The bucket starts off at point "*". The dashed line represents the software enforced constraint. The solid line in the left plot is the simulated response if the closed-form inverse kinematics and reduced rank Jacobian is used map task-space position and velocity. The solid line in the right plot is the simulated response if the constraints are enforced at the cylinder level. Note the large jumps in this response.

3.3 Cylinder-Space to Joint-Space Kinematics

In the case of a backhoe/excavator an additional layer of kinematics are necessary for Cartesian control. Not only do relationships between task-space coordinates and joint angles need to be resolved, but also the relationships between joint angles and cylinder lengths. One nice property of these relationships is that they are decoupled. For example, the boom cylinder length, y_2, only affects the second joint angle, θ_2. This means that the Jacobian relating velocity and force in the coordinate systems are also decoupled. Given y_2, $\dot{y}_2$, and F_{c_2}, the following online calculations will produce θ_2, $\dot{\theta}_2$ and τ_2 (Figure 3.10). Note that the $\partial\theta_2/\partial y_{c_2}$ is essentially a single degree of freedom Jacobian between the coordinates y_2 and θ_2.

3.3.1 Swing Cylinder

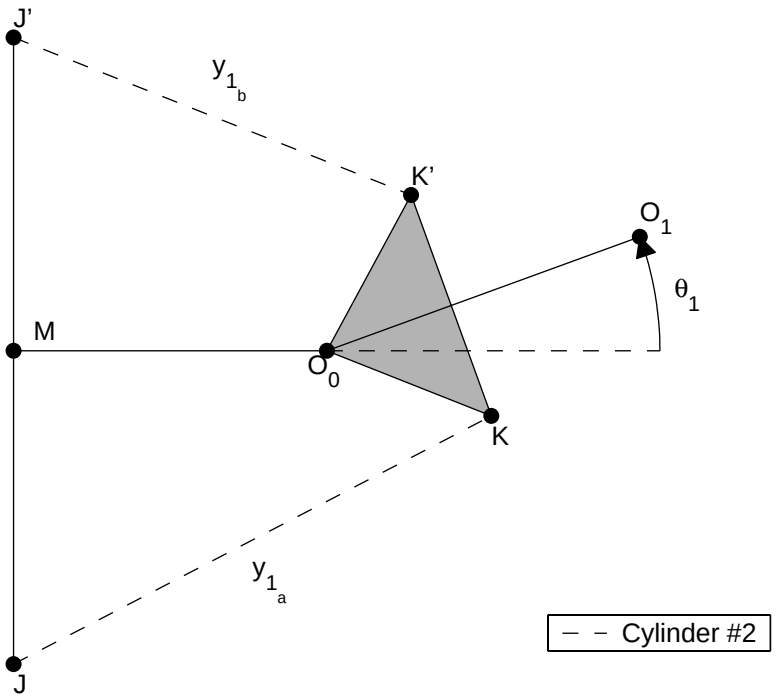

Figure 3.9: Swing angle and cylinder length.

From Figure 3.9 the following equation can be derived to calculate the cylinder-space swing variable (y_{1_a}, y_{1_b}, $\dot{y}_{1_a}$, $\dot{y}_{1_b}$) from the joint-space variables (θ_1, $\dot{\theta}_1$).

$$\theta_{K0J} = \theta_{MJ0} + \pi/2 + \theta_1 - \theta_{10K} \tag{3.66}$$

$$y_{1_a} = \sqrt{R_{0K}^2 + R_{0J}^2 - 2cos(\theta_{K0J})} \tag{3.67}$$

$$\dot{y}_{1_a} = \frac{\partial y_{1_a}}{\partial \theta_1}\dot{\theta}_1 = -\frac{R_{0K}R_{0J}sin(\theta_{K0J})}{y_{1_a}}\dot{\theta}_1 \tag{3.68}$$

$$\theta_{K'0J'} = \theta_{MJ'0} + \pi/2 + \theta_1 - \theta_{10K'} \tag{3.69}$$

$$y_{1_a} = \sqrt{R_{0K'}^2 + R_{0J'}^2 - 2cos(\theta_{K'0J'})} \tag{3.70}$$

$$\dot{y}_{1_a} = \frac{\partial y_{1_b}}{\partial \theta_1}\dot{\theta}_1 = -\frac{R_{0K'}R_{0J'}sin(\theta_{K'0J'})}{y_{1_a}}\dot{\theta}_1 \tag{3.71}$$

$$\begin{bmatrix} \dot{y}_{1_a} \\ \dot{y}_{1_b} \end{bmatrix} = \begin{bmatrix} \frac{\partial y_{1_a}}{\partial \theta_1} \\ \frac{\partial y_{1_b}}{\partial \theta_1} \end{bmatrix} \dot{\theta}_1 \tag{3.72}$$

On the machine used in this study the swing is actuated by two cylinders and the angle is measured using a rotary sensor. Due to the kinematics of this linkage the swing angle is not a function of either one of the cylinder lengths. This is because of the singularities that occur when either K' aligns with J' and O_0 or K aligns with J and O_0 3.9. However, both cylinder lengths are functions of swing angle. This means that it is better to measure and control swing angle rather than the swing cylinder lengths. For control the Jacobian between swing angle and cylinder lengths is used to calculate the proper cylinder speeds (fluid flows) from the desired joint angular velocity specified by the controller law for θ_1. Due the singularities, the corresponding inverse Jacobian can not be used. In some backhoes only one cylinder is used to actuate the swing and in excavators the boom, stick and bucket linkage rotates with the cab which is typically actuated by a hydraulic motor.

3.3.2 Boom Cylinder

From Figure 3.10 the following equation can be derived to calculate the boom joint-space variables (θ_2, $\dot{\theta}_2$, τ_2) from the cylinder-space variables (y_2, $\dot{y}_2$, F_{c_2}).

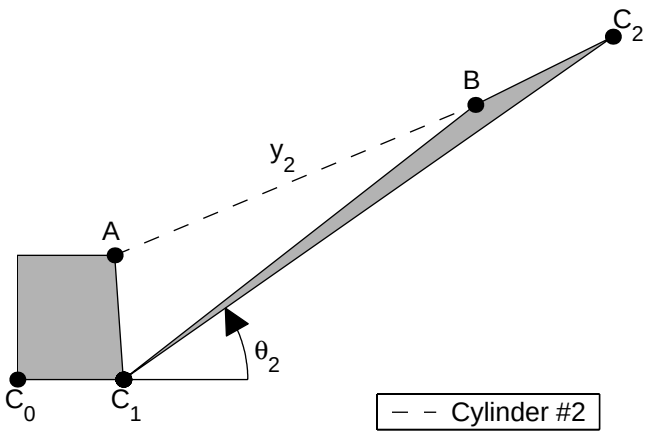

Figure 3.10: Second cylinder to joint kinematics: This figure shows the geometry relating the second cylinder length to the second joint angle.

$$\theta_{A1B} = acos\left(\frac{R_{1A}^2 + R_{1B}^2 - y_{c_2}^2}{2R_{1a}R_{1B}}\right) \tag{3.73}$$

$$\theta_2 = \pi - \theta_{01A} - \theta_{A1B} - \theta_{B12} \tag{3.74}$$

$$\frac{\dot{\theta}_2}{\dot{y}_{c_2}} = \frac{\partial\theta_2}{\partial y_{c_2}} = -\frac{\partial\theta_{A1B}}{\partial y_{c_2}} = -\frac{y_{c_2}}{R_{1A}R_{1B}\sin(\theta_{A1B})} \tag{3.75}$$

$$\dot{\theta}_2 = \frac{\partial\theta_2}{\partial y_{c_2}}\dot{y}_{c_2} \tag{3.76}$$

$$\tau_2 = \frac{\partial y_{c_2}}{\partial\theta_2}F_{c_2} \tag{3.77}$$

For the second cylinder the conversion from joint-space variables (θ_2, $\dot{\theta}_2$, τ_2) to cylinder-space variables (y_2, $\dot{y}_2$, F_{c_2}) can be done by rearranging equations 3.73 - 3.77. They could also be derived directly from Figure 3.10.

$$\theta_{A1B} = \pi - \theta_{01A} - \theta_2 - \theta_{B12} \tag{3.78}$$

$$y_{c_2} = \sqrt{R_{1A}^2 + R_{1B}^2 - 2R_{1A}R_{1B}cos(\theta_{A1B})} \tag{3.79}$$

$$\frac{\dot{y}_{c_2}}{\dot{\theta}_2} = \frac{\partial y_{c_2}}{\partial\theta_2} = -\frac{R_{1A}R_{1B}sin(\theta_{A1B})}{y_{c_2}} \tag{3.80}$$

$$\dot{y}_{c_2} = \frac{\partial y_{c_2}}{\partial\theta_2}\dot{\theta}_2 \tag{3.81}$$

$$F_{c_2} = \frac{\partial\theta_2}{\partial y_{c_2}}\tau_2 \tag{3.82}$$

3.3.3 Stick Cylinder

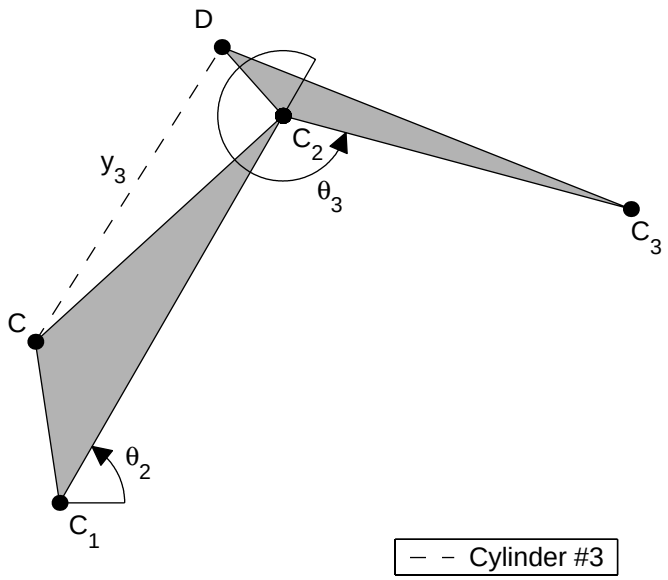

Figure 3.11: Third cylinder to joint kinematics: This figure shows the geometry relating the third cylinder length to the third joint angle.

From Figure 3.11 the following equation can be derived to calculate the stick joint-space variables (θ_3, $\dot{\theta}_3$, τ_3) from the cylinder-space variables (y_3, $\dot{y}_3$, F_{c_3}).

$$\theta_{C2D} = acos\left(\frac{R_{2C}^2 + R_{2D}^2 - y_{c_3}^2}{2R_{2C}R_{2D}}\right) \tag{3.83}$$

$$\theta_3 = \pi - \theta_{12C} - \theta_{C2D} - \theta_{D23} \tag{3.84}$$

$$\frac{\dot{\theta}_3}{\dot{y}_{c_3}} = \frac{\partial\theta_3}{\partial y_{c_3}} = -\frac{\partial\theta_{C2D}}{\partial y_{c_3}} = -\frac{y_{c_3}}{R_{2C}R_{2D}\sin(\theta_{C2D})} \tag{3.85}$$

$$\dot{\theta}_3 = \frac{\partial\theta_3}{\partial y_{c_3}}\dot{y}_{c_3} \tag{3.86}$$

$$\tau_3 = \frac{\partial y_{c_3}}{\partial\theta_3}F_{c_3} \tag{3.87}$$

Again for the third cylinder the conversion from joint-space variables (θ_3, $\dot{\theta}_3$, τ_3) to cylinder-space variables (y_3, $\dot{y}_3$, F_{c_3}) can be done by rearranging equations 3.83 - 3.87 or could be derived directly from Figure 3.11.

$$\theta_{C2D} = \pi - \theta_{12C} - \theta_3 - \theta_{D23} \tag{3.88}$$

$$y_{c_3} = \sqrt{R_{2C}^2 + R_{2D}^2 - 2R_{2C}R_{2D}cos(\theta_{C2D})} \tag{3.89}$$

$$\frac{\dot{y}_{c_3}}{\dot{\theta}_3} = \frac{\partial y_{c_3}}{\partial \theta_3} = -\frac{R_{2C}R_{2D}sin(\theta_{C2D})}{y_{c_3}} \tag{3.90}$$

$$\dot{y}_{c_3} = \frac{\partial y_{c_3}}{\partial \theta_3}\dot{\theta}_3 \tag{3.91}$$

$$F_{c_3} = \frac{\partial \theta_3}{\partial y_{c_3}}\tau_3 \tag{3.92}$$

3.3.4 Bucket Cylinder

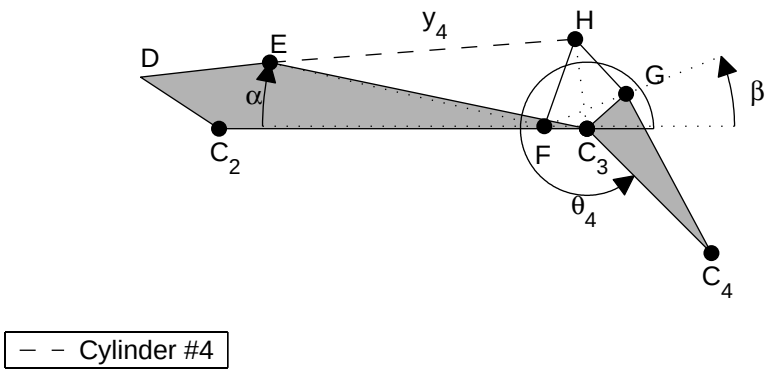

Figure 3.12: Fourth cylinder to joint kinematics: This figure shows the geometry relating the fourth cylinder length to the fourth joint angle.

From Figure 3.12 the following equation can be derived to calculate the bucket joint-space variables (θ_4, $\dot{\theta}_4$, τ_4) from the cylinder-space variables (y_4, $\dot{y}_4$, F_{c_4}). These equations are much more involved than the equivalent equations for the boom and stick because the bucket cylinder is attached to a four-bar mechanism instead of the respective link.

$$\theta_{EFH} = acos\left(\frac{R_{EF}^2 + R_{FH}^2 - y_{c_4}^2}{2R_{EF}R_{FH}}\right) \tag{3.93}$$

$$R_{FH_x} = R_{FH}\cos(\alpha + \theta_{EFH}) \tag{3.94}$$

$$R_{FH_y} = R_{FH}\sin(\alpha + \theta_{EFH}) \tag{3.95}$$

$$R_{3H_x} = R_{3I} + R_{FH_x} \tag{3.96}$$

$$R_{3H_y} = R_{FI} + R_{FH_y} \tag{3.97}$$

$$\theta_{23H} = atan2(R_{3H_y}\, R_{3H_x}) \tag{3.98}$$

$$R_{3H} = \sqrt{R_{3H_x}^2 + R_{3H_y}^2} \tag{3.99}$$

$$\theta_{H3G} = acos\left(\frac{R_{3H}^2 + R_{3G}^2 - R_{HG}^2}{2R_{3H}R_{3G}}\right) \tag{3.100}$$

$$\theta_4 = \pi - (\theta_{23H} + \theta_{H3G} + \theta_{G34}) \tag{3.101}$$

$$\frac{\dot{\theta}_{EFH}}{\dot{y}_{c_4}} = \frac{\partial\theta_{EFH}}{\partial y_{c_4}} = \frac{y_{c_4}}{R_{EF}R_{FH}sin(\theta_{EFH})} \tag{3.102}$$

$$\frac{\dot{\theta}_{23H}}{\dot{\theta}_{EFH}} = \frac{\partial\theta_{23H}}{\partial\theta_{EFH}} = \frac{R_{3I}R_{FH_x} + R_{FI}R_{FH_y} + R_{FH}^2}{R_{3H}^2} \tag{3.103}$$

$$\frac{\dot{\theta}_{H3G}}{\dot{\theta}_{EFH}} = \frac{\partial\theta_{H3G}}{\partial\theta_{EFH}} = \frac{(R_{FI}R_{FH_x} - R_{3I}R_{FH_y})(R_{3G}cos(\theta_{H3G}) - R_{3H})}{R_{3H}^2 R_{3G}sin(\theta_{H3G})} \tag{3.104}$$

$$\dot{\theta}_4 = -\dot{\theta}_{23H} - \dot{\theta}_{H3G} \tag{3.105}$$

$$\frac{\partial\theta_4}{\partial y_{c_4}} = \frac{\partial\theta_4}{\partial\theta_{EFH}}\frac{\partial\theta_{EFH}}{\partial y_{c_4}} = \left(\frac{\partial\theta_{23H}}{\partial\theta_{EFH}} + \frac{\partial\theta_{H3G}}{\partial\theta_{EFH}}\right)\frac{\partial\theta_{EFH}}{\partial y_{c_4}} \tag{3.106}$$

$$\dot{\theta}_4 = \frac{\partial\theta_4}{\partial y_{c_4}}\dot{y}_{c_4} \tag{3.107}$$

$$\tau_4 = \frac{\partial y_{c_4}}{\partial\theta_4}F_{c_4} \tag{3.108}$$

From Figure 3.12 the following equation can be derived to calculate the bucket cylinder-space variables (y_4, $\dot{y}_4$, F_{c_4}) from the joint-space variables (θ_4, $\dot{\theta}_4$, τ_4).

$$R_{3G_x} = R_{3G}cos(\theta_4 + \theta_{G34}) \tag{3.109}$$

$$R_{3G_y} = R_{3G}sin(\theta_4 + \theta_{G34}) \tag{3.110}$$

$$R_{FG} = \sqrt{(R_{3G_y} - R_{FI})^2 + (R_{3I} + R_{3G_x})^2)} \tag{3.111}$$

$$\beta = asin\left(\frac{R_{3G_y} - R_{FI}}{R_{FG}}\right) \tag{3.112}$$

$$\theta_{GFH} = acos\left(\frac{R_{FH}^2 + R_{FG}^2 - R_{GH}^2}{2R_{FH}R_{FG}}\right) \tag{3.113}$$

$$\theta_{EFH} = \pi - \alpha - \beta - \theta_{GFH} \tag{3.114}$$

$$y_{c_4} = \sqrt{(R_{EF}^2 + R_{FH}^2 - 2R_{EF}R_{FH}cos(\theta_{EFH})} \tag{3.115}$$

$$\frac{\dot{\beta}}{\dot{\theta}_4} = \frac{\partial\beta}{\partial\theta_4} = \frac{(R_{FG} + R_{FI}sin(\beta))R_{3G_x} + R_{3I}sin(\beta)R_{3G_y}}{R_{FG}^2 cos(\beta)} \tag{3.116}$$

$$\frac{\dot{\theta}_{GFH}}{\dot{\theta}_4} = \frac{\partial\theta_{GFH}}{\partial\theta_4} = -\frac{(R_{FH}cos(\theta_{GFH}) - R_{FG})(R_{FI}R_{3G_x} + R_{3I}R_{3G_y})}{R_{FH}R_{FG}^2 sin(\theta_{GFH})}\dot{\theta}_4 \tag{3.117}$$

$$\dot{\theta}_{EFH} = -\dot{\beta} - \dot{\theta}_{GFH} \tag{3.118}$$

$$\frac{\dot{y}_{c_4}}{\dot{\theta}_{EFH}} = \frac{\partial y_{c_4}}{\partial\theta_{EFH}} = \frac{R_{EF}R_{FH}sin(\theta_{EFH})}{y_{c_4}} \tag{3.119}$$

$$\frac{\partial y_{c_4}}{\partial\theta_4} = \frac{\partial y_{c_4}}{\partial\theta_{EFH}}\frac{\partial\theta_{EFH}}{\partial\theta_4} = -\left(\frac{\partial\beta}{\partial\theta_4} + \frac{\partial\theta_{GFH}}{\partial\theta_4}\right)\frac{\partial\theta_{EFH}}{\partial\theta_4} \tag{3.120}$$

$$\dot{y}_{c_4} = \frac{\partial y_{c_4}}{\partial\theta_4}\dot{\theta}_4 \tag{3.121}$$

$$F_{c_4} = \frac{\partial\theta_4}{\partial y_{c_4}}\tau_4 \tag{3.122}$$

In the case of an excavator, these equations are slightly different because the cylinders are generally located below the boom link, but the process is identical. An almost identical method can be used to map the stick cylinder variables to the third joint variables. Relating the bucket cylinder variables to the fourth joint angle is more complicated. This is because bucket cylinders are attached to four-bar linkage instead of directly to the bucket. This makes the transformation more involved and computationally expensive. An alternative is to make a polynomial approximate of the function $\theta_i = f(y_i)$ and $y_i = f(\theta_i)$ and use the derivative of the approximations as an approximation of the partial derivatives [132].

3.4 Summary

This chapter presents the kinematics algorithms necessary for coordinated haptic control of a backhoes/excavators. First, task-space to joint-space transforms are presented. Tests and analysis demonstrate the importance of dealing with cylinder

constraints. Two methods for dealing with these constraints are derived and implemented. A constraint designed to avoid the only singularity in the task-space to cylinder-space mapping is presented and implemented. Lastly, the joint-space to cylinder-space mappings are derived including Jacobians that relate cylinder velocity and force to joint-space angular velocity and torque. The primary contribution of this chapter is the material related to cylinder constraints. Understanding the kinematics is important because this enables bucket motion to be described in task-space and mapped low-level cylinder velocity/flow commands.

CHAPTER IV

HYDRAULIC CONTROL

The primary goal of this project is to explore how haptic interfaces can enhance the ability of novice and expert operators to control hydraulic machinery such as backhoes loader and hydraulic excavator. However, the focus of this chapter is the hydraulic control system required by this closed-loop haptic control.

This topic can be divided into controlling the pump pressure and controlling the flow rates to the cylinders in order to achieve coordinated motion. Section 4.2 describes the hydraulic system used on the HEnRE test-bed. The control techniques related to control of pump pressure are described in Section 4.3. One major contribution of this chapter is a scheme designed to decouple pump pressure from the flow control states. This is accomplished using pressure compensators and an electronic load-sensing scheme. A Moving-Window-Max-Filter is designed and implemented. These two contributions are published in Kontz and Book [71]. The importance of a flow limiter is demonstrated. For coordinated motion it is desirable to proportionally scale back all velocity commands. This means that pump pressure can be maintained and the desired direction of the coordinated motion is preserved. This result was published in Kontz et al [74]. Section 4.4 discusses actuator flow control. The effect of variation in the actual flow versus desired flow is discussed since the valve command is produced from the desired cylinder velocity in a feedforward fashion. Another significant contribution in this section is an input deadzone function that can eliminate limits cycles around zero velocity. These limits cycles are created by the combination of feedback control, valve deadband sandwiched between slow valve dynamics and the controller's inverse deadband or jump through function. The effectiveness of these

flow control strategies are demonstrated by two simple task-space trajectories that are mapped into cylinder-space (Section 4.4.4). This coordinated motion controller builds on the pressure and flow control as well as the kinematic algorithm in Chapter 3. The work related to coordinated flow control was published in Kontz et al. [67].

4.1 Hydraulics Background

While hydraulic systems offer a practical application of haptic feedback, their characteristics can be detrimental to the implementation. In the case of proportional directional control valves these characteristics include nonlinear valve orifice coefficients, delay, dead-band and slow dynamics. When implemented on mobile equipment, dynamics associated with the pump and primary pressure/flow control must also be considered. Closing the loop on these dynamics can create instabilities.

The valve dead-band is an issue of concern when closing the loop around a proportional directional control valve. One way to deal with dead-band is to use a dead-band inverse in the control. In the case of a servo valve with fast dynamics this can be achieved with good performance [28]. In the case of a proportional valve the effectiveness of the dead-band inverse is limited by the dynamics of valves [89, 135]. This is due to the dead-band nonlinearity being sandwiched between the spool dynamics and the dynamic of the rest of the hydraulic system [135]. The inverse dead-band is located at the input and corrects the desired spool position; however, the limitation on how fast the spool can move determines how fast the desired spool position can be achieved. In turn, this limits how well the system can track a desired trajectory. One way to minimize the effect of spool dead-band and improve overall performance is to increase the responsiveness of the spool control stage. Tafazoli et al. [149] created a custom differential PWM pilot stage that could move the spool faster in order to improve the responsiveness of the main spool used on their haptic mini-excavator.

Another factor that can limit how fast a system responds is the rate at which the

main system pressure can build up [84]. This is especially true of load-sensing systems that react to the maximum line pressures of any of the open flow control valves. This type of design is good from an energy savings point of view, but is detrimental to closed-loop control which is necessary for haptic teleoperation [76, 132, 133] or autonomous operation [38, 126, 139]. The system has to wait in order for pressure to build up when starting from rest and the pressure can drop and may need to build up again when the valve orifices are temporarily closed as the valves change the direction of the flow. This problem could be minimized by using a pressure regulating valve with an electronically controlled set point. The pressure can be built up as the spool moves through the dead-band. Another factor that can compound this problem is that the pilot pressure that is used by the main spool is supplied from a pressure reducing valve that is fed by the main system pressure. When all the spools are in the dead-band region, the main system pressure drops below the set point of the pressure reducing valve. Due to this the spool pilot pressure drops along with the responsiveness of the spool.

From an energy and performance standpoint, being able to optimize the pressure of the system is particularly important on this type of system. Typically on larger equipment such as backhoe loaders and hydraulic excavator have variable displacements pump(s) and a separate pilot system. The variable displacement pump allows both pump flow(s) and pressure(s) to be adjusted in response to the demands of the task. Having a separate pilot system allows the main pump pressure to drop to very low pressure without reducing the pilot pressure. These features are less likely to be installed on smaller machines such this tractor mounted backhoe and mini-excavators due to hardware cost and size constraints.

Flow allocation must also be considered. The main pressure regulator is essentially a pressure relief valve that is modulating the pressure of the system. Three different

pressure regulating configurations are explored: the original hydro-mechanical load-sensing pressure regulator, a constant pressure relief valve and an electronic load-sensing pressure relief valve. One thing that all three of these configurations have in common is that if they are not bypassing a sufficient amount of flow they are not able to regulate the system pressure. This can be solved by limiting the flow commanded by the controller.

4.2 Hydraulic System

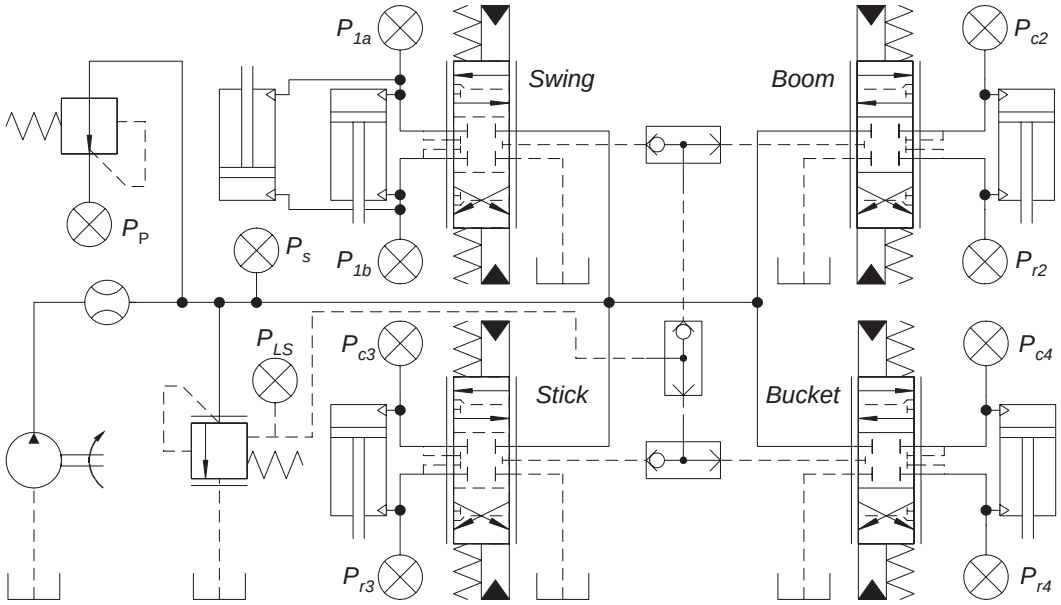

Figure 4.1: Schematic of the overall PVG-32/PVES system with hydro-mechanical load-sensing control of the pressure relief valve regulating pump pressure, Ps. A pressure reducing valve is used to regulate the pilot pressure, Pp, which is used by the electro-hydraulic proportional spool control stages show in Figure 4.4.

The schematic of the hydraulic system is shown in Figure 4.1. Four Sauer-Danfoss PVG-32 proportional valves are used to regulate the flow going to the four degrees of freedom of the backhoe. These valves are designed to be controlled by electronic joysticks for use in mobile hydraulic applications. They are designed to deliver a steady-state flow proportional to the input voltage signal with the addition of pressure compensators making them ideal for this application. These valves can be stacked

and can operate with a constant displacement pump with the addition of a main pressure regulator to control pump pressure. The main pressure regulator is essentially a pressure relief valve that is modulating the system/pump pressure, P_s, and bypassing all the flow that is not being sent to the actuators back to tank. At the same time the individual closed-center proportional valves can hold the actuators in place while the valves are in their neutral position. The PVG-32/PVES valves have three major components: main spools, pilot spool controllers (PVES modules) and a main pressure regulator. A pressure reducing valve is also used to regulate the pilot pressure, P_p, which is used by the hydraulic wheat-stone bridge in Figure 4.2 that controls the motion of the main spool. Not shown in Figure 4.2 and Figure 4.1 are optional pressure compensators. The pressure compensators are used to maintain a constant pressure drop across the main spool. This essentially makes the input proportional to flow. Without the pressure compensator, the input is proportional to the orifice created by the main spool. This section will focus on how the main spools and pilot spool controllers work and how pump pressure is controlled using a pressure relief valves.

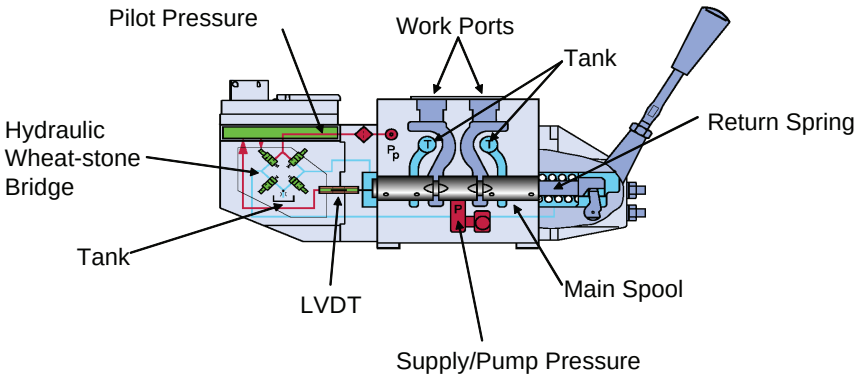

Figure 4.2: PVES/PVG32 valve

4.2.1 Proportional Directional Control Valves

The spool position controls the main flow going to the cylinders by changing the orifice between one port and tank and the other port and supply. The spool is moved back and forth in order to adjust the orifice size between one port and tank and another orifice between the other port and the pump pressure, P_s. When a neutral signal is given to the valves the spool centers itself so that the overlap in the spool prevents internal leakage. It is this overlap that causes the dead-band in the system. These orifices can be described using the orifice equation[101]. The relationship between flow, Q, and pressure drop across the orifice, ΔP, can be described in general using the following equation.

$$Q = C_d A_0 \sqrt{\frac{2}{\rho} \Delta P} = K_q(x_{sp}, T) \sqrt{|\Delta P|} \tag{4.1}$$

Where C_d is the discharge coefficient and A_0 is the orifice area. The combined term $C_d A_0$ is a function of spool position, X_{sp}, because the area and shape of the orifice change as the spool moves. As the temperature increases density, ρ, will go down and C_d will go up due to a decrease in viscosity of the oil. Both of these will result in more flow for the same pressure drop. This decrease the accuracy of the feedforward flow contrl. The effect of oil temperature will be ignored since temperature will not vary a lot in the laboratory environment where the test-bed is located. The effect that variations in actual versus expect flow cause this has on control performance will be discussed more in Section 4.4. In short, variation in temperature will decrease the accuracy of any desired motion, but can be partially compensated for by feedback. In general, colder oil will result in a slow more damped response and hotter oil will decrease system damping. For controller simplicity, it is assumed that flow is only a function of pressure drop and spool position. If

$$Q_c = sign(\Delta P_c) K_{q_c}(x_{sp}, T) \sqrt{|\Delta P_c|} \tag{4.2}$$

$$Q_r = sign(\Delta P_r) K_{q_r}(x_{sp}, T) \sqrt{|\Delta P_r|} \tag{4.3}$$

Valve orifice flow coefficients, K_{q_c} and K_{q_r}, control the flow going in and out of the capside and rodside of the cylinder. The pressure drop, ΔP, is measured across the valve orifice from the main system pressure to port or tank to port. Pressure compensators linearize the relationship between input voltage versus steady-state flow. This is accomplished by regulating the pressure drop across the orifice receiving flow from the pump. This is beneficial since the compensators can adjust to changes in pressure faster than the closed-loop dynamics of the spool. However, they do add an additional set of dynamics. An additional possibility would be to have a three dimensional map relating spool position to flow and pressure drop. The advantage of using a three dimensional map over the equation shown in Equation 4.1 is that it is not necessary to assume turbulent flow. This assumption is not necessarily true for low flow and high pressure drop, but it is the basis for assuming the flow is proportional to the square-root of pressure drop for a given spool position.

The PVG-32 spools are modulated using the PVES electronically controlled spool stages. This stage design is shown in Figures 4.2 and 4.3. Four small solenoid valves are arranged in a wheatstone bridge configuration in order to move the main spool back and forth. This wheatstone bridge is supplied with pressure and flow from a

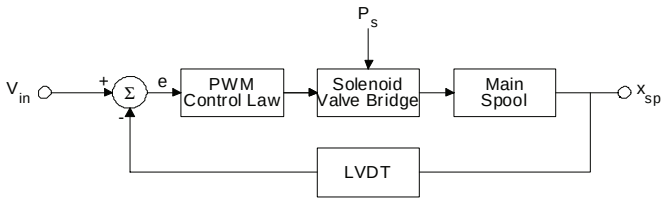

Figure 4.3: Block diagram of PVES pilot spool controller.

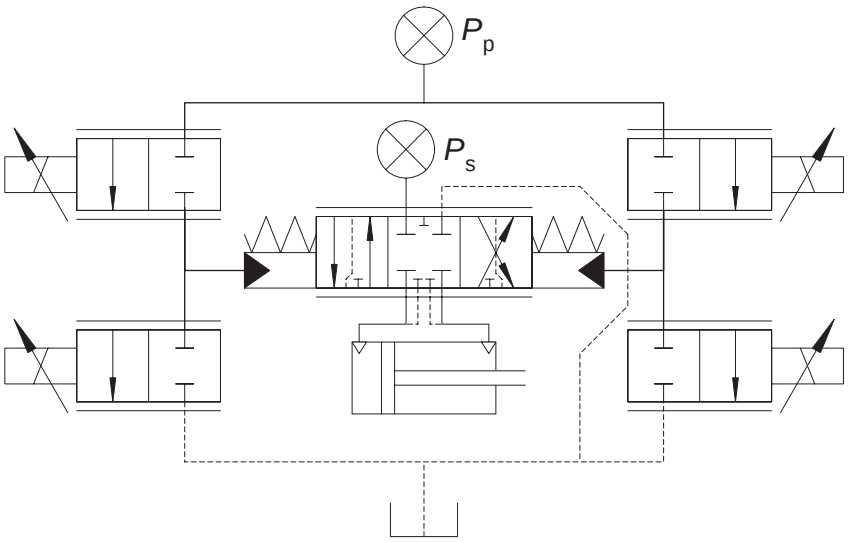

Figure 4.4: Schematic of Sauer-Danfoss PVG32/PVES spool position controller. The pilot pressure, Pp, is controlled by the pressure reducing valve in Figure 4.1. The four solenoids in the wheatstone bridge are controlled by a 40Hz PWM (pulse width modulated) signal.

pressure reducing valve shown in Figure 4.4. The solenoid valves are modulated using a PWM (pulse width modulated) signal at $40Hz$. This frequency is important because it is directly related to the valve's delay, but it not adjustable in these modules. In turn delay not only slows down the response of the system, but also reduces the phase margin which is related to damping and the achievable closed-loop bandwidth of the system. As a point of comparison, Tafazoli et al. [129] determined that 100Hz was necessary for the differential PWM spool controller used on the University of British Columbia's haptic mini-excavator. Using PWM frequency on the order of 100-200Hz to control electro-hydraulic valves is not uncommon. The dynamics between the input voltage, V_{in}, and the spool position, X_{sp}, can be approximated for low frequencies using a second order system with a pure delay element. This delay is likely a result of the $40Hz$ frequency of the PWM controller.

$$\frac{V_{X_{sp}}(s)}{V_{in}(s)} = \frac{k\omega_n^2 e^{-\tau s}}{s^2 + 2\zeta\omega_n s + \omega_n^2} = \frac{0.43623 \cdot 1947 e^{-0.0125s}}{s^2 + 62.1s + 1947} \tag{4.4}$$

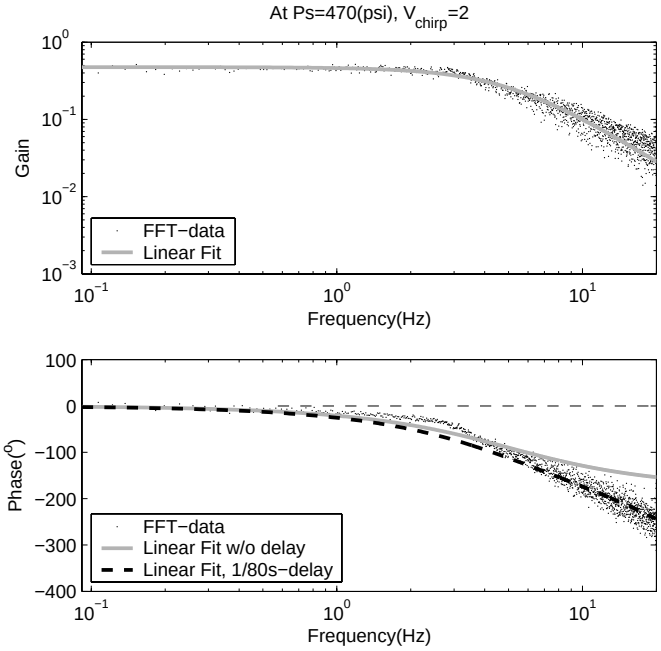

Figure 4.5: Bode plot of spool position response: $\zeta = 0.703$ and $\omega_n = 44.1 rad/s \Rightarrow f_n = 7.02 Hz$. Note that the gain in the top subfigure is the same with or without delay.

Experimental results, similar to the test shown in Figure 4.5, indicate that Equation 4.4 is a good approximation for system pressures above about $2.06 MPa (300 psi)$. In this range the bandwidth of the spool control stage is around $7 - 8 Hz$ and the damping ratio is about 0.7. The actual dynamics vary with oil temperature and pump pressure, Ps. If pump pressure is below this range the bandwidth of the spool significantly drops off. This is because the pressure reducing valve regulating Pp is not properly pressurized. This is consistent with the fact that the pressure reducing valve regulates the pilot pressure used by the spool stage at $1.5 MPa (217 psi)$.

If all the main valves are closed or moving through the dead-band region, the system pressure drops to its minimum pressure around $1.03 - 1.38 MPa (150 - 200 psi)$ because none of the ports are pressurizing the load-sense pressure line. When the system pressure is low, experimental results in Figure 4.6 indicate it takes longer for the spool to pass through the spool's dead-band region when the system pressure

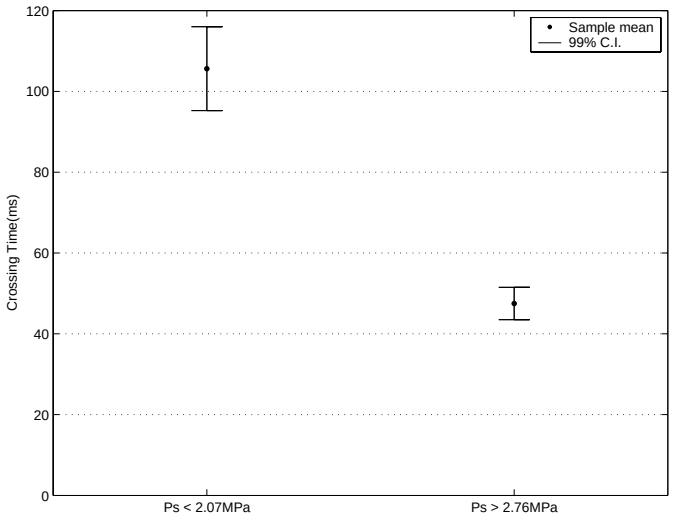

Figure 4.6: ime in milliseconds that it take the spool to cross through the dead-band at with low system pressure (less than $2.07MPa/300psi$) and high system pressure (more than$2.76MPa/400psi$).

and therefore pilot pressure is too low. Normally, it would take about $50ms$ to pass through the valve dead-band. When the system pressure and therefore the pilot pressure drop, the $50ms$ dead-band crossing time increases to as much as $110ms$.

4.2.2 Main Pressure Regulator Designs

Three different pressure regulator designs are used in the following experiments: a hydro-mechanical load-sensing pressure regulator, a constant pressure regulator and an electronically controlled load-sensing pressure regulator. The hydro-mechanical load-sensing pressure regulator is built into the Sauer-Danfoss valve assembly.

4.2.2.1 Hydro-Mechanical Regulation

The main pressure regulator is essentially a pressure relief valve that opens to tank when the system pressure, P_s, surpasses some value. The system pressure is then used by the individual proportional valves that operate each degree of freedom. With load-sensing enabled, the pressure regulator tries to maintain P_s at a preset pressure margin, P_{margin}, above the load-sense pressure, P_{LS}. The load-sense pressure is driven

by the maximum pressure of the ports receiving flow from the pump. These spools are designed to open the port pressures to the load-sense line right before they move enough to create a control orifice. This is good from an energy savings point of view, but it adds delay to the system. The relationship between P_s and P_{LS} can be approximated by the following experimentally derived transfer function.

$$\frac{P_s(s)}{P_{LS}(s) + P_{margin}} = \frac{1}{\tau_{_{P_s}} s + 1} \tag{4.5}$$

The pressure margin, P_{margin}, is around $1.05MPa$ ($153psi$) and the time constant, $\tau_{_{P_s}}$, is around 0.012 seconds ($12.6Hz$). The pressure margin is the minimum pressure differential between the pump pressure and the load-sensing pressure. It also sets the minimum pressure drop across the control orifices of the proportional valves. It is set by the force balance on the pressure relief valve. There is also a dynamic relationship between the port pressures and the load-sense pressure. For each degree of freedom

$$P_{LS_i} = \begin{cases} P_c & if\ the\ i^{th}\ cylinder\ is\ extending \\ P_{min} \neq 0 & if\ the\ i^{th}\ spool\ is\ in\ the\ dead-zone \\ P_r & if\ the\ i^{th}\ cylinder\ is\ retracting \end{cases} \tag{4.6}$$

Only the largest of the four P_{LS_i} signals drive the load-sense pressure and the main system pressure. The maximum pressure is selected using a series of shuttle valves (Figure 4.1). There is also a dynamic relationship between the maximum P_{LS_i} and $P_{_{LS}}$.

$$\frac{P_{LS}(s)}{max\{P_{LS_{1-4}}\}(s)} = \frac{1}{\tau_{_{LS}} s + 1} \tag{4.7}$$

This experimental time constant, $\tau_{_{LS}}$ is equal to 0.018 seconds ($8.9Hz$). This model was derived empirically from the data shown in Figure 4.7, but it is similar to a pressure valve model derived analytically by Kappi and Ellman [61].

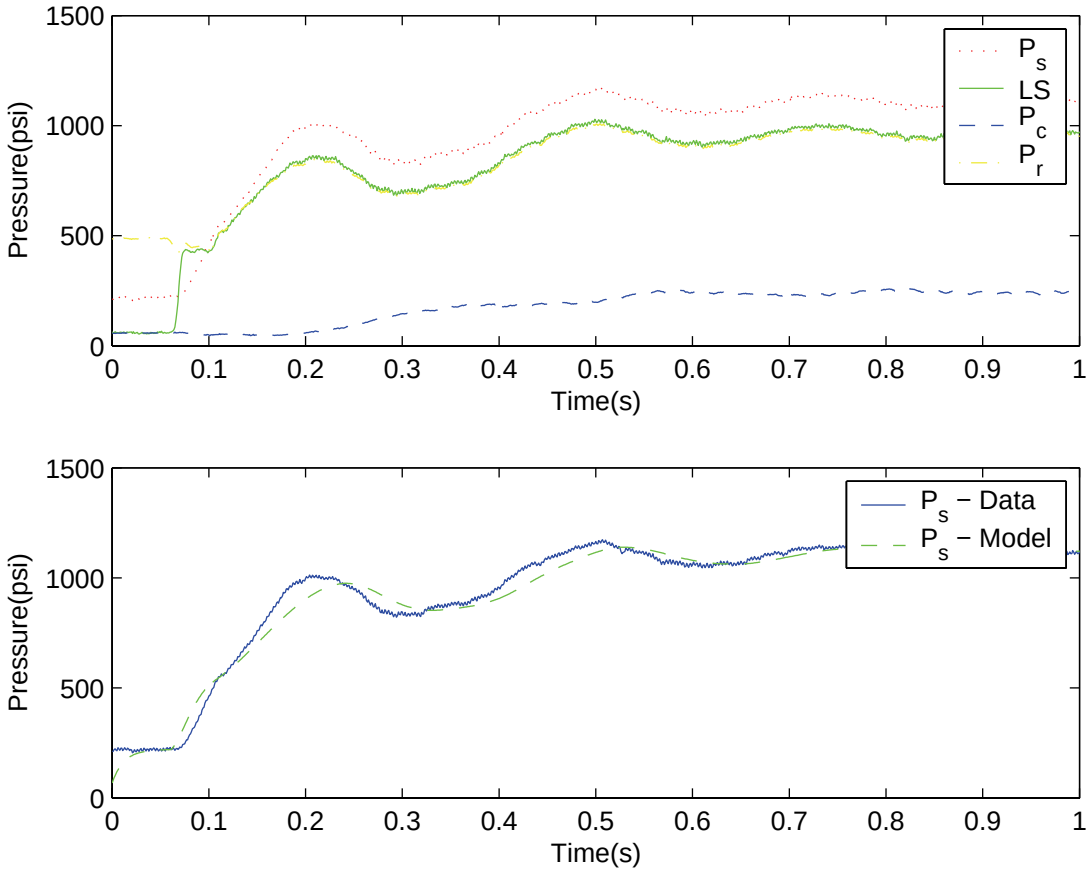

Figure 4.7: This plot shows the system pressure response to a negative step in boom input voltage. Notice how the P_{LS} jumps up to P_r and P_s builds up to a value offset from the P_{LS} pressure. The bottom plot compares the measured P_s to the value for P_s calculated from P_r and the dynamic model.

4.2.2.2 Constant Pressure Regulation

The relief value located inside the Sauer-Danfoss PVG-32 assembly can be converted into a constant pressure relief valve by replacing a plug/orifice with a plug that blocks off the load-sensing network. In this configuration, the main pressure relief valve located inside the PVG-32 valve assembly maintains the pressure below a manually adjustable constant value. This also enables an external pressure valve to control the main pressure. When both the internal and external pressure relief valves shown in Figure 4.8 are installed at the same time, only the one with the lower pressure setting has any affect on the system pressure.

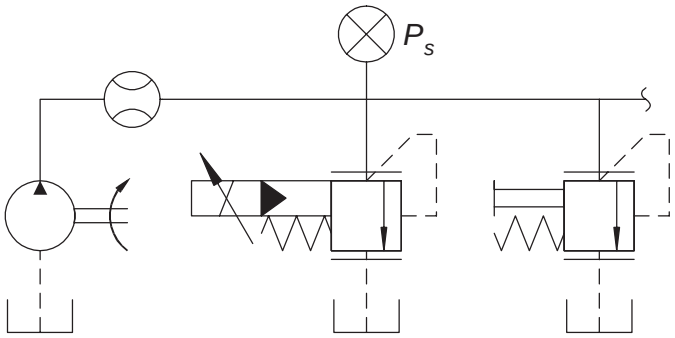

Figure 4.8: The relief valve on the left is the external electro-proportional relief valve. The second relief valve is the same relief valve shown in Figure 4.1 that is built into the PVG-32 assembly; however, in this diagram the load-sensing is disabled. With both relief valves installed, the valve with the lower setting will control the system pressure.

4.2.2.3 Electro-proportional Regulation

Electronic load-sensing pressure control can be achieved using the external electro-hydraulic pressure relief valve shown in Figure 4.8. This adds flexibility to how the main system pressure is controlled. For example, the pressure minimum can be set such that the pilot pressure is high enough to assure maximum spool responsiveness. It also allows pressure to be built up or held constant while the spool is moving through the dead-band. These changes in how the pressure is controlled can improve the responsiveness of these valves. At the same time, the energy efficiency is still better than if the system pressure was held at a constant value. Using the electro-proportional relief valve enables the system pressure to be varied for efficiency without sacrificing smoothness or responsiveness.

4.3 Pump Pressure Control

From an efficiency and heat generation point of view it is important to vary the pump pressure. The hydro-mechanical load-sensing is a convenient way to control the pump pressure based on the need of the system. However, it also creates dynamic coupling that can be driven unstable under feedback control. This coupling can be seen graphically in Figure 4.9. While the load-sensing pressure compensator is itself a mechanical feedback system, it was designed to run under open-loop control in the sense that it would receive a signal from a joystick and the input to the valve would not be varied by any kind of position, velocity or flow data.

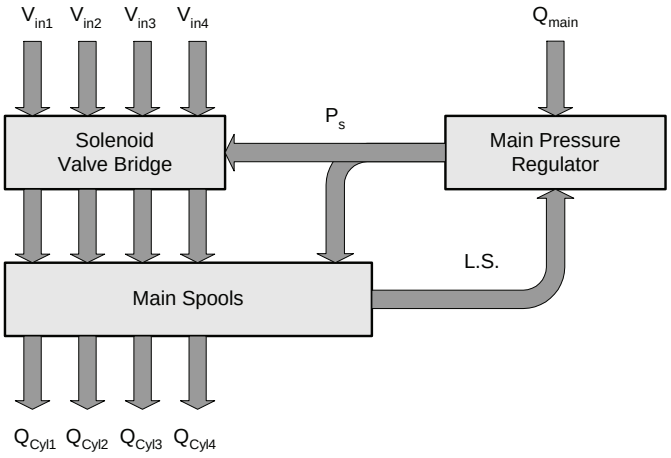

Figure 4.9: Block diagram of the hydro-mechanical load-sensing pressure regulator built into the PVE/PVG32 assembly.

4.3.1 Dynamic Coupling

A deeper understanding is possible by modeling the pump and cylinder states, linearizing and putting in state-space form. In this model it is assumed that the cylinder is retracting and receiving flow from the pump on the rodside of the cylinder. If this was the boom degree of freedom, this would correspond to raising the boom with all other functions not moving. For the following equations this would mean that θ was

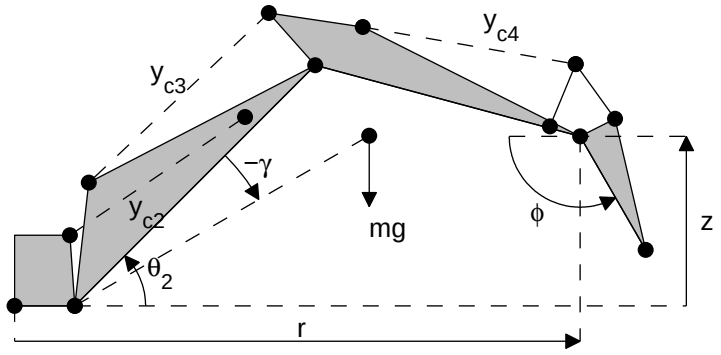

Figure 4.10: Cylinder-space and task-space variables. The centroid and gravitational force is also shown for the last three links assuming the third and fourth cylinders are locked.

equal to the boom joint angle, θ_2 and x_c was equal to the boom cylinder length, y_{c_2} (Figure 4.10). To skip the details of the derivation go to Equations 4.37 - 4.43.

Starting with the generalized rigid body equation.

$$J\ddot{\theta} + G(\theta) = \tau = \frac{\partial x_c}{\partial \theta} F_c \tag{4.8}$$

Note that the joint torque, τ, can be related to cylinder force, F_c, via the joint angle to cylinder length Jacobian [70, 130]. For a single degree of system, the Coriolis and centrifugal term, $V(\theta, \dot{\theta})$, is 0 because the kinetic energy is not a function of the generalized coordinate, θ. An equivalent mass in the cylinder domain, M_{eq}, can be found by expressing the kinetic energy, KE, in terms of the time derivatives of both θ and x_c.

$$KE = \frac{1}{2} J \dot{\theta}^2 = \frac{1}{2} J \left(\frac{\partial \theta}{\partial x_{cyl}} \dot{x}_{cyl} \right)^2 = \frac{1}{2} M_{eq} \dot{x}_{cyl}^2 \tag{4.9}$$

Using cylinder-space variables, Equation 4.8 becomes

$$M_{eq} \ddot{x}_{cyl} = -\frac{\partial \theta}{\partial x_{cyl}} G(\theta(x_{cyl})) + F_{cyl} \tag{4.10}$$

$$G(x_{cyl}) = mgl \cos(\theta(x_{cyl}) + \alpha) \tag{4.11}$$

$$F_{cyl} = \frac{\partial \theta}{\partial x_{cyl}} \tau = A_c P_c - A_r P_r - sign(\dot{x}_{cyl}) F_{Coul} - b_v \dot{x}_{cyl} \tag{4.12}$$

Combining Equations 4.10 - 4.12.

$$M_{eq} \ddot{x}_{cyl} = -\frac{\partial \theta}{\partial x_{cyl}} mgl \cos(\theta(x_{cyl}) + \alpha) + A_c P_c - A_r P_r + F_{Coul} - b_v \dot{x}_{cyl} \tag{4.13}$$

Hydraulics:

$$Q_c = K_{sp}(x_{sp}) \sqrt{P_c} \tag{4.14}$$

$$Q_r = -K_{sp}(x_{sp}) \sqrt{P_s - Pr} \tag{4.15}$$

$$\begin{aligned} \dot{P}_c &= \tfrac{B_e}{V_c} \left(-A_c \dot{x}_{cyl} + Q_c \right) \\ &= \tfrac{B_e}{V_c} \left(-A_c \dot{x}_{cyl} + K_{sp}(x_{sp}) \sqrt{P_c} \right) \end{aligned} \tag{4.16}$$

$$\begin{aligned} \dot{P}_r &= \tfrac{B_e}{V_r} \left(A_r \dot{x}_{cyl} + Q_r \right) \\ &= \tfrac{B_e}{V_r} \left(A_r \dot{x}_{cyl} - K_{sp}(x_{sp}) \sqrt{P_s - Pr} \right) \end{aligned} \tag{4.17}$$

Spool Model

$$\frac{X_{sp}(s)}{V_{in}(s)} = \frac{\omega_n^2}{s^2 + 2\zeta\omega_n s + \omega_n^2} \tag{4.18}$$

$$K(x_{sp}) = k_{sp}(x_{sp} - \Delta_{sp} sign(x_{sp}) \tag{4.19}$$

where Δ_{sp} is the dead-band of the spool. For the retracting case

$$K(x_{sp}) = k_{sp}(x_{sp} + \Delta_{sp}) \tag{4.20}$$

System pressure and load-sense pressure equations while system is retracting.

$$\frac{P_{LS}(s)}{P_r(s)} = \frac{1}{\tau_{_{LS}} s + 1} \tag{4.21}$$

$$\frac{P_s(s)}{P_{LS}(s) + P_{margin}} = \frac{1}{\tau_{_{P_s}} s + 1} \tag{4.22}$$

For a given $\bar{x}_{cyl}$ and $\dot{\bar{x}}_{cyl}$ it is possible to find the rest of the equilibrium states.

$$\dot{P}_c = 0 \Rightarrow 0 = -A_c \dot{\bar{x}}_{cyl} + K_{sp}(\bar{x}_{sp}) \sqrt{\bar{P}_c} \tag{4.23}$$

$$\dot{P}_r = 0 \Rightarrow 0 = A_r \dot{\bar{x}}_{cyl} - K_{sp}(\bar{x}_{sp}) \sqrt{P_{margin}} \tag{4.24}$$

$$\ddot{x}_{cyl} = 0 \Rightarrow 0 = -\frac{\partial \theta}{\partial x_{cyl}} mgl \cos(\theta(x_{cyl}) + \alpha) + A_c P_c - A_r P_r + F_{Coul} - b_v \dot{x}_{cyl} \tag{4.25}$$

With the three unknowns being $\bar{P}_c$, $\bar{P}_r$ and $K_{sp}(\bar{x}_{sp})$, Equations 4.23 - 4.25 can be solved numerically. The rest of the equilibrium states can be solved from these quantities.

$$K_{sp}(\bar{x}_{sp}) = k_{sp}(\bar{x}_{sp} + \Delta_{sp}) \tag{4.26}$$

$$\dot{\bar{x}}_{sp} = 0 \tag{4.27}$$

$$\bar{V}_{in} = \bar{x}_{sp} \tag{4.28}$$

$$\bar{P}_{LS} = \bar{P}_r \tag{4.29}$$

$$\bar{P}_s = \bar{P}_r + P_{Margin} \tag{4.30}$$

The equations of motion can be linearized about this equilibrium point resulting in the following state equations.

$$
\begin{aligned}
M_{eq}\ddot{\tilde{x}}_{cyl} &= \tfrac{\partial\theta}{\partial x_{cyl}}(\bar{x}_{cyl})mgl\sin(\bar{\theta}+\alpha)\tfrac{\partial\theta}{\partial x_{cyl}}(\bar{x}_{cyl})\tilde{x}_{cyl} - b_v\dot{\tilde{x}}_{cyl} + A_c\tilde{P}_c - A_r\tilde{P}_r \\
\ddot{\tilde{x}}_{cyl} &= \tfrac{mgl}{J}\sin(\theta(\bar{x}_{cyl})+\alpha)\tilde{x}_{cyl} - \tfrac{b_v}{M_{eq}}\dot{\tilde{x}}_{cyl} + \tfrac{A_c}{M_{eq}}\tilde{P}_c - \tfrac{A_r}{M_{eq}}\tilde{P}_r
\end{aligned} \tag{4.31}
$$

$$
\ddot{\tilde{x}}_{sp} = -\omega_n^2\tilde{x}_{sp} - 2\zeta\omega_n\dot{\tilde{x}}_{sp} + \omega_n^2\tilde{V}_{in} \tag{4.32}
$$

$$
\dot{\tilde{P}}_s = \frac{1}{\tau_{P_s}}(-\tilde{P}_s + \tilde{P}_{LS}) \tag{4.33}
$$

$$
\dot{\tilde{P}}_{LS} = \frac{1}{\tau_{LS}}(-\tilde{P}_{LS} + \tilde{P}_r) \tag{4.34}
$$

$$
\begin{aligned}
\dot{\tilde{P}}_c &= -\mu_c A_c\dot{\tilde{x}}_{cyl} + \mu_c k_{sp}\sqrt{\bar{P}_c}\tilde{x}_{sp} + \tfrac{\mu_c K_{sp}(\bar{x}_{sp})}{2\sqrt{\bar{P}_c}}\tilde{P}_c \\
\mu_c &= \tfrac{B_e}{V_c}
\end{aligned} \tag{4.35}
$$

$$
\begin{aligned}
\dot{\tilde{P}}_r &= \mu_r A_r\dot{\tilde{x}}_{cyl} - \mu_r k_{sp}\sqrt{\bar{P}_s - \bar{P}_r}\tilde{x}_{sp} + \tfrac{\mu_r K_{sp}(\bar{x}_{sp})}{2\sqrt{\bar{P}_s-\bar{P}_r}}\left(\tilde{P}_r - \tilde{P}_s\right) \\
\mu_r &= \tfrac{B_e}{V_r}
\end{aligned} \tag{4.36}
$$

It is assumed that the orifice coefficient, K_{sp}, is linear with spool position, x_{sp}, when x_{sp} is outside of the dead-band region around zero. The tildes on the following state vector and the state variables represent that they are relative to the nominal values of the linearization. The nominal valves are denoted by over bars.

$$
\tilde{X} = [\tilde{x}_{cyl}\ \dot{\tilde{x}}_{cyl}\ \tilde{x}_{sp}\ \dot{\tilde{x}}_{sp}\ \tilde{P}_c\ \tilde{P}_r\ \tilde{P}_s\ \tilde{P}_{LS}]^T \tag{4.37}
$$

The linear state space equation is found by linearizing Equations 4.31 - 4.36 for a given position and velocity of the cylinder.

$$
\dot{\tilde{X}} = A\tilde{X} + B\tilde{V}_{in} \tag{4.38}
$$

where

$$A = \left[\begin{array}{cccccc|cc} 0 & 1 & 0 & 0 & 0 & 0 & 0 & 0 \\ c_1 & -\frac{b_v}{M_{eq}} & 0 & 0 & \frac{A_c}{M_{eq}} & -\frac{A_r}{M_{eq}} & 0 & 0 \\ 0 & 0 & 0 & 1 & 0 & 0 & 0 & 0 \\ 0 & 0 & -\omega_n^2 & -2\zeta\omega_n & 0 & 0 & 0 & 0 \\ 0 & -\mu_c A_c & \mu_c k_{sp}\sqrt{\bar{P}_c} & 0 & \frac{\mu_c K_{sp}(\bar{x}_{sp})}{2\sqrt{\bar{P}_c}} & 0 & 0 & 0 \\ 0 & \mu_r A_r & c_2 & 0 & 0 & c_3 & -c_3 & 0 \\ \hline \cdots & \cdots & \cdots & \cdots & \cdots & \cdots & \cdots & \cdots \\ \hline 0 & 0 & 0 & 0 & 0 & 0 & -\frac{1}{\tau_{P_s}} & \frac{1}{\tau_{P_s}} \\ 0 & 0 & 0 & 0 & 0 & \frac{1}{\tau_{LS}} & 0 & -\frac{1}{\tau_{LS}} \end{array}\right] \tag{4.39}$$

where

$$c_1 = \frac{mgl}{J}\sin(\theta(\bar{x}_{cyl}) + \alpha) \tag{4.40}$$

$$c_2 = -\mu_r k_{sp}\sqrt{\bar{P}_s - \bar{P}_r} \tag{4.41}$$

$$c_3 = \frac{\mu_r K_{sp}(\bar{x}_{sp})}{2\sqrt{\bar{P}_s - \bar{P}_r}} \tag{4.42}$$

$$B = \left[\begin{array}{cccccccc} 0 & 0 & 0 & \omega_n^2 & 0 & 0 & 0 & 0 \end{array}\right]^T \tag{4.43}$$

In this state vector the first six states are associated with the specific cylinder and the last two are associated with the pump pressure. The pump pressure states are coupled to the dynamics of the cylinders in two ways. The first is through the port pressure receiving flow from the pump. In general when multiple functions are used, this ties the pump directly to the pressures of all the ports receiving flow from the pump. For the one cylinder case shown in Equation 4.39 this coupling is shown by the coefficient "$-c_3$." The other coupling is from the port pressure that is driving the load-sensing state. This is shown in Equation 4.39 by the "$1/\tau_{LS}$" term.

This means that if the pressure driving the load-sensing pressure causes P_s to change, then both the port pressures and spool positions have to change in order to maintain the desired cylinder motion. This is troublesome if the port pressure driving the load-sensing becomes oscillatory. The closed-loop bandwidth of the spool is also slower than the speed of the pressure change.

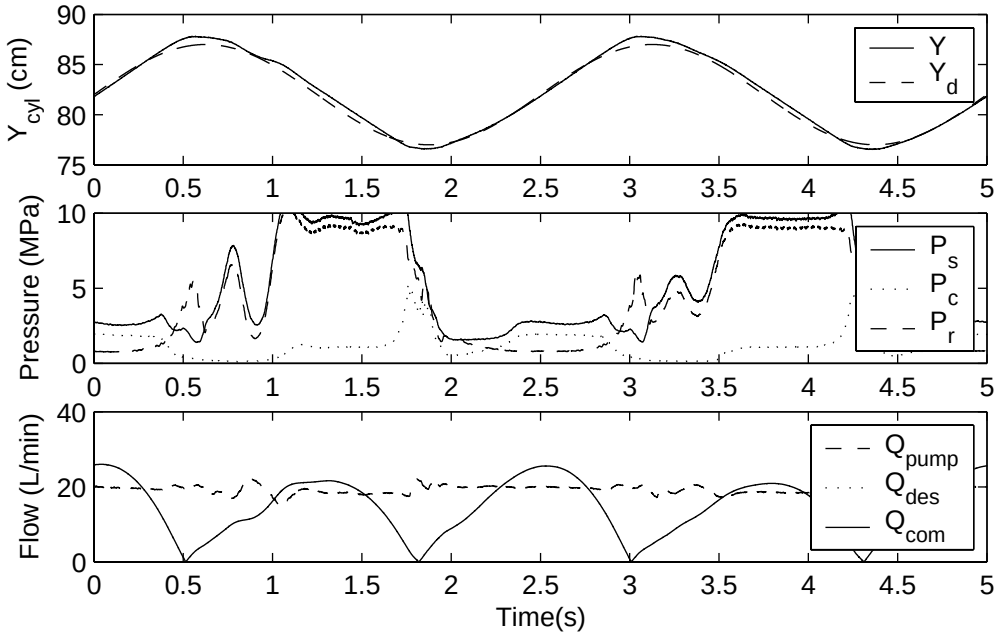

Figure 4.11: Hydro-mechanical loading-sensing pressure regulation.

This problem is demonstrated by the data in Figure 4.11. The boom is given a sine trajectory. Y and Y_d are the actual and desired cylinder lengths. P_s, P_c and P_r are system, capside and rodside pressures. When the pressure needs to increase for the boom to rise (cylinder retract), both the rodside pressure and pump pressure begin to oscillate together. This could potentially destabilize other functions if they were being used.

One possible method to deal with this problem would be to design a robust controller that accounted for variation in the system's coupled dynamics. An example of applying linear MIMO robust control to a complex hydraulic system is presented in

Zhang et al. [154]. In comparison, the strategy utilized in this paper aims to decouple the pump pressure from the port pressures of the proportional flow valves. One way to nearly eliminate part of this coupling is to use pressure compensators [111]. As long as the pump pressure remains high enough, the pressure drop across the orifice receiving flow from the pump remains constant regardless of pump pressure because the pressure compensator will maintain a constant pressure drop across the control orifice regardless of pump pressure. This removes both the "c_3" and "$-c_3$" terms from Equation 4.39 and replaces the $P_s - P_r$ in c_2 and c_3 with a near constant pressure drop.

How the coupling between the port pressure driving the load-sense and the pump pressure is removed is discussed in Section 4.3.4. The first step is to replace the hydro-mechanical load-sensing system with an electro-proportional regulator.

4.3.2 Cylinder Position Control

One controller design, proposed by Sepehri et al. [121], that can be applied to proportional valves incorporates a nonlinear feedforward term and a PD control law. The line pressures are measured and the desired flow is calculated from the desired cylinder speed. These variables are used to calculate the desired orifice size which corresponds to a desired spool position. It is important that the line pressures are used in this calculation. The feedforward term is used to get the valve close to the desired spool position and the PD term forces the system to track the desired velocity and position. A similar form of this controller was later used by Tafazoli et al. [120, 133] and Johnson et al. [59].

Ideally it would be possible to directly control the velocity of each cylinder. Similar to many other proportional directional control valves, the input to the valves used in this system actually corresponds to a steady-state spool position. An internal feedback loop controls the spool position using a PWM regulated solenoid valve

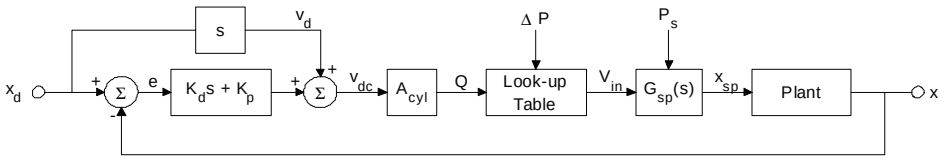

Figure 4.12: Cylinder position controller block diagram.

bridge (Figure 4.3). Spool position feedback is supplied from a LVDT (Linear Variable Differential Transformer). Currently, the spool position measurement is only available externally on one of the PVE electronic spool control modules and is only used for monitoring. The spool position determines an orifice size that controls the flow between each port and either tank or the pressurized main gallery. The general block diagram of the proposed controller is shown in Figure 4.12. This control has several important features including:

1. A feedforward term, $v_d = \dot{x}_d$, is used to minimize the control effort generated by the feedback error signal. This term essentially supplies the nominal cylinder velocity needed to follow the desired trajectory.

2. PD control to reject position and velocity error.

3. Look-up table to find the desired spool position command (V_{in}) that will produce the flow corresponding to the desired corrected cylinder velocity ($v_{dc} = v_d + k_d\dot{e} + k_p e$).

Finding the desired spool position (V_{in}) requires knowing the desired flow as well as the pressure drop across the port being controlled. This is represented by the ΔP input into the look-up table. If pressure compensators are installed, then the pressure drop, ΔP, is constant and the input, V_{in} can be calculated using only the required flow, Q. Similarly, main system pressure, P_s, is an input into the spool dynamics block ($G_{sp}(s)$) because P_s affects the response of this controller.

Spool dead-band will limit the ability of a system to track an input profile. However, if the controller is designed correctly it will always track as well as possible and will maintain system stability when crossing through the dead-band. It is also desirable that the controller is robust to a variety of uncertainties including: oil temperature, orifice modeling error, spool dynamics, pressure regulator dynamics and the mass/inertia of the manipulator. This controller will actually be implemented as a multi-rate system because the spool position control loop (Figure 4.3) has a fixed 40Hz update rate and the outer cylinder velocity control loop (Figure 4.12) will run at $1000Hz$.

4.3.3 Flow Limiter

Another factor that can destabilize pump pressure under feedback control is the amount of flow being commanded by the proportional valves. This is because a minimal amount of flow needs to be bypassed through the pressure relief valve and pressure reducing valve in order for the relief valves to maintain system pressure. Bypass flow is the difference between the pump flow and the flow being diverted to the proportional valves. The relief valve can only regulate pressure if there is flow going through it.

Typically feedback control is not used to control mobile equipment. This means that if more flow is commanded than what is available, the flow will naturally be sent to the lower pressure circuits and nothing bad happens. At some point the system's maximum flow could be reached even with a larger constant displacement pump or a larger variable displacement pump. With position based feedback control, the cylinder being starved of flow will slow down even as input or commanded flow to that cylinder increases. This causes the proportional valve to create a large metering orifice. Then once pump pressure is able to build up this cylinder would jump due to the large metering orifice and a sudden increase in pump pressure. If the pump pressure was

being controlled using a load-sensing scheme, this sudden motion would cause a jump in port pressure that would be fed in the pump pressure via the load-sensing network.

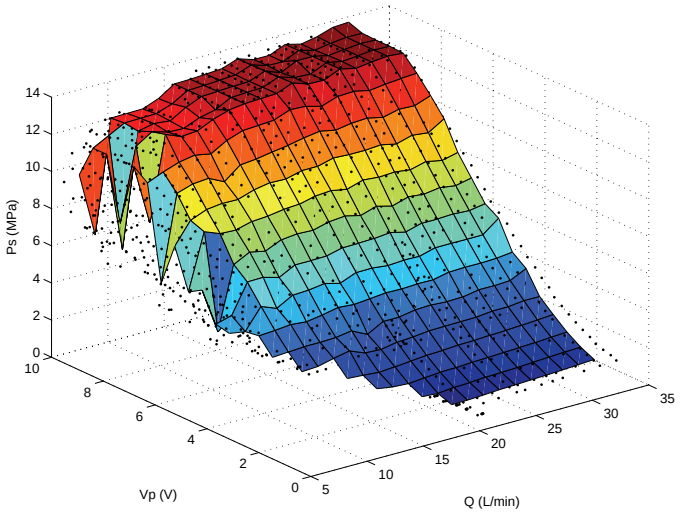

Figure 4.13: This 3D-surface shows system/pump pressure as a function of input voltage and bypass flow. Notice how the pressure drops off at low flow regardless of input.

One addition to the control strategy described in the previous section that is necessary for closed-loop control is a flow limiting or flow allocating algorithm. Voltage input to the electro-proportional relief valve is plotted versus bypass flow and achieved system pressure in Figure 4.13. At lower flows the valve is not able to maintain system pressure.

As can be seen in Figure 4.14 the pressure relief valve does a good job of maintaining system pressure for a given input at bypass flow above 10L/min (2.6GPM). Below this value, the pressure drops off sharply. This means that flow allocated to the actuators must be limited in order to assure the pressure regulator can work properly.

The need for this type of flow limiting control is demonstrated by the boom cycles in Figure 4.15. Y and Y_d are the actual and desired cylinder lengths. P_s, P_c and P_r are system, capside and rodside pressures. Q_{pump}, Q_{des} and Q_{com} are pump flow, desired flow from pump to cylinder and commanded flow from pump to cylinder. While the

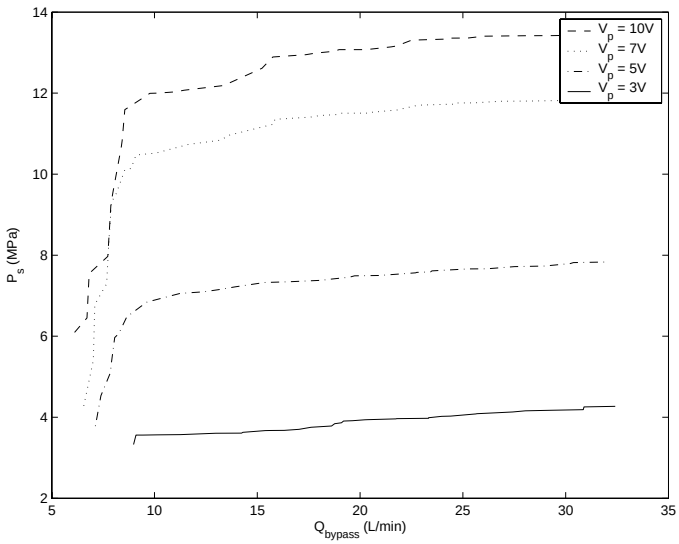

Figure 4.14: System pressure vs. bypass flow for constant pressure valve inputs.

cylinder is retracting (boom rising) pressure must be maintained in order to overcome gravity. On the other hand, when the cylinder is extending (boom lowering) pressure drops to less than half of the commanded value. This is not a problem for single degree-of-freedom motion; however, this is problematic if another degree-of-freedom requires this pressure and the boom motion is bleeding off the flow/pressure. A solution to this problem is to limit the total flow being sent to the cylinders. This is shown in Figure 4.16. Tracking is greatly reduced since this limits cylinder velocity, but note the improved pressure regulation.

A similar response without flow limits is shown for the original hydro-mechanical regulator is shown in Figure 4.17 and with the electronic load-sensing regulator in Figure 4.18. An additional benefit of the electronic load-sensing control is that the pressure state seems to be more stable. Figure 4.19 shows the electronic regulator with low pump flow and flow limited control. This assures that enough system pressure is maintained in order to guarantee proper pressurization of the pilot pressure and maximum spool responsiveness. Note how the pressure never falls below 3.5MPa (500psi).

Figure 4.20 shows the same response with high pump flow. This means the flow limiting control is not as active. Note the smaller deviations between desired cylinder flow (dotted line) and commanded cylinder flow (solid line). This means that there is relatively good tracking since more flow is allocated to the cylinders and pressure is maintained since a proper amount of flow is always being bypassed through the relief valve.

The end goal is to achieve a smooth and responsive multi-degree-of-freedom control using a haptic manipulator. Being able to maintain system pressure is necessary to achieve this goal. Maintaining pressure keeps the spool pilot line pressurized and stops oscillatory behavior caused by system pressure falling and then building back up. Limiting flow does cause the response to deviate from the desired command coming from the haptic interface. However, it is better to proportionally scale back all the commands and maintain smooth motion than allow system pressure to oscillate as the bypass flow dips below the critical value.

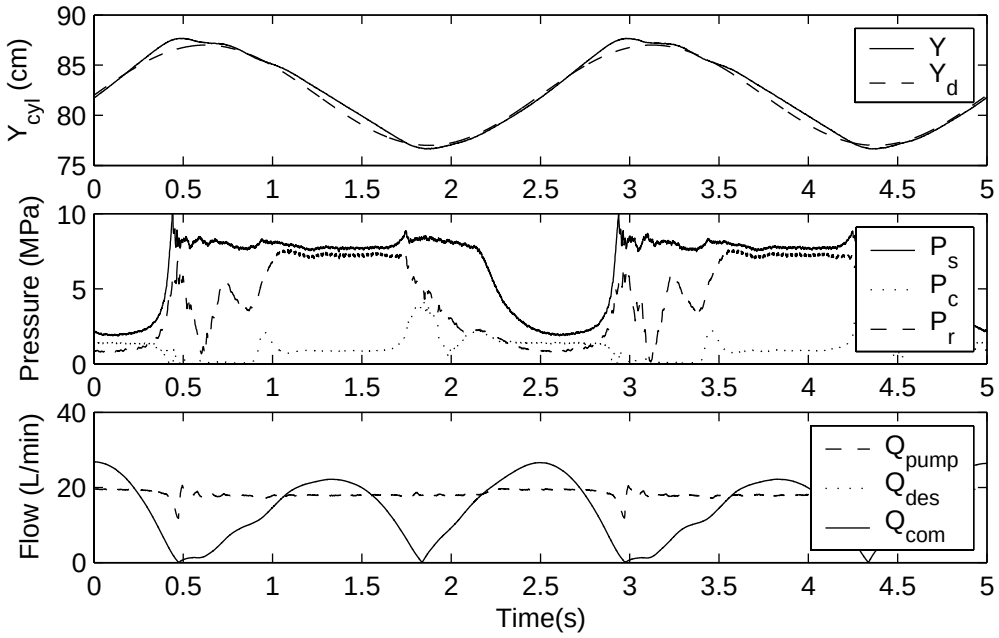

Figure 4.15: Constant system pressure command with low pump flow and no flow limiter.

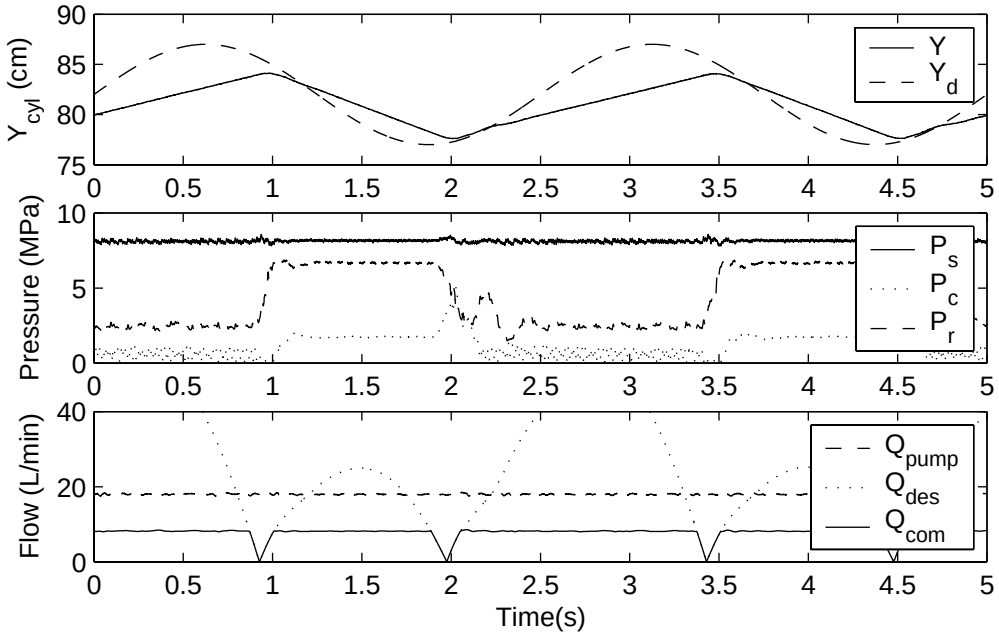

Figure 4.16: Constant system pressure command with low pump flow and flow limited motion.

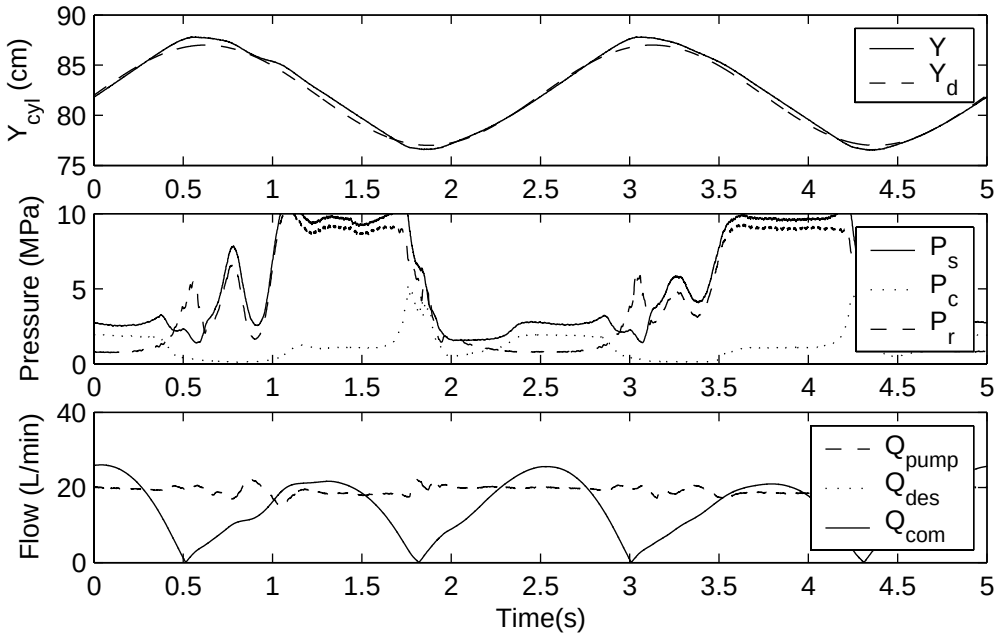

Figure 4.17: Hydro-mechanical loading-sensing pressure regulation with low pump flow and no flow limiter.

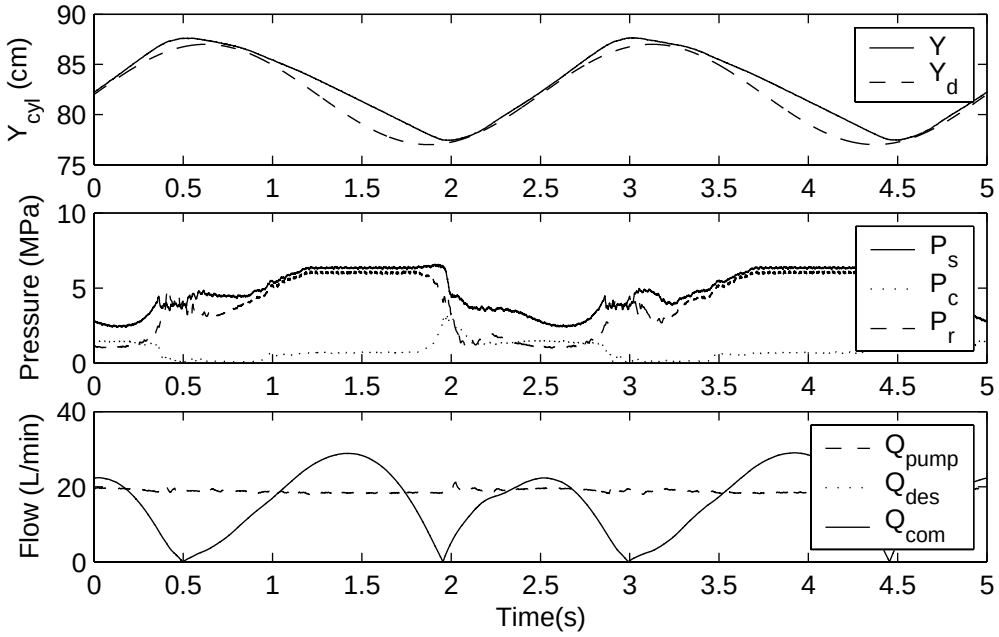

Figure 4.18: Electronic loading-sensing pressure regulation with low pump flow and no flow limiter.

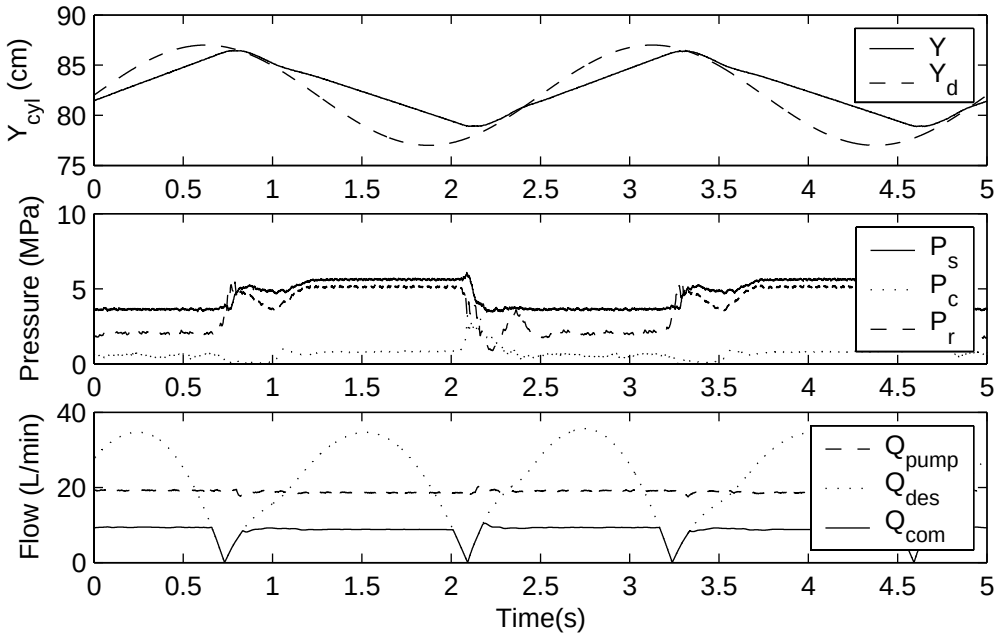

Figure 4.19: Electronic loading-sensing pressure regulation with low pump flow and flow limited motion.

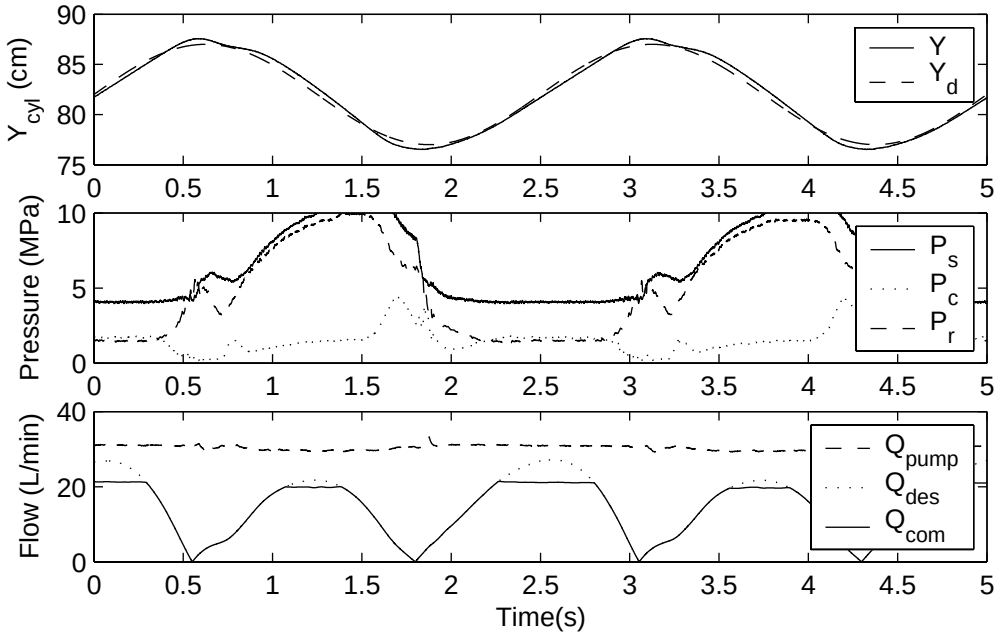

Figure 4.20: Electronic loading-sensing pressure regulation with high pump flow and flow limited motion.

4.3.4 Max Pressure Filter

How the system pressure is controlled can play an important role in both energy consumption and system stability. Using a constant displacement pump and relief valve is not a very efficient setup, but they are common on smaller backhoes and mini-excavators due to their low cost and compact size. A major source of inefficiency is the throttling loss of the relief valve. The power loss is the product of the bypass flow through the valve and the system pressure. Since the flow can not be adjusted, it is desirable to vary the system pressure based on the need of the proportional valves. The pressure needed by the proportional valves can also be lowered by cutting the spools in an asymmetric fashion based on the average load and the geometry of the asymmetric cylinders.

A hydro-mechanical load-sensing pressure valve was originally used to control pump pressure. In principle this type of system works the same as a typical load-sensing system where pressure is fed back to control the flow, or swash plate angle, of a variable displacement pumps. For a review of work on load-sensing systems see Wu et al. [147]. In this system, the pressure relief valve maintains a pressure margin between the system pressure and the highest pressure of the ports receiving flow from the pump. This pressure feedback is triggered by the position of the spools and a series of shuttle valves picks the highest pressure in Figure 4.1.

As discussed in Section 4.3.1, the primary draw back is that the system is always coupled to one of the port pressures. This means that oscillation in one function is fed into the other functions. This also introduces complex dynamic interactions that can be driven unstable by feedback control. Another draw back is that at times the PVES spool control modules shown in Figure 4.4 is starved of pressure. In addition to supplying the pressure being used by the proportional spools, it also supplies pressure to a reducing valve that regulates pressure going to the PVES modules. When this happens the spools cannot be moved as fast and the dynamics slow down.

This compounds the delay associated with the spools moving through the dead-zone region.

One solution is to use a relief valve with a constant pressure setting. While this solution improves the dynamics response of the system it does so at the expense of efficiency and system temperature. An alternative is to use an electro-proportional relief valve. This enables the controller to decouple these states while still using the port pressure information to set the pump pressure. The merit of such a strategy is motivated by Section 4.3.1. The method presented here uses a Moving-Window-Max-Filter (MWMF) to achieve the seeming conflicting goals of using port pressures to control pump pressure while dynamically decoupling these states.

$$P_{MWMF}(k) = max\{P_{LS}(k), \cdots, P_{LS}(k-N)\} \tag{4.44}$$

The P_{LS} in Equation 4.44 is the same as in Equation 4.7; however, it is calculated electronically in the controller so the time constant is essentially zero since the sampling time is $1000Hz$. In addition, the switch that sets P_{LS_i} equal to P_c, 0 or P_r is triggered by the desired flow, not the position of the spool. This means that pressure is building as the spool moves through the dead-band region. Computational resources including memory and comparisons can be minimized by splitting the window into subintervals. When the latest subinterval is full the oldest subinterval is dropped and a new one is started. This causes the exact length of the window to vary. The important thing is to always have the filter window wider than the period of any system oscillations.

Since it is a max function the high frequency component of an increase in desired pressure is not filtered out. However, if the port pressure driving the pump oscillates then the MWMF holds the desired pump pressure at the crest of the oscillation. Even though the load-sense pressure is oscillating, the MWMF removes most of the oscillations in the load-sense pressure from the system pressure. This is demonstrated

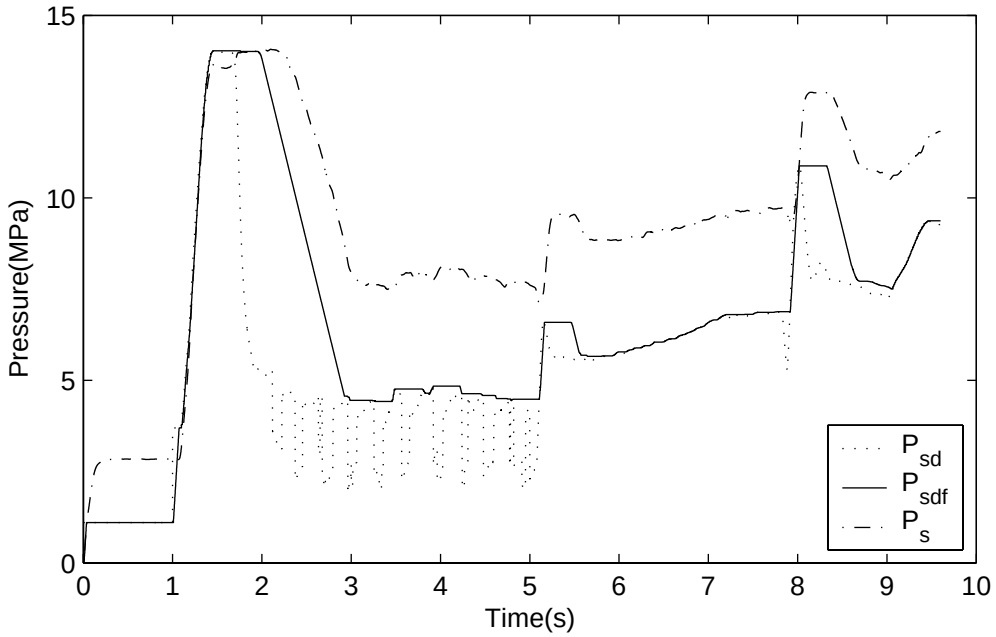

Figure 4.21: The dotted line is the original desired pump pressure signal generated from the port pressures without a pressure margin. Applying the MWMF to this signal removes the oscillations. The dashed line is the resulting supply pressure.

in Figure 4.21. A rate limiter is also used when the pressure is decreased. The downside is that pressure is held higher longer than it is actually needed. However, this is an acceptable compromise given that this enables the information to be used to vary the pressure. Figure 4.14 demonstrates that above a minimum bypass flow, the pressure primarily depends on input voltage. The pressure does increase a little with additional bypass flow. This is likely due to flow forces [98] changing the force balance of the spool.

Data of pressure valve voltage versus pump pressure and bypass flow is used to create a three dimensional map. This three dimensional map is represented using a neural network that is trained off-line. The inputs to the network are system pressure and bypass flow and the output is the voltage. The bypass flow is the difference between the pump flow which is measured and the flow being diverted to the proportional valves. Flow is measured using a HYDAC EVS 3100-1 impeller type

flow meter with a range of $6-60L/min$. Due to the engine speed range of the tractor and the constant displacement pump, the pump flow will stay between $15-35L/min$. The time constant of this flow meter is on the order of $50ms$. Since the data used to train the neural network is steady-state data, the time constant of the flow is not a factor. Even though bypass flow can be estimated, it is not used in the algorithm that calculates the pressure valve input because pressure spikes are fed through the flow meter. Doing so has a chaotic and destabilizing affect on the pressure control. Instead it is always assumed that only the minimum bypass flow set by the flow limiting control algorithm is passing through the relief valve. This still guarantees that the pump pressure is not lower than required.

The effectiveness of the MWMF is demonstrated using the trajectory in Figure 4.22. The trajectory is a right angle path in the $r-z$ plane in the workspace of the backhoe. The coordinates r and z are cylindrical coordinates that describe the motion of the wrist of the bucket relative to a reference frame located on the swing axis. These cylindrical coordinates r and z as well as the bucket angle, ϕ, and the cylinder length variables y_{c_2}, y_{c_3} and y_{c_4} are defined graphically in Figure 4.10. Since this desired path is described using task-space variables (r, z & ϕ), they must be mapped to joint-space variables and then to cylinder-space variables (y_{c_2}, y_{c_3} & y_{c_4}). Details on these mappings were presented in Chapter 3. The bucket angle, ϕ, is maintained at a constant angle measured from the horizontal plane. The swing is not used. This motion requires the boom, stick and bucket to move at the same time. Pressure compensators are used and the desired flow command is generated using the following control law.

$$Q = A_{c(r)} \left(\dot{x}_d - k_p \left(x_d - x_c \right) \right) \tag{4.45}$$

Where x_d is the desired cylinder position and x_c is the actual cylinder position. The proportional feedback gain is 5 and the time derivative of the desired position

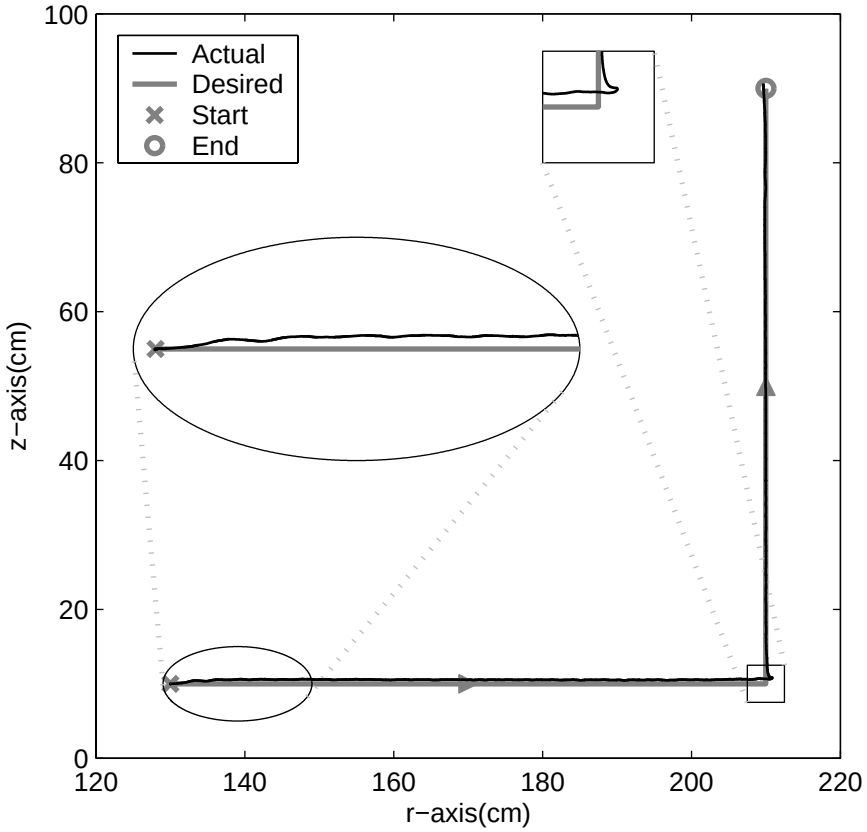

Figure 4.22: The trajectory is described in the workspace of the backhoe. Since the absolute bucket angle, ϕ, is held constant, the boom, stick and bucket must all work together.

is a feedforward term which is a partial plant inversion. The effect of the MWMF is shown in Figure 4.23 which shows data corresponding to the sharp change in direction in Figure 4.22. All three relevant cylinder lengths are shown. The pump pressure, P_s, and the two port pressures driving the electronic load-sense are shown. Before y_{c_2} starts to retract around 15.4 seconds, P_{r_3} is driving the load-sense and at this time the pressure driving the load-sense changes to P_{r_2}. Due to the sharp change in direction, P_{r_2} is oscillating after this transition. However, due to the MWMF this oscillation is not sent to the valve controlling P_s. It can be seen in the blown up box in Figure 4.22, that the motion of the backhoe overshoots, but is critically damped.

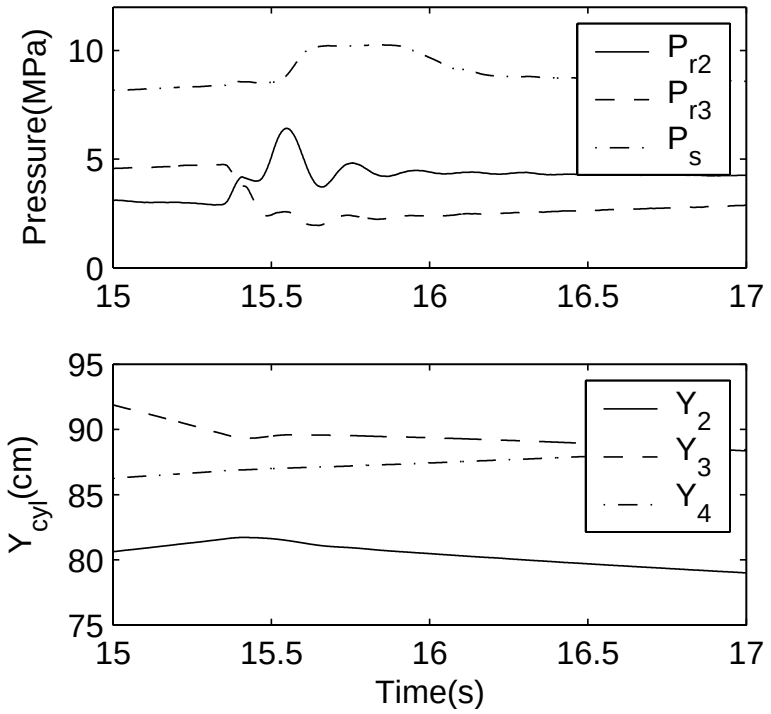

Figure 4.23: Cylinder position and pressure as the backhoe changes direction in Figure 4.22. Only the two port pressures driving the electronic load-sense are shown in the plot with pump pressure, P_s.

This demonstrates the effectiveness of the MWMF which is enabled by the flexibility of the electro-proportional relief valve. In comparison, pump pressure shown in Figure 4.11 has sustained oscillation in pump pressure, P_s, for a single degree of freedom sinusoidal trajectory. While Figures 4.22 and 4.23 show a sharp change in direction using three cylinders simultaneously there is no resulting oscillation in pump pressure. What this means is that the electronic load-sensing scheme is able to capture the strength of both the hydro-mechanical load-sensing scheme and the hydro-mechanical constant pressure scheme. It allows pump pressure to follow the demands of the system without the oscillations caused by the coupling of the port pressure and pump pressure in the hydro-mechanical load-sensing scheme.

4.4 Actuator Flow Control

The previous section addresses the issue of controlling of pump pressure. While this is very important, the end goal of the hydraulic system is to control the motion of the manipulator which is accomplished by controlling the flow going to and from the actuators. A brief description of the flow control was presented in Section 4.3.2; however, this was only designed to provided enough information to understand the experimental results related to the control of pump pressure. This section expands on this topic. One issue that is central to both the control of pump pressure and flow control is pressure compensation. Another issue that is central to accurate motion control is the ability of the system to produce the commanded flow. The effect of this on tracking performance is shown and a compensation technique is presented. A small input deadzone is proposed which is designed to prevent a limit cycle around zero velocity that is caused by the sandwiched dead-band and closed-loop control that include an inverse dead-band function[135]. This section is concluded with experimental results showing coordinated motion using the boom, stick and bucket cylinders.

4.4.1 Pressure Compensation

In the flow control strategy used in Figures 4.15 - 4.20, pressure was supplied to the spool directly from the pump pressure set by the relief valve. This hardware configuration is typical of many advanced controllers found for directional proportional valves found in the literature: differential-PWM pilot control for impendence control [129, 133], adaptive robust control [150] and passive control [76, 86]. An alternate hardware configuration is to use pressure compensators with the proportional spool valve. This is not a new concept [101], but is still a topic of research [3, 61, 146]. Using a pressure compensator maintains a near constant pressure across the spool orifice given that the difference between the pump pressure and port pressure is greater than

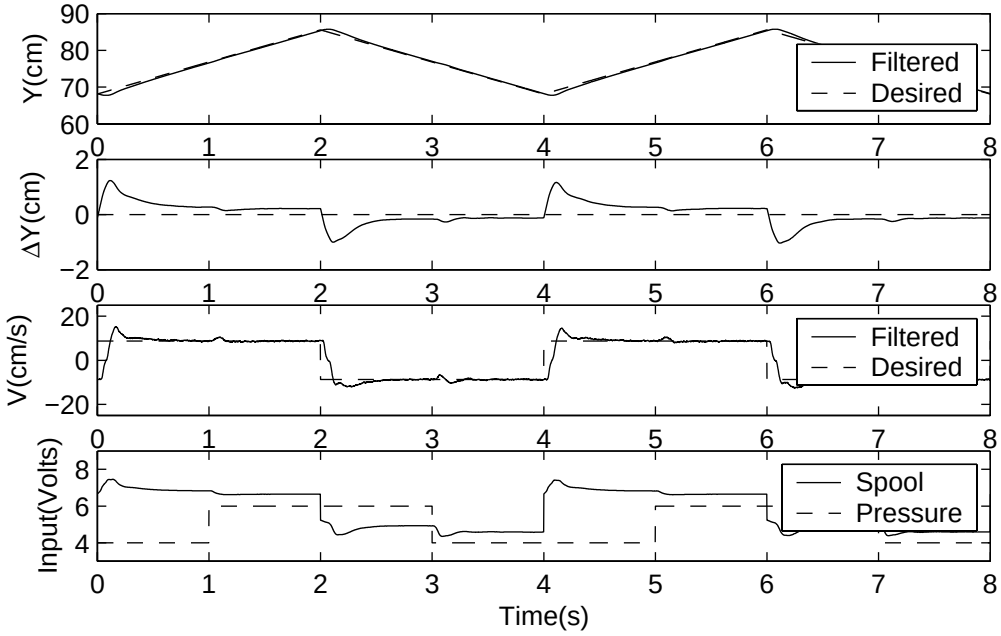

Figure 4.24: Response to saw-tooth input without a pressure compensator. Notice the small jumps in speed when the pressure input is changed also notice corresponding change in spool position.

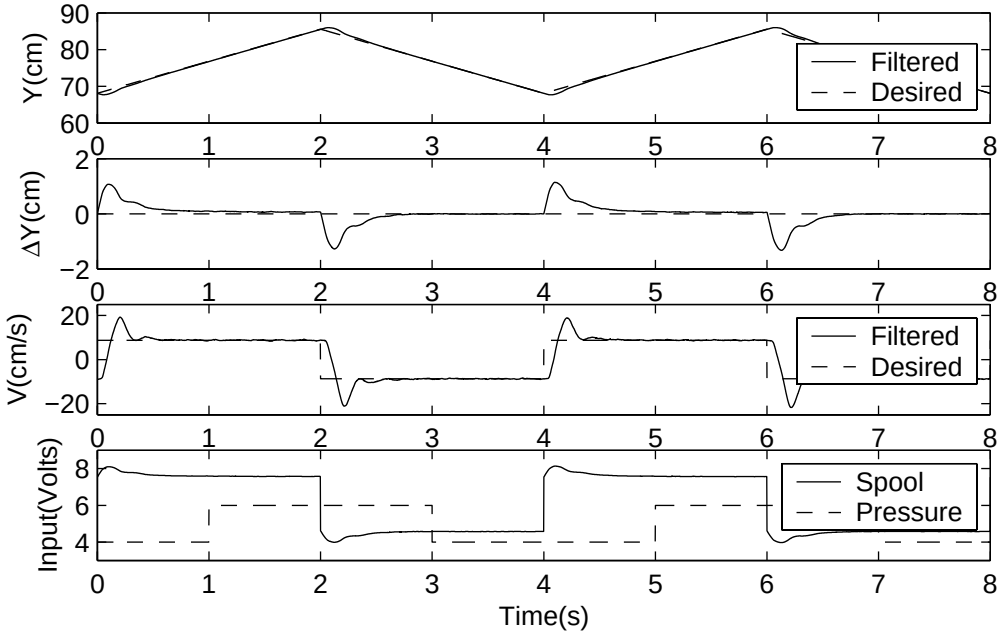

Figure 4.25: Response to saw-tooth input with a pressure compensator. There is no detectable change in either velocity or spool input when the pressure input is changed.

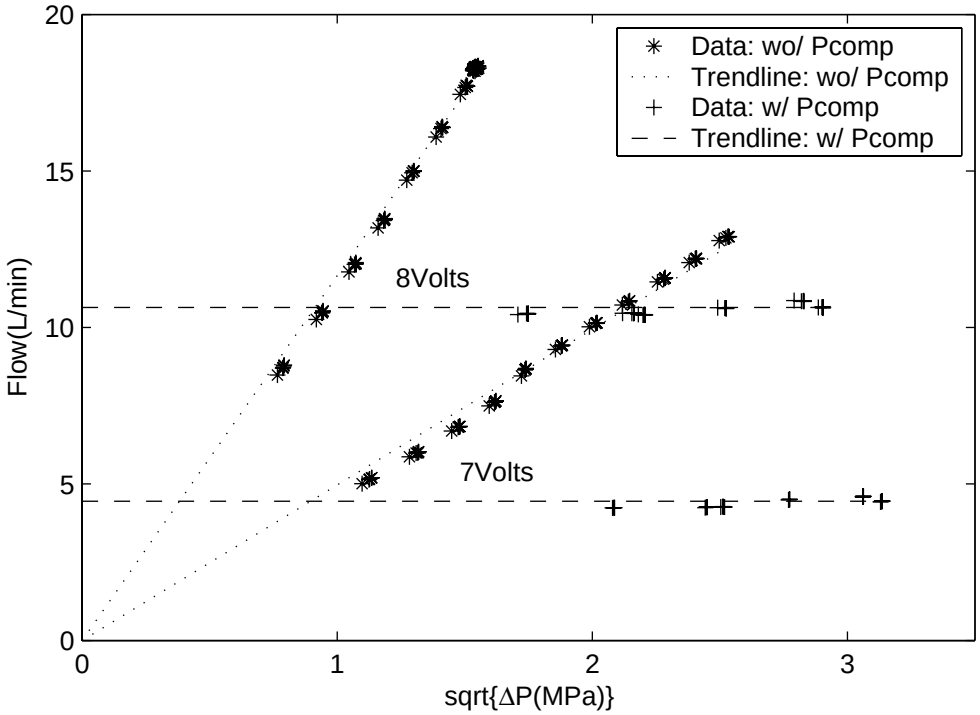

Figure 4.26: Flow control curves: The data in this plot was takin while the bucket cylinder is extending with input voltages equal to 7 and 8 Volts. Without the pressure compensators the relationship between flow and the square-root of pressure drop is linear as the orifice equation suggests. However, with the pressure compensator the flow is nearly constant above 1MPa (150psi) where the pressure compensator starts to regulate the pressure drop across the orifice.

or equal to this value.

In addition, to linearizing the relationship between spool position and flow, it can also improve the system's reaction to changes in pressure [146]. These changes in pressure can be a result of either changes in pump pressure or load changing the port pressure. This is demonstrated by Figure 4.24 - 4.25. In Figure 4.24 the system does not have pressure compensation. The input to the pump pressure (dashed line in fourth subplot) is given step changes in the middle of the ramp commands. This results in a disruption to the velocity as the spool's orifice size adjusts to compensate for the disturbance and change in pressure. In Figure 4.25 the same test is done with pressure compensators installed. The pressure compensators respond to the change

in pressure fast enough that there is no apparent change in either input or velocity. This implies that the dynamics of the pressure compensators are much faster than the closed-loop dynamics of the spool. This also implies a decoupling between P_s and the port pressure receiving flow from the pump. Alternatively, this removes "c_3" from the A-matrix in Equation 4.39. The only difference to the controller used in Figure 4.25 is that the desired flow is fed into a look-up table relating flow to input voltage. Figure 4.26 demonstrates the difference in flow versus the square-root of pressure differential, $\sqrt{P}$, for two different spool inputs. The pressure differential is defined as the pump pressure minus the port pressure receiving flow from the pump.

The data without pressure compensation is nearly linear when flow is plotted versus the square-root of $\sqrt{P}$. With the pressure compensators installed, the flow is essentially constant for different pressures. The trend lines were generated from the respective look-up tables used in the tests shown in Figure 4.24 - 4.25.

Without pressure compensators, the main spool operates with no restriction between the pump and spool (Figure 4.27). The relationship between flow, Q, and pressure drop across the orifice, ΔP, can be described using the orifice equation.

$$Q = C_d A_0 \sqrt{\frac{2}{\rho} \Delta P} \tag{4.46}$$

Where C_d is the discharge coefficient and A_0 is the orifice area. The combined term $C_d A_0$ is a function of spool position, x_{sp}, because the area and shape of the orifice change as the spool moves. As the temperature increases, density, ρ, will go down and C_d will go up due to a decrease in viscosity of the oil. Both of these will result in more flow for the same pressure drop.

As shown in Figure 4.28, there is an additional two-way valve between the pump and spool that acts as the pressure compensator. The principal behind the pressure compensator is similar to that of relief and reducing valves, the two most common types of pressure valves.

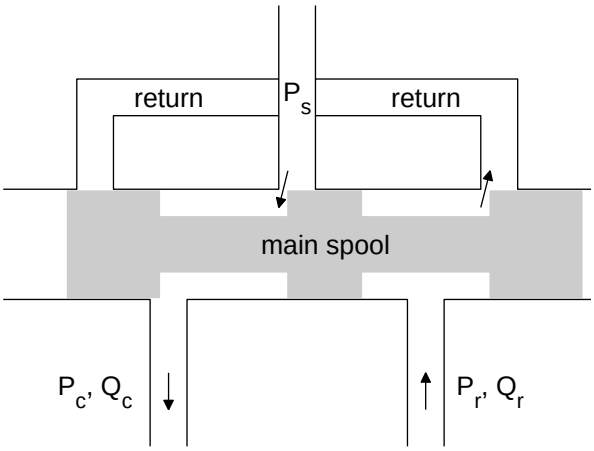

Figure 4.27: Valve without pressure compensator: Without a pressure compensator the main spool is fed with pressure directly from pump.

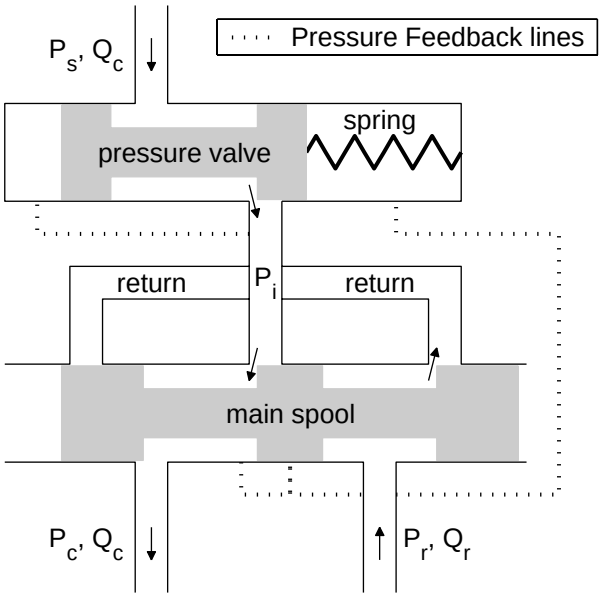

Figure 4.28: Valve with pressure compensator: The two pressure feedback lines are used to maintain a near constant pressure drop across the metoring orifice of the main spool.

$$F_0 - A_v P_i + A_v P_p + F_x = M_v \ddot{x}_v + K_e x_v \tag{4.47}$$

The governing equations of motion for a pressure compensator shown in Equation 4.47 is similar to those presented for a pressure relief valve in Merrit [101] and Manring [98]. The variable F_0 is the preload on the spool, A_v is the area of the spool, P_i is the intermediate pressure between the compensator and spool, P_p is the port pressure, F_x is the flow force, M_v is the mass of the pressure spool, K_e is equivalent stiffness and x_v is spool position. These valves are designed such that the primary forces dominating the steady-state position will be

$$F_0 = A_v \left(P_i - P_p\right) = A_v \Delta P \tag{4.48}$$

In other words, the nominal pressure differential across the main spool will be F_0/A_v. Change to flow, oil temperature and pressure across the pressure spool will only create a minor change in pressure drop across the main spool. Adding orifices in the pressure feedback lines is often necessary to add damping and stabilize the otherwise lightly damped dynamics of pressure valve [61, 101].

4.4.2 Velcoity/Flow Control Law

The primary goal of this hydraulic system is to control the motion of a manipulator. In this case, the object being controlled is the bucket of a backhoe. Kinematic mappings relate the position and orientation and their time derivatives to cylinder position and velocity and ultimately the flows produced by the valves. How the position and velocity is mapped as well as methods to deal with workspace limitations was discussed in Chapter 3. Even though the end goal is to have coordinated motion with haptic feedback, the focus here is on the hydraulic level speed control of the cylinders.

The general structure of the cylinder level is shown in Figure 4.29. A higher level controller will specify both cylinder position and velocity in the case of coordinated

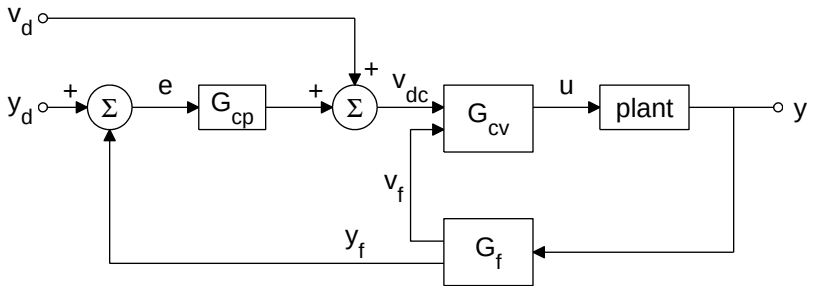

Figure 4.29: Block diagram of the overall control structure.

position mode or just velocity in the case of coordinated rate mode. It is assumed that both signals are available. If a proportional term is used the control law will be as follows.

$$v_{dc} = v_d + K_p\left(y_d - y\right) = \dot{y}_d + K_p\left(y_d - y\right) \tag{4.49}$$

Assuming the dynamics of the pressure compensator are significantly faster than the valve, it is possible to ignore the complex dynamics of the pressure compensator in the control design. Based on the test presented in Figure 4.24 - 4.25, this is a good assumption. This assumption is consistent with experimental and theoretical results presented by Wu et al. [146]. If v_{dc} is used to calculate the flow command the plant can be modeled as an integrator with second order dynamics.

$$G_p = \frac{Y(s)}{V_{dc}} = \frac{K_{flow}e^{-\tau s}}{s^3 + s^2 2\zeta/\omega_n + s} \tag{4.50}$$

In this equation, the gain F_{flow} is defined as the actual flow at steady state divided by the expected flow at steady-state.

$$K_{flow} \equiv \frac{actual \;\; steady-state \;\; flow}{expected \;\; steady-state \;\; flow} \tag{4.51}$$

In this transfer function $f_n = \omega_n/(2\pi) \approx 7Hz$, $\zeta \approx 0.7$ and $\tau = 1/80$ (half the PWM period). An approximation of the zero-order-hold in the s-domain is to add

a delay equal to half the sampling time [23]. The same approximation will be used here for the effect of the PWM in the s-domain. This transfer function was shown to be a good approximation if the pump pressure is sufficiently higher than the setting of the reducing valve feeding the PVES spool control modules (Figure 4.5).

The flow gain, K_{flow}, includes the uncertainty in commanded flow introduced by modeling error, variations in oil temperature and pressure. It will be assumed that $0 < K_{flow} < 1 + \Delta_{max}$. The pressure compensators will keep this gain close to unity. In the case where pump pressure can not be increased to maintain the pressure margin, the gain could drop significantly below 1. This limits the uncertainty to $-1 < \Delta < \Delta_{max}$ where $K_{flow} = 1 + \Delta$. If the pressure compensator is working properly and is sufficiently fast, then Δ_{max} should be closer to zero than one. Using the control law in Equation 4.49 and the plant transfer function in Equation 4.50, the steady-state error can be found using the final value theorem. If a constant velocity input (position ramp) is given to the system the equation for steady-state position error is as follows.

$$e_{ramp} = \frac{\Delta}{(1+\Delta)K_p} \tag{4.52}$$

If $K_{flow} = 1$ the system will perfectly track a ramp even though it is only a Type I system [30]. This is because the velocity feedforward term is producing the nominal input signal meaning that the error will be driven to zero by the position feedback.

While the pressure compensator does help limit Δ it would still be good to design a controller that can track velocity with zero steady-state position error even with $\Delta \neq 0$. One way to do this is to add integral action to G_{cp}. This has two drawbacks. First, it is necessary to implement a flow limiting controller to guarantee that the pressure relief valve regulating the pump pressure can work properly. The flow gain, γ, ranges between zero and unity (Figure 4.30). The gain is shared by all cylinder controllers in order to maintain the desire direction of velocity even if the magnitude

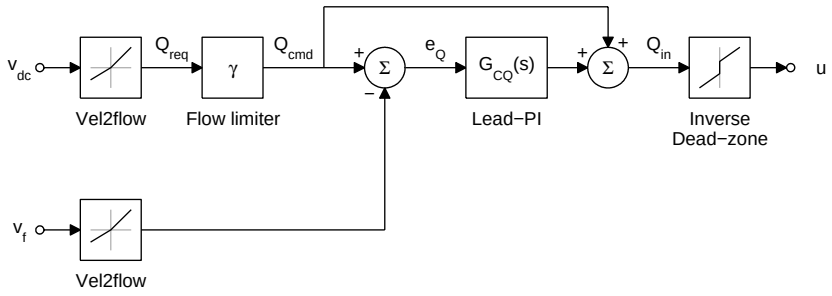

Figure 4.30: Block diagram of the velocity/flow control structure.

is not achievable. Second, it would be best not to integrate position error during constrained bucket motion. The alternative is to add integral action to G_{cv}. On this test-bed only position signals are available. The block G_f is a filter that estimates both position and velocity

$$G_{fy} = \frac{Y_f(s)}{Y(s)} = \frac{1}{s^2/\omega_f^2 + s2\zeta/\omega_f + 1} \tag{4.53}$$

$$G_{fy} = \frac{V_f(s)}{Y(s)} = \frac{s}{s^2/\omega_f^2 + s2\zeta/\omega_f + 1} \tag{4.54}$$

The compensator chosen was double lead-PI. Adding another pole at zero from the PI part of the compensator will assure that that the steady-state velocity error for a constant velocity command will be driven to zero error. The double-lead zeros are designed to cancel out the complex poles from the valve spools (Equation 4.50). This moves the start of the root locus paths heading towards the right half plane from the valve poles to the faster complex poles of the lead compensator (Figure 4.31). The transfer function of this double-lead-PI compensator is as follows.

$$G_{CQ} = K_Q \left(\frac{s^2/\omega_{zL}^2 + s2\zeta/\omega_{zL} + 1}{s^2/\omega_{pL}^2 + s2\zeta/\omega_{pL} + 1} \right) \left(\frac{s/\alpha_{PI} + 1}{s} \right) \tag{4.55}$$

Anti-windup was added to the integrator in order stop the valve input from being saturated. In order to facilitate the anti-windup algorithm [30], the PI part of this

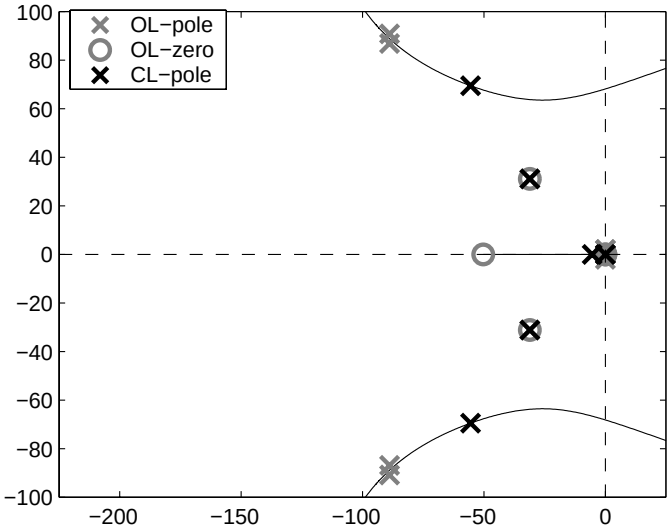

Figure 4.31: Root locus plot of dominant poles and zeros of the proportional valve, low-pass differentiator and lead-PI compensator.

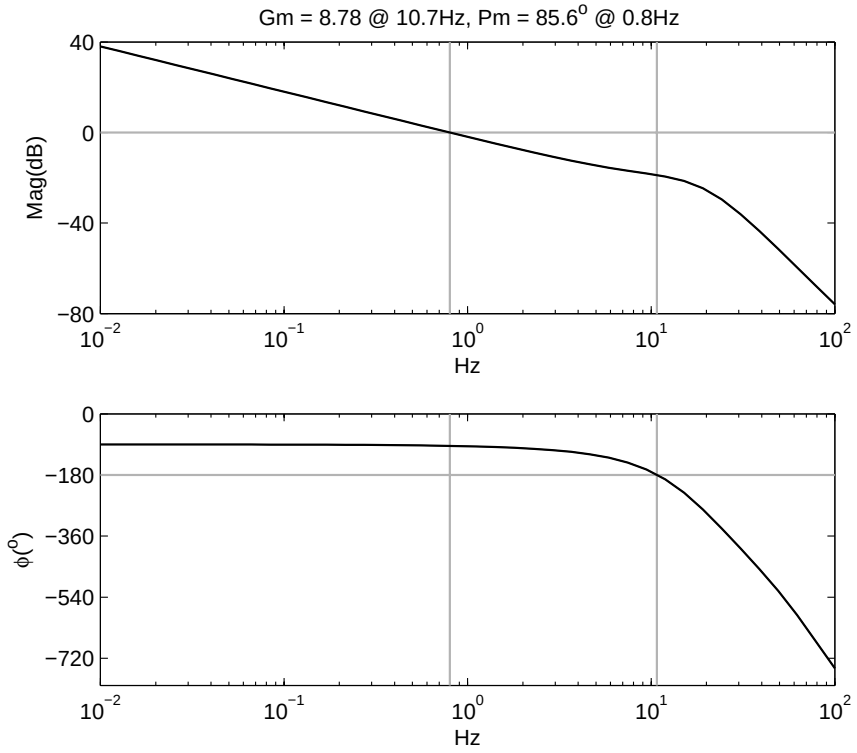

Figure 4.32: Bode plot of velocity/flow compensator, plant and low-pass differentiator.

control block as separated from and placed after the lead compensator. Adding the action to the inner velocity loop has the same effect as setting $K_{flow} = 1$. The choice of filters and compensators was designed using the Bode plot shown in Figure 4.32. This Bode plot includes the dynamics from the compensator, plant and filter. Linear simulation was used to check the response and effect of sensor noise. Three things limited the achievable cutoff frequency: (1) bandwidth of valves, (2) delay or phase introduced by the PWM and (3) sensor noise. The numerical value of this controller is summarized in Table 1. All of the controller transfer functions were implemented digitally using Tustin's method. The parameters used in this compensator are shown in Table 4.1.

Table 4.1: Controller parameters

Parameters	Description	Value[units]
K_Q	Gain	5 [ ]
ω_{zL}	Lead zeros	72π [rad/s]
ω_{pL}	Lead poles	202π [rad/s]
ω_{PI}	PI zero	82π [rad/s]
ω_f	Filter cutoff	202π [rad/s]
K_p	Position P-Gain	5 [1/sec]
ζ	Damping ratio	$2^{-1/2} \approx 0.7$ [ ]

As mentioned early it was assumed that desired position, y_d, and velocity, v_d, were available. In the case of coordinate or resolved rate mode, only desired velocity would be received from the human-machine interface. With no position signal, K_p would be set to zero and $v_{dc} = v_d$. Using the same velocity/flow compensator without position feedback results in a loop gain between v_d and v_f that is a Type I system. This means that a step in velocity or constant velocity inputs will have zero steady-state velocity error.

Linear simulations and experiments both verify the effect of Δ on performance.

Positive Δ will result in less damping and extremely negative values with result in sluggish, but stable performance. The same test shown in Figure 4.24 - 4.25 is repeated in Figure 4.33 with the velocity feedback control loop. Notice that there is no steady state position error and good dynamics response.

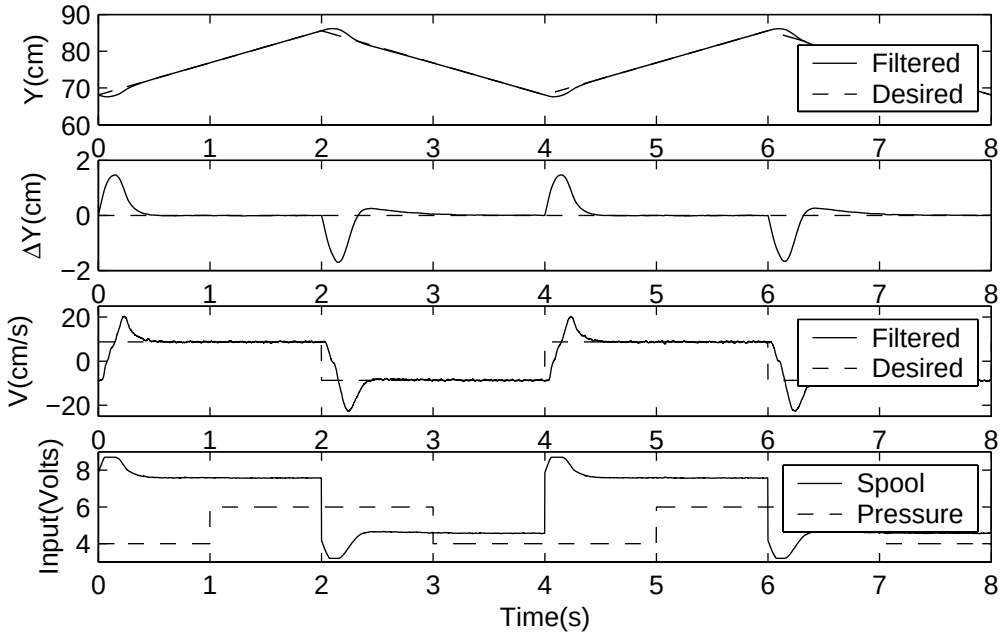

Figure 4.33: Response to saw-tooth input with pressure compensator and velocity/flow feedback with integral action. Note that there is no steady-state position error to these ramps.

4.4.3 Dead-band Transition

The proportional spool valve can be approximated by two linear regions separated by a dead-band. The dead-band is designed to hold the load when flow is not being sent to either one of the ports. It also limits how fast the valve can change the direction of the flow. This makes it hard for the valve to regulate flow around zero and can lead to a limit cycle [89] from the dead-band nonlinearity being sandwiched between the valve and plant dynamics. This means that the valve dynamics are between the dead-band and any inverse dead-zone function used in the controller. One way to eliminate the limit cycle is to reintroduce a small dead-zone before the inverse dead-band function. This is done by modifying the cylinder input velocity, v_{dc}, using the following nonlinearity.

$$v_{dc}^* = \begin{cases} v_{dc} - \Delta_v e^{\Delta_v(\Delta_v - v_{dc})} & \Delta_v < v_{dc} \\ 0 & -\Delta_v \neq v_{dc} \neq \Delta_v \\ v_{dc} + \Delta_v e^{\Delta_v(\Delta_v + v_{dc})} & v_{dc} < -\Delta_v \end{cases} \tag{4.56}$$

In this controller, Δ_v is set to 1mm/s. This nonlinear function will have almost no effect on v_{dc} at higher speeds due to the exponential terms going to zero. The down fall of this method is that it will introduce some position error around zero velocity. This can be bounded by setting $v_d = 0$ in Equation 4.49 and comparing to Δ_v.

$$|e_{zv}| \leq \frac{\Delta_v}{k_p} \tag{4.57}$$

In this equation, the position error at zero velocity is bounded by $\Delta_v/k_p = 0.2mm$. This is acceptable because it eliminates a limit cycle of greater amplitude. In Figure 4.34, the boom cylinder is transitioning from retract to extend. With the input dead-zone, the cylinder stops and the spool is maintained in the middle of the dead-band. With out this additional non-linearity, the cylinder enters a limit cycle as the cylinder overshoots and the spool moves from one side of the dead-band to the other. Notice

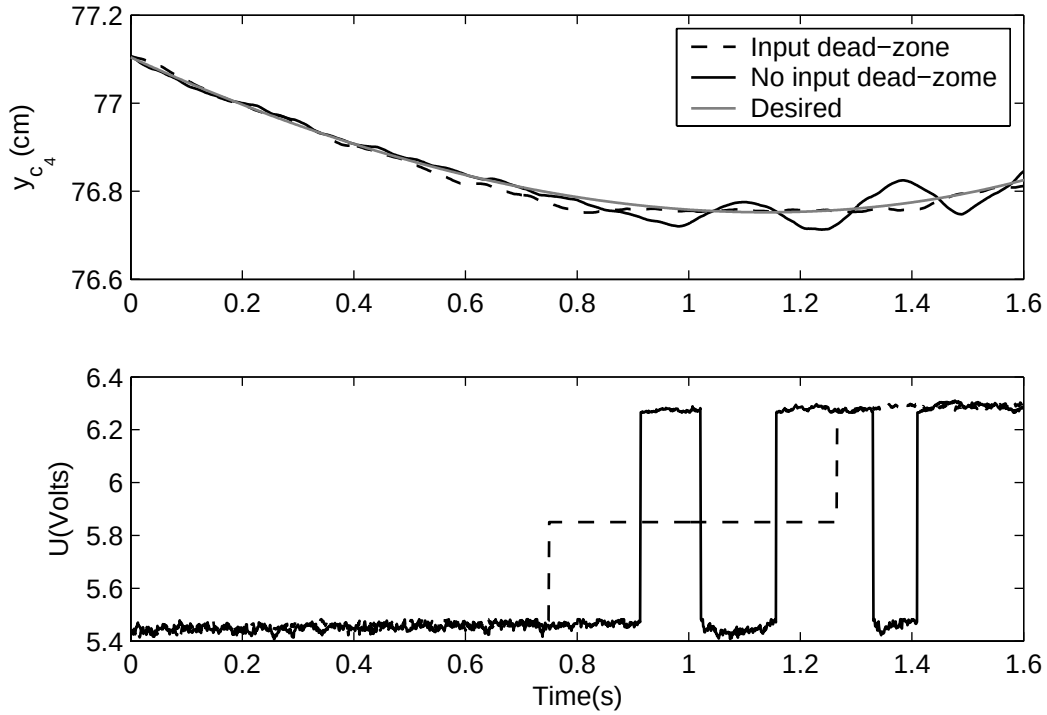

Figure 4.34: Input deadzone: Changing cylinder direction with and without the small velocity input dead-zone.

the delay between when the spool command is given and when the velocity or flow changes direction. This delay should be on the order of $50ms$ (Figure 4.6).

The output of this non-linearity is also used to decide the requested pump pressure for that particular cylinder. If the modified cylinder velocity command, v_{dc}^*, is zero the pump pressure request for that cylinder will be zero. Otherwise it will be the appropriate port pressure depending on the sign of the velocity. The integrator action is also reset to zero while $v_{dc}^* = 0$. This is implemented by modifying the saturation points of the nonlinearity in the anti-windup algorithm depending on the sign of v_{dc}^*.

4.4.4 Coordinated Motion

Two tests were conducted to demonstrate the coordinated motion of the backhoe test-bed. One moved the bucket along an arc and the other moves the bucket along a trajectory with a right angle elbow. In addition, two different controllers are used:

the PI-lead and one with only the position feedback ($K_Q = 0$). The swing which is kinematically decoupled from the boom, stick and bucket is not used. This allows the trajectory to be described using the task-space cylindrical coordinates r and z and the absolute bucket angle ϕ. The cylindrical coordinates r and z describe the translational motion of the wrist of the bucket. The absolute bucket angle, ϕ, is measured from the horizontal plane and is maintained at a constant angle. Both the "elbow" and "arc" trajectories are plotted in Figure 4.35.

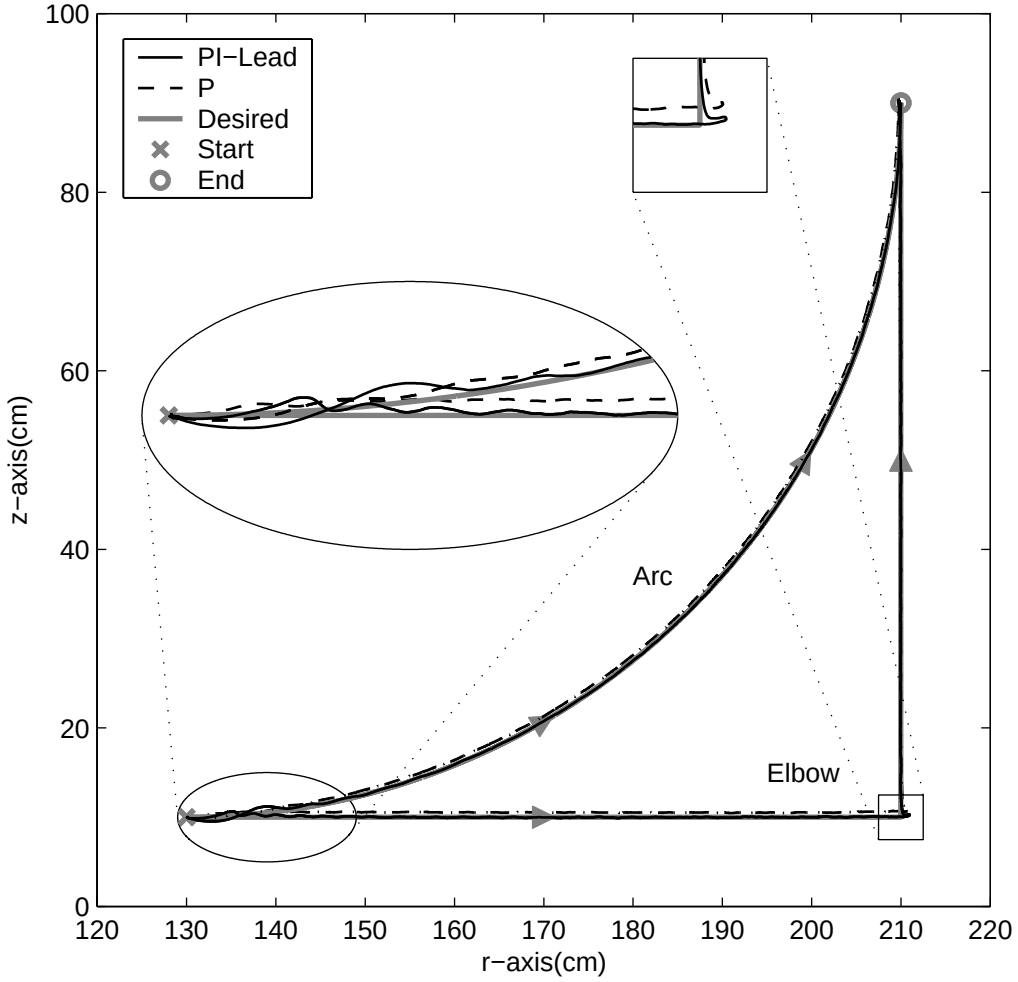

Figure 4.35: Coordinated motion in the r-z plane with the PI-lead control and P only control.

In both cases, the backhoe starts at rest. While the desired position and velocity

of these trajectories can be easily described in task space, these signals must be mapped into cylinder-space coordinates. For coordinated position mode, the desired position and velocity are mapped directly from the human-machine interface. If a more traditional rate scheme is employed, then the rate command mapped from the position of the human-machine interface is set equal to v_{dc} and k_p in Equation 4.49 will be set to zero removing the position feedback loop.

Figures 4.36 and 4.37 show the error signals corresponding to the task-space coordinates (r, z and ϕ) and cylinder-space coordinates (y_{c_2}, y_{c_3} and y_{c_4}) for the "elbow" and "arc" trajectories respectively. In both tests, there is some ripple in the boom cylinder as the boom starts to drop. This is probably caused by the pressure compensator going from fully open to almost completely closed. Due to gravity forces and the asymmetric cylinders, cap pressure is very low when receiving flow from the pump. Since the cylinder is above the boom, the cylinder must extend in order to lower the boom. With symmetric spools this results in a high pressure demand when raising the boom and a low pressure demand when lowering the boom. Having low pressure means that the pressure drop across the pressure compensator need to be high. Especially at low flows, this requires the pressure compensator to be almost closed to achieve a small orifice and work at the extreme of the compensator's design. Before the pressure compensator closes, the flow gain, K_{flow}, could be much higher than one. This drives some of the poles in the root locus towards the right-half-plane (Figure 4.31). Then once the pressure compensator spool moves into metering range the oscillation dies out as the flow gain returns to around one. Comparing the two controllers, it can be seen that tracking error is eliminated with the PI-lead controller. However, oscillations in the boom cylinder do not occur with the controller that only utilizes position feedback.

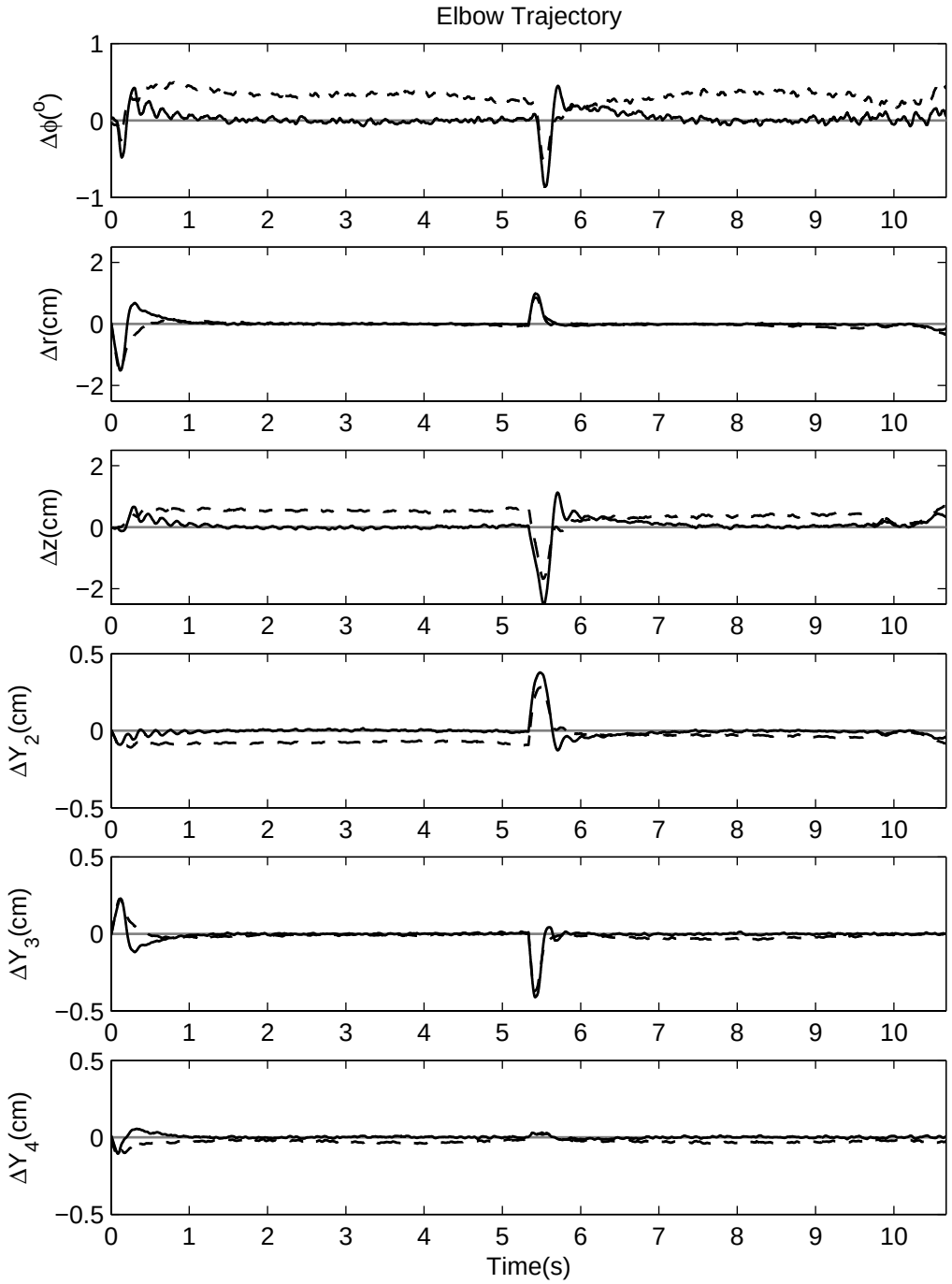

Figure 4.36: Tracking error for the "Elbow" trajectory shown in Figure 4.35. The dashed line is the response with only proportional position control.

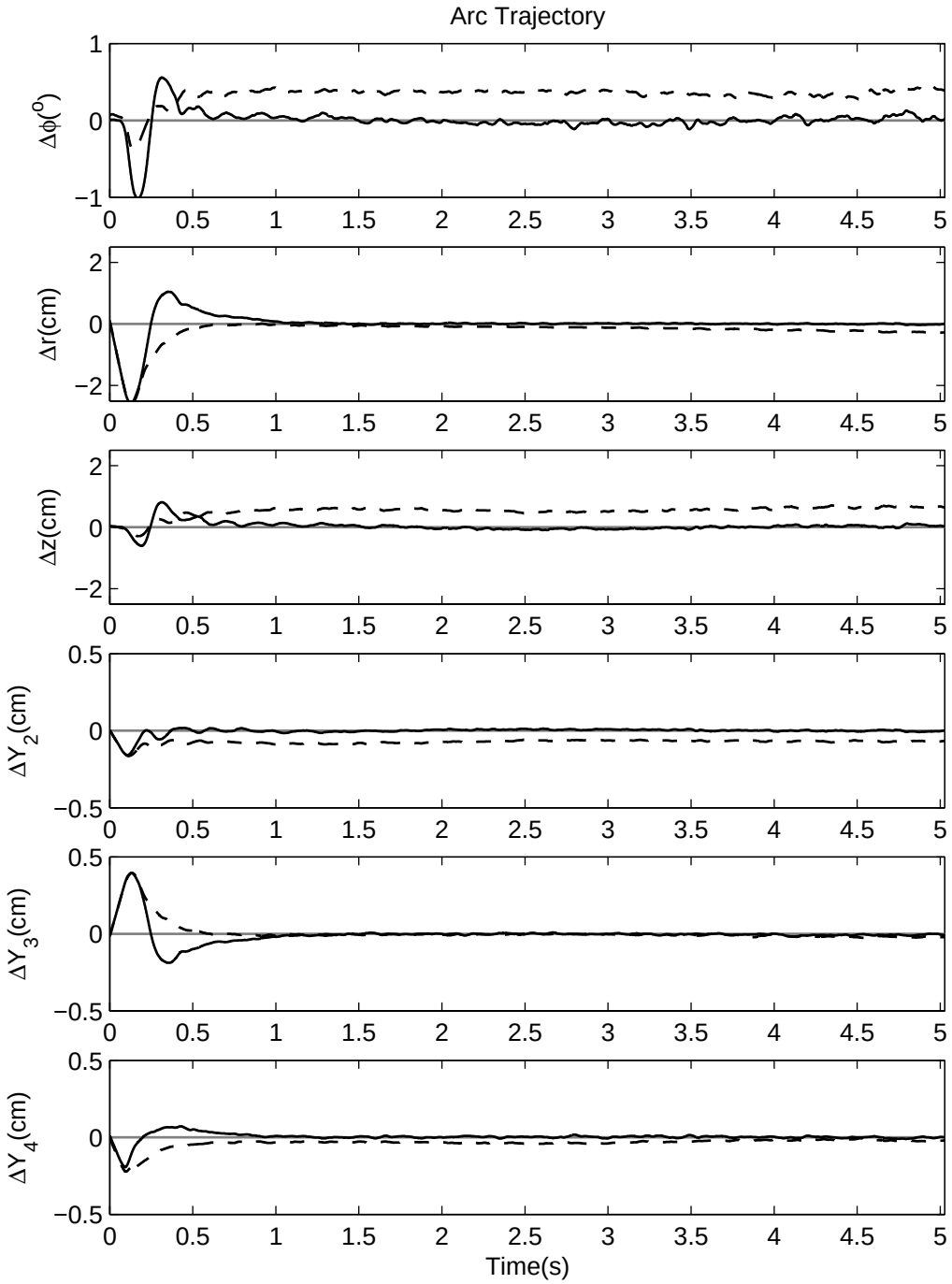

Figure 4.37: Tracking error for the "Arc" trajectory shown in Figure 4.35. The dashed line is the response with only proportional position control.

4.5 Summary

This chapter addresses the topics of controlling pump pressure and cylinder flow. Arguments for using an electronic load-sensing pressure control strategy are presented. Using this type of pressure regulation scheme allows pressure to be built up as the spool moves through the dead-zone and raises the minimum system pressure to ensure that the spool control stage is always properly pressurized. This improves the overall responsiveness of the system. Combining the cylinder velocity control with a flow limiting algorithm is also necessary. If the total flow being sent to the actuators is too much, the pressure regulator can not maintain system pressure. This results in oscillations in the system pressure and, ultimately, jerky motion.

Using an electrical load-sensing scheme allows the pump pressure to be varied for efficiency while not compromising system stability. A moving-window-max-filter is presented. The max filter does not introduce lag while pressure is increasing. This means that it does not slow down pressure build up in the pump. However, it can remove oscillation in the desired pressure up to the period of the filter. When combined with using the pressure compensator on the proportional valve, this helps decouple the pump pressure from oscillations in the port pressures being used to dictate the pump pressure in the load-sensing scheme. While the pump pressure is held high for a slightly longer period of time, it enables the pressure to be varied without compromising system stability.

Decoupling the pump pressure states from the flow states is important to the overall goal of this project which are to apply coordinated motion and haptic feedback to backhoes/excavators. This means that additional position and force loops can be added without exciting dynamic interactions between the pump pressure states and the states of the proportional valves. In a more general frame work, this decoupling strategy could be applied to any load-sensing system that was being controlled under feedback control.

In this system, it was found experimentally that the system could respond faster to changes in pressure if pressure compensators were used. This will also limit the gain of the system by limiting the pressure across the spool. This simplifies the controller design. In addition to the outer position feedback loop, an inner velocity loop is proposed. This loop is designed to improve the flow accuracy of the system and improve tracking. A small input dead-zone is proposed in order to eliminate limit cycles around zero flow. This nonlinearity has no effect at higher flow and trades a limit cycle around zero velocity for position error which is less than the amplitude of the limit cycle. Finally, coordinated motion is demonstrated using two trajectories that are described in task-space and mapped into cylinder space. Controlling pressure and flow enables smooth and response cylinder control which is central to the major goal of this project, i.e., achieving coordinate haptic control of backhoes/excavators.

CHAPTER V

BUCKET FORCE

Using pressure transducers to estimate the exogenous force acting on an end effector could be useful for a number of applications. These include load estimation or diagnostics. In this case, it is motivated by haptic control of backhoes/excavators. Using pressure transducers is attractive from a cost point of view because they are relatively inexpensive and, more importantly, already present on many electro-hydraulic systems. Measuring the cylinder pressure and multiplying by the respective areas gives the total force on each cylinder produced by the hydraulic pressure. Embedded in this force are cylinder and structural friction, gravitational forces, inertial/Coriolis/centrifugal forces and exogenous forces acting on the end effector. Particularly challenging is the friction inside the cylinders which is not only velocity dependent, but also pressure dependent. The friction increases as the pressure inside the cylinders pushes harder on the seal. This section discusses how to remove the unwanted force components which result in an estimation of the exogenous force on the end effector. Experimental results are presented and the new method is compared with previous work related to this topic.

There are two common ways of measuring this force: pressure transducers on the cylinders and load pins. One place to install the load pins are at the base of the cylinders in order to obtain an indirect joint torque reading [128]. The load pins can also be placed at other strategic locations such as the pins connecting the bucket to the stick in order to supply a more direct force measurement [38]. By multiplying the cylinder port pressure by the capside and rodside areas the hydraulic force on the cylinder can be calculated. The hydraulic force is the result of different

types of forces: friction, gravity, dynamic (inertia, Coriolis and centrifugal) and the external or exogenous forces acting on the bucket. Haptic force reflection requires a measurement or estimation of the exogenous force. Between the other three force components gravity and friction dominate and the friction is primarily located inside the cylinder [132].

Friction is one of nature's nastiest phenomenons to model and is a topic of research by itself. In the control literature, most of this work is focused on developing control laws that compensate for friction in hydraulic control systems [131, 87, 132, 12] or other types of systems [60, 40, 32]. In addition to standard phenomenon such as stick-slip friction [60], hydraulic cylinders also have been found to have pressure dependent friction [12].

The contribution of this chapter is a force estimation scheme that only utilizes pressure and position sensors for force estimation and training. Both the training method and parameter estimation technique is derived and implemented. The challenge of using pressure sensors is dealing with the pressure components that are not generated from the force acting on the end of the bucket. Experimental results are presented comparing the pressure based method to a direct bucket force measurements taken from a two-axis load cell and axial load-cell. This work has been partially publish in Kontz et al. [72].

5.1 Pressure Based Force Estimation

In the force estimation method presented in this section, only the gravity and friction terms are removed from the cylinder force calculated from the port pressure. Ideally, dynamic forces would also be removed. However, the position measurement is already being filtered to find velocity so estimating acceleration to remove inertial forces or multiplying velocity signals to remove Coriolis and centrifugal forces would not be practical. Unlike in the case of Tafazoli et al. [128, 132], this test-bed does not have

load pins on the cylinder bases. Combining pressure and load-pins measurements the friction inside the cylinder can be measured and other structural friction is negligible [128]. This technique only uses the pressure readings for both the identification of gravity and friction parameter and ultimately exogenous force estimation. The tests to find these parameters were designed to eliminate inertial, centrifugal and Coriolis forces by moving one joint at a time with a constant speed. Speed, pressure and orientation were varied as much as possible. Similar to Tafazoli et al. [128, 132, 130] linear least-squares is utilized to find the parameters. Unlike Tafazoli et al. [132], the dynamic parameters from the inertia matrix and Coriolis/centrifugal matrix are not found. The assumption is that cylinder friction and gravity forces are greater than the dynamic forces of the manipulator. This means that what is really being estimated is not the exogenous force, but rather the exogenous force plus the dynamic forces.

5.1.1 Friction Models

The friction force is the hardest to cancel due to its nonlinear nature. One approach is to use a viscous-Coulomb model with parameters b_v and b_c.

$$F_f \approx b_v \dot{y}_c + b_c sign(\dot{y}_c) \tag{5.1}$$

This approach was used by Tafazoli et al. [132] and Malaguti [97] to estimate the internal friction in the cylinder. Another approach that was proposed by Bonchis et al. [12] estimates the cylinder friction using pressure measurements. This nonlinear equation has five coefficients, c_{1-5}.

$$F_f \approx c_1 e^{c_2 \dot{y}_c} + c_3(P_c - P_r) + c_4 P_r + c_5 \dot{y}_c \tag{5.2}$$

For both the Bonchis and Tafazoli models the parameters are solved empirically from experiment data taken from the respective test-beds. The strength of the Bonchis model is that it takes into account the fact that high port pressures, P_c and P_r,

will result in more friction since the normal force on the seals in greater. Experiments by Bonchis et al. demonstrate that the model in Equation 5.2 does a better job of modeling cylinder friction than the simpler model in Equation 5.1. If the parameters are being found using $F_{hydr} = A_c P_c - A_r P_r$, the Bonchis method breaks down. This is because the term F_{hydr} is a linear combination of the port pressures and the port pressures also span two of the bases in this friction model. This results in a trivial solution. One measurement that would enable the use of the more accurate pressure based model described by Bonchis et al. [12] would be to have load pins installed on the cylinders. Having load pins installed on the cylinders means that you can directly calculate F_c [128]. Since F_{hydr} is calculated from the port pressure, it is also possible to calculate cylinder friction, $F_f = F_{hydr} - F_c$. Knowing F_f means that the force being used to find friction is no longer a linear combination of P_c and P_r meaning that a pressure dependent model such as the Bonchis model should work.

$$F_f \approx b_v \dot{y}_c + b_q |\dot{y}_c| \dot{y}_c \tag{5.3}$$

The friction model in Equation 5.3 that is used in this identification has a term that increases exponentially with velocity (or actually the square) similar to the Bonchis model [12]. Having a quadratic term instead of an exponential term means that linear least-square (LLS) can still be utilized. Note that at low velocity, the exponential term in the Bonchis model is the same as a Coulomb term. A Coulomb term is not included in the friction model used in this chapter. When the Coulomb term is used, the gravity parameters using the pressure based force measure are not realistic. This implies that the Coulomb friction is not sufficiently orthogonal to the gravity terms. Also different friction parameters will be found for the asymmetric cylinders depending on if the cylinders are extending or retracting. Later in this chapter superscripts are added that denote if the cylinder is extending "+" or retracting "-".

5.1.2 LS-Estimation

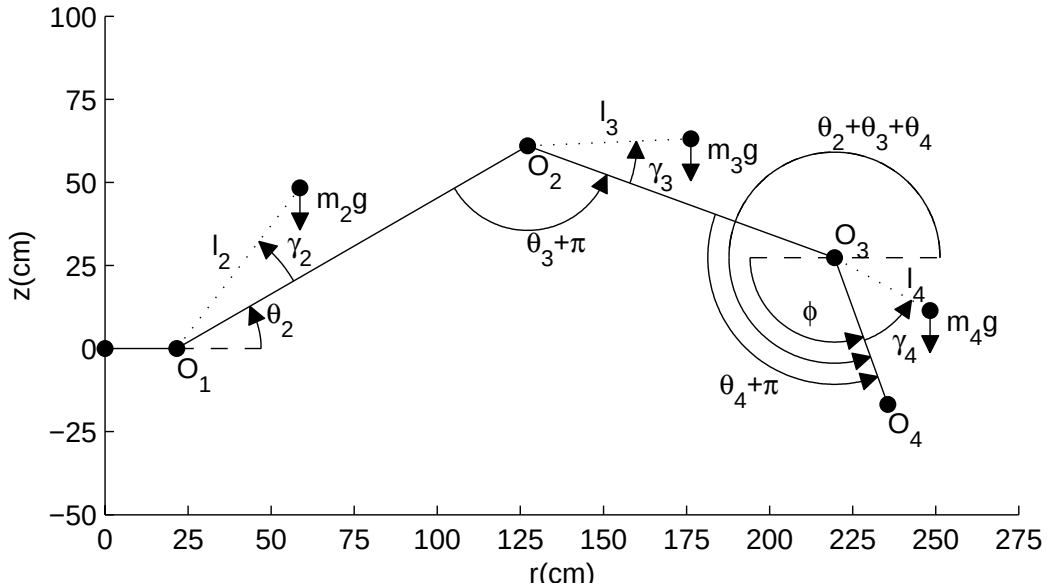

Figure 5.1: Locations of the link's centroid and variables used to describe the resulting torques.

In order to estimate exogenous force from the pressure signals it is useful to start with the dynamic equations.

$$\boldsymbol{M}(\boldsymbol{\Theta})\ddot{\boldsymbol{\Theta}} + \boldsymbol{V}(\boldsymbol{\Theta}, \dot{\boldsymbol{\Theta}}) + \boldsymbol{G}(\boldsymbol{\Theta}) = \boldsymbol{\tau} \tag{5.4}$$

How to find these terms using Lagrange's method and the resulting gravity terms, $\boldsymbol{G}(\boldsymbol{\Theta})$, is described in Appendix B. The vector $\boldsymbol{\Theta}$ is the vector of joint angle and $\boldsymbol{\tau}$ is the vector of corresponding net joint torques. The net joint torque, $\boldsymbol{\tau}$ is equal to the torque generated by the respective hydraulic cylinders, $\boldsymbol{\tau}_c$, minus the torque generated by environment or exogenous forces acting on the bucket, $\boldsymbol{\tau}_e$. In the experiment used for identification $\boldsymbol{\tau}_e$ is zero because the bucket is moving in free space. The second, third and fourth elements in the vectors $\boldsymbol{\Theta}$ and $\boldsymbol{\tau}$ correspond to the boom, stick and bucket joints. The respective joint angles and centroids are described graphically in Figure 5.1.

$$[m_{i,1} \cdots m_{i,4}]\ddot{\boldsymbol{\Theta}} + \frac{\partial^2 KE}{\partial \Theta \partial \dot{\theta}_i}\dot{\Theta} - \frac{\partial KE}{\partial \theta_i} + \frac{\partial PE}{\partial \theta_i} = \tau_i \tag{5.5}$$

In the case of these experiments the i^{th} joint velocity is constant and the other joint velocities are zero. This means that all the joint accelerations are zero. Less obvious is the fact that the centrifugal and Coriolis term also go to zero if the other joint velocities are zero. This simplifies the Equation 5.5 to Equation 5.6 for the identification test runs.

$$G_i \equiv \frac{\partial PE}{\partial \theta_i} = \tau_i \tag{5.6}$$

There is not an exogenous force on the bucket, so $\tau_{e_i} = 0$ and $\tau_i = \tau_{c_i}$. Furthermore τ_{c_i} can be related to the i^{th} cylinder force f_{c_i} which is equal to the hydraulic force, F_{hydr_i} minus the friction force, F_{f_i}. This results in the following relationship.

$$G_i = J_i(F_{hydr_i} - F_{f_i}) \tag{5.7}$$

The partials of potential energy or gravity terms are shown in Equation B.43 - B.46. For the case where the bucket is extending.

$$m_4 g l_4 cos(\theta_{24} + \gamma_4) + b_{4v}^{+}\dot{y}_c + b_{4q}^{+}|\dot{y}_c|\dot{y}_c = J_4 F_{hydr_4} \tag{5.8}$$

Similarly if the bucket is retracting

$$m_4 g l_4 cos(\theta_{24} + \gamma_4 + b_{4v}^{-}\dot{y}_c + b_{4q}^{-}|\dot{y}_c|\dot{y}_c = J_4 F_{hydr_4} \tag{5.9}$$

In order to apply linear least-square (LLS) to the problem, two modifications need to be made to Equation 5.8-5.9. First it is necessary to separate the terms with the unknown parameter γ_4 from θ_{24}. This is done using the trig identity $cos(\alpha + \beta) = cos(\alpha)cos(\beta) - sin(\alpha)sin(\beta)$. This allows the terms with γ_4 to be placed in the parameter vector, $\boldsymbol{\Phi}$, and the terms with θ_{24} to be placed in the weight matrix, $\boldsymbol{W}$.

Second, velocity needs to be separated into positive velocity and negative velocity components since friction is direction dependent.

$$\dot{y}_{c_i}^{+} = \begin{cases} \dot{y}_{c_i} & \dot{y}_{c_i} > 0 \\ 0 & else \end{cases} \tag{5.10}$$

$$\dot{y}_{c_i}^{-} = \begin{cases} \dot{y}_{c_i} & \dot{y}_{c_i} < 0 \\ 0 & else \end{cases} \tag{5.11}$$

This results in the following matrix and vectors.

$$\begin{aligned} \boldsymbol{W}_4^T &= \begin{bmatrix} g\boldsymbol{c}_{24} \\ -g\boldsymbol{s}_{24} \\ \boldsymbol{J}_4\dot{\boldsymbol{y}}_{c_4}^{+} \\ \boldsymbol{J}_4\dot{\boldsymbol{y}}_{c_4}^{-} \\ \boldsymbol{J}_4|\dot{\boldsymbol{y}}_{c_4}^{+}|\dot{\boldsymbol{y}}_{c_4}^{+} \\ \boldsymbol{J}_4|\dot{\boldsymbol{y}}_{c_4}^{-}|\dot{\boldsymbol{y}}_{c_4}^{-} \end{bmatrix} \\ &= \begin{bmatrix} g\left(c_{24}(1) \ \cdots \ c_{24}(n)\right) \\ -g\left(s_{24}(1) \ \cdots \ s_{24}(n)\right) \\ J_4(1)\dot{y}_{c_4}^{+}(1) \ \cdots J_4(n) \ \dot{y}_{c_4}^{+}(n) \\ J_4(1)\dot{y}_{c_4}^{-}(1) \ \cdots J_4(n) \ \dot{y}_{c_4}^{-}(n) \\ J_4(1)|\dot{y}_{c_4}^{+}(1)|\dot{y}_{c_4}^{+}(1) \ \cdots \ J_4(n)|\dot{y}_{c_4}^{+}(n)|\dot{y}_{c_4}^{+}(n) \\ J_4(1)|\dot{y}_{c_4}^{-}(1)|\dot{y}_{c_4}^{-}(1) \ \cdots \ J_4(n)|\dot{y}_{c_4}^{-}(n)|\dot{y}_{c_4}^{-}(n) \end{bmatrix} \end{aligned} \tag{5.12}$$

where

$$c_{24} = cos(\theta_{24}) \tag{5.13}$$

$$s_{24} = sin(\theta_{24}) \tag{5.14}$$

$$\boldsymbol{\Phi}_4 = \begin{bmatrix} m_4 l_4 cos(\gamma_4) \\ m_4 l_4 sin(\gamma_4) \\ b_{4v}^{+} \\ b_{4v}^{-} \\ b_{4q}^{+} \\ b_{4q}^{-} \end{bmatrix} \tag{5.15}$$

where

$$c_{\gamma_4} = cos(\gamma_4) \tag{5.16}$$

$$s_{\gamma_4} = sin(\gamma_4) \tag{5.17}$$

$$\begin{aligned} \boldsymbol{B}_4 &= \boldsymbol{J}_4 \boldsymbol{F}_{hydr_4} = \boldsymbol{J}_4 (A_{c_4} \boldsymbol{P}_{c_4} - A_{r_4} \boldsymbol{P}_{r_4}) \\ &= [J_4(1) F_{hydr_4}(1) \ \cdots \ J_4(n) F_{hydr_4}(n)]^T \end{aligned} \tag{5.18}$$

If there are n data points, the weight matrix, $\boldsymbol{W}$, is nx6, the parameter vector, $\boldsymbol{\Phi}$, is 6x1 and the bias vector, $\boldsymbol{B}$, is nx1. The LLS solution is $\boldsymbol{\Phi} = (\boldsymbol{W}^T \boldsymbol{W})^{-1} \boldsymbol{W}^T \boldsymbol{B}$ which can be solved numerically using the Matlab command $\boldsymbol{W} \backslash \boldsymbol{B}$.

A similar set of equations can be found for the stick. The only difference is that the bucket's gravity term solved for in the previous LLS optimization is subtracted from both sides of the equation.

$$\boldsymbol{W}_3^T = \begin{bmatrix} g\boldsymbol{c}_{23} \\ -g\boldsymbol{s}_{23} \\ \boldsymbol{J}_3 \dot{\boldsymbol{y}}_{c_3}^{+} \\ \boldsymbol{J}_3 \dot{\boldsymbol{y}}_{c_3}^{-} \\ \boldsymbol{J}_3 | \dot{\boldsymbol{y}}_{c_3}^{+} | \dot{\boldsymbol{y}}_{c_3}^{+} \\ \boldsymbol{J}_3 | \dot{\boldsymbol{y}}_{c_3}^{-} | \dot{\boldsymbol{y}}_{c_3}^{-} \end{bmatrix} \tag{5.19}$$

where

$$c_{23} = cos(\theta_{23}) \tag{5.20}$$

$$s_{23} = sin(\theta_{23}) \tag{5.21}$$

$$\boldsymbol{\Phi}_3 = \begin{bmatrix} m_3 l_3 cos(\gamma_3) + m_4 a_3 \\ m_3 l_3 sin(\gamma_3) \\ b_{3v}^{+} \\ b_{3v}^{-} \\ b_{3q}^{+} \\ b_{3q}^{-} \end{bmatrix} \tag{5.22}$$

where

$$c_{\gamma_3} = cos(\gamma_3) \tag{5.23}$$

$$s_{\gamma_3} = sin(\gamma_3) \tag{5.24}$$

$$\boldsymbol{B}_3 = \boldsymbol{J}_3 \boldsymbol{F}_{hydr_3} - m_4 g l_4 cos(\boldsymbol{\theta}_{24} + \gamma_4) \tag{5.25}$$

Similarly for the boom.

$$\boldsymbol{W}_2^T = \begin{bmatrix} g\boldsymbol{c}_2 \\ -g\boldsymbol{s}_2 \\ \boldsymbol{J}_2 \dot{\boldsymbol{y}}_{c_2}^{+} \\ \boldsymbol{J}_2 \dot{\boldsymbol{y}}_{c_2}^{-} \\ \boldsymbol{J}_2 |\dot{\boldsymbol{y}}_{c_2}^{+}| \dot{\boldsymbol{y}}_{c_2}^{+} \\ \boldsymbol{J}_2 |\dot{\boldsymbol{y}}_{c_2}^{-}| \dot{\boldsymbol{y}}_{c_2}^{-} \end{bmatrix} \tag{5.26}$$

where

$$c_2 = cos(\theta_2) \tag{5.27}$$

$$s_2 = sin(\theta_2) \tag{5.28}$$

$$\boldsymbol{\Phi}_2 = \begin{bmatrix} m_2 l_2 cos(\gamma_2) + (m_3 + m_4) a_2 \\ m_2 l_2 sin(\gamma_2) \\ b_{2v}^{+} \\ b_{2v}^{-} \\ b_{2q}^{+} \\ b_{2q}^{-} \end{bmatrix} \tag{5.29}$$

where

$$c_{\gamma_2} = cos(\gamma_2) \tag{5.30}$$

$$s_{\gamma_2} = sin(\gamma_2) \tag{5.31}$$

$$\begin{aligned} \boldsymbol{B}_2 = \quad & \boldsymbol{J}_2 \boldsymbol{F}_{hydr_2} - m_3 g l_3 cos(\boldsymbol{\theta}_{23} + \gamma_3) \\ & + m_4 g (a_3 \boldsymbol{c}_{\theta_3} + l_4 cos(\boldsymbol{\theta}_{24} + \gamma_4)) \end{aligned} \tag{5.32}$$

One problem with doing a sequential optimization is the errors add from distal to proximal links [132]. Evidence of this is shown in the boom gravity parameters shown in Table 5.2. The term $m_2 l_2 s_{\gamma_2}$ should not be negative since most of the mass in the boom and connected cylinder are above the line between O_1 and O_2 (Figure 5.1). This implies that γ_2 is positive. Another approach is to do a concurrent LLS optimization. The matrices and vectors used in the sequential optimization can be reorganized into a single set of linear equations that can be solved concurrently. These two ways of solving these equations will be be referred to as Sequential LLS and Concurrent LLS.

$$
\boldsymbol{W}_{24}^{T} = \left[\begin{array}{c|c|c}
g\boldsymbol{c}_{24} & g\boldsymbol{c}_{24} & g\boldsymbol{c}_{24} \\
-g\boldsymbol{s}_{24} & -g\boldsymbol{s}_{24} & -g\boldsymbol{s}_{24} \\
\boldsymbol{J}_4\dot{\boldsymbol{y}}_{c_4}^{+} & \boldsymbol{0} & \boldsymbol{0} \\
\boldsymbol{J}_4\dot{\boldsymbol{y}}_{c_4}^{-} & \boldsymbol{0} & \boldsymbol{0} \\
\boldsymbol{J}_4|\dot{\boldsymbol{y}}_{c_4}^{+}|\dot{\boldsymbol{y}}_{c_4}^{+} & \boldsymbol{0} & \boldsymbol{0} \\
\boldsymbol{J}_4|\dot{\boldsymbol{y}}_{c_4}^{-}|\dot{\boldsymbol{y}}_{c_4}^{-} & \boldsymbol{0} & \boldsymbol{0} \\
\hline
\boldsymbol{0} & g\boldsymbol{c}_{23} & g\boldsymbol{c}_{23} \\
\boldsymbol{0} & -\boldsymbol{g}s_{23} & -g\boldsymbol{s}_{23} \\
\boldsymbol{0} & \boldsymbol{J}_3\dot{\boldsymbol{y}}_{c_3}^{+} & \boldsymbol{0} \\
\boldsymbol{0} & \boldsymbol{J}_3\dot{\boldsymbol{y}}_{c_3}^{-} & \boldsymbol{0} \\
\boldsymbol{0} & \boldsymbol{J}_3|\dot{\boldsymbol{y}}_{c_3}^{+}|\dot{\boldsymbol{y}}_{c_3}^{+} & \boldsymbol{0} \\
\boldsymbol{0} & \boldsymbol{J}_3|\dot{\boldsymbol{y}}_{c_3}^{-}|\dot{\boldsymbol{y}}_{c_3}^{-} & \boldsymbol{0} \\
\hline
\boldsymbol{0} & \boldsymbol{0} & g\boldsymbol{c}_2 \\
\boldsymbol{0} & \boldsymbol{0} & -g\boldsymbol{s}_2 \\
\boldsymbol{0} & \boldsymbol{0} & \boldsymbol{J}_2\dot{\boldsymbol{y}}_{c_2}^{+} \\
\boldsymbol{0} & \boldsymbol{0} & \boldsymbol{J}_2\dot{\boldsymbol{y}}_{c_2}^{-} \\
\boldsymbol{0} & \boldsymbol{0} & \boldsymbol{J}_2|\dot{\boldsymbol{y}}_{c_2}^{+}|\dot{\boldsymbol{y}}_{c_2}^{+} \\
\boldsymbol{0} & \boldsymbol{0} & \boldsymbol{J}_2|\dot{\boldsymbol{y}}_{c_2}^{-}|\dot{\boldsymbol{y}}_{c_2}^{-}
\end{array}\right] \tag{5.33}
$$

$$\boldsymbol{\Phi}_{24} = \begin{bmatrix} \Phi_4 \\ \Phi_3 \\ \Phi_2 \end{bmatrix} = \begin{bmatrix} m_4 l_4 cos(\gamma_4) \\ m_4 l_4 sin(\gamma_4) \\ b_{4v}^{+} \\ b_{4v}^{-} \\ b_{4q}^{+} \\ b_{4q}^{-} \\ m_3 l_3 cos(\gamma_3) + m_4 a_3 \\ m_3 l_3 sin(\gamma_3) \\ b_{3v}^{+} \\ b_{3v}^{-} \\ b_{3q}^{+} \\ b_{3q}^{-} \\ m_2 l_2 cos(\gamma_2) + (m_3 + m_4) a_2 \\ m_2 l_2 sin(\gamma_2) \\ b_{2v}^{+} \\ b_{2v}^{-} \\ b_{2q}^{+} \\ b_{2q}^{-} \end{bmatrix} \tag{5.34}$$

$$\boldsymbol{B}_{24} = \begin{bmatrix} \boldsymbol{J}_4 \boldsymbol{F}_{hydr_4} \\ \boldsymbol{J}_3 \boldsymbol{F}_{hydr_3} \\ \boldsymbol{J}_2 \boldsymbol{F}_{hydr_2} \end{bmatrix} \tag{5.35}$$

Table 5.1 summarizes the MSE (mean-square-error) of the two LLS optimization techniques separated by degree-of-freedom. The parameters found from both methods are shown in Table 5.2. In addition the gravity terms are also calculated by solid modeling [29]. The aforementioned problem with the negative boom gravity term is eliminated by the concurrent LLS optimization; however, a similar problem

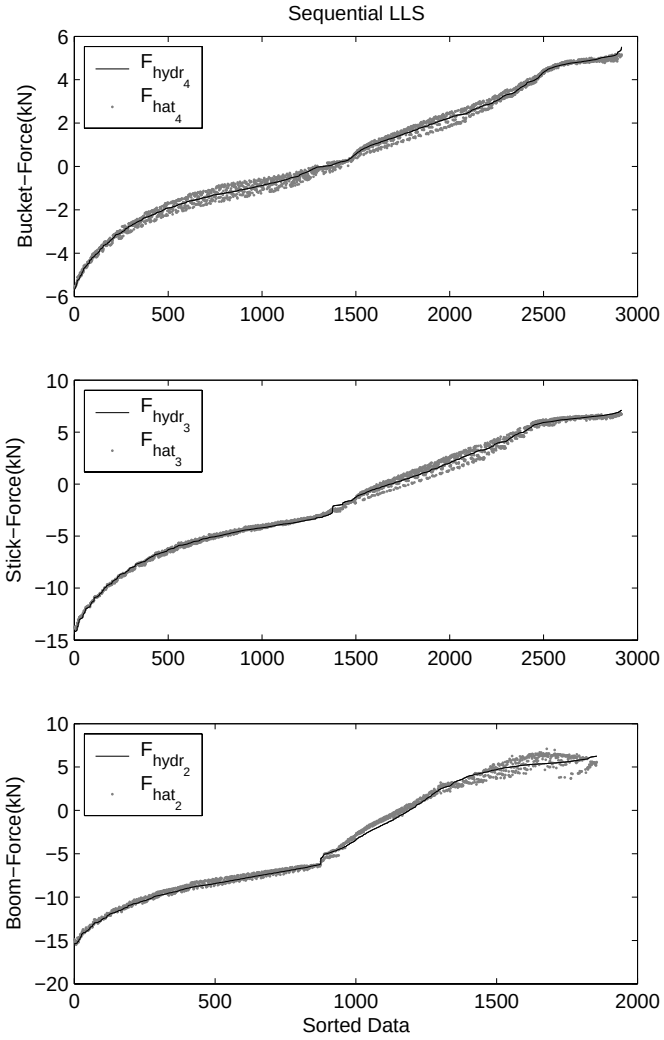

Figure 5.2: F_{hydr} and estimate $\hat{F}_{hydr}$ using sequential LLS optimization.

with one of the bucket inertia arises. The measured and estimated hydraulic forces, $F_{hydr} = A_c P_c - A_r P_r$, are plotted in Figure 5.2 & 5.3 using the sequential and concurrent methods respectively. The exogenous force estimate is found using the original equation of motion.

$$\boldsymbol{M}(\boldsymbol{\Theta})\ddot{\boldsymbol{\Theta}} + \boldsymbol{V}(\boldsymbol{\Theta}, \dot{\boldsymbol{\Theta}}) + \boldsymbol{G}(\boldsymbol{\Theta}) = \boldsymbol{\tau} = \boldsymbol{\tau}_{hydr} - \boldsymbol{\tau}_f - \boldsymbol{\tau}_e \tag{5.36}$$

The variables $\boldsymbol{\tau}_{hydr}$ and $\boldsymbol{\tau}_f$ are related to $\boldsymbol{F}_{hydr}$ and $\boldsymbol{F}_f$ using the joint to cylinder Jacobians. Solving for $\boldsymbol{\tau}_{hydr}$ and subtracting the gravity and friction estimates result

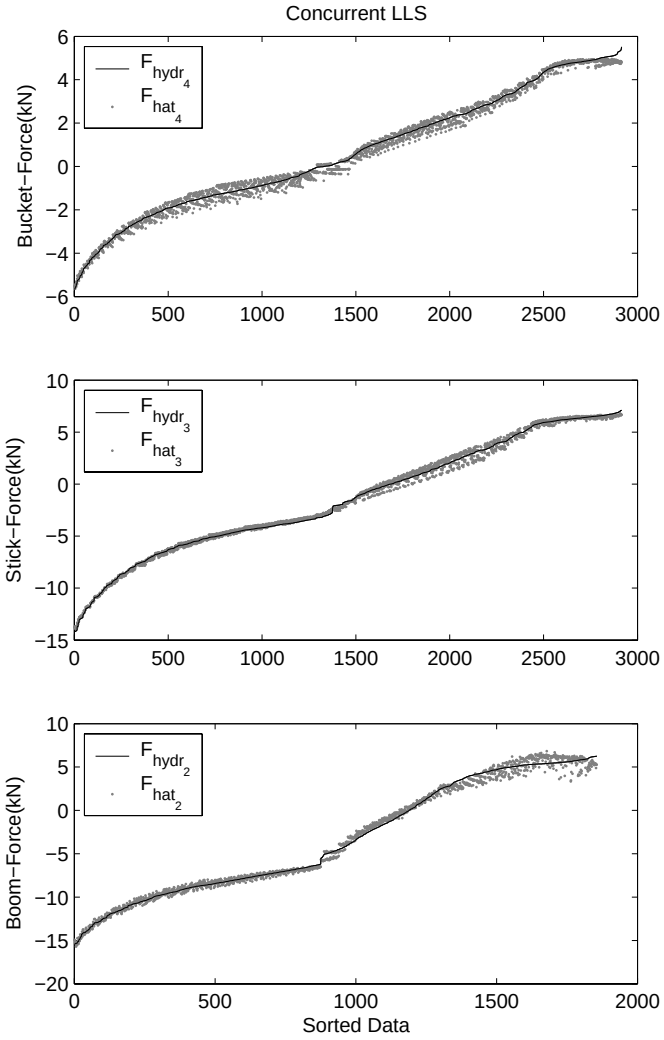

Figure 5.3: F_{hydr} and estimate $\hat{F}_{hydr}$ using concurrent LLS optimization.

in the following equation

$$\begin{aligned} \hat{\boldsymbol{\tau}}_e &= \boldsymbol{\tau}_{hydr} - \hat{\boldsymbol{\tau}}_f - \hat{\boldsymbol{G}}(\boldsymbol{\Theta}) \\ &= \boldsymbol{\tau}_e + \boldsymbol{M}(\boldsymbol{\Theta})\ddot{\boldsymbol{\Theta}} + \boldsymbol{V}(\boldsymbol{\Theta}, \dot{\boldsymbol{\Theta}}) + \tilde{\boldsymbol{\tau}}_f + \tilde{\boldsymbol{G}}(\boldsymbol{\Theta}) \end{aligned} \tag{5.37}$$

The estimates, $\hat{\boldsymbol{G}}(\boldsymbol{\Theta})$ and $\hat{\boldsymbol{\tau}}_f$, are denoted by hats and the residual error terms, $\tilde{\boldsymbol{G}}(\boldsymbol{\Theta})$ and $\tilde{\boldsymbol{\tau}}_f$, are denoted with tildes. Equation 5.37 shows that there will be an error term resulting from the dynamic forces that were ignored in addition to the modeling error of the gravity and friction terms. It is assumed that both acceleration and velocity is relatively low during a normal digging operation so that the dynamic terms should

Table 5.1: MSE for each degree-of-freedom.

Method	Boom	Stick	Bucket
Number of sets	1855	2915	2915
MSE - Sequential	$230E3\ N^2$	$74E3\ N^2$	$29E3\ N^2$
MSE - Concurrent	$219E3\ N^2$	$75E3\ N^2$	$44E3\ N^2$

be small. Finally, the standard robotics Jacobian, J, can be used to calculate the estimated task-space force/torque wrench, $\hat{F}_e$, acting on the bucket which is the end goal [29, 70].

$$\hat{\boldsymbol{F}}_e = \boldsymbol{J}^{-T}\hat{\boldsymbol{\tau}}_e \tag{5.38}$$

The goal is to estimate the exogenous force acting on the end effector of a hydraulic manipulator such as a backhoe or excavator. In this case only the port pressures are available. Ideally dynamic forces, gravity forces and friction forces could be removed. During digging operations the dynamics forces are assumed to be negligible and therefore only friction and gravity forces are removed from the pressure based force measurement. Using only the force calculated from the cylinder port pressures, two methods for estimating manipulator parameters were derived that can be solved using linear least-squares. These methods are compared with one another and the gravity parameters are compared with results from CAD modeling. Different friction models are discussed. In these experiments the traditional Coulomb friction was removed and a term proportional to the square of velocity was added to the standard viscous term.

Table 5.2: Parameters from sequential LLS methods, concurrent LLS method and CAD [29].

Parameter	Sequation LLS	Concurrent LLS	CAD
$m_4 l_4 c_{\gamma_4}\{kg \cdot m\}$	2.68	-0.491	5.79
$m_4 l_4 s_{\gamma_4}\{kg \cdot m\}$	1.92	0.674	2.49
$b^+_{4v}\{kN \cdot s/m\}$	13.0	11.2	na
$b^-_{4v}\{kN \cdot s/m\}$	5.85	7.72	na
$b^+_{4q}\{kN \cdot s^2/m^2\}$	38.9	45.1	na
$b^-_{4q}\{kN \cdot s^2/m^2\}$	52.8	46.9	na
$m_3 l_3 c_{\gamma_3} + m_4 a_3\{kg \cdot m\}$	67.2	63.7	45.2
$m_3 l_3 s_{\gamma_3}\{kg \cdot m\}$	4.80	5.30	3.13
$b^+_{3v}\{kN \cdot s/m\}$	36.3	32.9	na
$b^-_{3v}\{kN \cdot s/m\}$	21.7	23.6	na
$b^+_{3q}\{kN \cdot s^2/m^2\}$	167	185	na
$b^-_{3q}\{kN \cdot s^2/m^2\}$	239	232	na
$m_2 l_2 c_{\gamma_2} + (m_3 + m_4) a_2\{kg \cdot m\}$	164	115	115
$m_2 l_2 s_{\gamma_2}\{kg \cdot m\}$	-16.6	14.1	3.92
$b^+_{2v}\{kN \cdot s/m\}$	50.2	49.8	na
$b^-_{2v}\{kN \cdot s/m\}$	16.1	17.9	na
$b^+_{2q}\{kN \cdot s^2/m^2\}$	131	130	na
$b^-_{2q}\{kN \cdot s^2/m^2\}$	317	311	na

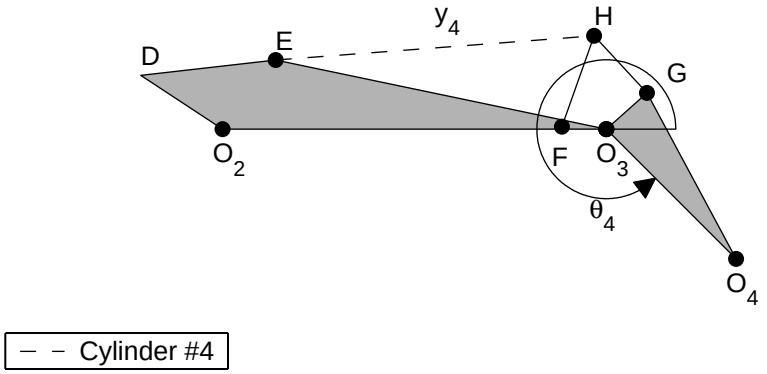

Figure 5.4: This figure shows the geometry of the bucket and bucket cylinder.

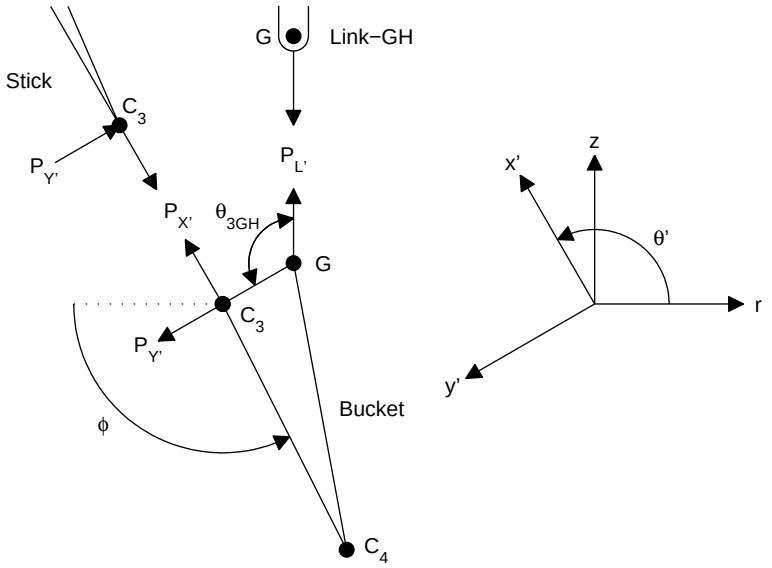

Figure 5.5: Force sensor measurements: This plot shows the force measurements taken by the load pin and the force S-Type load cell in link-GH. The point in this free-body diagram can be related to the bucket linkage shown in Figure 5.4.

The most direct way to measure the force acting on the bucket is at the two points where it is connected to the rest of the backhoe/excavator arm. These points are denoted as C_3 and G in Figure 5.4 and 5.5. A pin connects the bucket to the stick at C_3. This force is measured using a two-axis load pin. Another pin connects the bucket to a link that is part of a four-bar-linkage actuated by the bucket cylinder.

Since link-GH is a two-force-member, the force on this pin can be measured using an axial load-cell built into this link (Figures 5.4). In order to measure the force acting on the bucket by the rest of the manipulator the aforementioned two-axis load-pin and axial load-cell was added to the bucket(Figure 5.6).

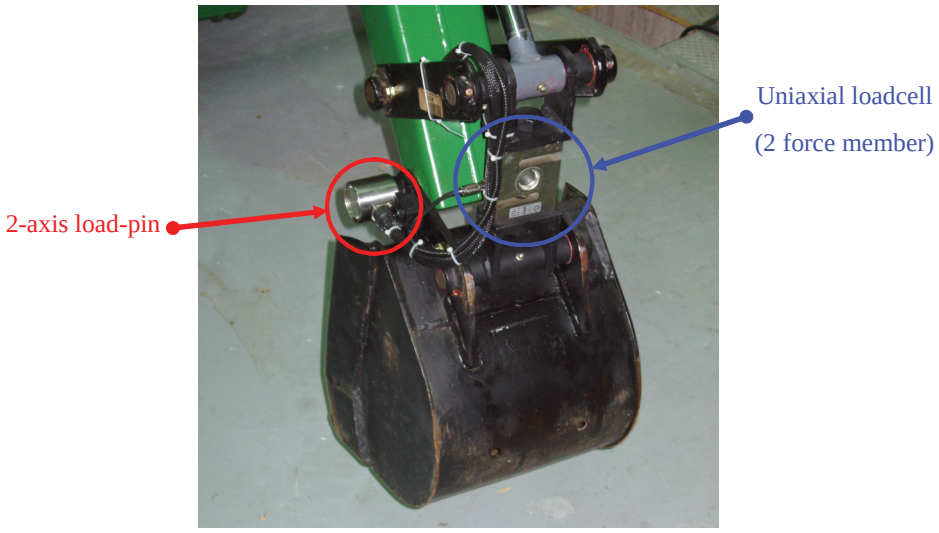

Figure 5.6: Picture of load-pin and axial load cell built into the backhoe.

$$\Sigma F_{x'} = P_x + P_L sin(\theta_{3GH}) = F_{x'} \tag{5.39}$$

$$\Sigma F_{y'} = P_y + P_L cos(\theta_{3GH}) = F_{y'} \tag{5.40}$$

$$\Sigma M_3 = P_L r_{3G} sin(\theta_{3GH}) = \tau' \tag{5.41}$$

$$\begin{aligned} \theta' &= \pi + \phi + \theta_{43G} + \pi/2 \\ &= \theta_2 + \theta_3 + \theta_4 + \theta_{43G} + \pi/2 \end{aligned} \tag{5.42}$$

$$\begin{bmatrix} F_r \\ F_z \\ \tau_\phi \end{bmatrix} = \begin{bmatrix} cos(\theta') & -sin(\theta') & 0 \\ sin(\theta') & cos(\theta') & 0 \\ 0 & 0 & 1 \end{bmatrix} \begin{bmatrix} F_{x'} \\ F_{y'} \\ \tau' \end{bmatrix} \tag{5.43}$$

Just like the hydraulic force include components from friction, gravity and inertia in addition the exogenous force acting on the bucket, the force measured from the load-pin and load-cell also have friction, gravity and inertia components. However, the inertia and gravity is only from the bucket and there is no cylinder friction.

Since the gravity, friction and inertia is only from the bucket and could be ignored. The other method would be to try to cancel out the gravity and friction like was done with the pressure based estimate. The components of the measured force from Equation 5.43 can be separated by looking at the dynamics equations of the bucket.

$$\Sigma F_r = F_r = m_4 \ddot{r}_{c_4} \tag{5.44}$$

$$\Sigma F_z = -m_4 g + F_z = m_4 \ddot{z}_{c_4} \tag{5.45}$$

$$\circlearrowleft \Sigma M_\phi = \tau_\phi - b\dot{\theta}_{24} - l_4 m_4 g cos(\theta_{24} + \gamma_4) = J_{4_3} \ddot{\theta}_{24} \tag{5.46}$$

Solving for the acceleration terms.

$$\ddot{r}_{c_4} = -l4\dot{\theta}_{24}^2 cos(\theta_{24} + \gamma_4) - l4\ddot{\theta}_{24} sin(\theta_{24} + \gamma_4) \tag{5.47}$$

$$\ddot{z}_{c_4} = -l4\dot{\theta}_{24}^2 sin(\theta_{24} + \gamma_4) + l4\ddot{\theta}_{24} cos(\theta_{24} + \gamma_4) \tag{5.48}$$

In order to separate the knowns form the unknowns the following trigonometric identities can be applied.

$$cos(\alpha + \beta) = cos(\alpha)cos(\beta) - sin(\alpha)sin(\beta) \tag{5.49}$$

$$sin(\alpha + \beta) = sin(\alpha)cos(\beta) + cos(\alpha)sin(\beta) \tag{5.50}$$

Applying these identities

$$\begin{aligned}\Sigma F_r = F_r &= m_4 l_4 \left(-\dot{\theta}_{24}^2(c_{24}c_{\gamma_4} - s_{24}s_{\gamma_4}) - \ddot{\theta}_{24}(s_{24}c_{\gamma_4} + c_{24}s_{\gamma_4})\right) \\ &= m_4 l_4 \left(-(\dot{\theta}_{24}^2 c_{24} + \ddot{\theta}_{24}s_{24})c_{\gamma_4} + (\dot{\theta}_{24}^2 s_{24} - \ddot{\theta}_{24}c_{24})s_{\gamma_4}\right)\end{aligned} \tag{5.51}$$

$$\begin{aligned}\Sigma F_z &= -m_4 g + F_z = m_4 l_4 \left(-\dot{\theta}_{24}^2(s_{24}c_{\gamma_4} + c_{24}s_{\gamma_4}) + \ddot{\theta}_{24}(c_{24}c_{\gamma_4} - s_{24}s_{\gamma_4})\right) \\ &= m_4 l_4 \left((-\dot{\theta}_{24}^2 s_{24} + \ddot{\theta}_{24}c_{24})c_{\gamma_4} - (\dot{\theta}_{24}^2 c_{24} + \ddot{\theta}_{24}s_{24})s_{\gamma_4}\right)\end{aligned} \tag{5.52}$$

$$\circlearrowleft \Sigma M_\phi = \tau_\phi - b\dot{\theta}_{24} - l_4 m_4 g(c_{24}c_{\gamma_4} - s_{24}s_{\gamma_4}) = J_{4_3}\ddot{\theta}_{24} \tag{5.53}$$

where

$$c_{24} = cos(\theta_{24}) \tag{5.54}$$

$$s_{24} = sin(\theta_{24}) \tag{5.55}$$

$$c_{\gamma_4} = cos(\gamma_4) \tag{5.56}$$

$$s_{\gamma_4} = sin(\gamma_4) \tag{5.57}$$

Equations 5.51 - 5.53 can be arranged and solved using linear least squares to find the gravity, inertia and friction parameters.

$$\boldsymbol{W\Phi = B} \tag{5.58}$$

$$\boldsymbol{W} = \begin{bmatrix} \mathbf{0} & -\dot{\boldsymbol{\theta}}_{24}^2 \boldsymbol{c}_{24} - \ddot{\boldsymbol{\theta}}_{24}\boldsymbol{s}_{24} & \dot{\boldsymbol{\theta}}_{24}^2 \boldsymbol{s}_{24} - \ddot{\boldsymbol{\theta}}_{24}\boldsymbol{c}_{24} & \mathbf{0} & \mathbf{0} \\ \mathbf{0} & -\dot{\boldsymbol{\theta}}_{24}^2 \boldsymbol{s}_{24} + \ddot{\boldsymbol{\theta}}_{24}\boldsymbol{c}_{24} & -\dot{\boldsymbol{\theta}}_{24}^2 \boldsymbol{c}_{24} - \ddot{\boldsymbol{\theta}}_{24}\boldsymbol{s}_{24} & \boldsymbol{g} & \mathbf{0} \\ \ddot{\boldsymbol{\theta}}_{24} & g\boldsymbol{c}_{24} & -g\boldsymbol{s}_{24} & \mathbf{0} & \dot{\boldsymbol{\theta}}_{24} \end{bmatrix} \tag{5.59}$$

$$\boldsymbol{B} = \begin{bmatrix} \boldsymbol{F}_r \\ \boldsymbol{F}_z \\ \boldsymbol{\tau}_\phi \end{bmatrix} \tag{5.60}$$

$$\mathbf{\Phi} = \begin{bmatrix} J_4 \\ l_4 m_4 c_{\gamma_4} \\ l_4 m_4 s_{\gamma_4} \\ m_4 \\ b \end{bmatrix} \tag{5.61}$$

5.3 Load Cell Comparison

The following plots compare the pressure based method with the forces measured directly from the load-call and load-pin. The bucket inertia, gravity and friction components are not removed as described in the previous section since these force are small compared to the range of forces on the bucket during normal digging. The Figure 5.7 shows force and torque measurements were the contact motion is primarily in the horizontal direction and Figure 5.7 shows force and torque measurements were the contact motion is primarily in the vertical direction. In these cases, the force measurement and estimate have good agreement in the direction of motion. However, the forces perpendicular to motion do not agree and don't even always have the same sign. This shows the promise of the pressure based estimate; however, unless otherwise stated all the experimental forces used for the rest of this document was measured using the load-pin and load-cell directly measuring the force acting on the bucket without compensation for bucket inertia, gravity or friction described in the previous section.

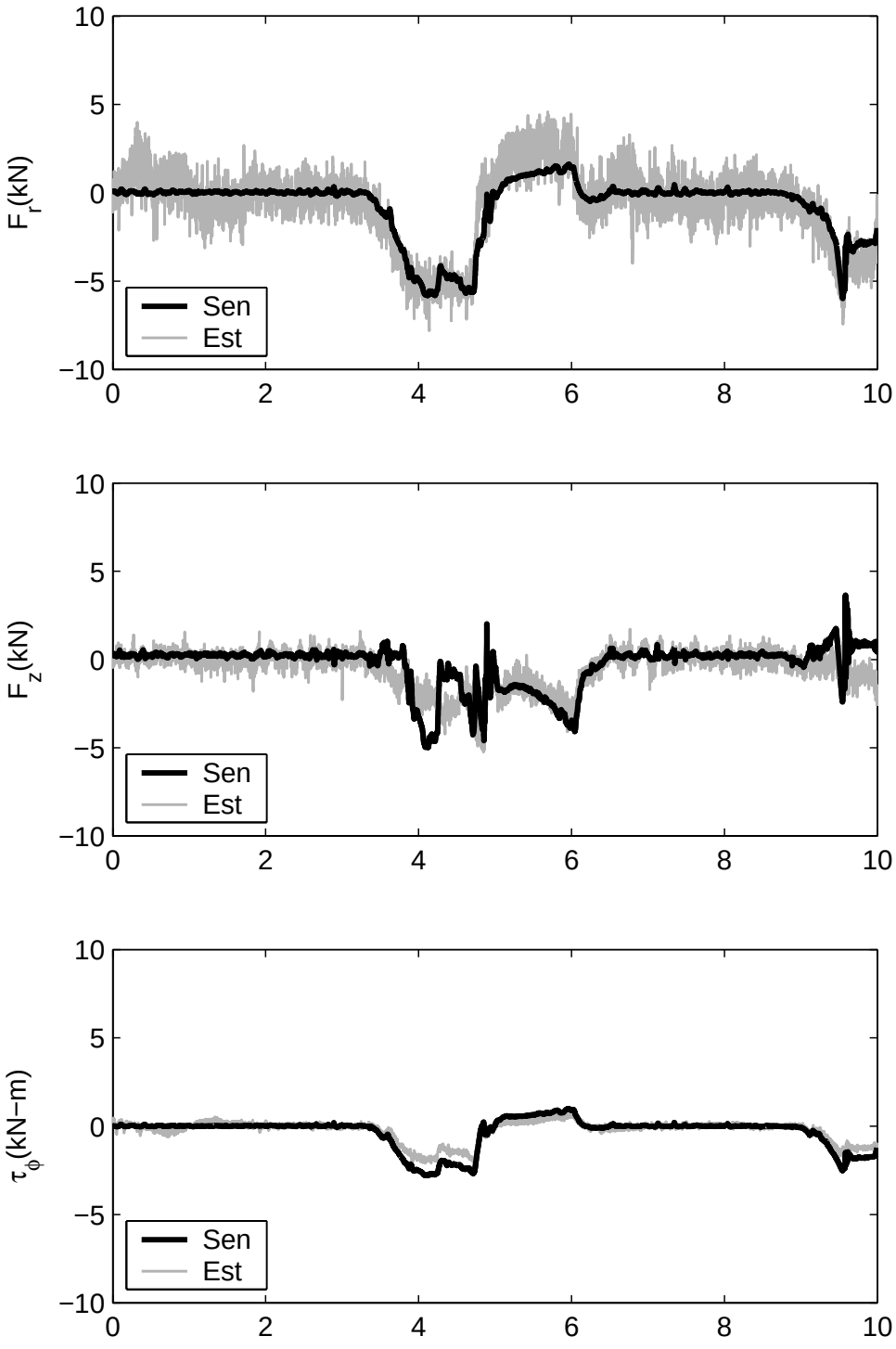

Figure 5.7: Force comparison between pressure based force estimate and load-cell measurement with a force predominately in the direction of the r-axis.

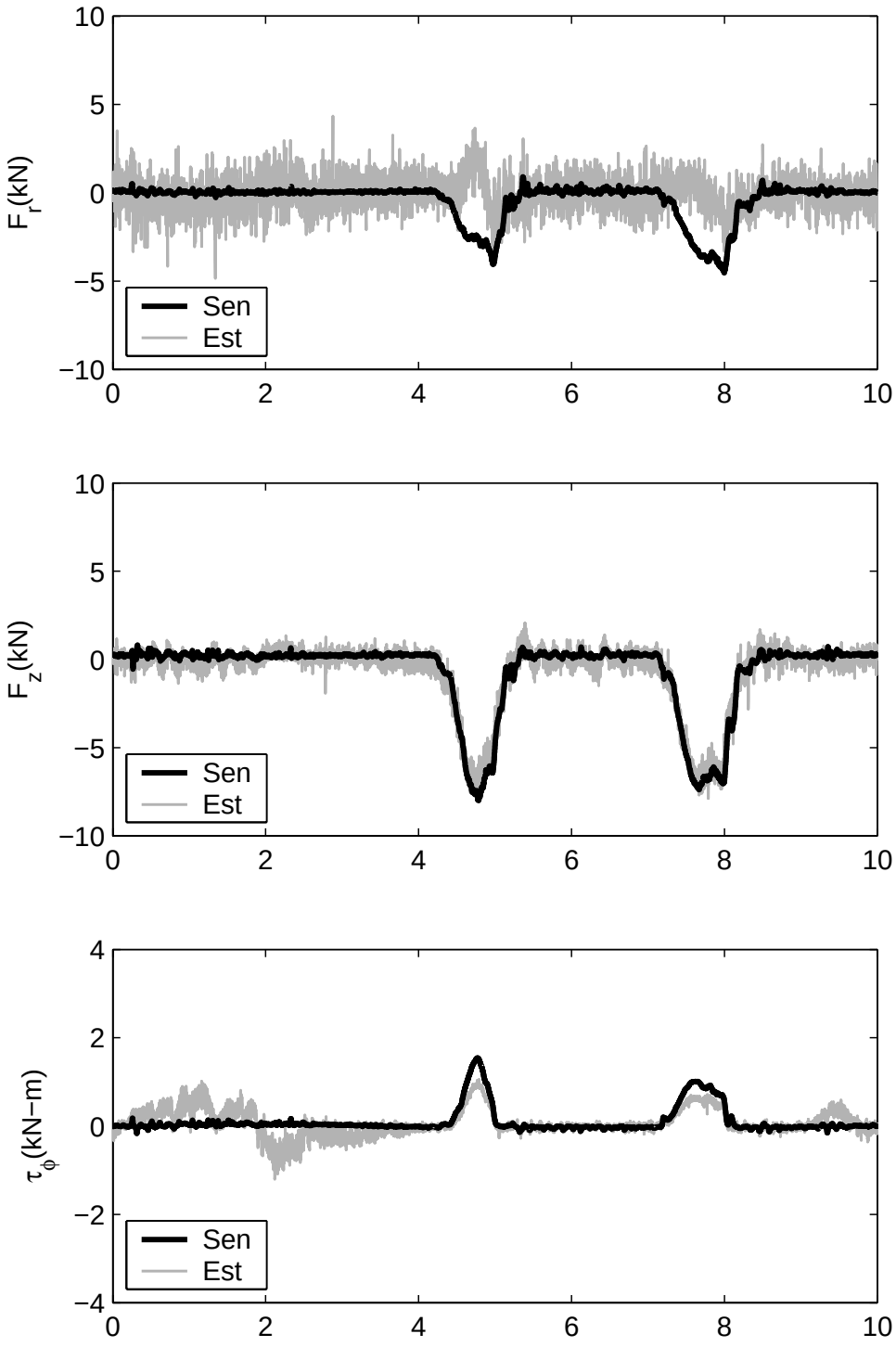

Figure 5.8: Force comparison between pressure based force estimate and load-cell measurement with a force predominately in the direction of the z-axis.

5.4 Summary

This chapter discusses the use of bucket force sensors and the estimation of bucket force from pressure sensors. A technique is derived and implemented that only utilizes pressure and position sensors. No higher cost force sensors are used. This pressure based force estimate agrees well with the force measurement in the direction of motion, but varies in the direction perpendicular to bucket motion. This demonstrates the promise and challenge of implementing this method. Using pressure sensors instead of force sensors is important because it helps limit the added cost of applying coordinated haptic feedback to backhoes and excavators.

CHAPTER VI

VIRTUAL BACKHOE

In order to evaluate the effectiveness of a haptic control strategy it is necessary to conduct human-in-the-loop experiments. Ideally this could be done using the actual hardware. However, due to the size of the soil-bin it is only possible to dig two trenches before having to replace and compact the soil. Doing so requires about 20-30 minutes limiting the amount of data that can be collected from test subjects. An alternative is to create a simulator that includes a backhoe model, soil model, graphic display and haptic interface. The block diagram of the virtual-HEnRE (V-HEnRE) simulator is shown in Figure 6.1. In terms of form and function, this simulator is modeled after the University of British Columbia's mini-excavator simulator [22, 133].

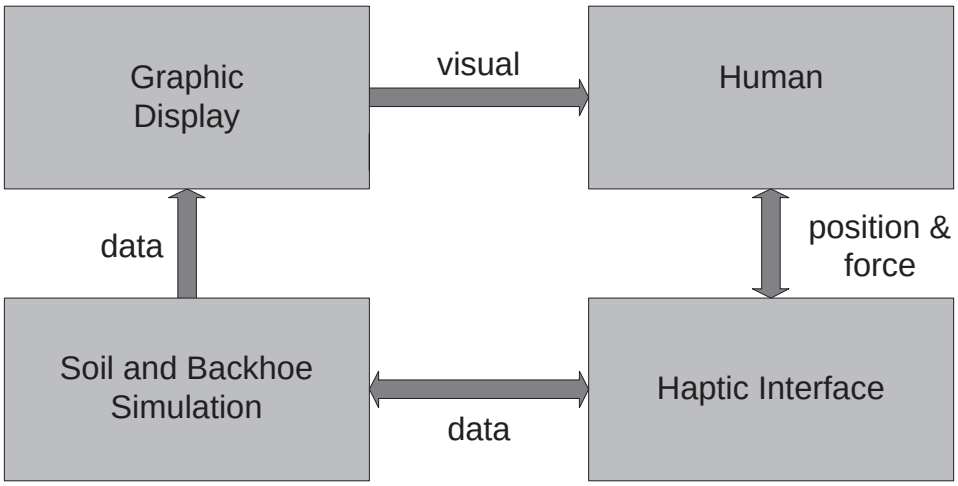

Figure 6.1: Block diagram of virtual backhoe simulation.

The haptic interface used withe V-HEnRE is the same PHANToM Omni used with the HEnRE test-bed (Section 2.5). The PHANToM [99] haptic interfaces are

built commercially by SensAble Technologies. The V-HEnRE simulator utilizes Mathwork's Simulink/xPC-target to model the backhoe and soil dynamics. The graphics are displayed using C++/OpenGL and the backhoe graphics are based of a ProE model of this backhoe created by Frankel ([29]). Since the controller for HEnRE is Simulink based, a lot of the components of the HEnRE controller can be shared with the V-HEnRE simulator without modifications. The components shared by HEnRE and V-HEnRe include the kinematic transformation blocks, the UDP blocks that communicate with the PHANToM Omni, hydraulic control blocks and other high-level control structure. Since the communication block is shared, the haptic interface can be shared including the control code. It is possible to switch between HEnRE and V-HEnRE by switching a single Ethernet cable on the computer controlling the PHANToM Omni. Similar to both the PHANTom Omni and the HEnRE controller, V-HEnRe has a fixed update rate of 1000Hz and runs in real-time.

The major things added to V-HEnRE not in the HEnRE controller were a simulation of the backhoe and a soil model to calculate interaction forces. Another UDP communication module is also required to send data to the graphic display showing the backhoe and soil. In theory, the computer running the graphics could be the same as the one controlling the PHANToM Omni; however, in practice the 1000Hz PHANToM Omni control will run better if the graphics are run on a different computer. The primary advantage of using a virtual backhoe and virtual soil is that this type of setup allows the soil to be instantly reset. It also allows objects to be buried and moved between trials.

6.1 Backhoe Model and Control

For the simulation to run in real-time, it is necessary to simplify the model and remove some of the stiff states associated with the hydraulic system. This is possible

by assuming that valve flow is only dependant on spool position. This is a reasonable assumption since the valves are pressure compensated [146]. Not only does this allow the complex rigid body dynamics to be ignored, it also allows the stiff pressure dynamics to be removed. This assumption is violated when the pump is not able to provide the pressure required to maintain this flow. In order to reproduce this phenomenon in the simulator, the speed or flow is reduced to zero around the loads that would result in the maximum pump pressure of the actual backhoe. This eliminates the need to model many of the fast dynamics associated with hydraulic systems. The primary dynamics remaining are the valve dynamics. The relationship between the valve input voltage, V_{in}, and the spool position, X_{sp}, can be modeled as a second-order system with a pure time delay Section 4.2.1

$$\frac{X_{sp}(s)}{V_{in}(s)} = \frac{k\omega_n^2 e^{-\tau s}}{s^2 + 2\zeta\omega_n s + \omega_n^2} \tag{6.1}$$

In this transfer function, $\omega_n/(2\pi) \approx 7Hz$, $\zeta \approx 0.7$ and $\tau = 1/80 seconds$. The valve dead-band is also modeled. The maximum flow of the pump is also set to a constant value like it would be on the actual test-bed. Combining the maximum flow with the kinematic model and cylinder areas, results in a position and velocity dependant maximum speed that is similar to the actual machine.

6.2 Soil Model

The soil model used in this work is based on the soil model presented by DiMaio et al. [22]. This model is primarily an impedance model that calculates a bucket force based on the state of the soil and the motion of the bucket. The bucket force includes components related to stiffness, damping, Coulomb friction and accumulated load. This simulator was created in conjunction with the mini-excavator impedance control described in Salcudean et al. [120] and Tafazoli et al. [133]. For a literature review of relevant soil modeling see DiMaio et al. [22].

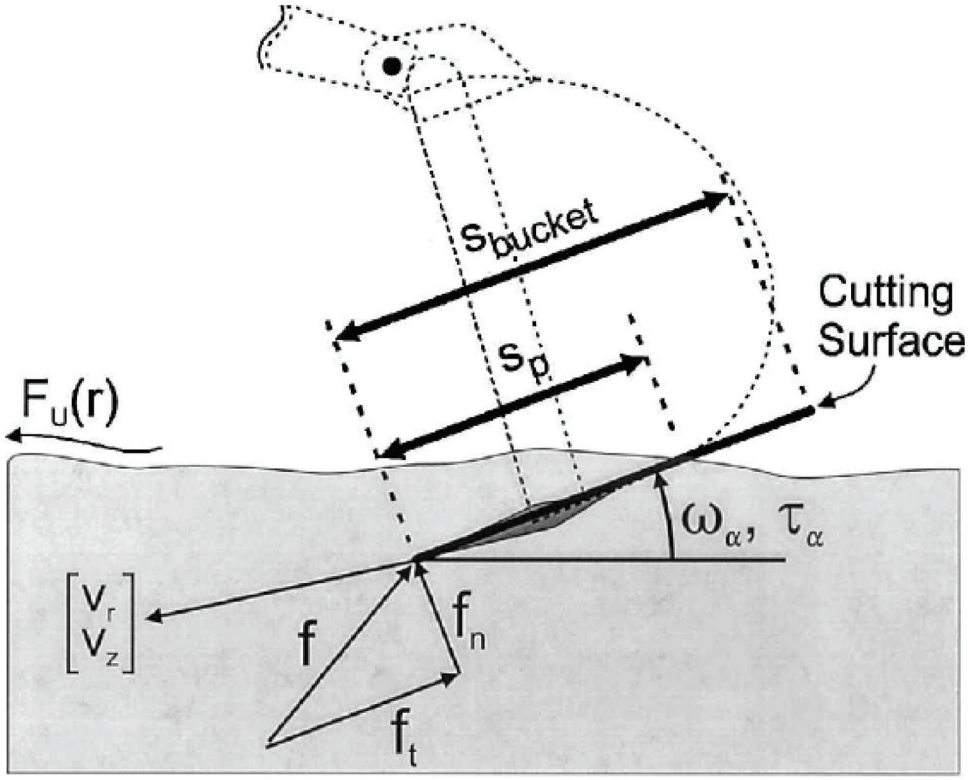

Figure 6.2: The cutting edge reference frame and coordinates used in the soil model presented in DiMaio et al.[22]. Even though it is not indicated in DiMaio's figure, the angle α is measure from horizontal line that ω_α is referenced.

This soil model is primarily based on the motion of the bucket tip as shown in Figure 6.2. Tangential, t, and normal, n, coordinates are introduced that are measured relative to a reference frame attached to the bucket. These are related to cylindrical coordinates, r and z by the rotation matrix $R(\alpha)$. The angle α (Fig 6.2) is offset from ϕ by a constant angle. The damping force is calculated using the tangential damping coefficient, b_{to}, the normal damping coefficient, b_{no} and the area of the cutting surface, S_p.

$$\alpha = \phi - \pi + \delta \tag{6.2}$$

where $\delta = 0.425rad = 24.3^o$

$$\begin{bmatrix} f_{br} \\ f_{bz} \end{bmatrix} = -R(\alpha) \begin{bmatrix} s_p b_{to} & 0 \\ 0 & s_p b_{no} \end{bmatrix} R^T(\alpha) \begin{bmatrix} \dot{r} \\ \dot{z} \end{bmatrix} \tag{6.3}$$

$$\tau_b = -s_p(r, z, \alpha) b_{\alpha o} \dot{\alpha} \tag{6.4}$$

A stiffness force is calculated relative to a stiffness center. Initially, this stiffness center is the point where the tip of the bucket enters the soil.

$$\begin{bmatrix} f_{kt} \\ f_{kn} \end{bmatrix} = -R^T(\alpha) k \begin{bmatrix} r_c - r \\ z_c - z \end{bmatrix} \tag{6.5}$$

$$\tau_k = k_\alpha(\alpha_c - \alpha) \tag{6.6}$$

The shear stress in the soil induced by the bucket can cause a chuck of soil to break off. A simplifying assumption is to make the shear surface a plane in the direction of the normal force, f_n (Figure 6.2). In reality, this shear surface is more complicated, does not necessarily start out in the normal direction, and actually changes directions creating a spiraling surface [95]. Once the soil shears, the stiffness center is reset and forces are relieved inside the soil. Shearing occurs when the total force in the normal direction, f_n, creates stress that surpasses the shear strength, S, of the soil:

$$if \quad f_n \geq (S \cdot w \cdot d_p), \quad then \begin{bmatrix} r_c \\ z_c \end{bmatrix} = \begin{bmatrix} r \\ z \end{bmatrix} \tag{6.7}$$

Here w is the width of the bucket and d_p is the distance to the surface of the soil. Resetting the stiffness after shearing is consistent with the physics of shearing material. Updating the stiffness center is less obvious when the soil is not shearing, entering the soil or leaving the soil. The damping and stiffness forces are localized, linearized models of more complex physics of the soil. It is hard to relate the stiffness center to the physics of the soil. Regardless of the explanation, the stiffness center

needs to change and should follow the path of the bucket. To model the behavior of the stiffness center, DiMaio et al. [120] proposed updating the stiffness center by low-pass filtering the position of the bucket's tip. In order to make it easier to move in the direction of the bucket's teeth, the time constant in the tangential direction, T_{rt}, is smaller than the time constant in normal direction, T_{rn}. Modeling soil as a low-pass filter is a gross oversimplification of the rich and complex set of behaviors observed in the study of soil; however, this assumption does allow the stiffness model to move with the path of the bucket while producing resistance.

$$\begin{bmatrix} r_c(s) \\ z_c(s) \end{bmatrix} = R(\alpha) \begin{bmatrix} \frac{1}{T_{rt}s+1} & 0 \\ 0 & \frac{1}{T_{rn}s+1} \end{bmatrix} R(\alpha)^T \begin{bmatrix} r(s) \\ z(s) \end{bmatrix} \tag{6.8}$$

One modification to the DiMaio soil model is the calculation of the force related to the accumulation of soil in the bucket. As soil enters the bucket, two types of forces are created. First the weight of the soil in the bucket creates a downward force. This force is ignored because it is small compared to soil interaction forces. Secondly, there is additional resistive force due to churning or moving the soil already in the bucket. The bucket fills with dirt if the bucket keeps moving forward. Eventually, force on the bucket builds until the hydraulic system reaches its maximum pressure. In order to model this phenomenon, the stiffness center calculation is modified. In order to understand this modification, it is helpful to decouple Eqn. 6.8 and remove the Laplace operators.

$$\begin{bmatrix} \dot{t}_c \\ \dot{n}_c \end{bmatrix} = \begin{bmatrix} -\frac{\lambda}{T_{rt}} & 0 \\ 0 & -\frac{1}{T_{rn}} \end{bmatrix} \begin{bmatrix} t_c - t \\ n_c - n \end{bmatrix} \tag{6.9}$$

A new variable λ is added to Eqn. 6.9. The affect of the soil accumulation force is approximated using λ. If $\lambda = 1$, the update is just like it was in Eqn. 6.8. If $\lambda = 0$, the stiffness center in the tangential bucket direction does not change. This means that force builds up between the bucket and the soil.

$$\lambda = \begin{cases} 0 & t < t_c \ \ \& \ \ V_{max} \ \leq \ V_{load} \\ \frac{V_{max} - V_{load}}{V_{max}} & t < t_c \ \ \& \ \ 0 < V_{load} < V_{max} \\ 1 & else \end{cases} \tag{6.10}$$

Note that the tangential coordinate, t, points into the bucket opposite the direction of the teeth (Figure 6.2).

6.3 Graphics

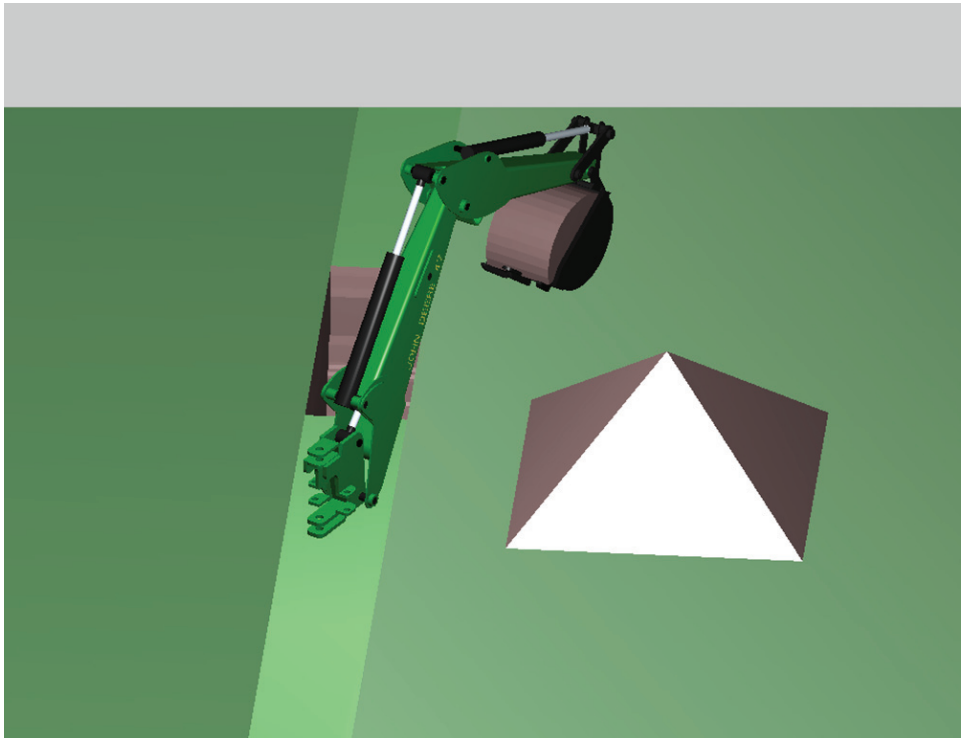

Figure 6.3: V-HEnRE's graphic display.

Visual feedback from V-HEnRE is generated using a C++/OpenGL application running in a Windows environment (Fig 6.3). This display provides feedback on the backhoe's orientation, trench depth, volume of dirt in the bucket and quantity of dirt removed. The graphics were displayed on a 20inch monitor. The backhoe links and cylinders were created using a solid modeling program [29] and exported as a ".slp" file. The ".slp" file renders the surface of each part as colored triangles. This

information can be systematically converted into OpenGL functions that draw the corresponding part. The advantage of this method is that it allows a pre-existing solid model to be leveraged in the creation of visual displays. Similarly, Simulink modeling of the backhoe or excavator can also be utilized. Information related to the backhoe orientation, trench depth, bucket load and removed dirt volume is received via UDP from the xPC-target application simulating the backhoe and soil. To avoid a conflict of computer resources and update rates the OpenGL based graphic display is run on a different Windows-based PC than the one controlling the PHANToM.

6.4 Comparison Plots

Several simplifying assumptions were made to eliminate the stiff states from the model of the hydraulic system. In addition, the model does not capture uncertainity since the actual flow will match the expected flow. The following tests use the same "Arc" and "Elbow " trajectories from Chapter 4. Figure 6.4 plots the responses from HEnRE and V-HEnRE for these two trajectories in task-space or on the r-z plane. The bucket angle is held at a constant value. Figures 6.5 and 6.6 plot the coordinates error for each trajectory. The simulator has less overshoot and goes to zero steady-state error. The response times seems to be similar for both the simulator and the test-bed.

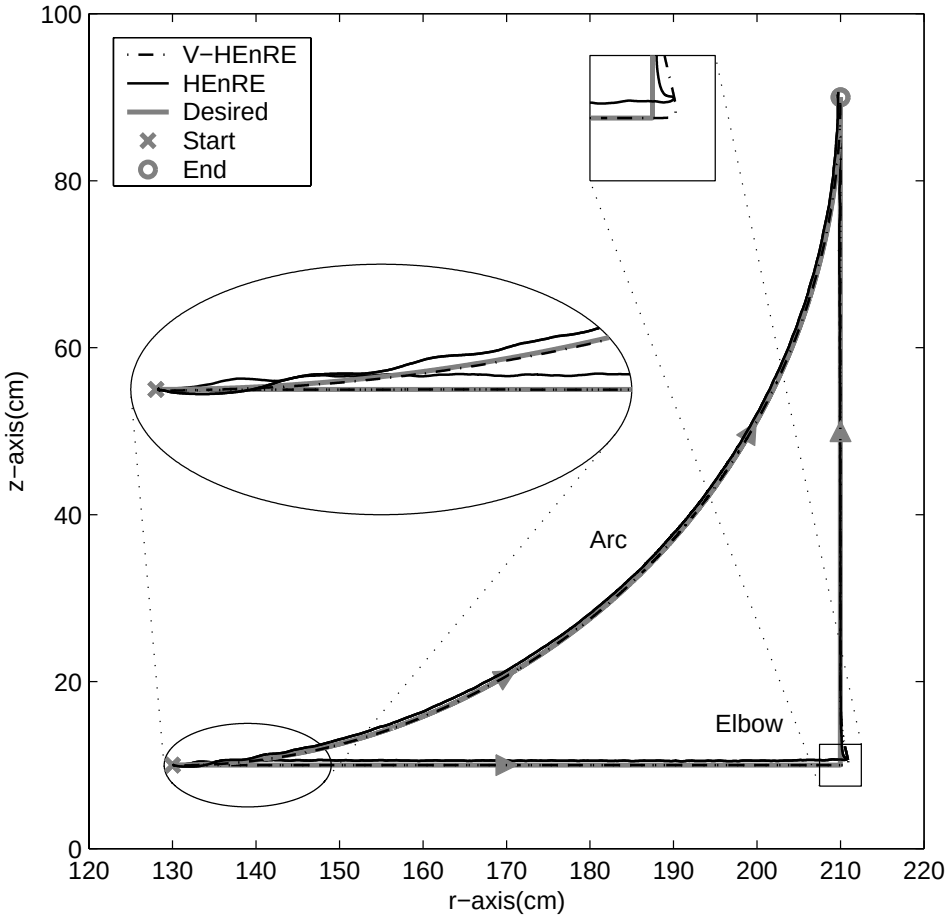

Figure 6.4: V-HEnRE and HEnRE response to an "Elbow" and an "Arc" trajectories. The dash-dot line is the tracking error from V-HEnRE and the solid line is the error from HEnRE.

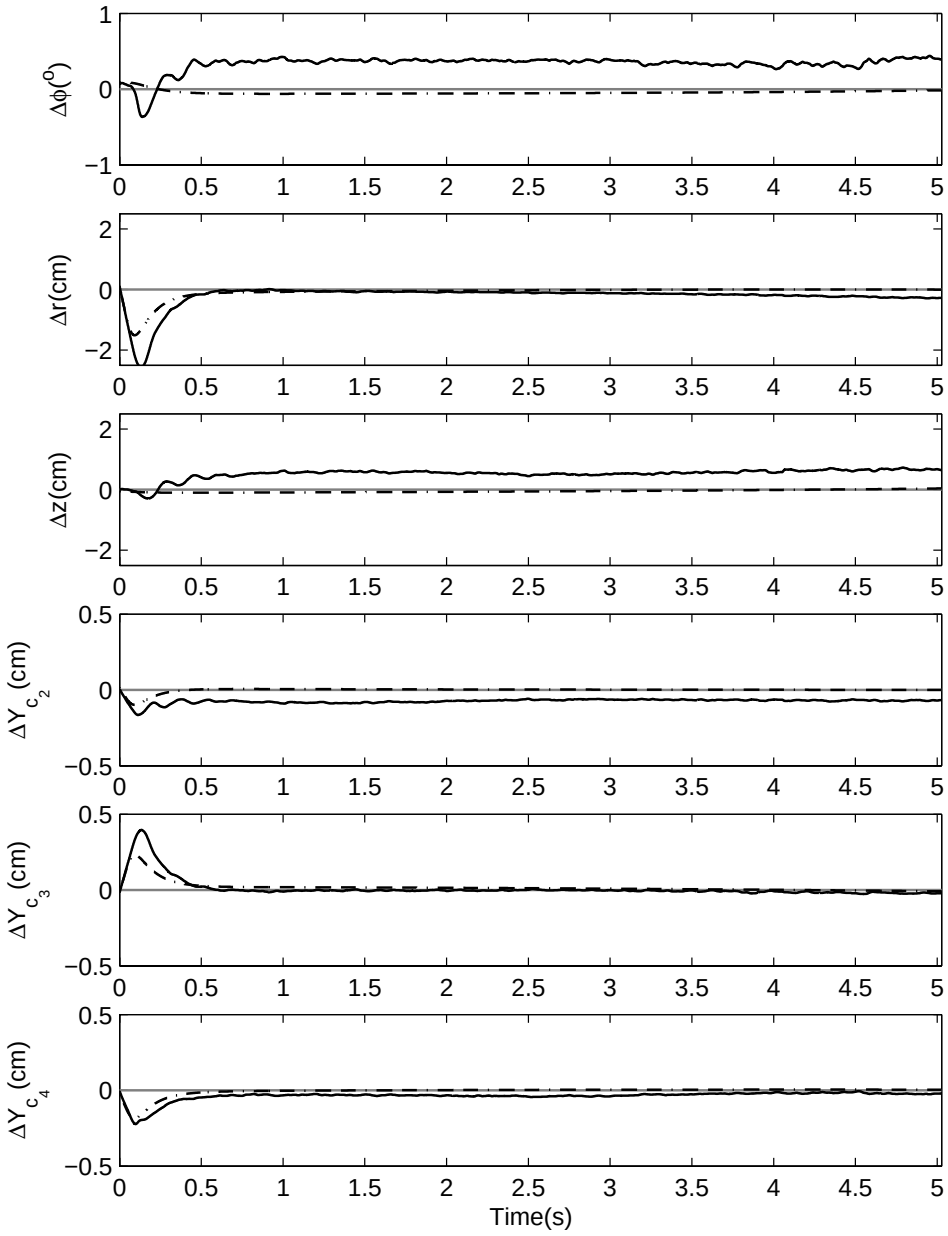

Figure 6.5: Task-space (r,z,ϕ) and cylinder-space (Y_{c_2},Y_{c_3},Y_{c_4}) error plots for the "Arc" trajectory. The dash-dot line is the tracking error from V-HEnRE and the solid line is the error from HEnRE.

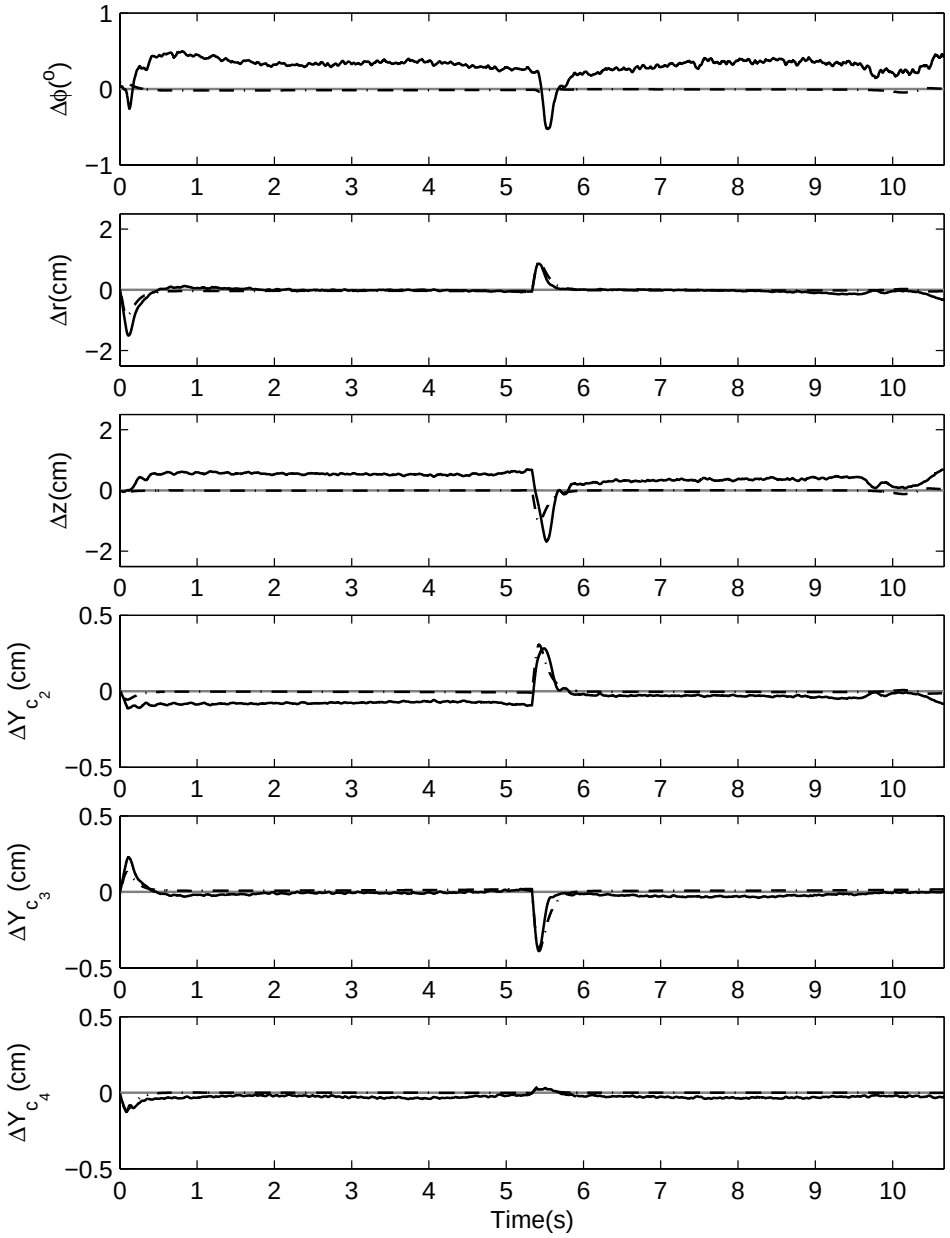

Figure 6.6: Task-space (r,z,ϕ) and cylinder-space (Y_{c_2},Y_{c_3},Y_{c_4}) error plots for the "Elbow" trajectory.

6.5 Summary

This chapter describes a simulator based on the backhoe test-bed used in this project. The backhoe and soil are simulated in Simulink/xPC-target. The graphics are displayed using C++/OpenGl and the backhoe links in the graphics orginate from a ProE model. Haptic feedback is supplied using the same Omni PHANToM and software used to control the actual backhoe test-bed. While this backhoe simulator is not a scientific contributions, this setup could be easily modified for future controllers or other test-beds. This simulator is important to this project because it is used for the human factors testing of the coordinated haptic control scheme developed for backhoes and excavators described in the next chapter.

CHAPTER VII

HAPTIC CONTROL AND EVALUATION

The primary goal of this project is to explore how haptic interfaces can enhance the ability of novice and expert operators to control hydraulic machinery such as backhoe-loaders and hydraulic excavators. Applying haptic control to mobile hydraulic equipment presents a practical yet challenging application. One criticism of many newer electro-hydraulic systems is a lack of "feel." To a haptics researcher this sounds like a call for haptic feedback in the human-machine interface. If a mechanical linkage is used to connect the main flow control spool to the control levers, there is some haptic feedback in the levers that is related to the pressures in the system due to the flow forces acting on the spools. As the pressures increase, the joystick stiffens. This haptic feedback, albeit small, is essentially eliminated in most pilot operated joysticks and totally removed in electro-hydraulic joysticks. However, a big part of the "feel" of the system comes from how the actual system responds to forces or higher work port pressures. At some point the high pressures slow down the system or naturally redirect flow to lower pressure circuits in a hydro-mechanical system. How this is done plays a large part in the "feel" of the system. In this chapter, a paradigm is presented that tries to merge these two concepts of "feel." Instead of trying to make the system transparent, the goal is to make the system react to forces in the system and then use haptic feedback to help alert the operator to these forces. By considering the system as an idealized two-port network, the goal is not to drive the output impedance term to zero in order to achieve transparency. Instead the goal is to shape this impedance so that the system provides a response or "feel" that is closer to an excavator with open center flow control valves.

Section 7.1 presented the basic coordinate and haptic control law used to control the endpoint of the backhoe test-bed and simulator. In section 7.2, a haptic force control method is derived and implemented called Impedance Shaping. This technique is designed to mimic the "feel" or force response of a backhoe or excavator contrlled with open-center flow control valves. Results from a series of human factors testing is presented that evaluate the Impedance Shaping technique in Section 7.3. Section 7.4 discusses the possible use of haptic feedback based on virtual fixtures. Virtual fixtures represent an other way that haptic feedback could be used to enhance operator control [69]. Section 7.5 shows how passivity monitoring or time domain could be used to enforce stability or passivity of backhoes or excavators. The primary motivation for using time domain passivity is to maintain stability if a direct feedforward force term was added to the haptic feedback being displayed by the impedance shaping. The major contributions from this Chapter are the Impedance Shaping control and the evaulation of this technique using 25 human subjects. These topics are included in [73].

7.1 Coordinated Haptic Control

The basic coordination control law uses a position scheme. This means that the position of the master in Cartesian coordinates is mapped to the Cartesian position of the backhoe's bucket. In comparison, on a standard backhoe/excavator the displacement of each axis of the joystick/lever is mapped to the rate (flow) of a cylinder. The velocity and position of the haptic interface is mapped and scaled into the workspace of the backhoe. The motion of the haptic interface is amplified by 25. This is often referred to as the velocity scale. The force scale is not explicitly used in the next section, but it would need to be on the order of $10,000$. This motion in Cartesian or task-space variables are then mapped into joint-space variables and then cylinder-space variables as described in Chapter 3. The haptic interface's position, x_h and

velocity, v_h are mapped into the backhoe's workspace and used to calculate the desired corrected or commanded velocity of the backhoe cylinders in Equation 4.49. In the following equation, the subscript h denotes haptic or hand and the subscript e denotes the endpoint of the backhoe.

$$v_{dc} = v_h + k_p \left(x_h - x_e \right) \tag{7.1}$$

The valve flow command is produced using the desired corrected velocity, v_{dc}, which is defined in Eq. 7.1. The v_d feedforward term represents a partial plant inversion as discussed in Chapter 4. The backhoe endpoint position, x_e, is fedback and low-pass filtered using poles that are similar to the valve spool. This results in a pair of closed-loop zeros that match the poles of the valve spools.

The haptic feedback force, F_h, is generated using a virtual spring that couples the motion of the haptic display to the motion of the bucket.

$$F_h = -k_h \left(x_h - x_b \right) \tag{7.2}$$

The constraints imposed by the backhoe are indirectly reflected through this virtual spring force. One example of this is workspace constraints. The backhoe's desired motion, x_d and $\dot{x}_d$, must be projected into the workspace of the backhoe. When this is implemented with the virtual spring force, it results in a virtual fixture [66, 114] in the shape of the backhoe's workspace [70]. A pump imposed flow limitation combined with cylinder area and backhoe kinematics results in a position and velocity dependent velocity limit that is also reflected through the virtual spring as a damping like haptic force sensation.

7.2 Impedance Shaping

In this section a new haptic/force control strategy is presented that will be referred to as "impedance shaping." This name is motivated by two-port networks [42] which

are often used to analyze haptic controllers. This technique reflects force by changing the remote manipulator's impedance instead trying to achiece transparency of the system. In comparison, to the definition of transparency in Chapter 2, a standard excavator could be described using the following idealized two-port network

$$\begin{bmatrix} F_h \\ -V_e \end{bmatrix} = \begin{bmatrix} -\frac{k_{spr}}{s} & 0 \\ -\frac{S_{vel}}{s} & \frac{1}{Z_{out}} \end{bmatrix} \begin{bmatrix} V_h \\ F_e \end{bmatrix} \tag{7.3}$$

In this equation, k_{spr} is the centering spring in the joystick/lever, S_{vel} is the gain relating the displacement of the lever to velocity of the corresponding cylinder and Z_{out} is the impedance seen by the corresponding cylinder. Typically, S_{vel} would not be a constant but rather a nonlinear function with a dead-zone around zero velocity and curves on each side with slopes that increase with increasing lever position. The output impedance, Z_{out}, is related to how the velocity of the excavator or backhoe changes based on the forces acting on the bucket. On many machines, this impedance remains high until the system pressure is high enough to open a relief valve. Since the impedance remains high, the force on the bucket or work port pressure has little effect on the commanded motion until it abruptly stops as the system's relief valve opens. In comparison, a system with open-center flow control valves redirects flow to lower pressure circuits, resulting in a gradual transition from high impedance to the system stalling out and a stall force or pressure that is related to lever position. This can limit digging force by limiting lever displacement, thus open-center excavators/backhoes are often said to have a better "feel," but are sometimes perceived to be weaker than their closed-center counterparts with equivalent pump capabilities.

Similarly, the controller used in this paper can be described as follows using an idealized two-port network. Starting with the haptic force in Eqn. 7.2.

$$F_h = -\frac{k_h}{s}\left(V_h - \frac{V_e}{S_{vel}}\right) \tag{7.4}$$

Even though it is not used in the human factors experiment, a direct force term is also added to this analysis.

$$F_h = -\frac{k_h}{s}\left(V_h - \frac{V_e}{S_{vel}} + \frac{F_e}{S_{force}}\right) \tag{7.5}$$

The hydraulic flow control can be approximated as follows.

$$-V_e = -S_{vel}V_h + \frac{1}{Z_{out}}F_e \tag{7.6}$$

Substituting Eqn 7.6 into Eqn. 7.5

$$F_h = \left(\frac{k_h}{sZ_{out}} + \frac{1}{S_{force}}\right)F_e \tag{7.7}$$

Resulting in the following two-port network.

$$\begin{bmatrix} F_h \\ -V_e \end{bmatrix} = \begin{bmatrix} 0 & \left(\frac{k_h}{sZ_{out}} + \frac{1}{S_{force}}\right) \\ -S_{vel} & \frac{1}{Z_{out}} \end{bmatrix} \begin{bmatrix} V_h \\ F_e \end{bmatrix} \tag{7.8}$$

As mentioned, the direct feedforward force term is not used in the user experiment, but could be added to enhance the force reflection. If it were present, it would show up as it does in Eqn. 7.8 as the "$1/S_{force}$" term. This means that the force feedback in this work originates from the $k_h/(sZ_{out})$ term with Z_{out} sufficiently high there is negligible force reflection. Since the valves are pressure compensated, Z_{out} remains high until the pressure relief valve controlling P_s is not able to maintain the required pressure drop across the orifice that the pressure compensator is regulating.

To reflect force through the impedance, Z_{out}, it is necessary to modify Z_{out} by changing the velocity command given to the valve based on the force on the bucket. This is done using the task-space coordinates r, z and ϕ (Fig. 7.1). The corresponding forces and torque F_r, F_z and τ_ϕ could be calculated from pressure transducers [72, 133]. In the results presented related to Impedance Shaping, a less noisy measurement of

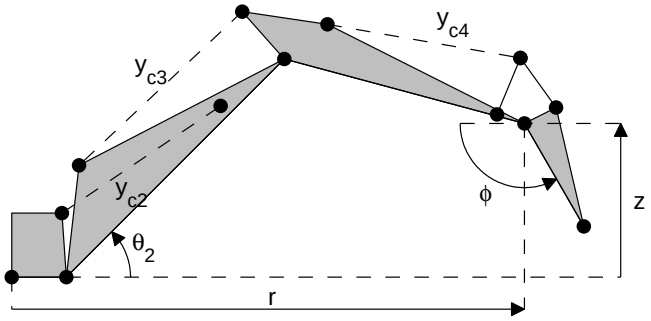

Figure 7.1: Description of backhoe coordinates.

these forces and torque is provided by a two-axis load-pin and an axial load cell that directly measures the forces acting on the bucket pins.

The first step to shaping the impedance is to define a stall curve. In this work the stall curve is defined as follows.

$$F_{stall} = F_{max}\sqrt{\frac{||v_{dc}||}{V_{max}}} \tag{7.9}$$

The modified velocity command is calculated using F_{stall}.

$$\beta = \begin{cases} 1 - \frac{||F_e||}{F_{stall}} & if \;\; 0 < v_{dc} \cdot F_e \;\; \& \;\; ||F_e|| < F_{stall} \\ 0 & if \;\; 0 < v_{dc} \cdot F_e \;\; \& \;\; F_{stall} \leq ||F_e|| \\ 1 & else \end{cases} \tag{7.10}$$

Note that the sign convention used for the force, F_e, represents the force that the backhoe is exerting on the environment. This means that when $v_{dc} \cdot F_e$ is positive, work is being done by the backhoe on the environment. The impedance shaping velocity gain, β, is multiplied by the task-space version of desired corrected velocity from Eqn. 7.1 to create a modified velocity command for the backhoe.

$$v''_{dc} = \beta \; v_{dc} \tag{7.11}$$

The boom and stick cylinders can be mapped to task-space coordinates r and z.

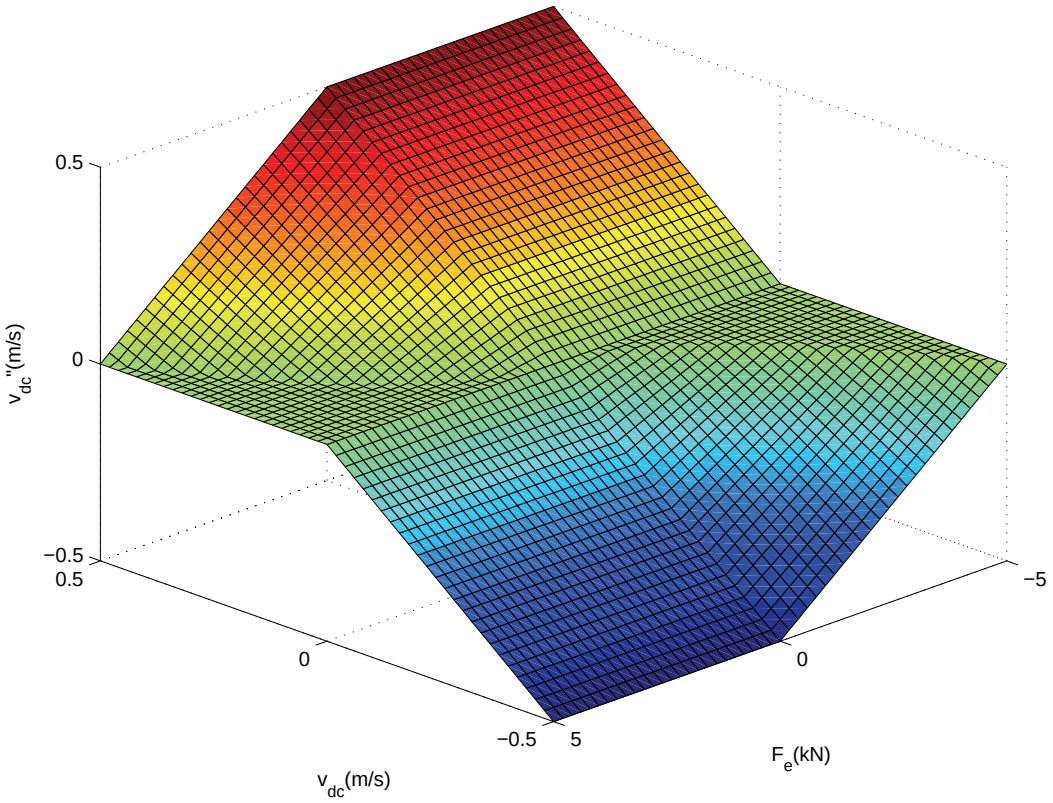

Figure 7.2: Impedance shaping velocity modification.

To preserve the desired direction, β is calculated for r and z jointly and then for ϕ. It is important to modify ϕ because large forces can be produced by the bucket due to the mechanical advantage of the bucket compared to the boom and stick. In Fig 7.2, the velocity modification can be visualized by ploting v_{dc}^{*} versus v_{dc} and F. There is nothing special about the specific stall force described in Eqn. 7.9 or the interpolation scheme in Eqn. 7.10. The important thing is that β is varied between 0 and 1 based on the forces and torque acting on the bucket.

The variable β is essetially an implementation variable; however, it is indirectly related to the backhoe's impedance. This can be see by taking a cross section of Figure 7.2 as shown in Figure 7.3.

$$v_{dc}'' = v_{dc} - \frac{F_e}{Z_{out}} \tag{7.12}$$

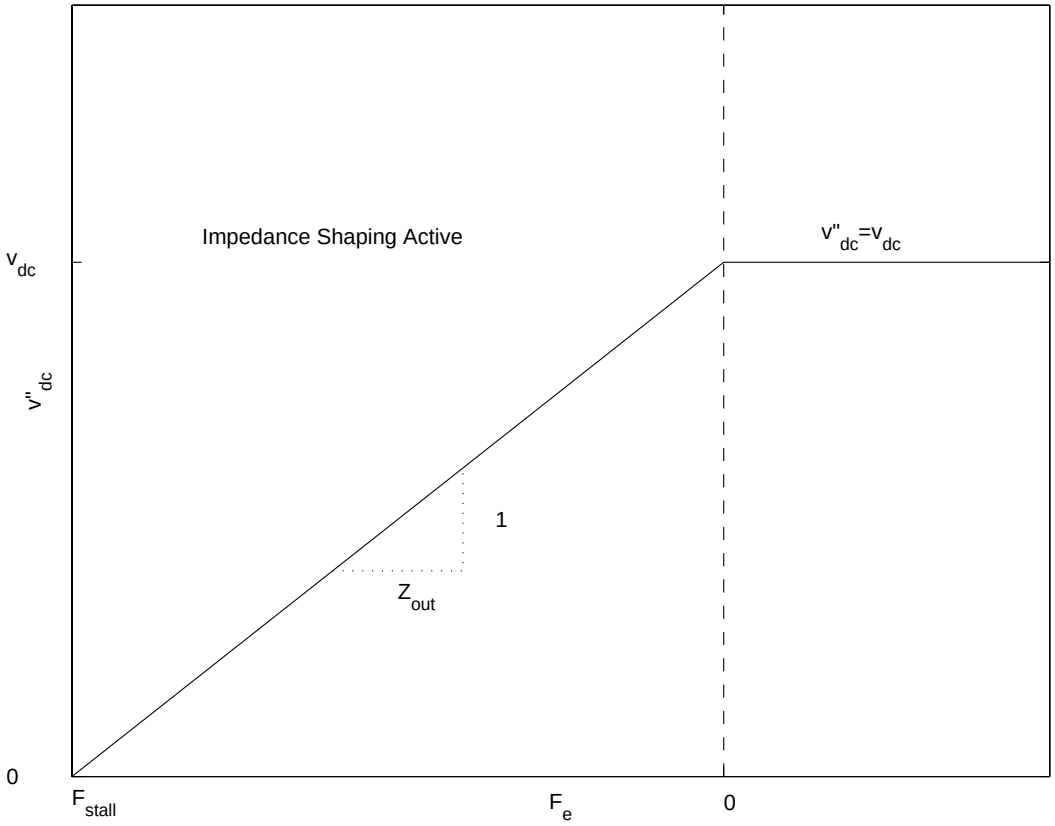

Figure 7.3: Cross section of impedance shaping controller.

Solving Equation 7.11 for β

$$\beta = \frac{v''_{dc}}{v_{dc}} \tag{7.13}$$

Substiting Equation 7.12 into Equation 7.13 results in

$$\beta = \frac{v''_{dc}}{v_{dc}} = 1 - \frac{F_e}{v_{dc} Z_{out}} \tag{7.14}$$

At $F_e = F_{stall}$

$$\beta = 1 - \frac{F_{stall}}{v_{dc} Z_{out}} = 0 \tag{7.15}$$

Solving for Z_{out}

$$Z_{out} = \frac{v_{dc}}{F_{stall}} \tag{7.16}$$

Substituting for the F_{stall} from Equation 7.9

$$Z_{out} = \sqrt{v_{dc}} \left(\frac{\sqrt{v_{dc}}}{F_{max}} \right) \tag{7.17}$$

Note that the shaped impedance is a function of velocity command and the parameters of the impedance shaping function. One interesting characteristic of this scheme is that the sensitivity of the force feedback can be adjusted using the parameter F_{max} in Eqn. 7.9 since Z_{out} is related to the force reflection term described in Equation 7.8. For example, if an operator is digging around a gas line one might want to reduce F_{max} to limit the bucket force and increase force reflection. On the other hand, if the goal is moving dirt as fast as possible the operator might want to turn off the impedance shaping control.

7.3 Human Factors Evaluation

Figure 7.4: V-HEnRE test setup.

In order to evaluate the impedance shaping scheme, a series of human factors tests were conducted. Twenty-five volunteer operators were used, primarily Georgia Tech students. Most operators had no prior experience with backhoes or excavators. Eight volunteers indicated between 0-10 hours of experience. The primary task was to dig trenches. These trenches were dug using the backhoe simulator described in Chapter 6 and the actual test-bed described in Section 2.5. The test setup for the backhoe simulator is shown in Figure 7.4. In the next subsection, the procedure will be summarized. Following this the objective results will be summarized. These results can be broken up into three catagories: environment force, digging productivity and detection. Two types of environmental forces will be addressed. First, the force during normal digging will be addressed. Second and most important is the force acting on buried objects because this is related to damage to things such as buried pipe lines. Therefore, lower object force would be better. During normal digging, higher is better for digging productivity, defined as volume of dirt removed per time. Lastly, examining subject's detection of buried objects, detection rate, detection time and hits before detection are recorded.

7.3.1 Controller

Four controllers were examinted. The controller denoted by "full" means that $F_{max} = 5kN$ (Eqn. 7.9). This is approximately the force that this backhoe test-bed can produce using the boom and stick. This corresponds to a maximum system/pump pressure, P_s, of $12MPa(1750psi)$. This force varies with configuration. Note that more force can be produced using the bucket due to mechanical advantage. The controller denoted by "half" means that $F_{max} = 2.5kN$ and "off" means that the impedance shaping is turned off and the velocity is not modified until the maximum system pressure is reached. The fourth controller whose results are not presented had impedance shaping on F_r and F_z, but no impedance shaping on τ_ϕ. Due to the

fact that there was no limit on bucket cylinder force and resistance in the r and z direction, this version of the simulation resulted in more bucket motion commanded by the operators and unrealistically large force; thus it will not be discussed further.

7.3.2 Procedure

The operators were given a two-part goal. First, dig dirt from the trench as quickly as possible and place the dirt in a pile off to the side. Second, detect objects when they were hit and minimize the force exerted on the objects. Each trial or trench was completed when a predetermined quantity of dirt was removed from the trench or the operator detected an object and pressed a button at the end of the handle twice

Each operator was allowed to dig 2 or 3 warm-up trenches to become familiar with the haptic interface and simulation display. A handle was attached to the PHANToM Omni. This handle is 1.5inches in diameter which is roughly the size of a tennis racket handle. The base of this handle or the end-point of the Omni is mapped to the wrist of bucket and supplied with translational force feedback. Handle rotation is mapped to the absolute bucket angle, ϕ, described in Fig. 7.1. One limitation of this interface is that there is no haptic feedback on the handle's rotation. In addition, the two angles of rotation that are not used are also unconstrained.

After becoming familiar with the control and simulator, each subject dug 32 virtual trenches. The controller type was systematically changed between trenches to distribute any learning effects across the different controllers. The location of the buried objects was randomly varied from trench to trench. The three objects used were planes at different angles.

After completing the 32 simulated trenches, the operator dug two trenches in the soil bin using the actual backhoe test-bed. For consistency, the viewpoint of the simulator was similar to the viewpoint when they operated the backhoe. The first trench was straight back from the backhoe and the second trench was dug at an angle.

The dirt was dumped in a second container located besides the primary soil bin. An uninstrumented object was placed in one of the two trenches. The operator sat on a platform next to the tractor. This was done because putting the operator and haptic interface directly on the tractor resulted in unstable behavior due to coupling between the backhoe and the base of the backhoe being fedback through the interface. One issue that could be playing a role in exaggerating this behavior is backlash between the tractor and base of the backhoe. This is a characteristic unique to tractor-mounted backhoes mounted to the tractor's three-point hitch. More details on the precedure and data collected is presented in Appendix D.

7.3.3 Statistical Analysis

All the confidence intervals plotted in the following sections have 95% or 99% confidence intervals and assume a normal distribution with an unknown standard deviation. The only 95% or 99% confidence interval are the plotted checking for learning trends in Section 7.3.8. The statistical methods used to calculate confidence intervals and test hypotheses are presented in Appendix C.1. The test of hypothesis used is commonly referred as the paired t-test. It is used to compare the mean of two normal populations and does not assume that the population variances are equal. The calculations for the confidence intervals and paired t-tests presented are located in Appendix C.2.

7.3.4 Force on Environment

As a point of comparison, confidence intervals related to peak digging force is plotted in Fig. 7.5 for both HEnRE and V-HEnRE. The average force peaks are higher for the simulation. Paired t-tests verifies that there is statistically significant difference is digging force peaks between HEnRE and V-HEnRE (Table 7.1). There are many possible explainations for this difference, including operators being more carefull with the actual backhoe, and variations between the soil and backhoe simulation models

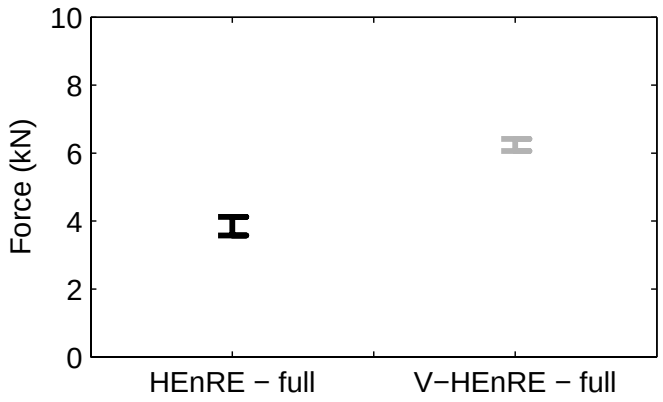

Figure 7.5: Comparison of force peaks during normal digging for HEnRE and V-HEnRE. (Corresponding paired t-test and the confindence interval calculations are located in Table 7.1 and Table C.12 respectively)

Table 7.1: HEnRE and V-HEnRE digging force paired t-test. (The corresponding confidence interval plot and paired t-test data are located in Figure 7.5 and Table C.13 respectively)

Controller #1	Controller #2	claim	$\Delta x(N)$	confidence
V-HEnRE-full	HEnRE-full	$\mu_{V-HEnRE} - \Delta x > \mu_{HEnRE}$	2098	99%

and the actual test-bed.

The stiffness of the object used in the simulation was experimentally determined by contacting the backhoe with a hard cement floor. This experimentally determined stiffness of $120,000 N/m$ actually has more to do with the stiffness of the backhoe than the stiffness of the floor, which should be orders of magnitude higher. This is a rough estimate of the backhoe's stiffness because the actual stiffness varies with configuration. Instead of modeling the backhoe's compliance, this stiffness was lumped with the object's stiffness.

One of the challenges of detecting buried objects captured by this soil model is that force peaks resulting from normal digging (Fig. 7.6 - black) are on the same order as the force peaks resulting from hitting an object (Fig. 7.7 - grey). These values should be even closer for objects with lower stiffness. The reason less force would

build up for an object with more compliance is that the response of the impedance shaping control is limited by the bandwidth and delay of the valve (Equation. 6.1). The backhoe continues to move as the valves close. The slower the valve closes, the more the cylinder moves resulting in higher forces. The dynamics of a natural hydraulic system stall is not slowed down by the dynamics of the valves. This only happens with an artificial stall induced by the impedance shaping control.

Two different metrics of digging forces are presented in Fig. 7.6. The black confidence intervals are related to the force peaks of the different controllers and the grey confidence intervals show the average digging force while the backhoe is digging but not contacting a buried object. Paired t-tests on these two metrics indicate statistically significant differences with the three controllers (Tables 7.2 & 7.3). These peak metrics are presented in Fig. 7.7 for contact with buried objects. The grey confidence intervals include all the force peaks each time contact is made with the object. The black ones only include the largest of these force peaks for each trench. Paired t-tests on the metrics of object force also indicate statistically significant differences between the controllers (Tables 7.4 & 7.5). In all of these cases, the forces are smaller for the "half" controller and largest for the "off" controller. Since the magnitude of this force is related to damage to the buried object the lower force represents an improvement.

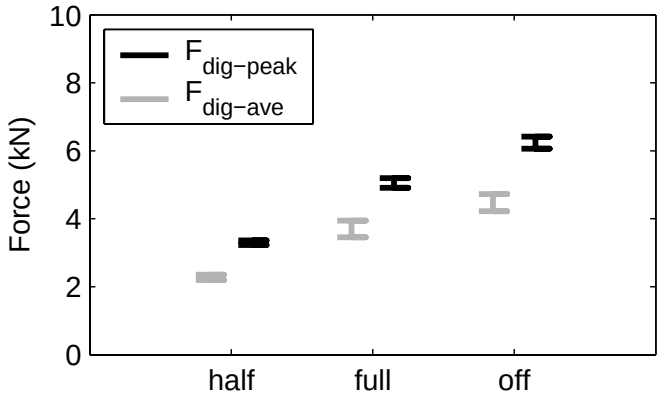

Figure 7.6: Force peaks during digging are summarized for the three controllers with the black confidence intervals. The grey ones represent the average force during digging. This data only includes trenches where contact was not made with any objects. (Corresponding paired t-tests and the confindence interval calculations are located in Tables 7.2-7.3 and Tables C.14-C.15 respectively)

Table 7.2: Paired t-test comparing digging force peaks with the V-HEnRE controllers. (The corresponding confidence interval plot and paired t-test data are located in Figure 7.6 and Table C.16 respectively)

Controller #1	Controller #2	claim	$\Delta x(N)$	confidence
full	half	$\mu_{full} - \Delta x > \mu_{half}$	1615	99%
off	full	$\mu_{off} - \Delta x > \mu_{full}$	982	99%
off	half	$\mu_{off} - \Delta x > \mu_{half}$	2773	99%

Table 7.3: Paired t-test comparing average digging force with the V-HEnRE controllers. (The corresponding confidence interval plot and paired t-test data are located in Figure 7.6 and Table C.17 respectively)

Controller #1	Controller #2	claim	$\Delta x(N)$	confidence
full	half	$\mu_{full} - \Delta x > \mu_{half}$	119	99%
off	full	$\mu_{off} - \Delta x > \mu_{full}$	460	99%
off	half	$\mu_{off} - \Delta x > \mu_{half}$	1963	99%

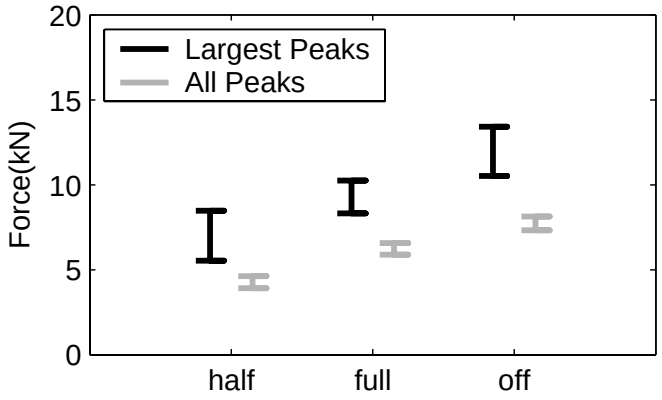

Figure 7.7: This plot demonstrates the peak forces on the object. The grey represent every time contact is made with an object and the black only represent the largest force peak on the object for each trench. (Corresponding paired t-tests and the confindence interval calculations are located in Tables 7.4-7.5 and Tables C.18-C.19 respectively)

Table 7.4: Paired t-test comparing the largest force peaks on the object with the V-HEnRE controllers. (The corresponding confidence interval plot and paired t-test data are located in Figure 7.7 and Table C.20 respectively)

Controller #1	Controller #2	claim	$\Delta x(N)$	confidence
full	half	$\mu_{full} - \Delta x > \mu_{half}$	708	99%
off	full	$\mu_{off} - \Delta x > \mu_{full}$	460	99%
off	half	$\mu_{off} - \Delta x > \mu_{half}$	1963	99%

Table 7.5: Paired t-test comparing all force peaks on the object with the V-HEnRE controllers. (The corresponding confidence interval plot and paired t-test data are located in Figure 7.7 and Table C.21 respectively).

Controller #1	Controller #2	claim	$\Delta x(N)$	confidence
full	half	$\mu_{full} - \Delta x > \mu_{half}$	1517	99%
off	full	$\mu_{off} - \Delta x > \mu_{full}$	1017	99%
off	half	$\mu_{off} - \Delta x > \mu_{half}$	2970	99%

7.3.5 Digging Productivity

The same trend is seen for digging productivity shown in Fig. 7.8; however, for digging productivity larger is better. Again paired t-tests verifies these trends for digging productivity (Table 7.6). The digging productivity is defined as volume of dirt removed per time interval. The data used to create this plot was only taken from the trials where no objects were hit. This indicates that the impedance shaping control reduces the digging efficiency. However, the percent decrease in productivity is less than the percent decrease in force. The decrease in productivity might be explained by the increased resistance or awareness of forces acting on the bucket. It is interesting to note that the average haptic force for the "full" and "half" controllers are nearly identical (Fig. 7.9). However, test of hypothesis indicate with 95% confidence that the haptic force is less with the impedance shaping turned off (Table 7.7).

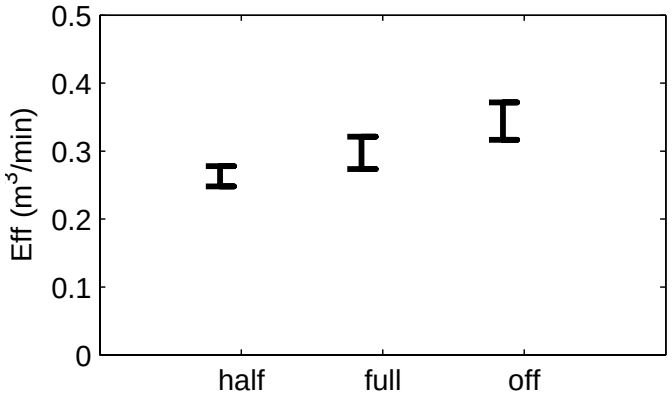

Figure 7.8: Digging productivity in soil volume per time. (Corresponding paired t-test and the confindence interval calculations are located in Table 7.6 and Table C.22 respectively)

Table 7.6: Paired t-test comparing digging productivity with the V-HEnRE controllers. (The corresponding confidence interval plot and paired t-test data are located in Figure 7.6 and Table C.23 respectively)

Controller #1	Controller #2	claim	$\Delta x(m^3/min)$	confidence
full	half	$\mu_{full} - \Delta x > \mu_{half}$	0.009145	99%
off	full	$\mu_{off} - \Delta x > \mu_{full}$	0.0141	99%
off	half	$\mu_{off} - \Delta x > \mu_{half}$	0.0529	99%

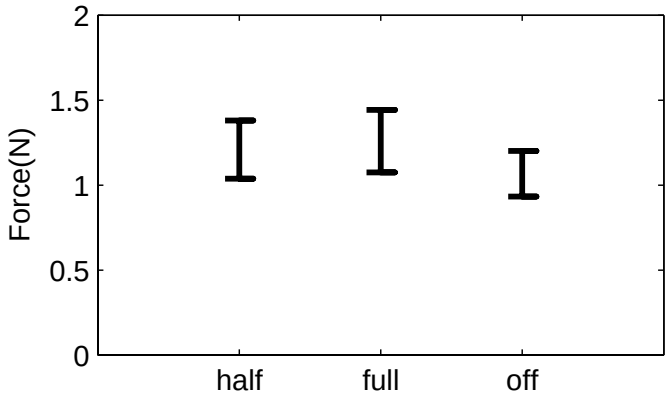

Figure 7.9: Average haptic force for each controller. (Corresponding paired t-tests and the confindence interval calculations are located in Table 7.7 and Table C.24 respectively)

Table 7.7: Paired t-test comparing average haptic force with the V-HEnRE controllers. (The corresponding confidence interval plot and paired t-test data are located in Figure 7.9 and Table C.25 respectively)

Controller #1	Controller #2	claim	$\Delta x(N)$	confidence
full	half	no claim	na	95%
off	full	$\mu_{off} - \Delta x > \mu_{full}$	0.0479	95%
off	half	$\mu_{off} - \Delta x > \mu_{half}$	0.00540	95%

7.3.6 Detection

The ultimate goals of haptic force reflection would be to minimize the damage or force exerted on objects such as buried utility lines. This can be approached in two ways. One way is to have the backhoe react to the forces acting on the bucket and another way is to improve the operator's ability to detect the objects and proceed accordingly. Figure 7.7 indicates that the impedance shaping can reduce the force on buried objects. Results related to detecting the objects are presented in Figures. 7.10 & 7.11. The detection success rates are shown in Table 7.9. With the enhanced force reflection, the success rate is higher for the "half" controller and lowest for the

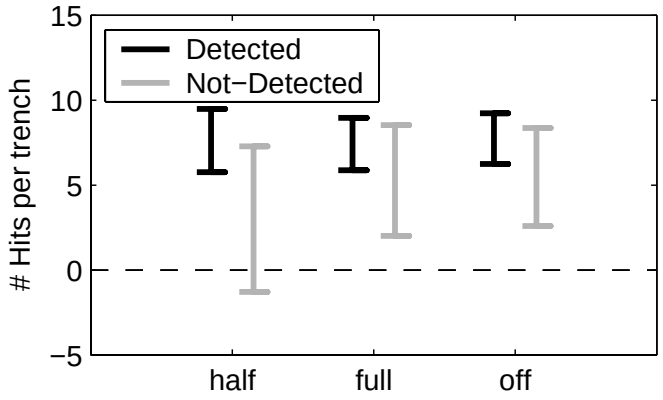

Figure 7.10: Number of time the object is hit if it is hit at least once. (Corresponding paired t-tests and the confindence interval calculations are located in Table 7.8 and Tables C.26 & C.27 respectively)

Table 7.8: Paired t-test comparing number of hits when the object is detected versus when it is not detected. (The corresponding confidence interval plot and paired t-test data are located in Figure 7.10 and Table C.28 respectively)

Controller	claim	$\Delta x(hits)$	confidence
half	$\mu_{detected} - \Delta x > \mu_{not}$	2.51	90%
full	$\mu_{detected} - \Delta x > \mu_{not}$	0.431	90%
off	$\mu_{detected} - \Delta x > \mu_{not}$	0.707	90%

"off" controller. Figure 7.10 shows the number of times contact is made if the object is hit at least once. It is interesting to note that the objects were hit more often and with a smaller standard deviation when the objects were detected. Test of hypothesis verifies that the objects were hit more times with 90% confidence when they were detected (Table 7.8). This is likely due to the operators probing the object in order to determine if there actually was an object. The number of hits was almost identical for all three controllers.

The detection time from the first nick and hardest hit are shown in Fig. 7.11. The detection time seems to be a little higher when the impedance shaping is turned off. The increased detection time from the first nick is modest and can only be claimed

Table 7.9: Success rate detecting the objects for different controllers.

Controller	detected	missed	Percent
half	52	15	77.6%
full	67	29	69.8%
off	80	38	67.8%

with 80% confidence (Table 7.10). One surprising result is that the hardest hits seem to occur significantly and consistently after the initial nicks. This is shown with 99% confidence (Table 7.11). This implies that the hardest hits and therefore maximum damage actually occurs when the operators are probing the object to see if there really is an object. This brings up two questions: Could the operator be trained to probe the object with more care in order to reduce the maximum force/damage to the object? Could the detection be enhanced and the damage minimized by using a direct feedforward force term that would make the haptic control more transparent?

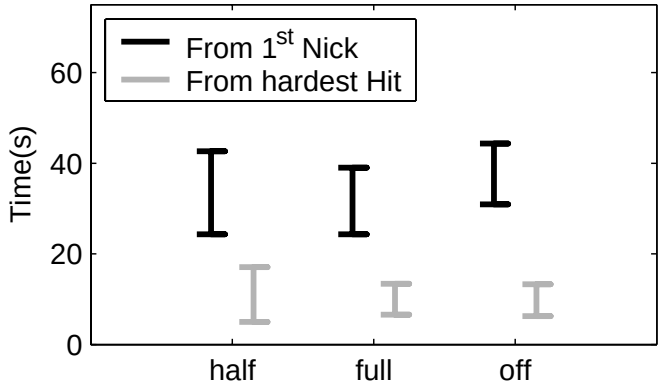

Figure 7.11: Detection time from first nick and hardest hit. (Corresponding paired t-tests and the confindence interval calculations are located in Tables 7.10-7.11 and Tables C.29-C.30 respectively)

Table 7.10: Paired t-test comparing detection time from first nick with the V-HEnRE controllers. (The corresponding confidence interval plot and paired t-test data are located in Figure 7.11 and Table C.31 respectively)

Controller #1	Controller #2	claim	$\Delta x(sec.)$	confidence
full	half	no claim	na	80%
off	full	$\mu_{off} - \Delta x > \mu_{full}$	2.80	80%
off	half	$\mu_{off} - \Delta x > \mu_{half}$	0.560	80%

Table 7.11: Paired t-test comparing the detection time from the first nick versus the hardest hit. (The corresponding confidence interval plot and paired t-test data are located in Figure 7.11 and Table C.32 respectively)

Controller	claim	$\Delta x(sec.)$	confidence
half	$\mu_{nick} - \Delta x > \mu_{hardest}$	12.7	99%
full	$\mu_{nick} - \Delta x > \mu_{hardest}$	14.4	99%
off	$\mu_{nick} - \Delta x > \mu_{hardest}$	21.1	99%

7.3.7 Subjective Comments

Comments from test subjects varied; however, some patterns emerged.

- The most frequent positive comment was that the backhoe and simulator were "quick to learn and intuitive."

- The most frequent complaint was that the backhoe was "hard to lineup, jittery, bucket vibrated, hard to control swing." The cause of this is mechanical backlash at both ends of the swing cylinder. Some people had few problems controlling the swing, while other could not keep the swing from shaking. The complaint about the bucket vibrating is actually caused by the swing. When a limit cycle is enduced in the swing, the bucket wiggles back and forth causing an audible vibration. Fixing this problem would require a combination of mechanical changes to reduce the backlash and possible changes in the hydraulic control system.

- There were also frequent complaints about the "interface design, ergonomics, bucket/hand motion, bucket out of range and no wrist force feedback." All of these comments relate to the haptic interface: the Omni has two major drawbacks. First, it does not have haptic feedback around the wrist joint so it is impossible to tell when the bucket command is out of range or how much torque is being applied to the bucket. Second, there is a kinematical coupling of human between the rotating the handle (bucket angle) and moving the handle (translation of the bucket). Addressing these comments would require replacing and/or redesigning the haptic interface.

- Another common complaint was that "it was difficult to interpret forces related to a full bucket, obstacle contact and workspace constaints." These comments were primarily directed at the simulation. This implies that the subjects were

relying on other cues such as audible and better visual feedback when they operated the actual backhoe. Unfortunately, all these force are present and can all produce large haptic forces. This is a challenge that can not be avoided.

- There was also a few complaints about the haptic interface "slipping" or "letting go." This is caused by the operator overpowering the relatively small and weak Omni. The Omni will temporarily shut off its motors in order to avoid over heating. When this occurs it is very confusing to the user. Overpowering the haptic interface can be avoided by keeping a light touch on the display.

There were also comments about how the backhoe and simulator were similar or different.

- The most frequent comment was that they were "for the most part similar".
- The most frequently reported dissimilarity was noise. The interesting thing is that there was an identical number of people who thought the sounds were distracting as there were comments that the audible enhanced the ability to detect objects.
- The next most frequent comment was that the "2-D display used by the simulatation was inferior to the 3-D visual feedback with the actual backhoe."

Other comments that were only made by one or two participants include

- "The system was sentative to speed (of the operator's hand) and it can't go too fast". This comment is probably related to the comments about the haptic interface "slipping" or "letting go." Since the speed of the backhoe is limited, the operator will feel extra resistance if they tell it to go faster than what is possible.

- "Bucket filled with dirt automatically in the simulation, hard to fill the actual backhoe's bucket". The automatic filling is a result of simplying assumption necessary to make the soil model work.

- "Digging the second trench was harder." This comment was actually only made by one person; however, this difficultly was observed with many of the test subject by the test administrator. One possible explaination is the second trench (with the actual backhoe) was dug at an angle. The first trench dug in the soil bin and all the simulated trenches were dug straight back from the backhoe. This meant that it was a different motion. Just like some operators did not excite the swing backlash, some operators did not have a problem digging at an angle. This problem is probably also related to the ergonomic design of the user interface.

- "Joystick geometry didn't match the backhoe." Even though the kinematics are mapped, some people expect the joints and links of the haptic interface to be directly related to the backhoe. This might not be a problem if the kinematics of the haptic interface and the backhoe were completely different. Since they are similar it is a common assumption.

Many of the author's (test administrator's) subjective observations mirror the comments of the test subjects.

- The biggest draw back of the interface was the bucket control. The Omni with the custom handle had three drawbacks:

    1. There was no haptic feedback on rotation so the users couldn't feel the torque being produced by the bucket.
    2. Two degrees of rotation in the handle were not used. This means that the operator could move the handle without sending a motion command to the backhoe.

3. There was kinematic coupling through the human arm between the bucket translation and rotation.

- On the test-bed, some operators excited a limit cycle in the swing due to mechanical backlash. This limits cycle was very dependent on the operator or human dynamics.
- Many operator overpowered the joystick
- On the test-bed, many operators seemed to struggle with the trench that was dug at an angle as opposed to straight back from the backhoe. Since this motion was coordinated, this also means that the motion of the operator hand during digging was straight back from the Omni if the backhoe was straight back from the tractor. This is likely because this was a different motion than what they learned on the simulator.

Suggestions:

- Operate the swing or θ_1 in rate mode and consider moving to the other hand.
- Move bucket angle control to another hand or use a finger. This would mean that the major muscle in one arm would only be controlling r and z which are the two translational variable during digging.
- Create a buried object in the soil bin that can not be remove with the bucket.
- Instrument the immovable buried object so that force (or at least contact with the bucket) could be detected.

7.3.8 Learning

As previously mentioned, the controller type was periodically varied in an attempt to cancel out any learning effects related to the control. The location of the buried object was also randomly varied so the operator could not predict when and were it would be located. In order to look at learning trends three important metrics were split into bins. Bin #1 includes trails 1-4, Bin #2 includes trials 5-8 and so forth. The three metric chosen were largest force peaks on buried objects, all force peaks on objects and digging productivity. Confidence intervals for each bin with 95% confidence are ploted in Figures 7.12 - 7.14 From these plots it was concluded that there were no significant learning trends.

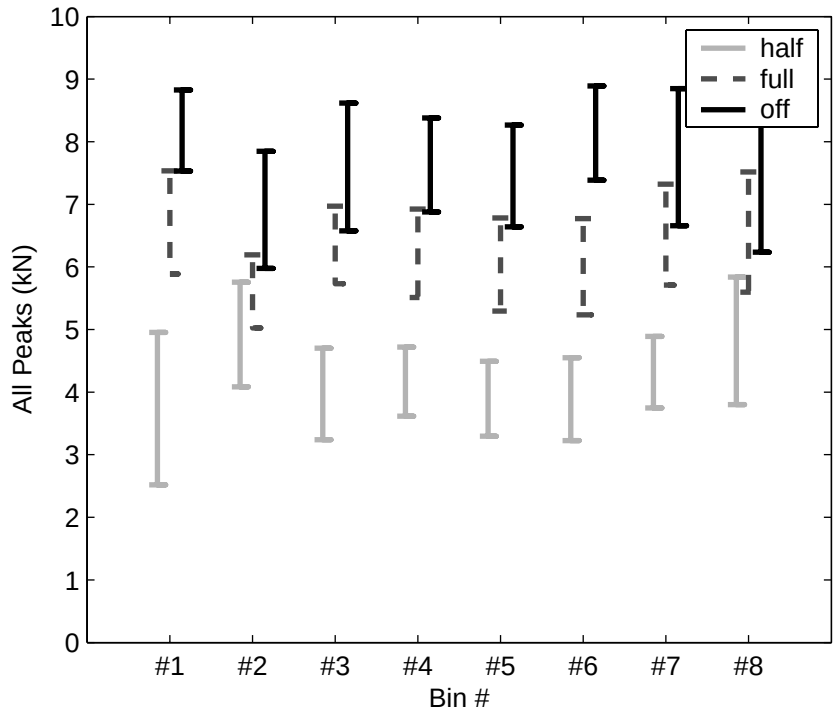

Figure 7.12: 95% confidence intervals on all force peaks seperated by bin.

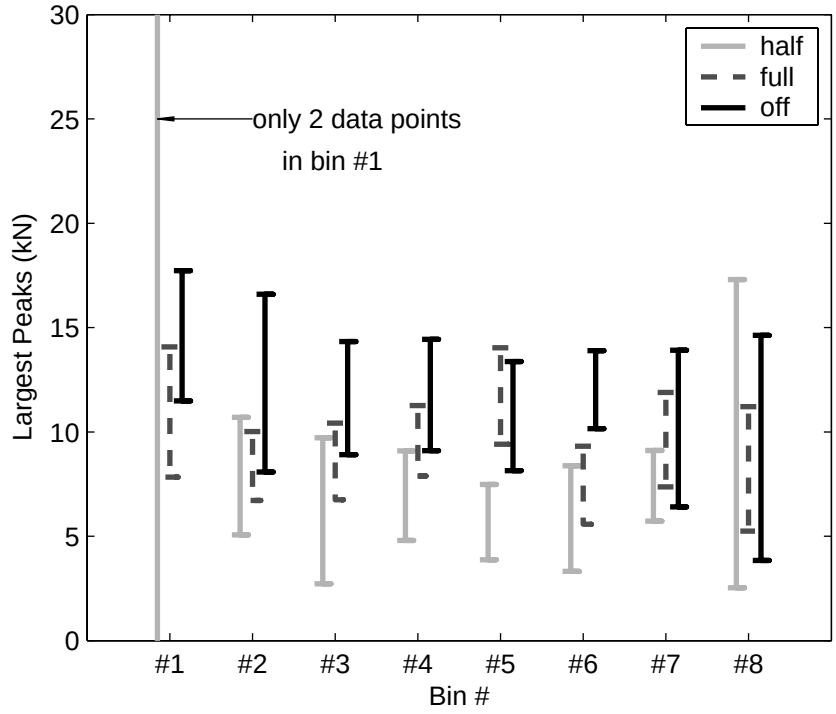

Figure 7.13: 95% confidence intervals on largest force peaks seperated by bin.

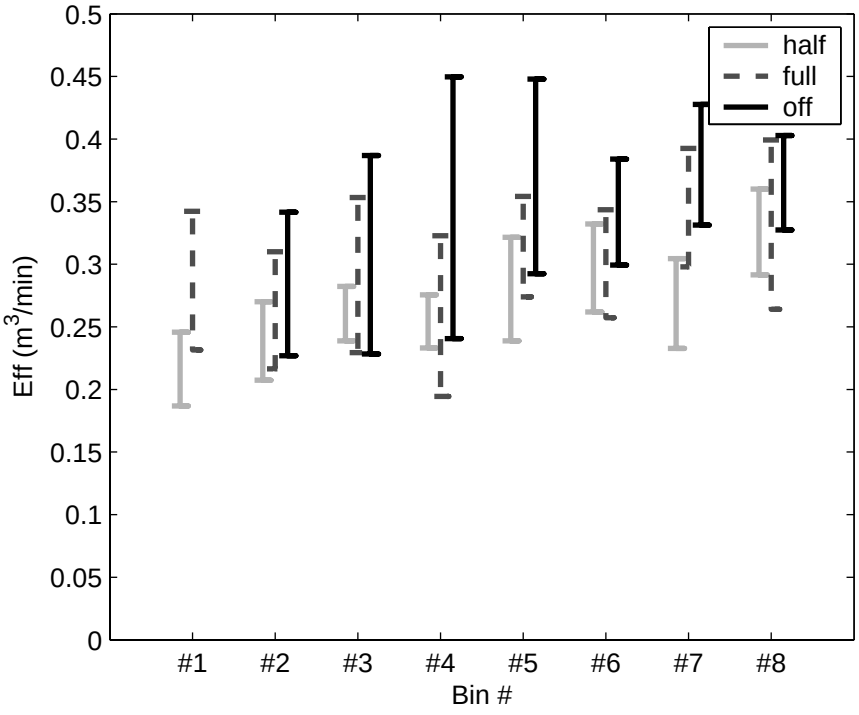

Figure 7.14: 95% confidence intervals on productivity seperated by bin.

7.4 Virtual Fixtures

Another way to produce haptic feedback during the operation of backhoes/excavators is to use virtual fixtures. A virtual fixture is a programmable virtual object that can produce haptic feedback. The use of virtual fixtures has been used for medical applications [114, 138]. Using a virtual fixture in this way is similar to using a ruler to draw a straight line [114]. It should be able to improve both speed and accuracy. Human factors testing in Kontz et al. [66] indicated the haptic feedback from a virtual fixture is beneficial doing pick and place maneuvers with a forklift truck.

One challenge of applying virtual fixtures to a digging task is its unstructured nature. However, a virtual fixture could be use to help avoid buried object or improve the accuracy of a trench or excavation. Ground penetrating radar [153] and previous knowledge (or some other detection technique) could be used to determine the location of buried objects, creating a virtual fixture to avoid contact with and therefore damage to a buried object. In the case of backhoes and excavators, a virtual fixture could be used to relay information about the desired grade or trench depth. The position of the digging implement could be estimated via a combination of GPS, a laser positioning system and joint sensors [143]. This position could then be compared with the desired shape of the ground being dug up. Operation would be normal during the bulk of the digging. Then, once the desired depth or shape was reached a haptic force would alert the operator that their commands were modified to achieve the desired result. This would mean that the operator would know that the desired grade had been reach and allow the operator to focus on another area.

Another application for a virtual fixture is to enforce workspace limits. When coordinated motion control is used, the workspace of the master will not necessarily be similar to the workspace of the slave device. One method would be to make the master similar to the slave which would enable the mechanical stop of the master device to supply the constraint forces [107]. Kinematic transformations allow the position of

the end effector (e.g. bucket) to be described using task-space coordinates, joint-space coordinates or cylinder-space coordinates. Displacements, velocity and forces can be mapped between the three sets of coordinates. This means that dissimilar devices can be used. However, it is critical to take into account the cylinder constraints in the inverse kinematic algorithm. It is advantageous to enforce software constraints that are just short of the actual mechanical constraints. If the mechanical stops are avoided it will decrease wear and stop spikes in the system pressure. If coordinated haptic control is being used an added benefit of not hitting the mechanical stops is force estimation. Pressure reading can also be used to estimate bucket force for haptic force reflection [133]. However, hitting the mechanical stop would cause an additional set of forces that would be added to and corrupt the force estimated by the pressure signals.

Under coordinated motion control, hitting either a physical or software cylinder travel constraint has an effect on the kinematic mapping as demonstrated in Chapter 3, essentially reducing the degree-of-freedom of the system. Both the position and velocity mapping between task-space and joint-space need to be changed when a constraint is present. This cannot be done at the joint-space to cylinder space conversion because these transformations are inherently decoupled from one another. When a cylinder constraint is hit the motion of the other cylinders must also be varied to maintain the best possible path. This was demonstrated in Figure 3.8. From a haptic standpoint, this can also be looked at as a virtual fixture. This is demonstrated in Figure 7.15. In this example HEnRE is commanded to go outside of the workspace. When the desired path of HEnRE (denoted by Path-hand) goes outside of the workspace the kinematic mapping modifies the trajectory to the closed path along the edge of the workspace. As distance between HEnRE and operator's hand builds, a haptic force is generated by a virtual spring. This coupling haptic force lets the operator know that the edge of the workspace has been reached.

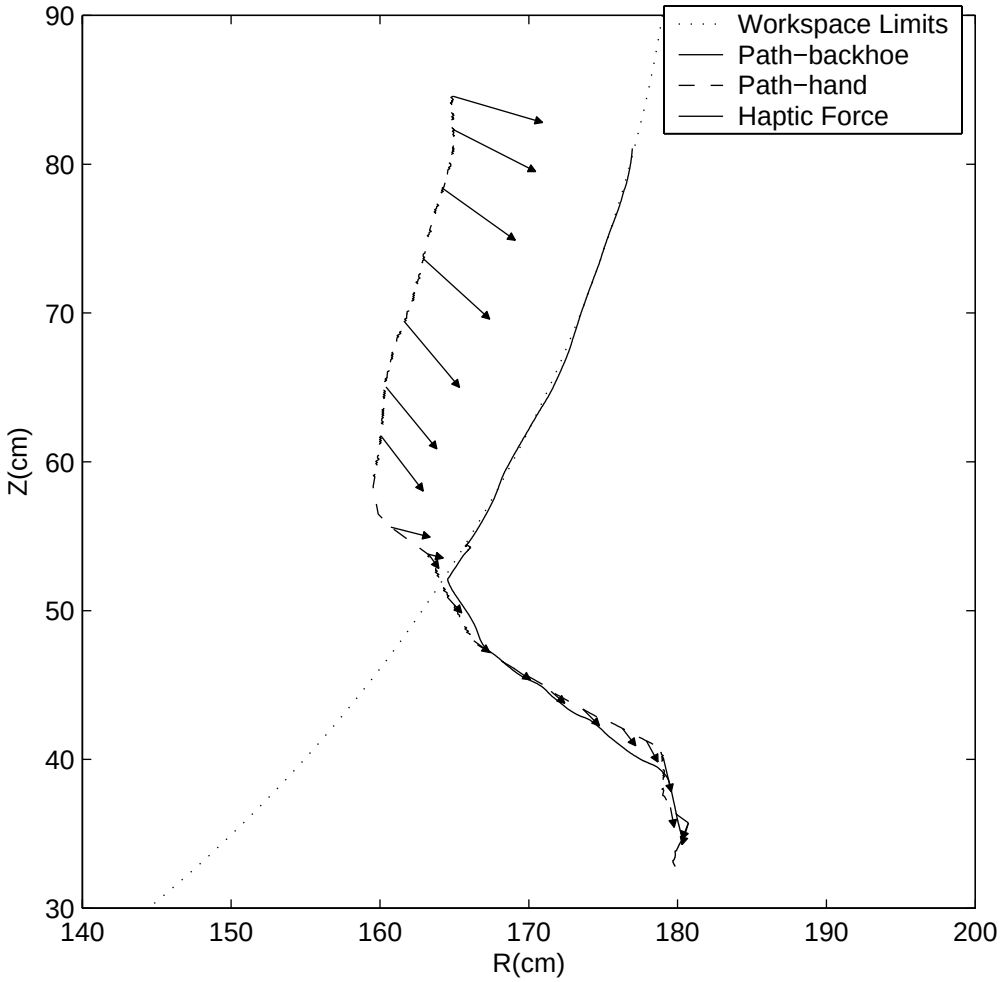

Figure 7.15: Haptic workspace constraints: The operator instructs HEnRE to move outside of the allowable workspace. The kinematic transforms enforce the cylinder constraints and result in a trajectory that stays in the workspace. A virtual coupling spring creates a haptic force denoted by the arrows that alert the operator of the edge of the workspace.

7.5 Passive Energy Balance Monitoring

Using the direct feedforward force term shown in Equations 7.5 & 7.8 has the possiblity of enhancing the user's ablity to detect buried objects by supplying a crisper and more transparent reflection of forces acting on the bucket. However, it has been observed that adding this term can cause unstable or non-passive behavior. This behavior is also operator dependent. One way to enforce passivity is to use a passivity monitoring technique or time-domain passivity. Such a controller will not stop the system from becoming non-passive, but adds damping to the system as needed in order to dissipate energy and restore passivity. If it is possible to add damping to the system, this controller does not need to assume anything about existing controllers. All it needs to do is monitor the flow of energy in and out of the system and add damping when needed. Note that the impedance shaping scheme does not introduce a direct force term and is implemented in such a way that it will only limit the energy output of the slave manipulator. This means that it essentially acts like a passive/dissipative brake on the backhoe.

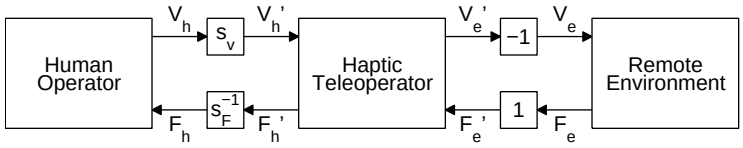

Figure 7.16: Generic 1-DOF haptic teleoperator.

Consider the passivity of the generic 1-DOF haptic teleoperator shown in Figure 7.16. This can be evaluated without loss of generality since the energy flow in a multi-DOF system can be evaluated in the same fashion and the variables that describe the flow of energy can be looked at using different coordinate system. In the case of a backhoe, this is important since the flow of energy can be described using Cartesian space, joint space or cylinder space variables.

The physical power entering the system from the human operator is

$$P_h = \boldsymbol{v}_h \cdot \boldsymbol{f}_h \tag{7.18}$$

and the physical power entering the system from the environment is

$$P_e = -\boldsymbol{v}_e \cdot \boldsymbol{f}_e \tag{7.19}$$

Where P is power, $\boldsymbol{v}$ is a velocity vector and $\boldsymbol{f}$ is the corresponding force vector. Since force and velocity scaling are used between the haptic interface and remote manipulator the passivity of the teleoperator needs to be evaluated in terms of an equivalent energy flow. The rate of "equivalent" energy, P'_h, flowing into the teleoperator from the human into the teleoperator is

$$P'_h = \boldsymbol{v}'_h \cdot \boldsymbol{f}'_h = (s_v s_f)(\boldsymbol{v}_h \cdot \boldsymbol{f}_h) = (s_v s_f) P_h \tag{7.20}$$

Similarly the rate of "equivalent" energy flowing into the system from the environment, P'_e, is

$$P'_e = \boldsymbol{v}'_e \boldsymbol{f}'_e = -\boldsymbol{v}_e \cdot \boldsymbol{f}_e = P_h \tag{7.21}$$

The total rate of energy flowing into the system is

$$P' = P'_h + P'_e = \boldsymbol{v}'_h \cdot \boldsymbol{f}'_h + \boldsymbol{v}'_e \cdot \boldsymbol{f}'_e = \boldsymbol{u}^T \boldsymbol{y} \tag{7.22}$$

where,

$$\boldsymbol{u} = \begin{bmatrix} \boldsymbol{v}'_h \\ \boldsymbol{f}'_e \end{bmatrix} \boldsymbol{y} = \begin{bmatrix} \boldsymbol{f}'_h \\ \boldsymbol{v}'_e \end{bmatrix} \tag{7.23}$$

Let, V be the "equivalent" energy in the teleoperator. From here on the word energy will refer to the "equivalent" energy or the "scaled" energy in the system as opposed to the actual physical energy that the teleoperator is exchanging with the human and the remote environment. If the system is passive

$$\int_0^t \boldsymbol{u}(\tau)\boldsymbol{y}(\tau) d\tau \geq V(t) - V(0) \quad \forall\ t \tag{7.24}$$

In other words, the net flow of energy into the system must be greater than or equal to the change in the energy stored by the system. Alternatively the system is passive if

$$\dot{V}(t) = \boldsymbol{u}(t)^T \boldsymbol{y}(t) - c(t) \quad \forall\ t \tag{7.25}$$

and

$$c(t) \geq 0 \tag{7.26}$$

The term $c(t)$ can be thought of as dissipation. The traditional way to make a system passive is to design a controller which guarantees that the teleoperator is always passive. This often leads to overly conservative teleoperators and that have excess damping during unconstrained motion. Alternatively the method of passive energy balance monitoring uses an abstract energy storage element, V_s to keep track of the passivity of the system. Assuming that c(t) is zero,

$$V_s(t) = \int_0^t \boldsymbol{u}(\tau)^T \boldsymbol{y}(\tau) d\tau + V_s(0) \tag{7.27}$$

If the system is behaving passively or dissipating energy (i.e $c(t) > 0$), abstract energy will be built up in the storage element, V_s. When the system becomes non-passive, V_s becomes negative, and a passivity controller is used to increase the dissipation of energy in the non-passive ports. This is analogous to adding damping to the control system. During passive operation the damping like elements β_1 and β_2 are set to zeros. How these passivity controllers work are shown in Figure 7.17. With the addition of these passivity controllers the actual rate of energy being stored by the teleoperator becomes

$$\dot{V}(t) = \boldsymbol{u}(t)^T \boldsymbol{y}(t) - c(t) - \beta_1 \left(\boldsymbol{v}_h' \cdot \boldsymbol{v}_h'\right) - \beta_2 \left(\boldsymbol{f}_e' \cdot \boldsymbol{f}_e'\right) \tag{7.28}$$

So, even if $c(t)$ becomes negative or the system becomes non-passive, it is possible to restore passivity by adapting β_1 and β_2. In other words, this type of passivity

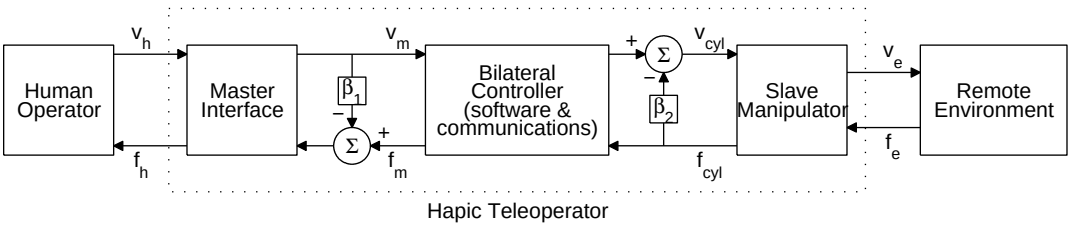

Figure 7.17: Passivity controller

control is designed to maintain passivity as opposed to guaranteeing passivity at any given instant in time.

As can be seen in Figure 7.17, the mechanical manipulator lies between the control system and the environment and human, respectively. The haptic interface is designed to have low inertia, low friction and is statically balanced. However, the slave manipulator has larger inertia, significant friction and is not statically balanced. This means that the backhoe can store both kinetic and potential energy and has significant energy dissipation due to friction. If the force is measured from pressure at the hydraulic cylinders all of these energy elements affect the energy that is actually delivered to the environment. The easiest method is to simply base the passivity control on the energy being imparted by the hydraulic cylinders. There the energy storage function for a given degree of freedom would simply be

$$V_{s_{cyl}}(t) = \int_0^t \left(\boldsymbol{v}'_h(\tau) \cdot \boldsymbol{f}'_h(\tau) + \boldsymbol{v}_{cyl}(\tau)' \cdot \boldsymbol{f}'_{cyl}(\tau) \right) d\tau + V_{s_{cyl}}(0) \tag{7.29}$$

Note the $\boldsymbol{v}'_{cyl} = \boldsymbol{v}'_e$. The difference between this storage function and the one used earlier is that the cylinder velocity and force are used instead of the end effector's force and velocity. Again assuming that coordinates are all represented in the same coordinate system, the velocities are equal, but the forces are not. Ideally the energy storage function being used could directly use the actual force acting between the end effector and the environment. This energy storage function will be renamed $V_{s_e}(t)$.

$$V_{s_e}(t) = \int_0^t \left(\boldsymbol{v}'_h(\tau) \cdot \boldsymbol{f}'_h(\tau) + \boldsymbol{v}'_e(\tau) \cdot \boldsymbol{f}'_e(\tau) \right) d\tau + V_{s_e}(0) \tag{7.30}$$

Taking the difference between these two energy storage functions results in the energy function of the mechanical manipulator.

$$V_{s_{mech}}(t) = V_{s_e}(t) - V_{s_{cyl}}(t) = \int_0^t \left(\boldsymbol{v}'_{cyl}(\tau) \cdot \left(\boldsymbol{f}'_e(\tau) - \boldsymbol{f}'_{cyl}(\tau) \right) \right) d\tau + V_{s_{mech}}(0) \quad (7.31)$$

Physically this function describes the energy being stored and dissipated by the mechanical manipulator. Ultimately the goal is to make $V_{s_e}(t)$ passive rather than $V_{s_{cyl}}(t)$. Note that $V_{s_{mech}}(t)$ is inherently passive since it can only store and dissipate energy. This means that if $V_{s_{cyl}}(t)$ is passive then $V_{s_e}(t)$ is passive, since

$$V_{s_e}(t) = V_{s_{cyl}}(t) + V_{s_{mech}}(t) \quad (7.32)$$

and combining multiple passive systems results in one passive system. However, this method would be by no means optimized. By dissecting $V_{s_{mech}}(t)$ it can be seen that

$$V_{s_{mech}}(t) = V_{s_{gravity}}(t) + V_{s_{friction}}(t) + V_{s_{inertia}}(t) \quad (7.33)$$

or alternately

$$\boldsymbol{f}'_e - \boldsymbol{f}'_{cyl} = \boldsymbol{f}_{gravity} + \boldsymbol{f}_{friction} + \boldsymbol{f}_{inertia} \quad (7.34)$$

Canceling out the effect of inertia would require a full dynamic model of the system. On the other hand, the effect of gravity is a function of position and therefore compensating for it would be more realistic. Friction is predominately a function of velocity even though it is also be affected by position and hydraulic pressure. From a performance point of view, compensating for friction is important because it would require additional passivity control or damping in the system to make $V_{s_{cyl}}(t)$ passive. From a passivity point of view it is important to never overestimate the friction.

7.6 Summary

This chapter addresses coordinated haptic control of backhoes and excavator, the central theme of this project. A new haptic/force control scheme is developed, called Impedance Shaping. This method is evaluated using a series of human factors tests.

The controllers are evaluated using measures such as digging productivity, the force built up on buried objects and detection rate. In addition to these major contributions, the use of virtual fixtures and time-domain passivity is discussed. Virtual fixtures or artificial force fields can be used to relay information related to workspace limits, desired trench depth or possibly buried objects. Time-domain passivity represents a passivity technique that could be applied to the haptic control presented in this thesis. Using time domain passivity would be particularly relevant if a direct feedforward force term was added to improve the "crispness" or "transparancy" of the force being reflected from the backhoe's bucket.

CHAPTER VIII

CONTRIBUTIONS AND FUTURE WORK

8.1 Summary

The major goal of this project is explore how haptic and coordinated control can be used to enhance an operator's ability to operate hydraulic machinery such as backhoes and excavators. Chapter 2 presents background work related to haptic theory, coordinated control and control of hydraulic machinery and describes the backhoe test-bed used in this work.

The kinematic algorithms necessary for coordinated haptic control of this backhoe are derived in Chapter 3, including task-space to joint-space and joint-space to cylinder-space mappings. This Chapter presents two methods for dealing with constraints imposed by the cylinder limits.

Chapter 4 describes the hydraulic system and the controllers used to regulate pump pressure and control the flow going to the actuators. A method is developed that aims to decouple pump pressure from cylinder flow using pressure compensators, electronic load-sensing and a new Moving-Window-Max-Filter. Other important features include a new type of input deadzone designed to implement limit cycles around zero velocity and a flow limiting scheme that guarantees bucket direction is always maintained even if the velocity command is reduced.

A technique is derived and implemented for pressure based force estimationin Chapter 5 that only utilizes pressure and position sensors.

Chapter 6 describes a virtual backhoe simulator (V-HEnRE) modeled after the backhoe test-bed (HEnRE).

Finally, coordinated haptic control is discussed in Chapter 7. A new haptic/force

scheme called Impedance Shaping is presented and implemented. This technique is evaluated using a series of human factors tests using 25 volunteers. Other topics discussed in this chapter include virtual fixtures, a direct feedforward force term and time-domain passivity.

8.2 Contributions

1. Chapter 3 demonstrates the importance of addressing kinematic constraints. Two different methods are presented. One is a closed-form solution based on mapping wrist of bucket and the other is more general solution that can be applied to the position of the bucket tip or teeth. The second requires a weighted numerical optimization. Using either method, it is also possible to create an additional constraint that avoids the kinematic singularity that occurs when the endpoint aligns with the first axis of rotation.

2. Section 4.3.1 presents a hydraulic system model which shows how pump pressure states can be decoupled from the flow control states. This explains how pressure compensators and electronic control of pump pressure can be used to decouple the control of pump pressure.

3. A Moving-Window-Max-Filter is proposed, implemented and verified in Section 4.3.4 for electronic load-sensing control of pump pressure. This filter allows cylinder port pressure to be used to specify the commanded pump pressure while removing any oscillations in the port pressures that could be fed back through the pump pressure.

4. An experimental identification technique is presented in Chapter 5 that can be used to determine gravity and friction terms. The identification data is obtained by moving one cylinder at a time at a constant rate. This eliminates inertia terms and the Coriolis/centrifugal term during the training runs. Only removing

gravity and friction terms from the measured hydraulic force, $F_{hydr} = A_c P_c - A_r P_r$ is a pragmatic solution since removing $M(\Theta)$ and $V(\dot{\Theta})$ require a clean acceleration estimate or measurement and a velocity estimate or measurement that is clean enough to be squared or multiplied by another velocity. This pressure based force estimate is compared with force measurement taken directly from force sensors attached to the buckets.

5. A new haptic/force control technique, referred to as Impedance Shaping, is proposed. This technique slows down the command velocity based on force resisting this motion. This is similar to the force response of an open-center excavator. With haptic coupling, the force acting on the bucket is indirectly displayed to the operator. Since this method can only drive the velocity toward zero, it eliminates the stability problems that must be address when the force is directly fed to the operator through the haptic interface. This method also offers the possibility of adjusting the feel by setting the maximum force parameter in the controller.

6. The Impedance Shaping technique is evaluated through a series of human factor tests with 25 novice operator. These results indicate the force or damage to objects can be minimized using Impedance Shaping. In addition, the detection of objects can be enhanced.

8.3 Future Work

A wise man once said, *Thesis projects are not completed, but rather they are abandoned*. With this thought in mind, here are some possible directions for future work.

1. One area of the future exploration is to look at alternative human interface designs. One major draw back of the current system is that there is no force feedback on the handle rotation. This means that there is no haptic feedback

related to bucket torque. In addition, two unconstrained rotational degree-of-freedom are not being used. This can be confusing because the operator can move without generating any commanded motion. Another problem is that even though the motion of haptic display relative to the backhoe is decoupled, there is coupling through the human's kinematics. For example, rotating the bucket without moving its position requires the axis of the handle to rotate without translational motion. In order to accomplish this motion, the operator's wrist must rotate and the major muscle in the arm must move the wrist in order to maintain the position of the handle's axis passing through the hand. An alternative would be to still use coordinated variables, but move some of them (e.g. swing angle, θ_1 and absolute bucket angle, ϕ), to the other hand [5]. This would mean that one hand controls r and z and the other controls θ_1 and ϕ.

2. Due to limitations on bandwidth and spatial scaling, a coordinated or resolved rate control with force reflection could be explored instead of the position based coordinated scheme used in this work.

3. Time-domain passivity experiments with the large spatial and power scaling that is needed for haptic backhoe control. The use of time-domain passivity is discussed in preceding chapter, but no experimental results are presented. One way to improve the operator's ability to detect buried objects would be to add a direct force forward term from the bucket forces. This has the potential to make the system non-passive and unstable. The time-domain passivity approach monitors the energy of the system and adds damping to the system in order to dissipate energy when the system is generating energy. Since this system does not need to assume any thing about the linearity or dynamics of the system is well suited to work the hydraulic control and Impedance Shaping strategies described in this work.

4. Human factors tests could examine both direct feedforward force term and impedance shaping. Time-domain passivity could be used to enforce passivity with the controller with the direct feedforward force term.

5. Expand on human testing related perception and cognitive issues related to how objects are perceived and detected.

6. In this work, the desired cylinder velocity fed forward to create a valve command related valve flow. One way this feedforward process could be improved would be to account for how the flow varies with oil temperature.

7. One current problem with the hydraulic level control is the backlash in the swing cylinders. A limit cycle has been observed. The existence and severity is highly dependent on the behavior of the human operator. This problem could be alleviated in two ways: reduce the amount of mechanical backlash and change the hydraulic control. One possible solution would be to change the spool cut in order to increase the compression force in the hydraulic cylinders. This would minimize the affect of the backlash by "pinching" the swing frame with the two swing cylinders.

8. Investigate the stability problem with placing the manipulator directly on the tractor. The basis of this problem is that moving the backhoe's manipulator moves the base of the backhoe which the haptic display is sitting on. This causes the haptic interface to move. This motion is amplified by the velocity scale, delayed and used to command the backhoe's motion. One issue that could be playing a role in exaggerated this behavior is backlash between the tractor and base of the backhoe. This is a characteristic unique to tractor-mounted backhoes mounted to the tractor's three-point hitch. Stiffening the connection between the tractor and backhoe bases could help this problem.

9. Install a bigger constant displacement pump or variable displacement pump to alleviate some of the flow restrictions.

10. Explore methods to improve flow control accuracy by considering changes in oil viscosity due oil temperature variations.

APPENDIX A

SFUN_BH_C2J.C

This a sample C s-function used in the simulink based HEnRE controller. It is a memoryless function that converts cylinder-space variables to joint-space variables.

```
/*************************************************************
sfun_bh_c2j.c
/*************************************************************

Author: Matthew Kontz
Date: June 23, 2004
Edit: October 21, 2005
Directions: "mex filename.c" on command prompt

Purpose:
The purpose of this file is to create a high-speed conversion
between position, velocity and effort variables for HEnRE.
This was changed in Oct 2005 to make it entirely discrete-time.
A new parameter was also added "Ts" or sampling time.



/*************************************************************
Based on sfuntmpl_basic.c: Basic 'C' template for a level 2
S-function
* Copyright 1990-2002 The MathWorks, Inc.
```

```
*************************************************************/

#define S_FUNCTION_NAME sfun_bh_c2j
#define S_FUNCTION_LEVEL 2

#include "simstruc.h" //  definition of the SimStruct
#include <math.h>
#include "bh_param.h"

static void mdlInitializeSizes(SimStruct *S)
{
    /* See sfuntmpl_doc.c for more details on the macros below */

    ssSetNumSFcnParams(S, 1);  /* Number of expected parameters */
    if (ssGetNumSFcnParams(S) != ssGetSFcnParamsCount(S)) {
        /* Return if number of expected != number of actual
         parameters */
        return;
    }

    ssSetNumContStates(S, 0);
    ssSetNumDiscStates(S, 0);

    if (!ssSetNumInputPorts(S, 1)) return;
    ssSetInputPortWidth(S, 0, 12);
    ssSetInputPortRequiredContiguous(S, 0, true); /*direct input
     signal access*/
```

```
    ssSetInputPortDirectFeedThrough(S, 0, 1); // direct feedthrough
     flag (1=yes, 0=no)

    if (!ssSetNumOutputPorts(S, 2)) return;
    ssSetOutputPortWidth(S, 0, 12);
    ssSetOutputPortWidth(S, 1, 2);

    ssSetNumSampleTimes(S, 1);
    ssSetNumRWork(S, 0);
    ssSetNumIWork(S, 0);
    ssSetNumPWork(S, 0);
    ssSetNumModes(S, 0);
    ssSetNumNonsampledZCs(S, 0);

    ssSetOptions(S, 0);
}

static void mdlInitializeSampleTimes(SimStruct *S)
{
time_T Ts = (time_T) *mxGetPr(ssGetSFcnParam(S, 0));
// sampling time
ssSetSampleTime(S, 0, Ts);
    ssSetOffsetTime(S, 0, 0.0);

ssSetInputPortSampleTime(S, 0, Ts);
ssSetInputPortOffsetTime(S, 0, 0.0);
```

```
ssSetOutputPortSampleTime(S, 0, Ts);
ssSetOutputPortOffsetTime(S, 0, 0.0);
}

#undef MDL_INITIALIZE_CONDITIONS   /* Change to #undef to remove
function */

#undef MDL_START  /* Change to #undef to remove function */

#undef MDL_UPDATE  /* Change to #undef to remove function */

#undef MDL_DERIVATIVES  /* Change to #undef to remove function */

static void mdlOutputs(SimStruct *S, int_T tid)
{
    const real_T *U = (const real_T*) ssGetInputPortSignal(S,0);
real_T *Y = (real_T*) ssGetOutputPortSignal(S,0);
real_T *Y2 = (real_T*) ssGetOutputPortSignal(S,1);


// variable and parameters definitions
real_T t1, t2, t3, t4;
real_T w1, w2, w3, w4;
real_T T1, T2, T3, T4;
real_T y1, y2, y3, y4;
real_T v1, v2, v3, v4;
real_T f1, f2, f3, f4;
```

```
real_T tA1B,  tC2D, tEFH, t23H, tH3G;
real_T rC, rS, r3Hx, r3Hy, r3H_2, r3H;
real_T C2, C3, C4, cH3G;
real_T wEFH, w23H, wH3G, wH2G;

/************************************************************
Cylinder-Space Input Variables
************************************************************

y = cylinder length
v = cylinder velocity
f = cylinder force
t = theta = joint angle
w = omega = joint velocity
T = tau = joint torque
************************************************************/

t1 = U[0];
y2 = U[1];
y3 = U[2];
y4 = U[3];
w1 = U[4];
v2 = U[5];
v3 = U[6];
v4 = U[7];
T1 = U[8];
f2 = U[9];
```

```
f3 = U[10];
f4 = U[11];

/*************************************************************
axis #2
*************************************************************/
tA1B = acos((r1A*r1A + r1B*r1B - y2*y2)/(2*r1A*r1B));
t2 = pi - t01A - tA1B - tB12;
C2 = -y2/(r1A*r1B*sin(tA1B));
w2 = C2*v2;
T2 = f2/C2;

/*************************************************************
axis #3
*************************************************************/
tC2D = acos((r2C*r2C + r2D*r2D - y3*y3)/(2*r2C*r2D));
t3 = pi-t12C-tC2D-tD23;
C3 = -y3/(r2C*r2D*sin(tC2D));
w3 = C3*v3;
T3 = f3/C3;

/*************************************************************
axis #4
*************************************************************/
tEFH = acos((rEF*rEF + rFH*rFH - y4*y4)/(2*rEF*rFH));
rC = rFH*cos(alpha+tEFH);
rS = rFH*sin(alpha+tEFH);
```

```
r3Hx = r3I + rC;

r3Hy = rFI + rS;

t23H = atan2(r3Hy,r3Hx);

r3H_2 = r3Hx*r3Hx + r3Hy*r3Hy;

r3H = sqrt(r3H_2);

cH3G = (r3H*r3H + r3G*r3G - rGH*rGH)/(2*r3H*r3G);

tH3G = acos(cH3G);

t4 = pi - (t23H + tH3G + tG34);


wEFH = y4/(rEF*rFH*sin(tEFH));

w23H = (r3I*rC + rFI*rS +rFH*rFH)/r3H_2*wEFH;

wH3G =

(rFI*rC - r3I*rS)*(r3G*cH3G - r3H)/(r3H_2*r3G*sin(tH3G))*wEFH;

C4 = -w23H - wH3G;

w4 = C4*v4;

T4 = f4/C4;


/************************************************************

Joint-Space Output Variables

************************************************************/


    Y[0] = t1;

Y[1] = t2;

Y[2] = t3;

Y[3] = t4;

Y[4] = w1;

Y[5] = w2;
```

```
Y[6] = w3;
Y[7] = w4;
Y[8] = T1;
Y[9] = T2;
Y[10] = T3;
Y[11] = T4;

Y2[0] = (r3G*r3G + rGH*rGH - r3H*r3H)/(2*r3G*rGH);
Y2[1] = sqrt(1 - Y2[0]*Y2[0]);
}



static void mdlTerminate(SimStruct *S)
{
}



/*=============================================================*
 * See sfuntmpl_doc.c for the optional S-function methods *
 *=============================================================*/

/*=============================*
 * Required S-function trailer *
 *=============================*/

#ifdef  MATLAB_MEX_FILE    /* Is this file being compiled
as a MEX-file? */
```

```
#include "simulink.c"      /* MEX-file interface mechanism */
#else
#include "cg_sfun.h"       /* Code generation registration
function */
#endif
)
```

APPENDIX B

LAGRANGIAN DYNAMICS

The dynamics of a backhoe/excavator is calculated here using the Lagragian approach. The Lagrangian is defined as in terms of the kinetic energy, KE and potential energy, PE.

$$L(\Theta, \dot{\Theta}) = KE(\Theta, \dot{\Theta}) - PE(\Theta) \tag{B.1}$$

where

$$\Theta = [\theta_1 \quad \theta_2 \quad \theta_3 \quad \theta_4]^T \tag{B.2}$$

Using the Lagragian the equations of motion can be found as follows.

$$\frac{d}{dt}\frac{\partial L}{\partial \dot{\Theta}^T} - \frac{\partial L}{\partial \Theta^T} = \tau \tag{B.3}$$

Kinetic energy is defined using the centroidal velocity of each link and the angular velocity of each link. The angular velocity, ω_i, is defined relative to the i^{th} local coordinate system. For revolute joints, a common robotics convention dictates that the z-axis is the axis of rotation and the x point from one origin to the next origin. Since this method takes the magnitude of the centroid velocity, it does need need to be described using the same set of coordinate systems as the angular velocities. The centroidal velocities, $\mathbf{v}_{c_i}$ are described using cylindrical coordinates relative to the base coordinate system. The kenetic energy is defined as follows

$$KE(\Theta, \dot{\Theta}) = \sum_{i=1}^{4} \frac{1}{2}\omega_i^T I_{c_i}\omega_i + \frac{1}{2}m_i \mathbf{v}_{c_i}^T \ \mathbf{v}_{c_i} \tag{B.4}$$

The inertia matrix I_{c_i} is defined at the centroid of the i^{th} link. The potential energy can be defined using the height of each centroid.

$$PE(\Theta) = m_2 g l_2 s_{2\gamma_2} + m_3 g(a_{s_2} + l_3 s_{2\gamma_3}) + m_4 g(a_{s_{23}} + l_4 s_{2\gamma_4}) \tag{B.5}$$

Equation B.3 can be rewrite as follows.

$$M(\Theta)\ddot{\Theta} + V(\Theta, \dot{\Theta}) + G(\Theta) = \tau \tag{B.6}$$

By expanding Equation B.3, it is possible write $M(\Theta)$, $V(\dot{\Theta}, \Theta)$ and $G(\Theta)$ in term of the partial derivative of the kinetic and potential energy. This enables the terms to found systematically with the aid of symbolic solver such as Maple.

$$\frac{\partial^2 KE}{\partial\dot{\Theta}\partial\dot{\Theta}^T}\ddot{\Theta} + \frac{\partial^2 KE}{\partial\Theta\partial\dot{\Theta}^T}\dot{\Theta} - \frac{\partial KE}{\partial\Theta} + \frac{\partial PE}{\partial\Theta} = \tau \tag{B.7}$$

$$M(\Theta) = \frac{\partial^2 KE}{\partial\dot{\Theta}\partial\dot{\Theta}^T} \tag{B.8}$$

where

$$M(\Theta) = \begin{bmatrix} m_{11} & m_{12} & m_{13} & m_{14} \\ m_{21} & m_{22} & m_{23} & m_{14} \\ m_{31} & m_{32} & m_{33} & m_{34} \\ m_{41} & m_{42} & m_{43} & m_{44} \end{bmatrix} \tag{B.9}$$

Each element of this matrix can be found using the following equation.

$$m_{ij} = \frac{\partial^2 KE}{\partial\dot{\theta}_i\partial\dot{\theta}_j} \tag{B.10}$$

The term $V(\Theta, \dot{\Theta})$ includes the Coriolis forces and centrifugal forces.

$$V(\Theta, \dot{\Theta}) = \frac{\partial^2 KE}{\partial\Theta\partial\dot{\Theta}^T}\dot{\Theta} - \frac{\partial KE}{\partial\Theta} \tag{B.11}$$

The gravity term, $G(\Theta)$ originates from the potential energy.

$$G(\Theta) = \frac{\partial PE}{\partial \Theta^T} = \left[\frac{\partial PE}{\partial \theta_1} \; \frac{\partial PE}{\partial \theta_2} \; \frac{\partial PE}{\partial \theta_3} \; \frac{\partial PE}{\partial \theta_4}\right]^T \tag{B.12}$$

Before solving for these terms it is helpful to define the following notation.

$$\begin{aligned}
c_1 &= \cos(\theta_1) \\
c_2 &= \cos(\theta_2) \\
c_{23} &= \cos(\theta_2 + \theta_3) \\
c_{24} &= \cos(\theta_2 + \theta_3 + \theta_4) \\
s_1 &= \sin(\theta_1) \\
s_2 &= \sin(\theta_2) \\
s_{23} &= \sin(\theta_2 + \theta_3) \\
s_{24} &= \sin(\theta_2 + \theta_3 + \theta_4)
\end{aligned} \tag{B.13}$$

These trigonometic evaluations can then be multiplied to form the following variables.

$$\begin{aligned}
a_{c_2} &= a_2 c_2 \\
a_{c_3} &= a_3 c_{23} \\
a_{c_4} &= a_4 c_{24} \\
a_{c_{23}} &= a_{c_2} + a_{c_3} \\
&\vdots \\
a_{c_{24}} &= a_{c_2} + a_{c_3} + a_{c4} \\
a_{c_{14}} &= a_1 + a_{c_2} + a_{c_3} + a_{c_4} \\
a_{s_2} &= a_2 s_2 \\
&\vdots \\
a_{s_{24}} &= a_{s_2} + a_{s_3} + a_{s_4}
\end{aligned} \tag{B.14}$$

$$
\begin{aligned}
c_{\gamma_1} &= cos(\gamma_1) \\
c_{\gamma_2} &= cos(\gamma_2) \\
c_{\gamma_3} &= cos(\gamma_3) \\
c_{\gamma_4} &= cos(\gamma_4) \\
c_{2\gamma_2} &= cos(\theta_2 + \gamma_2) \\
c_{2\gamma_3} &= cos(\theta_{23} + \gamma_3) \\
c_{2\gamma_4} &= cos(\theta_{24} + \gamma_4)
\end{aligned}
\tag{B.15}
$$

$$
\begin{aligned}
s_{\gamma_1} &= sin(\gamma_1) \\
s_{\gamma_2} &= sin(\gamma_2) \\
s_{\gamma_3} &= sin(\gamma_3) \\
s_{\gamma_4} &= sin(\gamma_4) \\
s_{2\gamma_2} &= sin(\theta_2 + \gamma_2) \\
s_{2\gamma_3} &= sin(\theta_{23} + \gamma_3) \\
s_{2\gamma_4} &= sin(\theta_{24} + \gamma_4)
\end{aligned}
\tag{B.16}
$$

The angular velocity terms are as follows.

$$
\omega_1 = \begin{bmatrix} 0 \\ 0 \\ \dot{\theta}_1 \end{bmatrix} \tag{B.17}
$$

$$
\omega_2 = \begin{bmatrix} -s_2\dot{\theta}_1 \\ c_2\dot{\theta}_1 \\ \dot{\theta}_2 \end{bmatrix} \tag{B.18}
$$

$$
\omega_3 = \begin{bmatrix} -s_{23}\dot{\theta}_1 \\ c_{23}\dot{\theta}_1 \\ \dot{\theta}_2 + \dot{\theta}_3 \end{bmatrix} \tag{B.19}
$$

$$\omega_{4|1} = \begin{bmatrix} -s_{24}\dot{\theta}_1 \\ c_{24}\dot{\theta}_1 \\ \dot{\theta}_2 + \dot{\theta}_3 + \dot{\theta}_4 \end{bmatrix} \tag{B.20}$$

It can be shown that the centroidal velocities are

$$\mathbf{v}_{c_1} = \begin{bmatrix} 0 \\ c_1 c_{\gamma_1}\dot{\theta}_1 \\ 0 \end{bmatrix} \tag{B.21}$$

$$\mathbf{v}_{c_2} = \begin{bmatrix} -l_2 s_{2\gamma_2}\dot{\theta}_2 \\ (a_1 + l_2 c_{2\gamma_2})\dot{\theta}_1 \\ l_2 c_{2\gamma_2}\dot{\theta}_2 \end{bmatrix} \tag{B.22}$$

$$\mathbf{v}_{c_3} = \begin{bmatrix} -(a_{s_2} + l_3 s_{2\gamma_3})\dot{\theta}_2 - l_3 s_{2\gamma_3}\dot{\theta}_3 \\ (a_{c_{12}} + l_3 c_{2\gamma_3})\dot{\theta}_1 \\ (a_{c_2} + l_3 c_{2\gamma_3})\dot{\theta}_2 + l_3 c_{2\gamma_3}\dot{\theta}_3 \end{bmatrix} \tag{B.23}$$

$$\mathbf{v}_{c_4} = \begin{bmatrix} -(a_{s_{23}} + l_4 s_{2\gamma_4})\dot{\theta}_2 - (a_{s_3} + l_4 s_{2\gamma_4})\dot{\theta}_3 - l_4 s_{2\gamma_4}\dot{\theta}_4 \\ (a_{c_{13}} + l_4 c_{2\gamma_4})\dot{\theta}_1 \\ (a_{c_{23}} + l_4 c_{2\gamma_4})\dot{\theta}_2 + (a_{c_3} + l_4 c_{2\gamma_4})\dot{\theta}_3 + l_4 c_{2\gamma_4}\dot{\theta}_4 \end{bmatrix} \tag{B.24}$$

Note that $m_{ij} = m_{ji}$. For HEnRE these coefficent are shown in Equations B.25 - B.34.

$$m_{44} = I_{4_{zz}} + l_4^2 m_4 \tag{B.25}$$

$$\begin{aligned} m_{43} = m_{34} &= m_{44} + m_4 a_3 l_4 cos(\theta_4 + \gamma_4) \\ &= I_{4_{zz}} + m_4(l_4^2 + a_3 l_4 cos(\theta_4 + \gamma_4)) \end{aligned} \tag{B.26}$$

$$\begin{aligned} m_{42} = m_{24} &= m_{43} + a_2 l_4 cos(\theta_{34} + \gamma_4) m_4 \\ = I_{4_{zz}} &+ m_4(l_4^2 + a_3 l_4 cos(\theta_4 + \gamma_4) + a_2 l_4 cos(\theta_{34} + \gamma_4)) \end{aligned} \tag{B.27}$$

$$\begin{aligned} m_{33} &= m_{43} + I_{3_{zz}} + m_3 l_3^2 + m_4(a_3^2 + a_3 l_4 cos(\theta_4 + \gamma_4)) \\ &= I_{3_{zz}} + m_3 l_3^2 + I_{4_{zz}} + m_4(a_3^2 + l_4^2 + 2a_3 l_4 cos(\theta_4 + \gamma_4)) \end{aligned} \tag{B.28}$$

$$\begin{aligned} m_{32} = m_{23} &= m_{33} + a_2 l_3 cos(\theta_3 + \gamma_3) m_3 + (a_2 a_3 cos(\theta_3) \\ &+ a_2 l_4 cos(\theta_{34} + \gamma_4)) m_4 \\ &= I_{3_{zz}} + I_{4_{zz}} + m_3(l_3^2 + a_2 l_3 cos(\theta_3 + \gamma_3)) \\ &+ m_4(a_3^2 + l_4^2 + a_2 a_3 cos(\theta_3) + a_2 l_4 cos(\theta_{34} + \gamma_4) + 2a_3 l_4 cos(\theta_4 + \gamma_4) \end{aligned} \tag{B.29}$$

$$\begin{aligned} m_{22} &= m_{32} + I_{2_{zz}} + l_2^2 m_2 + a_2 l_3 cos(\theta_3 + \gamma_3) m_3 \\ &+ m_4(a_2 a_3 cos(\theta_3) + a_2 l_4 cos(\theta_{34} + \gamma_4)) \\ &= I_{4_{zz}} + I_{2_{zz}} + I_{3_{zz}} + m_2 l_2^2 \\ &+ m_3(a_2^2 + l_3^2 + 2a_2 l_3 cos(\theta_3 + \gamma_3)) \\ &+ m_4(a_2^2 + a_3^2 + l_4^2 + 2a_2 a_3 cos(\theta_3) + 2a_2 l_4 cos(\theta_{34} + \gamma_4) + 2a_3 l_4 cos(\theta_4 + \gamma_4)) \end{aligned} \tag{B.30}$$

Note that if symmetry is assumed in the z-axis the next three equations become zero because the cross products involving z are zero. This term will be non-zero if symmetry is not assumed.

$$m_{41} = m_{14} = 0 \tag{B.31}$$

$$m_{31} = m_{13} = 0 \tag{B.32}$$

$$m_{21} = m_{12} = 0 \tag{B.33}$$

$$\begin{aligned} m_{11} &= I_{1_{zz}} + m_1(l_1 c_{\gamma_1})^2 \\ &+ s_2^2 I_{2_{xx}} + 2s_2 c_2 I_{2_{xy}} + c_2^2 I_{2_{yy}} + m_2(a_1 + l_2 c_{2\gamma_2})^2 \\ &+ s_{23}^2 I_{3_{xx}} + 2s_{23} c_{23} I_{3_{xy}} + c_{23}^2 I_{3_{yy}} + m_3(a_{c_{12}} + l_3 c_{2\gamma_3})^2 \\ &+ s_{24}^2 I_{4_{xx}} + 2s_{24} c_{24} I_{4_{xy}} + c_{24}^2 I_{4_{yy}} + m_4(a_{c_{13}} + l_4 c_{2\gamma_4})^2 \end{aligned} \tag{B.34}$$

$$V(\Theta,\dot{\Theta}) = \frac{\partial^2 KE}{\partial\Theta\partial\dot{\Theta}^T}\dot{\Theta} - \frac{\partial KE}{\partial\Theta^T} \tag{B.35}$$

$$V(\Theta,\dot{\Theta}) = \begin{bmatrix} V_1(\Theta,\dot{\Theta}) & V_2(\Theta,\dot{\Theta}) & V_3(\Theta,\dot{\Theta}) & V_4(\Theta,\dot{\Theta}) \end{bmatrix}^T \tag{B.36}$$

where

$$V_i(\Theta,\dot{\Theta}) = \frac{\partial^2 KE}{\partial\Theta\partial\dot{\theta}_i}\dot{\Theta} - \frac{\partial KE}{\partial\theta_i} \tag{B.37}$$

$$V_1(\Theta,\dot{\Theta}) = 0 \tag{B.38}$$

$$\begin{aligned} V_2(\Theta,\dot{\Theta}) = \{&c_2 s_2 (I_{2_{yy}} - I_{2_{xx}}) + (s_2^2 - c_2^2) I_{2_{xy}} + m_2(a_1 + l_2 c_{2\gamma_2}) l_2 s_{2\gamma_2} \\ &+ c_{23} s_{23} (I_{3_{yy}} - I_{3_{xx}}) + (s_{23}^2 - c_{23}^2) I_{3_{xy}} + m_3(a_{c_{12}} + l_3 c_{2\gamma_3})(a_{s_2} + l_3 s_{2\gamma_3}) \\ &+ c_{24} s_{24} (I_{4_{yy}} - I_{4_{xx}}) + (s_{24}^2 - c_{24}^2) I_{4_{xy}} - m_4(a_{c_{13}} + l_4 c_{2\gamma_4})(a_{s_{23}} + l_4 s_{2\gamma_4})\} \dot{\theta_1}^2 \end{aligned} \tag{B.39}$$

$$\begin{aligned} V_3(\Theta,\dot{\Theta}) = \{&c_{23} s_{23} (I_{3_{yy}} - I_{3_{xx}}) + (s_{23}^2 - c_{23}^2) I_{3_{xy}} + m_3(a_{c_{12}} + l_3 c_{2\gamma_3})(l_3 s_{2\gamma_3}) \\ &+ c_{24} s_{24} (I_{4_{yy}} - I_{4_{xx}}) + (s_{24}^2 - c_{24}^2) I_{4_{xy}} + m_4(a_{c_{13}} + l_4 c_{2\gamma_4})(a_{s_3} + l_4 s_{2\gamma_4})\} \dot{\theta_1}^2 \\ &+ (m_3 a_2 l_3 sin(\theta_3 + \gamma_3) + m_4 a_2 a_3 sin(\theta_3) + m_4 a_2 l_4 sin(\theta_{23} + \gamma_4))(\dot{\theta}_2^2 + \dot{\theta}_2\dot{\theta}_3) \\ &+ m_4 a_2 l_4 sin(\theta_{34} + \gamma_4)\dot{\theta}_2\dot{\theta}_4 \end{aligned} \tag{B.40}$$

$$\begin{aligned} V_4(\Theta,\dot{\Theta}) = \{&c_{24} s_{24} (I_{4_{yy}} - I_{4_{xx}}) + (s_{24}^2 - c_{24}^2) I_{4_{xy}} + m_4(a_{c_{13}} + l_4 c_{2\gamma_3}) l_4 s_{2\gamma_4}\} \dot{\theta_1}^2 \\ &+ m_4 a_2 l_4 sin(\theta_{34} + \gamma_4)(\dot{\theta}_2^2 + \dot{\theta}_2\dot{\theta}_3 + \dot{\theta}_2\dot{\theta}_4) \\ &+ m_4 a_3 l_4 sin(\theta_4 + \gamma_4)((\dot{\theta}_2 + \dot{\theta}_3)^2 + \dot{\theta}_2\dot{\theta}_4) + \dot{\theta}_3\dot{\theta}_4) \end{aligned} \tag{B.41}$$

Gravity term

$$G(\Theta) = \begin{bmatrix} \frac{\partial PE}{\partial\theta_1} & \frac{\partial PE}{\partial\theta_2} & \frac{\partial PE}{\partial\theta_3} & \frac{\partial PE}{\partial\theta_4} \end{bmatrix}^T \tag{B.42}$$

$$\frac{\partial PE}{\partial \theta_1} = 0 \tag{B.43}$$

$$\frac{\partial PE}{\partial \theta_2} = m_2 g l_2 c_{2\gamma_2} + m_3 g(a_{c_2} + l_3 c_{2\gamma_3}) + m_4 g(a_{c_2} + a_{c_3} + l_4 c_{2\gamma_4}) \tag{B.44}$$

$$\frac{\partial PE}{\partial \theta_3} = m_3 g l_3 c_{2\gamma_3} + m_4 g(a_{c_3} + l_4 c_{2\gamma_4}) \tag{B.45}$$

$$\frac{\partial PE}{\partial \theta_4} = m_4 g l_4 c_{2\gamma_4} \tag{B.46}$$

APPENDIX C

STATISTICS SUMMARY

C.1 Method

Here is a summary of the statistical tools[52] used in the analysis of the human factors tests presented in this Chapter 7. Given a sample set, X.

$$X = \{x_1, x_2, \ldots, x_n\} \tag{C.47}$$

$$\bar{x} = \frac{\sum_{i=1}^{n} x_i}{n} \tag{C.48}$$

$$S^2 = \frac{\sum_{i=1}^{n} (x_i - \bar{x})^2}{n-1} \tag{C.49}$$

Where S^2 is the unbiased sample variance assuming a normal distribution and $\bar{x}$ is the sample mean. Assuming that the real population variance, σ^2, is unknown, the $100(1-\alpha)\%$ confidence interval for the real population mean, μ, is calculated using Equation C.50. The variable t is known as the t-distribution.

$$\bar{x} - t_{\alpha/2,n-1}\frac{S}{\sqrt{n}} \leq \mu \leq \bar{x} + t_{\alpha/2,n-1}\frac{S}{\sqrt{n}} \tag{C.50}$$

It can be statistically shown that two sample spaces are not members of the same population by doing tests of hypotheses on their sample means and variances. This test is commonly referred to as a *Paired t-test*.

$$\begin{aligned} H_0 &: \mu_1 = \mu_2 \\ H_1 &: \mu_1 > \mu_2 \end{aligned} \tag{C.51}$$

The null hypothesis, H_0, is rejected if $t_0 > t_{\alpha,\nu}$. If the null hypothesis is rejected then the alternative hypothesis, H_1 is accepted with $100(1-\alpha)\%$ confidence. In other words it can be claimed that population 2 has a lower mean than population 1

with $100(1-\alpha)\%$ confidence. This method assumes that both of the real population variances are unknown and not necessarily equal.

$$t_0 = \frac{\bar{x}_1 - \bar{x}_2}{\sqrt{\frac{S_1^2}{n_1} + \frac{S_1^2}{n_2}}} \tag{C.52}$$

$$\nu = \frac{\left(\frac{S_1^2}{n_1} + \frac{S_2^2}{n_2}\right)}{\frac{\left(\frac{S_1^2}{n_1}\right)^2}{n_1+1} + \frac{\left(\frac{S_2^2}{n_2}\right)^2}{n_2+1}} - 2 \tag{C.53}$$

The value $t_{\alpha,\nu}$ can be evaluated using the Matlab command "tinv.m": $t_{\alpha,\nu} = tinv(1-\alpha,\nu)$.

C.2 Calculations

Table C.12: Confidence interval data for the digging force in Figure 7.5 which compares HEnRE and V-HEnRE.

Controller	$\bar{x}(N)$	$S(N)$	n	α	$t_{\alpha/2,n-1}$
HEnRE - Full	3850	1574	225	0.01	2.60
V-HEnRE - Full	6239	2131	993	0.01	2.58

Table C.13: Paired t-test data for digging force in Table 7.1 which compares HEnRE and V-HEnRE .

Controller #1	Controller #2	t_0	$t_{\alpha,\nu}$	α	ν	$\Delta x(N)$
V-HEnRE-full	HEnRE-full	19.1	2.34	0.01	434	2098

Table C.14: Confidence interval data for digging force peaks in Figure 7.6 which compares the V-HEnRE controllers .

Controller	$\bar{x}(N)$	$S(N)$	n	α	$t_{\alpha/2,n-1}$
half	3296	1161	1872	0.01	2.58
full	5054	1972	1290	0.01	2.58
off	6239	2131	993	0.01	2.58

Table C.15: Confidence interval data for average digging force in Figure 7.6 which compares the V-HEnRE controllers .

Controller	$\bar{x}(N)$	$S(N)$	n	α	$t_{\alpha/2,n-1}$
half	2276	338	129	0.01	2.61
full	3700	941	100	0.01	2.62
off	4474	837	78	0.01	2.64

Table C.16: Paired t-test data for digging force peaks in Table 7.2 which compares the V-HEnRE controllers.

Controller #1	Controller #2	t_0	$t_{\alpha,\nu}$	α	ν	$\Delta x(N)$
full	half	28.8	2.32	0.01	1905	1616
off	full	13.6	2.33	0.01	2049	983
off	half	40.5	2.33	0.01	1313	2774

Table C.17: Paired t-test data for average digging force in Table 7.3 which compares the V-HEnRE controllers.

Controller #1	Controller #2	t_0	$t_{\alpha,\nu}$	α	ν	$\Delta x(N)$
full	half	14.4	2.36	0.01	119	1192
off	full	5.8	2.35	0.01	175	460
off	half	22.1	2.37	0.01	92.8	1964

Table C.18: Confidence interval data for the largest force peaks in Figure 7.7 which compares the V-HEnRE controllers.

Controller	$\bar{x}(N)$	$S(N)$	n	α	$t_{\alpha/2,n-1}$
half	7006	4545	67	0.01	2.65
full	9282	3592	96	0.01	2.62
off	11965	6003	118	0.01	2.62

Table C.19: Confidence interval data for all force peaks on object in Figure 7.7 which compares the V-HEnRE controllers.

Controller	$\bar{x}(N)$	$S(N)$	n	α	$t_{\alpha/2,n-1}$
half	4272	2908	441	0.01	2.59
full	6235	3364	650	0.01	2.58
off	7728	4481	827	0.01	2.58

Table C.20: Paired t-test data for the largest force peaks on object in Table 7.4 which compares the V-HEnRE controllers.

Controller #1	Controller #2	t_0	$t_{\alpha,\nu}$	α	ν	$\Delta x(N)$
full	half	3.42	2.36	0.01	122	708
off	full	4.05	2.35	0.01	197	1128
off	half	6.33	2.35	0.01	171	3120

Table C.21: Paired t-test data for all force peaks on object in Table 7.5 which compares the V-HEnRE controllers.

Controller #1	Controller #2	t_0	$t_{\alpha,\nu}$	α	ν	$\Delta x(N)$
full	half	10.3	2.33	0.01	1030	1518
off	full	7.31	2.33	0.01	1474	1018
off	half	16.5	2.32	0.01	1221	2970

Table C.22: Confidence interval data for digging productivity in Figure 7.8 which compares the V-HEnRE controllers.

Controller	$\bar{x}(m^3/min)$	$S(m^3/min)$	n	α	$t_{\alpha/2,n-1}$
half	0.26	0.0651	129	0.01	2.61
full	0.297	0.0907	100	0.01	2.63
off	0.344	0.0916	77	0.01	2.64

Table C.23: Paired t-test data for digging productivity in Table 7.6 which compares the V-HEnRE controllers.

Controller #1	Controller #2	t_0	$t_{\alpha,\nu}$	α	ν	$\Delta x(m^3/min)$
full	half	3.209	2.35	0.01	174	0.00914
off	full	3.37	2.35	0.01	165	0.0141
off	half	6.80	2.36	0.01	123	0.0529

Table C.24: Confidence interval data for average haptic force in Figure 7.9 which compares the V-HEnRE controllers.

Controller	$\bar{x}(N)$	$S(N)$	n	α	$t_{\alpha/2,n-1}$
half	1.21	0.527	67	0.01	2.65
full	1.26	0.686	96	0.01	2.63
off	1.07	0.559	118	0.01	2.62

Table C.25: Paired t-test data for average haptic force in Table 7.7 which compares the V-HEnRE controllers.

Controller #1	Controller #2	t_0	$t_{\alpha,\nu}$	α	ν	$\Delta x(N)$
full	half	0.522	1.65	0.05	161	na
full	off	2.21	1.65	0.05	184	0.0479
half	off	1.72	1.66	0.05	146	0.00540

Table C.26: Confidence interval data for number hits if object is detected in Figure 7.10 which compares the V-HEnRE controllers.

Controller	$\bar{x}(hits)$	$S(hits)$	n	α	$t_{\alpha/2,n-1}$
half	7.62	5.01	52	0.01	2.67
full	7.42	4.75	67	0.01	2.65
off	7.74	5.04	80	0.01	2.64

Table C.27: Confidence interval data for number hits if object is not detected in Figure 7.10 which compares the V-HEnRE controllers.

Controller	$\bar{x}(hits)$	$S(hits)$	n	α	$t_{\alpha/2,n-1}$
half	3	5.57	15	0.01	2.98
full	5.28	6.35	29	0.01	2.76
off	5.47	6.54	38	0.01	2.72

Table C.28: Paired t-test data on the number of hits in Table 7.8 when the object is detect versus when it is not detected.

Controller	t_0	$t_{\alpha,\nu}$	α	ν	$\Delta x(N)$
half	2.89	1.32	0.1	22.0	2.51
full	1.63	1.30	0.1	43.1	0.431
off	1.88	1.30	0.1	59.8	0.707

Table C.29: Confidence interval data for detection time from first nick in Figure 7.11 which compares the V-HEnRE controllers.

Controller	$\bar{x}(sec.)$	$S(sec.)$	n	α	$t_{\alpha/2,n-1}$
half	33.5	24.7	52	0.01	2.68
full	31.7	22.7	67	0.01	2.65
off	37.6	22.8	80	0.01	2.64

Table C.30: Confidence interval data for detection time from hardest nick in Figure 7.11 which compares the V-HEnRE controllers.

Controller	$\bar{x}(sec.)$	$S(sec.)$	n	α	$t_{\alpha/2,n-1}$
half	11.0	16.3	52	0.01	2.68
full	9.99	10.5	67	0.01	2.65
off	9.76	11.9	80	0.01	2.64

Table C.31: Paired t-test data for first nick detection time in Table 7.10 which compares the V-HEnRE controllers.

Controller #1	Controller #2	t_0	$t_{\alpha,\nu}$	α	ν	$\Delta x(N)$
full	half	0.412	0.845	0.2	107	na
full	off	1.59	0.844	0.2	142	2.80
half	off	0.976	0.845	0.2	105	0.560

Table C.32: Paired t-test data comparing the detection time in Table 7.11 from the first nick versus the hardest hit.

Controller	t_0	$t_{\alpha,\nu}$	α	ν	$\Delta x(N)$
half	5.48	2.37	0.01	89.7	12.7
full	7.09	2.37	0.01	93.6	14.4
off	9.71	2.36	0.01	120	21.1

APPENDIX D

HUMAN TESTING PROCEDURE

Testing procedure:

1. Volunteers were give the consent form and allow time to read before signing it.
2. Volunteers were give questionnaire to fill out
3. The simulator was started in non-testing mode. This means that no data was recorded and the soil could be reset at will by the volunteer operator.
4. The test administator explained how the control works and dug a trench while the subjects watched.
5. After uncovering the objects, the simulator control was handed over to the volunteer operator so that they could feel the object.
6. Then the operator was to dig trenches and test out the simulator.
7. Once the operator felt comfortable, the simulator was restarted in test mode.
8. As part of entering test mode a subject number was entered unique to the volunteer operator.
9. An additional training was then done so assure that the operator understood how to indicate that they had detected a buried object by hitting a button at the end of the handle twice
10. These after 32 trials on the simulator, each operator did two trial or dug two trenches in the soil bin using the actual backhoe test-bed.

11. The test was complete with an open-ended survey.

Time series data collected at 100Hz

- Backhoe time: (milliseconds)
- Backhoe position: θ_1 (rad)
- Backhoe position: r (m)
- Backhoe position: z (m)
- Backhoe position: ϕ (rad)
- Backhoe force: F_r (N)
- Backhoe force: $F_z r$ (N)
- Backhoe force: τ_ϕ (N $\cdot$ m)
- Volume of dirt in backhoe's bucket: $Vload$ (cubic inches)
- Volume of dirt in pile: $Vpile$ (cubic inches)
- PHANToM Omni time: (milliseconds)
- PHANToM Omni position: x (mm)
- PHANToM Omni position: y (mm)
- PHANToM Omni position: z (mm)
- PHANToM Omni position: ϕ (rad)
- PHANToM Omni force: F_x (N)
- PHANToM Omni force: F_y (N)
- PHANToM Omni force: F_z (N)

- PHANToM Omni mode

Other data recorded:

- subject number (1-25)
- trial or trench number (1-32)
- flags (the sixteen flags that specify the control setting as an uint16)
- flagVector (the sixteen flags stored as an array of 16 booleans) flagVector: [0 0 0 0 1 0 1 0 0 0 0 0 1 1 1 0]
- Start time: (year, month, day, hour, minute, second, millisecond)
- End time: (year, month, day, hour, minute, second, millisecond)
- Final shape of trench: (an array of 256 uint8 variable which are linearly related to trench depth)

REFERENCES

[1] Adams, R. J. and Hannaford, B., "Stable haptic interaction with virtual environments," *IEEE Trans. Robot. Autom.*, vol. 15, pp. 465–474, Jun 1999.

[2] Aghili, F., "A unified approach for inverse and direct dynamics of constrained multibody system boased on linear projection operator: Application to control and simulation," *IEEE Trans. Robot.*, vol. 21, pp. 834–849, Oct 2005.

[3] Alirand, M., Favennec, G., and Lebrun, M., "Pressure components stability analysis: A revisited approach," *Intl. Journal Fluid Power*, vol. 3, pp. 33–45, Apr 2002.

[4] Allen, W. E., Anderson, P. D., Bradbury, W. J., Hadank, J. M., and League, R. B., "Coordinated control for a work implement." United States Patent (5,160,239), Nov 1992.

[5] Allen, W. E., Anderson, P. D., Bradbury, W. J., Hadank, J. M., and League, R. B., "Coordinated control for a work implement." United States Patent (5,424,623), Jun 1995.

[6] Anderson, R. J. and Spong, M. W., "Bilateral control of teleoperators with time delay," *IEEE Trans. Autom. Control*, vol. 34, pp. 494–501, May 1989.

[7] Andreychek, T., "T-Rex - a remotely operated excavator for hazartous environments," in *Proc. Seventh Topical Meeting on Robotics and Remote Systems*, (Augusta, GA), pp. 201–208, Apr 1997.

[8] Anon, "A remotely operated excavator," *Nuclear Engineering International*, vol. 37, pp. 41–43, Jan 1992.

[9] Barrientos, A., Luengo, O., and Mora, A., "Teleoperated backhoe excavator with haptic control," in *Int. Symp. Automation and Robotics in Construction*, (Madrid, Spain), pp. 491–496, Sep 1999.

[10] Berger, A. D., Chan, P. J. D. D. C., and Grupka, J. M., "Electronic control for a two-axis work implement." United States Patent (6,233,511), May 2001.

[11] Berger, A. D. and Patel, K. B., "Electronic coordinated control for a two-axis work implement." United States Patent (6,115,660), Sep 2000.

[12] Bonchis, A., Corke, P. I., and Rye, D. C., "A pressure-based, velocity independent, friction model for asymmetric hydraulic cylinders," in *Proc. Intl. Conf. Robotics and Automation*, (Detroit, MI), pp. 1746–1751, May 1999.

[13] Brandt, E. G. and Rickwood, B. D., "Apparatus and method for providing coordinated control of a work implement." United States Patent (6,374,153), Apr 2002.

[14] Brickner, C. T., Bright, E., Padgett, C. L., and Swick, W. C., "Method of modulating a boom assembly to perform in a linear manner." United States Patent (7,040,044), May 2006.

[15] Burks, B., Killough, S., and Thompson, D., "Remote excavation using the telerobotic small emplacement excavator," in *Proc. Conf. Robotics and Remote Systems Technolgy*, (Chicago,IL), pp. 170–174, Nov 1992.

[16] Cemenska, R. A., Schneider, M. P., and Buege, T. J., "Force feedback lever." United States Patent (4,800,721), Jan 1989.

[17] Ching, H. and Book, W. J., "Internet-based bilateral teleoperation based on wave variable with adaptive predictor and direct drift control," *ASME J. Dyn. Syst. Meas. and Control*, vol. 128, pp. 86–93, Mar 2006.

[18] Colgate, J. E., "Strictly positive real admittance for coupled stability," *Journal Franklin Institute*, vol. 329, no. 3, pp. 429–444, 1992.

[19] Colgate, J. E., "Coupled stability of multiport systems-theory and experiments," *ASME J. Dyn. Syst. Meas. and Control*, vol. 116, pp. 419–428, Sep 1994.

[20] Colgate, J. E., "Power and impedance scaling in bilateral manipulation," in *Proc. Intl. Conf. Robotics and Automation*, (Sacramento, CA), pp. 2292–2297, Apr 1991.

[21] Colgate, J. E. and Brown, J. M., "Factors affecting the z-width of a haptic display," in *Proc. Intl. Conf. Robotics and Automation*, (San Diego, CA), pp. 3205–3210, May 1994.

[22] DiMaio, S. and Salcudean, S. E., "A virtual environment for the simulation and programming of excavation trajectories," *Presence*, vol. 10, pp. 465–476, Oct 2001.

[23] Dorsey, J., *Continuous and Discrete Control Systems*. New York, NY: McGraw Hill, 2002.

[24] Ferrell, W. R., "Delayed force feedback," *Human Factors*, vol. 8, pp. 449–455, Oct 1967.

[25] Fite, K. B. and Goldfarb, M., "Transparency and stability robustness in two-channel bilateral telemanipulation," *ASME J. Dyn. Syst. Meas. and Control*, vol. 128, pp. 482–488, Sep 2006.

[26] Fite, K. B., Goldfarb, M., and Rubio, A., "Loop shaping for transparency and stability robustness in time-delayed bilateral telemanipulation," *ASME J. Dyn. Syst. Meas. and Control*, vol. 126, pp. 650–656, Sep 2004.

[27] Fite, K. B., Shao, L., and Goldfarb, M., "Loop shaping for transparency and stability robustness in bilateral telemanipulation," *IEEE Trans. Robot. Autom.*, vol. 20, pp. 620–624, Jun 2004.

[28] Fortgang, J., George, L., and Book, W., "Practical implementation of a dead zone inverse on a hydraulic wrist," in *ASME Intl. Mech. Engr. Congr. Expo., FPST-Vol. 9*, (New Orleans, LA), pp. 149–155, Nov 2002.

[29] Frankel, J. G., *Development of a Haptic Backhoe Testbed*. MS thesis, The Georgia Institute of Technology, G.W. Woodruff School of Mechanical Engineering, 2004.

[30] Franklin, G. F., Powell, J. D., and Emani-Naeini, A., *Feedback Control of Dynamic Systems*. Reading, MA: Addison-Wesley, 1994.

[31] Frenette, R. N. and Lawrence, P. D., "Hydraulic control system." United States Patent (5,062,264), Nov 1991.

[32] Friedland, B. and Mentzelopoulou, S., "On estimation of dynamic friction," in *Proc. Conf. Decision and Control*, (San Antonio, TX), pp. 1919–1924, Dec 1993.

[33] Gillespie, R. B. and Cutkosky, M. R., "Stable user-specific haptic rendering of the virtual wall," in *ASME Intl. Mech. Engr. Congr. Expo., DSC-Vol. 58*, (Atlanta, GA), pp. 397–406, Nov 1996.

[34] Goertz, R., "Mechanical master-slave manipulator," *Nucleonics*, vol. 12, pp. 45–46, Nov 1954.

[35] Goertz, R. and Thompson, W., "Electronically controlled manipulator," *Nucleonics*, vol. 12, pp. 46–47, Nov 1954.

[36] Goldenberg, A. A., Benhabib, B., and Fenton, R. G., "A complete generalized solution to the inverse kinematics of robots," *IEEE Trans. Robot. Autom.*, vol. 1, pp. 14–26, Mar 1985.

[37] Gosline, A. H. C. and Hayward, V., "Time-domain passivity control of haptic interfaces with tunable damping hardware," in *Proc. Eurohaptics Conf. and Symp. on Haptic Interfaces for Virtual Environment and Teleoperator Systems*, (Tsukuba, Japan), pp. 164–179, Mar 2007.

[38] Ha, B. Q., Santos, M., Nguyen, Q., Rye, D., and Durrant-Whyte, H., "Robotic excavation in construction automation," *IEEE Robotics and Automation Magazine*, vol. 9, pp. 20–28, Mar 2002.

[39] Hadank, J. M., Allen, W. E., Bradbury, W. J., and Anderson, P. D., "Intuitive joystick control for a work implement." United States Patent (5,002,454), Mar 1991.

[40] Haessig, D. A. and Friedland, B., "On the modeling and simulation of friction," *ASME J. Dyn. Syst. Meas. and Control*, vol. 113, pp. 354–362, Sep 1991.

[41] Haga, M., Hiroshi, W., and Fujishima, K., "Digging control system for hydraulic excavator," *Mechantronics*, vol. 11, pp. 665–676, Sep 2001.

[42] Hannaford, B., "A design framework for teleoperators with kinesthetic feedback," *IEEE Trans. Robot. Autom.*, vol. 5, pp. 426–434, Aug 1989.

[43] Hannaford, B. and Anderson, R., "Experimental and simulation studies of hard contact in force reflecting teleoperation," in *Proc. Intl. Conf. Robotics and Automation*, (Philadelphia, PA), pp. 584–589, Apr 1988.

[44] Hannaford, B. and Ryu, J.-H., "Time-domain passivity control of haptic interfaces," *IEEE Trans. Robot. Autom.*, vol. 18, pp. 1–10, Feb 2002.

[45] Hashtrudi-Zaad, K. and Salcudean, S. E., "On the use of local force feedback for transparent teleoperation," in *Proc. Intl. Conf. Robotics and Automation*, (Detroit, MI), pp. 1863–1869, May 1999.

[46] Hashtrudi-Zaad, K. and Salcudean, S. E., "Analysis of control architectures for teleoperation systems with impedance/admittance master and slave manipulators," *Intl. Journal Robotics Research*, vol. 20, pp. 419–445, Jun 2001.

[47] Haykin, S., *Active Network Theory*. London, England: Addison-Wesley, 1970.

[48] Heiser, R. K., Fulkerson, T. R., Hawkins, R. R., and Reed, J. R., "Boom control system." United States Patent (4,910,662), Mar 1990.

[49] Hendron, S. S., Clark, J. P., and Sulzer, B. D., "Automatic loader bucket orientation control." United States Patent (6,763,619), Jul 2004.

[50] Hendron, S. S. and Clark, J. P., "Automatic backhoe tool orientation control." United States Patent (6,609,315), Aug 2003.

[51] Heybroek, K., Larsson, J., and Palmberg, J.-O., "Open circuit solution for pump controlled actuators," in *Proc. FPNI-PhD Symp.*, (Sarasota, FL), pp. 27–40, Jun 2006.

[52] Hines, W. W., Montgomery, D. C., Goldsman, D. M., and Borror, C. M., *Probability and Statistics in Engineering*. Danvers, MA: John Wiley and Sons, Inc., 2003.

[53] Hirata, T., Yamagata, E., Watanabe, H., Haga, M., Fujishima, K., and Adachi, H., "Region limiting excavation control system for construction machine." United States Patent (5,835,874), Nov 1998.

[54] Hogan, N., "Impedance control: An approach to manipulation: Part i - theory," *ASME J. Dyn. Syst. Meas. and Control*, vol. 107, pp. 1–7, Mar 1985.

[55] Hogan, N., "Impedance control: An approach to manipulation: Part ii - implementation," *ASME J. Dyn. Syst. Meas. and Control*, vol. 107, pp. 8–16, Mar 1985.

[56] Hogan, N., "Impedance control: An approach to manipulation: Part iii - applications," *ASME J. Dyn. Syst. Meas. and Control*, vol. 107, pp. 17–24, Mar 1985.

[57] Howell, L. and Tripp, A., "Heavy-duty hydraulic manipulator," *Nucleonics*, vol. 12, pp. 48–49, Nov 1954.

[58] Inui, T., Ootsuka, K., Nogami, S., Igarashi, M., Horikoshi, T., and Izumi, K., "Semi-automatic hydraulic excavator." United States Patent (4,377,043), Mar 1983.

[59] Johnson, D. W., Lovell, G. H., and Murray, J. J., "Development of a coordinated motion controller for a front shovel excavator," in *Proc. Seventh Topical Meeting on Robotics and Remote Systems*, (Augusta, GA), pp. 239–246, Apr 1997.

[60] Karnopp, D., "Computer simulation of stick-slip friction in mechanical dynamic systems," *ASME J. Dyn. Syst. Meas. and Control*, vol. 107, pp. 100–103, Mar 1985.

[61] Käppi, T. J. and Ellman, A. U., "Analytical method for defining pressure compensator dynamics," in *ASME Intl. Mech. Engr. Congr. Expo., FPST-Vol. 7*, (Orlando, FL), pp. 121–125, Nov 2000.

[62] Kim, W. S., Tendick, F., Ellis, S. R., and Stark, L. W., "A comparison of position and rate control for telemanipulations with considerations of manipulator system dynamics," *IEEE Trans. Robot. Autom.*, vol. 3, pp. 426–436, Oct 1987.

[63] Koivo, A. J., "Kinematics of excavators (backhoes) for transferring surface material," *J. Aerospace Engineering*, vol. 7, pp. 17–32, Jan 1994.

[64] Koivo, A. J., Ramos, M. C., Kocaoglan, E., and Andrade-Cetti, J., "Modeling and control of excavator dynamics during digging operation," *J. Aerospace Engineering*, vol. 9, pp. 10–18, Jan 1996.

[65] Kontz, M. E., *Haptic Enhancement of Operator Capabilities in Hydraulic Equipment*. MS thesis, The Georgia Institute of Technology, G.W. Woodruff School of Mechanical Engineering, 2002.

[66] Kontz, M. E., Beckwith, J., and Book, W. J., "Evaluation of a teleoperated haptic forklift," in *Proc. Intl. Conf. Advanced Intelligent Mechatronics*, (Monterey, CA), pp. 295–300, Jul 2005.

[67] Kontz, M. E. and Book, W. J., "Flow control for coordinated motion and haptic feedback (under review)," *Intl. Journal Fluid Power*.

[68] Kontz, M. E. and Book, W. J., "Position/rate haptic control of a hydraulic forklift," in *ASME Intl. Mech. Engr. Congr. Expo., DSC-Vol. 72-1*, (Washington, D.C.), pp. 801–808, Nov 2003.

[69] Kontz, M. E. and Book, W. J., "Haptic enhancement of hydraulic equiupment," in *FPNI-PhD Symposium*, (Sarasota, FL), pp. 497–506, Jun 2006.

[70] Kontz, M. E. and Book, W. J., "Kinematic analysis of backhoes/excavators for closed-loop coordinated control," in *Proc. Intl. Symp. Robot Control*, (Bologna, Italy), Sep 2006.

[71] Kontz, M. E. and Book, W. J., "Electronic control of pump pressure for a small haptic backhoe," *Intl. Journal Fluid Power*, vol. 8, Aug 2007.

[72] Kontz, M. E., Book, W. J., and Frankel, J. G., "Pressure based exogenous force estimation," in *ASME Intl. Mech. Engr. Congr. Expo., FPST-Vol. 13*, (Chicago, IL), pp. 111–120, Nov 2006.

[73] Kontz, M. E., Herrera, M. C., Huggins, J. D., and Book, W. J., "Impedance shaping for improved feel in hydraulic systems(under review)," in *ASME Intl. Mech. Engr. Congr. Expo., FPST-Vol. 14*, (Seattle, WA), Nov 2007.

[74] Kontz, M. E., Huggins, J. D., Book, W. J., and Frankel, J. G., "Improved control of open-center systems for haptic applications," in *ASME Intl. Mech. Engr. Congr. Expo., DSC-Vol. 74-1A*, (Orlando, FL), pp. 823–831, Nov 2005.

[75] Kraft, B. W., "Force feedback control for backhoe." United States Patent (5,019,761), May 1991.

[76] Krishnaswamy, K. and Li, P. Y., "Bond graph based approach to passive teleoperation of a hydraulic backhoe," *ASME J. Dyn. Syst. Meas. and Control*, vol. 128, pp. 176–185, Mar 2006.

[77] Kuh, E. S. and Rohrer, R., *Theory of Linear Active Networks*. San Francisco, CA: Holden-Day, Inc, 1967.

[78] Lamgreth, R., "Smarter shovel," *Popular Science*, vol. 240, pp. 82–86, Jun 1992.

[79] Lawrence, D. A., "Stability and transparency in bilateral teleoperation," *IEEE Trans. Robot. Autom.*, vol. 9, pp. 624–637, Oct 1993.

[80] Lawrence, D. A., Pao, L. Y., Dougherty, A. M., Salada, M. A., and Pavlou, Y., "Rate-hardness: A new performance metric for haptic interfaces," *IEEE Trans. Robot. Autom.*, vol. 16, pp. 357–371, Aug 2000.

[81] Lawrence, P., Salcudean, S. E., Sepehri, N., Chan, D., Bachmann, S., Parker, N., Zhou, M., and Frenette, R., "Coordinated and force-feedback control of hydraulic excavators," in *Proc. Intl. Symp. Experimental Robotics IV*, (Stanford, CA), pp. 181–194, Jun 1995.

[82] Lawrence, P. D., Frenette, R. N., and Chan, D. C. K., "Resolved motion velocity control." United States Patent (5,312,217), May 1994.

[83] Lee, D. and Li, P. Y., "Toward robust passivity: A passive control implementation structure for mechanical teleoperators," in *Proc. Symp. Haptic Interfaces for Virtual Environment and Teleoperator Systems*, (Los Angeles, CA), pp. 132–139, Mar 2003.

[84] Lee, S.-U. and Chang, P. H., "Control of a heavy-duty robotic excavator using time delay control with switching action with integral sliding surface," in *Proc. Intl. Conf. Robotics and Automation*, (Seoul, Korea), pp. 3995–3960, May 2001.

[85] Li, P. Y., "Toward safe and human friendly hydraulics: The passive valve," *ASME J. Dyn. Syst. Meas. and Control*, vol. 122, pp. 402–409, Sep 2000.

[86] Li, P. Y. and Krishnaswamy, K., "Passive bilateral teleoperation of a hydraulic actuator using an electrohydraulic passive valve," *Intl. Journal Fluid Power*, vol. 5, pp. 43–56, Aug 2004.

[87] Lischinsky, P., Canudas de Wit, C., and Morel, G., "Friction compensation for an industrial hydraulic robot," *IEEE Control Systems Magazine*, vol. 19, pp. 25–32, Feb 1999.

[88] Liu, S. and Yao, B., "Characterization and attenuation of sandwiched deadband problem using describing function analysis and its application to electro-hydrualic systems controlled by closed-center valves," in *ASME Intl. Mech. Engr. Congr. Expo., DSC-Vol. 73-1A*, (Anaheim, CA), pp. 353–360, Nov 2004.

[89] Liu, S. and Yao, B., "Programmable valves: A solution to bypass deadband problem of electro-hydraulic systems," in *Proc. American Control Conf.*, (Boston, MA), pp. 4438–4443, Jul 2004.

[90] Llewellyn, F. B., "Some fundamental properties of transmission systems," *Proc IRE*, vol. 40, pp. 271–283, Mar 1952.

[91] L.Lohnes, R., Koch, R. D., Alig, J. S., and Price, R. J., "System for controlling movement of a work machine arm." United States Patent (6,915,599), Jul 2005.

[92] Love, L. J. and Book, W. J., "Force reflecting teleoperation with adaptive impedance control," *IEEE Trans. Syst. Man Cybern. B, Cybern*, vol. 34, pp. 159–165, Feb 2004.

[93] Love, L. J., *Adaptive Impedance Control*. Ph.d. thesis, The Georgia Institute of Technology, G.W. Woodruff School of Mechanical Engineering, 1995.

[94] Magnuson, C. and Rassmus-Gröhn, K., "Non-visual zoom and scrolling operations in a virtual haptic environment," in *EuroHaptics 2003*, (Dublin, Ireland), Jul 2003.

[95] Malaguti, F., "Soil machine interaction in digging and earthmoving automation," in *Int. Symp. Automation and Robotics in Construction*, (Brighton, UK), pp. 187–191, May 1994.

[96] Malaguti, F., "Variable structure control in excavator robot," in *Int. Symp. Automation and Robotics in Construction*, (Brighton, UK), pp. 263–267, May 1994.

[97] Malaguti, F., "Force sensor for construction machines by driving hydraulic cylinders," in *Int. Symp. Automation and Robotics in Construction*, (Taipei, Taiwan), pp. 483–487, Sep 2000.

[98] Manring, N. D., *Hydraulic Control Systems*. Hoboken, NJ: John Wiley and Sons, Inc., 2005.

[99] Massie, T. H. and Salisbury, J. K., "The PHANToM haptic interface: A device for probing virtual objects," in *ASME Intl. Mech. Engr. Congr. Expo., DSC-Vol. 55-1*, (Chicago, IL), pp. 295–301, Nov 1994.

[100] Mennen, K. C. and Plaff, J. L., "Automatic hydraulic load leveling system for a work vehicle." United States Patent (7,093,383), Aug 2006.

[101] Merritt, H., *Hydraulic Control Systems*. New York, NY: John Wiley and Sons, Inc., 1967.

[102] Minsky, M., Ouh-Young, M., Steele, O., Brooks, F., , and Behensky, "Feeling and seeing: Issues in force displays," *Computer Graphics*, vol. 24, pp. 235–243, Mar 1990.

[103] Munir, S. and Book, W. J., "Internet-based teleoperation using wave variables with prediction," *IEEE/ASME Trans. Mechatronics*, vol. 7, pp. 124–133, Jun 2002.

[104] Nguyen, Q., Ha, Q. P., Rye, D. C., and Durrant-Whyte, H. F., "Force/position tracking for electrohydraulic systems of a robotic excavator," in *Proc. Conf. Decision and Control*, (Sydney, Australia), pp. 5224–5229, Dec 2000.

[105] Niemeyer, G. and Slotine, J.-J. E., "Towards force-reflecting teleoperation over the internet," in *Proc. Intl. Conf. Robotics and Automation*, (Leuven, Belgium), pp. 1909–1915, May 1998.

[106] Opdenbosch, P., Sadegh, N., and Book, W. J., "Modeling and control of an electro-hydraulic poppet valve," in *ASME Intl. Mech. Engr. Congr. Expo., FPST-Vol. 11*, (Anaheim, CA), pp. 103–110, Nov 2004.

[107] Ostoja-Starzewski, M. and Skibniewski, M., "A master-slave manipulator for excavation and construction tasks," *Robotics and Autonomous Systems*, vol. 4, pp. 333–337, Apr 1989.

[108] Padgett, C. L., Knutson, D. M., Alig, J. S., and Swick, W. C., "Operator control station and method for a work machine having more than one function." United States Patent (6,643,577), Nov 2003.

[109] Parker, N. R., Salcudean, S. E., and Lawrence, P. D., "Application of force feedback to heavy duty hydraulic machines," in *Proc. Intl. Conf. Robotics and Automation*, (Atlanta, GA), pp. 375–381, May 1993.

[110] Parker, N. R., Lawrence, P. D., and Salcudean, S. E., "Velocity controller with force feedback stiffness control." United States Patent (5,513,100), Apr 1996.

[111] Pettersson, H., Krus, P., Jansson, A., and Palmberg, J.-O., "The design of pressure compensators for load sensing hydraulic systems," in *Proc. Int. Conf. Control, Vol 2*, (London, UK), pp. 1456–1461, Sep 1996.

[112] Rahmfeld, R. and Ivantysynova, M., "An overview about active oscillation damping of mobile machine structure by using working hydraulics," *Intl. Journal Fluid Power*, vol. 5, pp. 5–23, Aug 2004.

[113] Raibert, M. and Craig, J. J., "Hybrid position/force control of manipulators," *ASME J. Dyn. Syst. Meas. and Control*, vol. 103, pp. 126–133, Jun 1981.

[114] Rosenberg, L., "Virtual fixtures: Perceptual tools for telerobotic manipulation," in *Proc. Virtual Reality Annual Intl. Symp.*, (Seattle, WA), pp. 76–82, Sep 1993.

[115] Ryu, J.-H., Kwon, D.-S., and Hannaford, B., "Stability guarenteed control: Time domain passivity approach," *IEEE Trans. Control Syst. Technol.*, vol. 12, pp. 860–868, Nov 2004.

[116] Ryu, J.-H., Kwon, D.-S., and Hannaford, B., "Stable teleoperation with time-domain passivity control," *IEEE Trans. Control Syst. Technol.*, vol. 20, pp. 365–373, Apr 2004.

[117] Sahm, W. C. and Koehrsen, C. L., "Positioning system for an excavating work machine." United States Patent (7,079,931), Jul 2006.

[118] Salcudean, S. E. and Vlaar, T. D., "On the emulation of stiff walls and static friction with a magnetically levitated input/output device," *ASME J. Dyn. Syst. Meas. and Control*, vol. 1997, pp. 127–132, Mar 1997.

[119] Salcudean, S. E., Wong, N. M., and Hollis, R. L., "Design and control of a force-reflecting teleoperation system with magnetically levitated master and wrist," *IEEE Trans. Robot. Autom.*, vol. 11, pp. 844–858, Dec 1995.

[120] Salcudean, S. E., Hashtrudi-Zaad, K., Tafazoli, S., DiMaio, S. P., and Reboulet, C., "Bilateral matched impedance teleoperation with applications to excavator control," *IEEE Control Systems Magazine*, vol. 19, pp. 966–971, Dec 1999.

[121] Sepehri, N., Lawrence, P. D., Sassani, F., and Frenette, R., "Resolved-mode teleoperation control of heavy-duty hydraulic machines," *ASME J. Dyn. Syst. Meas. and Control*, vol. 116, pp. 232–240, Jun 1994.

[122] Sepehri, N., Frenette, R. N., and Lawence, P. D., "Hydraulic control system with pressure responsive rate control." United States Patent (5,218,820), Jun 1993.

[123] Sheridan, T., "Telerobotics," *Automatica*, vol. 25, pp. 487–507, Jul 1989.

[124] Slotine, J.-J. E. and Li, W., *Applied Nonlinear Control*. Upper Saddle River, NJ: Prentice Hall, Inc, 1991.

[125] Song, B. and Koivo, A. J., "Neural adaptive control of excavators," in *Proc. Intl. Conf. Intelligent Robots and Systems*, (Pittsburgh, PA), pp. 162–167, Aug 1995.

[126] Stentz, A., Bares, J., Singh, S., and Towe, P., "A robotic excavator for autonomous truck loading," in *Proc. Intl. Conf. Intelligent Robots and Systems*, (Victoria, B.C., Canada), pp. 1885–1893, Oct 1998.

[127] Tady, S. T., Rockwood, B. D., and Brandt, E. G., "Angular velocity control and associated method for a boom of a machine." United States Patent (6,473,679), Oct 2002.

[128] Tafazoli, S., Lawrence, P., Salcudean, S., Chan, D., Bachmann, S., and de Silva, C., "Parameter estimation and actuator friction analysis for a mini excavator," in *Proc. Intl. Conf. Robotics and Automation*, (Minneapolis, MN), pp. 329–334, Apr 1996.

[129] Tafazoli, S., Peussa, P., Lawrence, P., Salcudean, S., and de Silva, C., "Differential pwm operated solenoid valves in the pilot stage of mini excavators: Modeling and identification," in *ASME Intl. Mech. Engr. Congr. Expo., FPST-Vol. 3*, (Atlanta, GA), pp. 93–99, Nov 1996.

[130] Tafazoli, S., *Identification of Friction Effects and Structural Dynamics for Improved Control of Hydraulic Manipulators*. Ph.d. thesis, The University of British Columbia, Department of Electrical Engineering, 1997.

[131] Tafazoli, S., de Silva, C. W., and Lawrence, P. D., "Tracking control of an electrohydraulic manpulator in the presence of friction," *IEEE Trans. Control Syst. Technol.*, vol. 6, pp. 401–411, May 1998.

[132] Tafazoli, S., Lawrence, P. D., and Salcudean, S. E., "Identification of inertia and friction parameters for excavator arms," *IEEE Trans. Robot. Autom.*, vol. 15, pp. 966–971, Oct 1999.

[133] Tafazoli, S., Salcudean, S. E., Hashtrudi-Zaad, K., and Lawrence, P. D., "Impedance control of a teleopered excavator," *IEEE Trans. Control Syst. Technol.*, vol. 10, pp. 355–367, May 2002.

[134] Tan, C. P., Zweiri, Y. H., Althoefer, K., and Seneviratne, L. D., "Online soil parameter estimation scheme based on newton-raphson method for autonomous excavation," *IEEE/ASME Trans. Mechatronics*, vol. 10, pp. 221–229, Apr 2005.

[135] Taware, A., Tao, G., and Teolis, C., "Design and analysis of a hybrid control scheme for sandwiched nonsmooth nonlinear systems," *IEEE Trans. Autom. Control*, vol. 47, pp. 145–150, Jan 2002.

[136] Tognetti, L. and Book, W. J., "Effects of increased device dissipation on haptic two-port network performance," in *Proc. Intl. Conf. Robotics and Automation*, (Orlando, FL), pp. 3304–3311, May 2006.

[137] Tognetti, L. J., *Improved Design and Performance of Haptic Two-Port Networks through Force Feedback and Passive Actuators*. Ph.d. thesis, The Georgia Institute of Technology, G.W. Woodruff School of Mechanical Engineering, 2005.

[138] Turro, N., Khatib, O., and Coste-Maniere, E., "Haptically augmented teleoperation," in *Proc. Intl. Conf. Robotics and Automation*, (Seoul, Korea), pp. 386–392, May 2001.

[139] Vaha, K. P. and Skibniewski, M. J., "Cognitive force control of excavators," *J. Aerospace Engineering*, vol. 6, pp. 159–166, Apr 1993.

[140] Vaha, K. P. and Skibniewski, M. J., "Dynamic model of excavator," *J. Aerospace Engineering*, vol. 6, pp. 148–158, Apr 1993.

[141] Wallerstainer, U., Lawrence, P., and Sauder, B., "A human factors evaluation of two different machine control systems for log loaders," *Ergonomics*, vol. 26, pp. 927–934, Aug 1993.

[142] Wallersteiner, U., Stager, P., and Lawrence, P., "A human factors evaluation of teleoperated hand controllers," in *Proc. Intl. Symp. Teleoperation and Control*, (Bristol, UK), pp. 291–296, Jul 1988.

[143] Watanabe, H., Fujishima, K., and Haga, M., "Slope excavation controller of hydraulic shovel, target slope setting device and slope excavation forming method." United States Patent (6,076,029), Jun 2000.

[144] Watanabe, H., Hirata, T., Haga, M., and Fujishima, K., "Excavation area setting system for area limiting excavation control in construction machines." United States Patent (5,960,378), Sep 1999.

[145] Whitney, D. E., "Resolved motion rate control of manipulators and human prostheses," *IEEE Trans. Man-Mach. Syst.*, vol. mms-10, pp. 47–53, Jun 1969.

[146] Wu, D., Burton, R., Schoenau, G., and Bitner, D., "Analysis of a pressure-compensated flow control valve," *ASME J. Dyn. Syst. Meas. and Control*, vol. 129, pp. 203–211, Mar 2007.

[147] Wu, D., Schoenau, G., Burton, R., and Bitnet, D., "Model and experimental validation of a load sensing system," *Intl. Journal Fluid Power*, vol. 6, pp. 5–18, Nov 2005.

[148] Yamagata, E., Fujishima, K., Adachi, H., Watanabe, H., and Haga, M., "Area limiting excavation control system for construction machine." United States Patent (5,735,065), Apr 1998.

[149] Yan, J. and Salcudean, S., "Teleoperation controller design using h_∞-optimization with application to motion-scaling," *IEEE Trans. Control Syst. Technol.*, vol. 4, pp. 244–258, May 1996.

[150] Yao, B., Bu, F., Reedy, J., and Chiu, G. T.-C., "Adaptive robust control of single-rod hydraulic actuators: Theory and experiments," *IEEE/ASME Trans. Mechatronics*, vol. 5, pp. 79–91, Mar 2000.

[151] Yokokohji, Y., Imaida, T., and Yoshikawa, T., "Bilateral control with energy balance monitoring under time-varying communication delay," in *Proc. Intl. Conf. Robotics and Automation*, (San Francisco, CA), pp. 2684–2689, Apr 2000.

[152] Yokokohji, Y. and Yoshikawa, T., "Bilateral control of master-slave manipulator for ideal kinesthetic coupling - formulation and experiment," *IEEE Trans. Robot. Autom.*, vol. 10, pp. 605–620, Oct 1994.

[153] Young, G. N. and Alft, K. L., "Underground utility detection system and method." United States Patent (6,975,942), Dec 2005.

[154] Zhang, R., Alleyne, A., and Prasetiawan, E., "Modeling and H_2/H_∞ MIMO control of an earthmoving vehicle powertrain," *ASME J. Dyn. Syst. Meas. and Control*, vol. 124, pp. 625–636, Dec 2002.

[155] Zhang, R. and Alleyne, A. G., "Dynamic emulation using an indirect control input," *ASME J. Dyn. Syst. Meas. and Control*, vol. 127, pp. 114–124, Mar 2005.

[156] Zhang, R., Alleyne, A. G., and Carter, D. E., "Generalized multivariable gain scheduling with robust stability analysis," *ASME J. Dyn. Syst. Meas. and Control*, vol. 127, pp. 668–687, Dec 2005.

[157] Zhang, R., Alleyne, A. G., and Prasetiawan, E. A., "Performance limitations of a class of two-stage electro-hydraulic flow valves," *Intl. Journal Fluid Power*, vol. 3, pp. 47–531, Apr 2002.

[158] Zhu, M. and Salcudean, S., "Achieving transparency for teleoperator systems under position and rate control," in *Proc. Intl. Conf. Intelligent Robots and Systems*, (Pittsburgh, PA), pp. 7–12, Aug 1995.

[159] Zilles, C. B. and Salisbury, J. K., "A constraint-based god-object method for haptic displays," in *Proc. Intl. Conf. Intelligent Robots and Systems*, (Pittsburgh, PA), pp. 146–151, Aug 1995.

VITA

Matthew Kontz was born in Portland, Oregon and grew up in Lincoln City, Oregon. He received a B.S.E. with an emphasis in Mechanical Engineering from Walla Walla College (Walla Walla University as of September 1, 2007) in 2001. At the Georgia Institute of Technology, he received an M.S.M.E in 2002 and a M.S. from Electrical and Computer Engineering in 2007. After completing his doctorial studies, he will join the Hydraulic Systems Research Group at Caterpillar Inc. His graduate research has centered on haptic control of hydraulic machinery. Prior industrial experience includes internships at Honeywell and Caterpillar and independent consulting for Ross Controls. He was the primary author on the paper receiving the 2005 ASME IMECE FPST Division Best Paper Award.